# Non-elliptical point contacts : The Torus-on-Plane conjunction

Jean-David Wheeler

N°d'ordre NNT : 2016LYSEI131

**THESE de DOCTORAT DE L'UNIVERSITE DE LYON**
opérée au sein de
**L'INSA de LYON**

**Ecole Doctorale** N° 162
**Mécanique, Energétique, Génie civil, Acoustique (MEGA)**

**Spécialité de doctorat** :
**Discipline** : Mécanique

Soutenue publiquement le 05/12/2016, par :
**Jean-David Wheeler**

---

# Non-Elliptical Point Contacts: the Torus-on-Plane Conjunction

---

Devant le jury composé de :

| | | |
|---|---|---|
| Fabre, A | Maître de Conférences HdR Arts et Métiers ParisTech | Présidente |
| Evans, HP | Professeur des Universités Cardiff University | Rapporteur |
| Venner, CH | Professeur des Universités University of Twente | Rapporteur |
| Fillot, N | Maître de Conférences HdR INSA de Lyon | Examinateur |
| Vergne, P | Directeur de Recherches CNRS | Directeur de thèse |
| Philippon, D | Maître de Conférences INSA de Lyon | Co-directeur de thèse |
| Morales-E, G | Principal Scientist HdR SKF ERC | Invité |
| Molimard, J | Professeur des Universités MINES Saint-Etienne | Invité |

| SIGLE | ECOLE DOCTORALE | NOM ET COORDONNEES DU RESPONSABLE |
|---|---|---|
| CHIMIE | **CHIMIE DE LYON**<br>http://www.edchimie-lyon.fr<br><br>Sec : Renée EL MELHEM Bat Blaise Pascal 3e etage<br>secretariat@edchimie-lyon.fr<br>Insa : R. GOURDON | M. Stéphane DANIELE<br>Institut de Recherches sur la Catalyse et l'Environnement de Lyon<br>IRCELYON-UMR 5256<br>Équipe CDFA<br>2 avenue Albert Einstein 69626 Villeurbanne cedex<br>directeur@edchimie-lyon.fr |
| E.E.A. | **ELECTRONIQUE, ELECTROTECHNIQUE, AUTOMATIQUE**<br>http://edeea.ec-lyon.fr<br><br>Sec : M.C. HAVGOUDOUKIAN<br>Ecole-Doctorale.eea@ec-lyon.fr | M. Gérard SCORLETTI<br>Ecole Centrale de Lyon<br>36 avenue Guy de Collongue<br>69134 ECULLY<br>Tél : 04.72.18 60.97 Fax : 04 78 43 37 17<br>Gerard.scorletti@ec-lyon.fr |
| E2M2 | **EVOLUTION, ECOSYSTEME, MICROBIOLOGIE, MODELISATION**<br>http://e2m2.universite-lyon.fr<br><br>Sec : Safia AIT CHALAL<br>Bat Darwin - UCB Lyon 1<br>04.72.43.28.91<br>Insa : H. CHARLES<br>Safia.ait-chalal@univ-lyon1.fr | Mme Gudrun BORNETTE<br>CNRS UMR 5023 LEHNA<br>Université Claude Bernard Lyon 1<br>Bât Forel<br>43 bd du 11 novembre 1918<br>69622 VILLEURBANNE Cédex<br>Tél : 06.07.53.89.13 e2m2@ univ-lyon1.fr |
| EDISS | **INTERDISCIPLINAIRE SCIENCES SANTE**<br>http://www.ediss-lyon.fr<br><br>Sec : Safia AIT CHALAL<br>Hôpital Louis Pradel - Bron<br>04 72 68 49 09<br>Insa : M. LAGARDE<br>Safia.ait-chalal@univ-lyon1.fr | Mme Emmanuelle CANET-SOULAS<br>INSERM U1060, CarMeN lab, Univ. Lyon 1<br>Bâtiment IMBL<br>11 avenue Jean Capelle INSA de Lyon<br>696621 Villeurbanne<br>Tél : 04.72.68.49.09 Fax :04 72 68 49 16<br>Emmanuelle.canet@univ-lyon1.fr |
| INFOMATHS | **INFORMATIQUE ET MATHEMATIQUES**<br>http://infomaths.univ-lyon1.fr<br>Sec : Renée EL MELHEM<br>Bat Blaise Pascal<br>3e etage infomaths@univ-lyon1.fr | Mme Sylvie CALABRETTO<br>LIRIS – INSA de Lyon<br>Bat Blaise Pascal<br>7 avenue Jean Capelle<br>69622 VILLEURBANNE Cedex<br>Tél : 04.72. 43. 80. 46 Fax 04 72 43 16 87<br>Sylvie.calabretto@insa-lyon.fr |

| | | |
|---|---|---|
| Matériaux | **MATERIAUX DE LYON**<br>http://ed34.universite-lyon.fr<br><br>Sec : M. LABOUNE<br>PM : 71.70 –Fax : 87.12<br>Bat. Saint Exupéry<br>Ed.materiaux@insa-lyon.fr | M. Jean-Yves BUFFIERE<br>INSA de Lyon<br>MATEIS<br>Bâtiment Saint Exupéry<br>7 avenue Jean Capelle<br>69621 VILLEURBANNE Cedex<br>Tél : 04.72.43 71.70 Fax 04 72 43 85 28<br>Ed.materiaux@insa-lyon.fr |
| MEGA | **MECANIQUE, ENERGETIQUE, GENIE CIVIL, ACOUSTIQUE**<br>http://mega.universite-lyon.fr<br><br>Sec : M. LABOUNE<br>PM : 71.70 –Fax : 87.12 Bat. Saint Exupéry<br>mega@insa-lyon.fr | M. Philippe BOISSE<br>INSA de Lyon<br>Laboratoire LAMCOS<br>Bâtiment Jacquard<br>25 bis avenue Jean Capelle<br>69621 VILLEURBANNE Cedex<br>Tél : 04.72 .43.71.70 Fax : 04 72 43 72 37<br>Philippe.boisse@insa-lyon.fr |
| ScSo | **ScSo** *<br>http://recherche.univ-lyon2.fr/scso/<br><br>Sec : Viviane POLSINELLI<br>Brigitte DUBOIS Insa : J.Y. TOUSSAINT<br>viviane.polsinelli@univ-lyon2.fr | Mme Isabelle VON BUELTZINGLOEWEN<br>Université Lyon 2<br>86 rue Pasteur<br>69365 LYON Cedex 07<br>Tél : 04.78.77.23.86 Fax : 04.37.28.04.48 |

*ScSo : Histoire, Géographie, Aménagement, Urbanisme, Archéologie, Science politique, Sociologie, Anthropologie

# Résumé

Cette thèse est dédiée à l'étude des contacts lubrifiés tore-plan sous diverses conditions. Ces contacts se situent à l'interface entre l'extrémité torique des rouleaux et le collet de la bague dans les roulements à rouleaux. La première complexité de cette étude provient de la géométrie particulière des solides concernés. La deuxième est générée par la cinématique complexe qui règne dans ces contacts. Afin de comprendre les mécanismes physiques à l'œuvre, une approche duale (expérimentale et numérique) est adoptée.

Le banc d'essai Jérotrib permet une première étude basée sur l'hypothèse que le contact élastohydrodynamique tore-plan est similaire à un contact elliptique équivalent. Grâce à une méthode d'interférométrie optique en lumière blanche qui a été adaptée aux spécificités du contact en question, des mesures précises de l'épaisseur de film ont été effectuées dans un nombre significatif de conditions. Sur cette base, un modèle numérique thermo-élastohydrodynamique a été validé avec précision. Ce dernier a permis d'étudier les écoulements de fluide à l'entrée du contact afin de mettre en évidence leur influence sur le champ d'épaisseur de film.

Le modèle numérique a ensuite été amélioré afin de prendre en compte la vraie forme des solides. Il a été validé en épaisseur de film par le banc d'essai Tribogyr, dans des conditions similaires à celles rencontrées dans les vrais roulements. Il a été montré que le cisaillement du fluide est responsable de l'échauffement des solides, qui diminue par suite l'épaisseur de film : ceci souligne la nécessité de modéliser cet échauffement global pour prédire la séparation des surfaces. Par ailleurs, lors de l'étude, le champ de pression et d'épaisseur de film ont perdu leurs symétries à cause de la cinématique et de la forme des solides. Toutefois, le comportement du contact est resté similaire à celui d'un contact elliptique, en dehors de certains cas limites.



# Abstract

This thesis is dedicated to the study of torus on plane contacts under various operating conditions. They can be found at the interface between the torus roller-end and the flange in roller bearings. The first challenge of this thesis is to deal with unusual mating geometries. The other challenge is the presence of a complex kinematic which operates in these contacts. In order to further develop the understanding of such a contact, a dual approach (experimental and numerical) is adopted.

The Jérotrib test-rig enables a first study, by considering that the elastohydrodynamic torus on plane contact can be modelled by an elliptical equivalent contact. Thanks to a differential colorimetric interferometry method which was improved and adapted during the thesis, precise film thickness measurements are carried out under a rather wide range of operating conditions. A thermo-elastohydrodynamic numerical model is developed and validated by comparing its results to the ones of the test-rig. A numerical study on film forming is then proposed and the role of the contact ellipticity is investigated.

The numerical model is improved in order to take into account the actual shape of the solids. A film thickness validation of the model is proposed, thanks to measurements performed on the Tribogyr test-rig. The operating conditions are very similar to the one encountered in actual bearings, and the mating solids have representative geometries: it is an actual torus-on-plane contact. It is demonstrated that the lubricant shearing is responsible for the solids temperature rise, which in its turn, reduces the film thickness. It appears mandatory to be able to predict this global warming of the bodies. It is also demonstrated that the pressure and film thickness distributions lose their symmetry because of the spinning kinematic and the solids shape. However, the behaviour of the torus-on-plane contact appears very similar to the one of an elliptical equivalent contact, apart from some limit cases.

# Preface

It is with gratitude that I would like to introduce my thesis work. Firstly, I would like to thank my official supervisors, David and Philippe for their commitment in the Tribogyr project but also their interpersonal skills. Together with Nicolas F. and Guillermo, they offered me a very good context in which to collaborate and develop good relationships that I am sure will be long-lasting.

My thesis work would not have been possible without the meticulous help and kindness of Nicolas D.: our common work on different test-rigs was a success. I would like to thank Nathalie for her involvement in conducting experiments for me, but also for her great contribution to the warmth of the ML2 team. I am also thankful to Gérard who joined us for most of the Tribogyr meetings and shared fruitful advice. Lionel was also of great help during my thesis, and he was a nice office mate; I hope sharing his office with three kids wasn't too annoying! (These kids do swim, run and cycle, but still…).

I had wonderful times with my friends and colleagues Nicolas V. and Vincent, and I will always remember these three years with them! Whether it was in our office, talking about science, in foreign countries discovering local customs, or in town to taste nice beers, it was always a pleasure! Thank you guys, I wish our friendship will overcome distances and years! I am also thankful to the other PhD students in our team, on the first floor but also in the LaMCoS in general: we had really nice lunch and evening times!

As this work was done in partnership with SKF, I had the chance to meet and collaborate with several colleagues. I would like to thank Ralf, Dag, Jorg, Udo, Andreas, Albrecht, Ingemar and more specifically Armando.

Kees Venner and Pwt Evans reviewed my thesis manuscript, and I am thankful for their very relevant feedbacks and questions: I will remember the teachings coming from them. I would like to thank also Agnès Fabre and Jérôme Molimard for participating to the jury, with special thanks to Jérôme for sharing ideas on interferometry.

I would like to thank my family for their presence and support during the thesis but also for who they are. Having recently become a father, I am more grateful to my parents André and Ruth for their patient and loving work since my birth. I would like to thank my brothers Timothée and Jonathan for their friendship. And I have a very special thank you for my wonderful wife Kay! You have patiently listened to my thoughts about EHD and you are so encouraging to me! Maewyn, you have joined the adventure at the latest stage, but you supported me well at the PhD defense: thank you! I hope you will enjoy discovering the nature around you.

At last, I would like to thank the Author of the wonderful world that I had the honour to explore shortly as my main activity. I find the complexity and beauty of these visible things astonishing. They show something about You. And yet, You care about us little beings…

*For God so loved the world, that he gave his only Son, that whoever believes in him should not perish but have eternal life. For God did not send his Son into the world to condemn the world, but in order that the world might be saved through him.*

*The Bible, John 3.16-17*

# Table of contents

# Résumé étendu

## Introduction

C'est après plusieurs décennies de progrès scientifiques et industriels, que l'humain a pris conscience à partir du milieu du XX$^{ème}$ siècle des contraintes écologiques du monde qui l'entoure. Ces contraintes étant aussi couplées aux contraintes de rentabilité économique, les progrès industriels actuels et futurs sont conditionnés par une meilleure compréhension des phénomènes physiques qui les régissent. Cette thèse concerne les roulements, qui sont des éléments clés dans bon nombre de mécanismes. Afin d'améliorer la longévité et de décroitre les pertes d'énergie dans ces mécanismes, l'industrie d'aujourd'hui cherche à mieux maîtriser le comportement de ces roulements. Le centre d'intérêt est ici les contacts entre le collet et les rouleaux, qui se situent entre le flanc des éléments roulants et la bague extérieure et/ou intérieure. La Figure 1.1-1 situe un de ces contacts, localisé à l'extrémité de la flèche bleue. L'élément roulant est une pièce qui accommode la différence de vitesse de rotation entre les bagues. Il peut être de forme cylindrique (roulement à rouleaux cylindriques et à aiguilles), conique (roulement à rouleaux coniques), sphérique (roulement à billes) ou encore de forme plus complexe. C'est dans les deux premières catégories que l'on retrouve principalement le contact collet-rouleau.

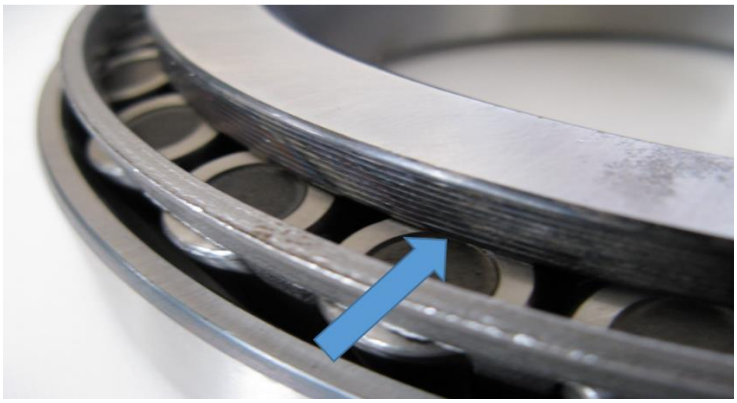

*Figure 1.1-1 - Roulement à rouleaux d'origine industrielle*

Etant chargé d'accommoder les vitesses de rotation entre les deux bagues, une cinématique complexe s'applique au contact. Le champ de vitesse du rouleau dans le repère de la bague intérieure est montré sur la Figure 1.1-2. La bague intérieure étant immobile dans ce repère, un glissement a lieu à l'interface entre l'extrémité du rouleau et le collet. Afin de limiter l'usure et le frottement, on lubrifie cette zone du roulement. Par ailleurs, différentes géométries sont

données au flanc du rouleau, dans le but d'optimiser la performance de la lubrification. Ici on étudiera le contact collet-rouleau, lorsque l'extrémité du rouleau est une portion de tore.

Cependant, pour espérer optimiser la lubrification de ce contact il est indispensable de développer une maîtrise avancée des différents phénomènes physiques qui entrent en jeu. A cause des charges importantes transmises par ces contacts, les solides se déforment significativement et le lubrifiant localisé dans l'entrefer est fortement comprimé. En réponse à cette compression, la viscosité du fluide augmente d'une façon considérable, ce qui lui permet de moins s'écouler, et d'assurer une séparation complète des surfaces lorsque celles-ci sont suffisamment lisses. Ce phénomène est appelé l'élasto-hydrodynamique (EHD). Cependant, la cinématique et la géométrie particulières sont à l'origine d'un cisaillement intense du lubrifiant, et cette sollicitation a pour effet :

- de fluidifier le liquide (effet non-Newtonien rhéo-fluidifiant) : il s'agit d'un effet rhéologique,

- et de provoquer une dissipation d'énergie importante. En réponse, la température du fluide augmente et ses propriétés rhéologiques diminuent: c'est un effet thermique.

Ces effets physiques sont connus, mais leur pleine compréhension est encore hors de portée, surtout s'ils se trouvent couplés avec la présence de solides à la géométrie inhabituelle.

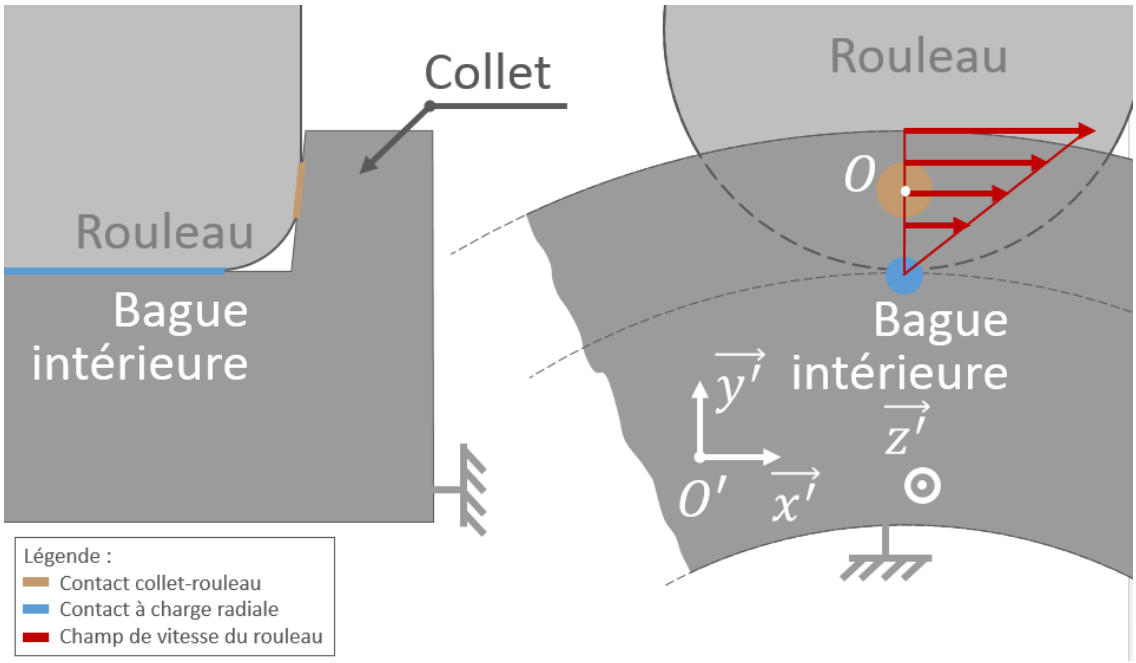


*Figure 1.1-2 – Le contact collet-rouleau*

Les solides en contact sont représentés sur la Figure 1.1-3. Le rouleau a une extrémité torique définie par le rayon mineur $R_t$ et le rayon majeur $r_t$. La bague, est de forme conique ou sphérique. Cependant, les rayons de courbures de la bague sont toujours importants, et par conséquent, la bague est représentée par un plan sur le schéma de la Figure 1.1-3 et dans la

suite de ce document. On remarque que la surface en contact à la fois avec le tore et le plan a une forme atypique : il s'agit d'un ellipsoïde courbée par l'arc de rayon $R_t + r_t \sin(\lambda)$, tel que celui représenté dans l'encart entouré d'un trait rouge pointillé. L'angle entre la normale au plan du contact et l'axe de symétrie du roulement est $\lambda$. On l'appelle angle de pivotement.

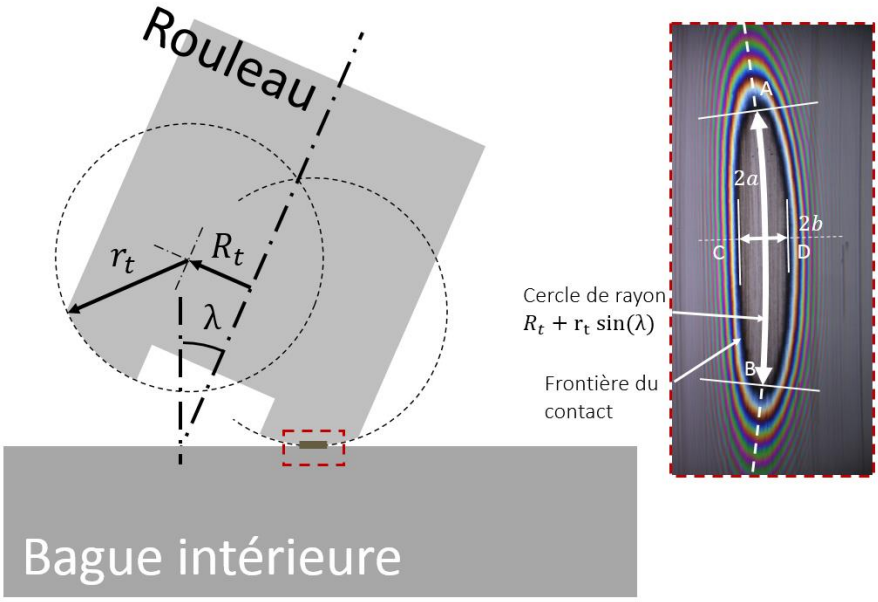


*Figure 1.1-3 – Le contact tore plan*

Faisant partie des contacts EHD ponctuels non-elliptiques, les contacts de cette étude ne trouvent que peu d'échos dans la littérature. Par conséquent, toute contribution expérimentale et numérique sur le sujet développera la connaissance que la communauté scientifique possède. Au sein des équipes de recherche et de l'industrie, on a associé pour l'instant ces contacts EHD ponctuels non-elliptiques à des contacts elliptiques équivalents qui ont les mêmes rayons de courbure au centre du contact. En l'occurrence il s'agit de contacts elliptiques étroits, mais eux aussi ont été relativement peu étudiés dans le passé. Par conséquent, on cherchera à les étudier au moyen d'une approche complémentaire de celles utilisées jusqu'ici. En particulier, on étudiera une plage variée de ratios d'ellipticité $k = b/a$, avec $b$ le demi-axe de l'ellipse perpendiculaire à l'écoulement, et $a$ le demi-axe parallèle à l'écoulement. Cette plage contiendra les contacts étroits, circulaires et larges, tels que décrits par la Figure 1.1-4, et on cherchera à isoler la variation de l'ellipticité par rapport aux variations des autres paramètres, tels que la charge ou la vitesse d'entrainement.

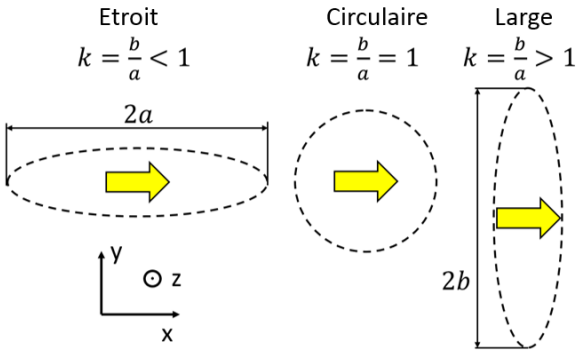


*Figure 1.1-4 – Les différentes configurations de contacts elliptiques, lorsque k varie (vitesse d'entrainement représentée par les flèches jaunes).*

Une première partie présentera les méthodes expérimentales employées dans cette thèse. On retrouvera en particulier la description d'une méthode de mesure d'épaisseur de film, et la description de deux tribomètres, Jérotrib et Tribogyr.

Dans une deuxième partie, on décrira le modèle numérique développé et employé dans les différentes études. On distinguera le modèle elliptique et le modèle tore-plan, qui sont deux versions d'un même modèle de contact.

Suite à la présentation de ces outils d'étude, une troisième partie présentera des validations apportées au modèle numérique par des expériences représentatives des conditions de fonctionnement des roulements industriels.

Enfin, la quatrième partie sera consacrée à l'étude du comportement du contact collet-rouleau. La formation du film de lubrifiant dans un contact elliptique sera analysée, afin de mieux comprendre les mécanismes physiques en jeu. Puis, dans un contact tore-plan, le rôle de l'angle de pivotement sera mis en évidence. Pour finir, une comparaison entre le modèle tore-plan et son équivalent elliptique sera proposée.

Pour conclure, une dernière section fera le bilan du travail, et explicitera les perspectives pour des travaux futurs.

### Méthodes expérimentales

Différents moyens expérimentaux ont permis d'étudier le contact EHD présenté dans l'introduction. La mesure de l'épaisseur de film est une approche assez développée dans la littérature, et elle a l'avantage de permettre à la fois l'obtention de valeurs locales de la séparation des surfaces et le champ complet de cette séparation dans la zone de contact. L'interférométrie colorimétrique en lumière blanche a été utilisée dans cette étude, et elle a été développée afin de l'adapter à des mesures sur des contacts de forme non-circulaire. Cette méthode a ensuite été employée pour des mesures avec deux bancs d'essais distincts. Le dispositif Jérotrib (présenté par Molimard (1)) a permis des mesures d'épaisseurs de film sur des contacts elliptiques étroits et larges, en plus des contacts circulaires déjà étudiés dans le passé. Tribogyr (présenté par Dormois (2)) a permis de reproduire des contact tore-plan dont la cinématique est représentative des contacts collet-rouleau de même géométrie.

*Mesure de l'épaisseur de film*

L'interférométrie colorimétrique en lumière blanche a été utilisée avec succès pour des mesures d'épaisseur de film dans les contacts EHD circulaires. Sur la base d'une méthode développée par Molimard et al. (3), des adaptations ont été effectuées. En effet, la méthode initiale nécessite que les contacts étudiés soient circulaires, car :

- dans les contacts sphère-plan statiques, on peut exprimer analytiquement l'épaisseur de film autour du contact, ce qui permet d'établir le lien entre l'épaisseur d'huile et l'intensité des couleurs des franges d'interférence, et donc d'obtenir la courbe d'étalonnage,

- et ils comportent une symétrie circulaire, ce qui autorise de moyenner les relations épaisseur d'huile – couleur, afin de diminuer le bruit de la courbe d'étalonnage.

Dans les contacts elliptiques ou tore-plan, il est possible de pallier l'absence d'expression analytique pour l'épaisseur de film autour du contact par l'analyse d'un interférogramme de ce contact en lumière monochromatique. Un de ces contacts tore-plan est représenté sur la Figure 1.1-5, sous un éclairage chromatique. Le même contact, dans les mêmes conditions opératoires, est cette fois-ci éclairé avec une lumière monochromatique, grâce à un filtre optique rouge de longueur d'onde $\lambda_{mc} = 635 \pm 4\ nm$ : l'interférogramme est présenté sur la Figure 1.1-6.

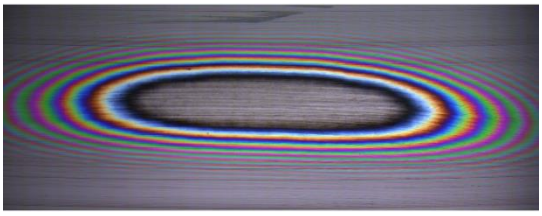

*Figure 1.1-5 - Contact tore plan éclairé en lumière blanche pour l'étape de calibration*

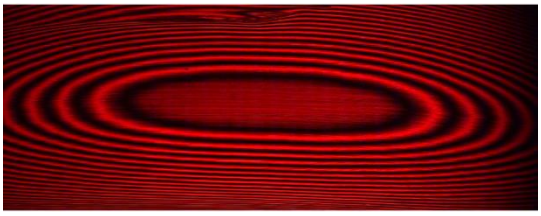

*Figure 1.1-6 - Contact tore plan éclairé en lumière monochromatique pour l'étape de calibration*

L'interférogramme de la Figure 1.1-6 permet de déterminer le bord du contact (défini par la frontière entre la zone centrale et la première frange), ainsi que le champ de l'épaisseur à la proximité du contact, grâce à la différence d'épaisseur de film qui existe entre deux franges sombres successives. Cet écart est :

$$h = \frac{\lambda_{mc}}{2\ n_{mc}} \qquad \textit{Equation 1}$$

avec $n_{mc}$ l'indice de réfraction du fluide. Toutefois, la connaissance de l'épaisseur de film au niveau des franges sombres n'est pas immédiate : l'épaisseur de film sur le lieu de la première frange sombre n'est pas connue à priori. Pour obtenir cette épaisseur, un solveur numérique a été créé. Il est capable d'obtenir la position de la frontière du contact et de calculer la hauteur

de film correspondant aux franges sombres. Sur cette base, le solveur fournit une carte de l'épaisseur de film à la proximité du contact statique. Etant donné que l'interférogramme chromatique donne la variation de la couleur sur la même zone, un second solveur établit une courbe d'étalonnage qui crée la relation entre épaisseur de film et couleur de l'image.

Le traitement des images statiques a été facilité par le développement d'une interface utilisateur, qui permet d'exploiter la capacité des solveurs d'une manière simplifiée.

Une fois la courbe d'étalonnage obtenue, il est possible d'analyser des interférogrammes EHD, comme celui représenté sur la Figure 1.1-7. En effet, la couleur de chaque pixel de l'interférogramme EHD peut être traduite en une unique épaisseur de film, permettant ainsi des mesures d'épaisseur de film précises sur ces contacts. On identifie en particulier l'épaisseur de film au centre $h_c$, les minimums d'épaisseurs de film sur les côtés $h_{m,l-}$ et $h_{m,l+}$ et le minimum de l'épaisseur de film le long de l'axe $x$ en sortie de contact qui est désigné par $h_{m,c}$.

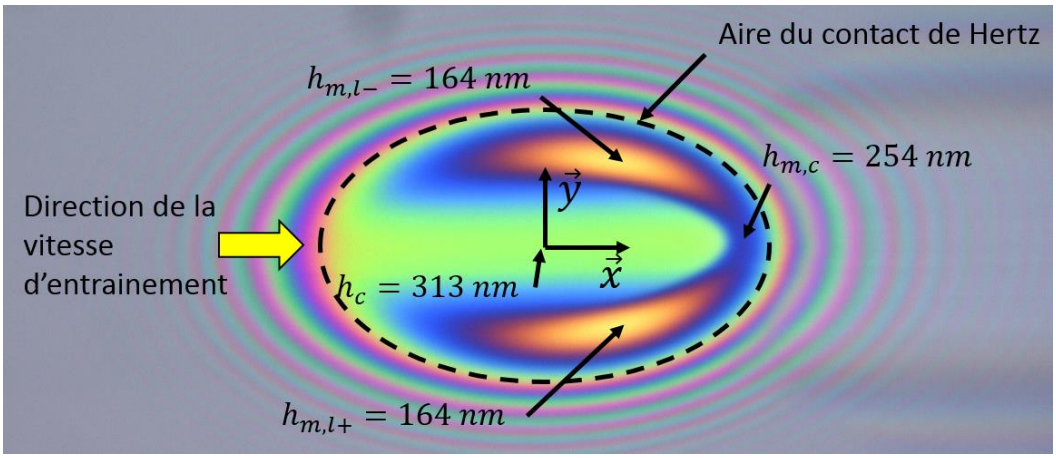


*Figure 1.1-7 – Contact elliptique EHD étroit*

### *Jérotrib*

Afin d'appliquer des conditions opératoires précises, on emploi le banc d'essai Jérotrib représenté sur la Figure 1.1-8. Il permet de reproduire des contacts lubrifiés pour des charges allant jusqu'à $w = 400\ N$ et une vitesse d'entrainement qui peut atteindre $7\ m/s$. Un disque (en verre, acier, saphir ou encore carbure de tungstène) est mis en contact avec un objet convexe de révolution en acier dont le rayon dans la direction de l'entrainement est $R_x = 12.7\ mm$ : le rayon transverse $R_y$ peut, quant à lui, varier ce qui autorise de reproduire des contacts elliptiques étroits et larges. Les deux éprouvettes ainsi que le bain d'huile dans lequel barbotte l'objet convexe sont représentés sur la Figure 1.1-9. La température de l'expérience est régulée précisément par la circulation d'un fluide caloporteur dans les parois de la cuve contenant le lubrifiant et les broches qui portent les deux éprouvettes.

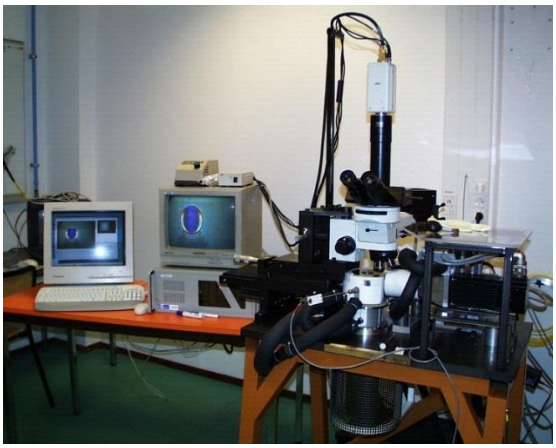

*Figure 1.1-8 – Banc d'essai Jérotrib*

Ce banc d'essai a été premièrement utilisé par Molimard et al. (1). Ces auteurs ont développé une méthode pour la mesure d'épaisseur de film dans les contacts circulaires, appelée interférométrie colorimétrique différentielle.

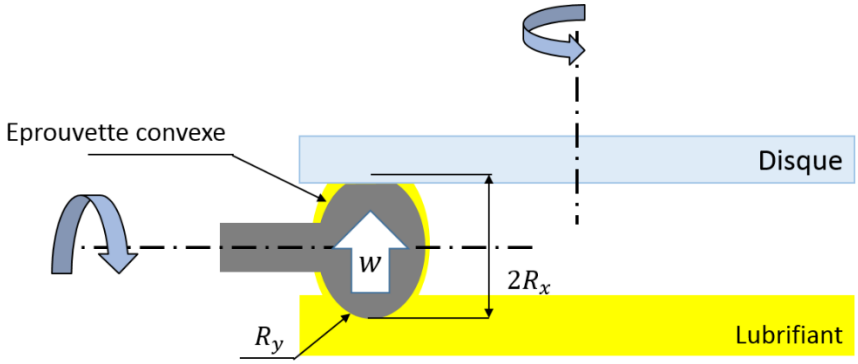


*Figure 1.1-9 – Les deux éprouvettes de Jérotrib*

Dans le contexte de cette thèse, il y a principalement deux éprouvettes convexes qui ont été utilisées sur Jérotrib. Elles sont toutes deux présentées dans la Table 1.1-1.

| **Eprouvette convexe** | $R_x$ **[mm]** | $R_y$ **[mm]** | $k = b/a$ | $a$ **[mm] *** | $b$ **[mm] *** |
|---|---|---|---|---|---|
| Elliptique étroit | 12.70 | 4.82 | 0.526 | 0.173 | 0.091 |
| Elliptique large | | 84 | 3.46 | 0.105 | 0.364 |

*Table 1.1-1 - Présentation des différentes éprouvettes convexes. Elles sont en acier ($E_b = 210e9\ Pa, \nu_b = 0.3$) et la dimension des ellipses (*) est calculée pour un contact avec un disque en verre ($E_t = 72e9\ Pa, \nu_t = 0.23$) pour $w = 20\ N$*

Par ailleurs, les propriétés physiques de ces éprouvettes sont détaillées Table 1.1-2. On remarque que les propriétés thermiques des matériaux sont données avec leurs propriétés élastiques. En effet, les contacts EHD sont sensibles à l'échauffement qui a lieu en leur sein : par conséquent les propriétés thermiques des éprouvettes en contact ont besoin d'être connues précisément.

| **Propriétés du disque en verre** | |
|---|---|
| **Paramètre [Unité]** | **Valeur** |
| $E_t\ [Pa]$ | $72 \times 10^9$ |
| $\nu_t\ [-]$ | 0.23 |
| $\rho_t\ [kg.m^{-3}]$ | 2530 |
| $k_t\ [W.m^{-1}.K^{-1}]$ | 0.937 |
| $C_{pt}\ [J.kg^{-1}.K^{-1}]$ | 880 |

| **Propriétés des éprouvettes en acier** | |
|---|---|
| **Paramètre [Unité]** | **Valeur** |
| $E_b\ [Pa]$ | $210 \times 10^9$ |
| $\nu_b\ [-]$ | 0.3 |
| $\rho_b\ [kg.m^{-3}]$ | 7850 |
| $k_b\ [W.m^{-1}.K^{-1}]$ | 50 |
| $C_{pb}\ [J.kg^{-1}.K^{-1}]$ | 470 |

*Table 1.1-2 – Propriétés des éprouvettes*

### *Tribogyr*

Un autre banc d'essai a été utilisé : il s'agit du dispositif Tribogyr représenté sur la Figure 1.1-10. La particularité de cette machine est sa capacité à reproduire des contacts collet-rouleau dans des conditions opératoires similaires à celles rencontrées dans les vrais roulements à rouleaux. En effet, la charge appliquée sur le contact ($800 - 3000\ N$), les vitesses d'entrainement ($0.5 - 10\ m/s$), les pressions de contact ($300 - 1000\ MPa$), ainsi que les particularités de la cinématique sont reproduites fidèlement.

*Figure 1.1-10 – Le banc d'essai Tribogyr*

Le collet a une extrémité torique, telle que définie sur la Figure 1.1-3. Par ailleurs, la disposition des deux éprouvettes l'une par rapport à l'autre est définie sur la Figure 1.1-11. En particulier, on note que le rayon de giration sur l'éprouvette métallique est $R_p$ tandis qu'il est désigné par $R_d$ sur le disque. La notion de rayon de giration est ici définie par la plus petite distance entre le contact rigide et l'axe de rotation. Les vitesses de rotation de ces éprouvettes sont respectivement $\Omega_b$ et $\Omega_t$. L'angle entre les axes de rotation des deux échantillons est $\lambda$.

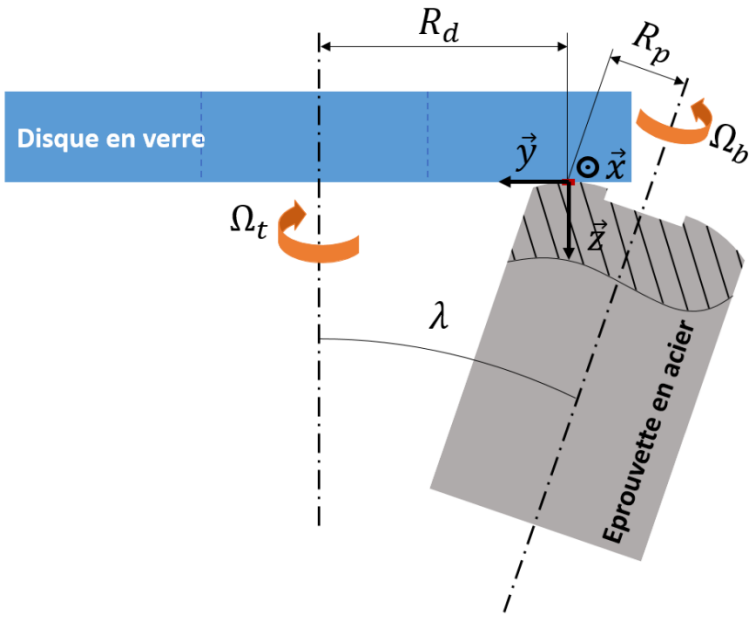


*Figure 1.1-11 – Cinématique des éprouvettes de Tribogyr*

Par conséquent, les vitesses à la surface des éprouvettes peuvent s'exprimer de la manière suivante :

$$\begin{aligned} u_{tx} &= +(R_d - y)\,\Omega_t \approx R_d\,\Omega_t \text{ as } R_d \gg y \\ u_{bx} &= -(R_p + y\cos(\lambda))\,\Omega_b \\ u_{ty} &= x\,\Omega_t \approx 0 \text{ as } x\,\Omega_t \ll x\,cos\lambda\,\Omega_b \\ u_{by} &= x\cos(\lambda)\,\Omega_b \end{aligned}$$

Equation 2

où les indices $t$ et $b$ désignent respectivement le disque en verre et l'éprouvette en acier, tandis que $x$ et $y$ indiquent la direction de la composante du champ de vitesse. Afin de déterminer précisément les vitesses à la surface des éprouvettes, il est nécessaire de connaître $R_p$ et $R_d$ : pour cela, la procédure développée par Hervé Dormois dans sa thèse (2) est améliorée et adaptée aux éprouvettes toriques. En dehors des spécificités détaillées ci-dessus, le travail de Dormois (2) présente en français et avec beaucoup de détails ce banc d'essai hors normes.

Les deux dispositifs expérimentaux présentés possèdent une certaine flexibilité dans leur utilisation, mais un modèle numérique est beaucoup plus versatile. C'est pourquoi une grande attention a été portée au développement de cet outil numérique. Sur la base du travail de Habchi (4) et de Doki-Thonon (5), des adaptations ont été effectuées afin d'inclure les spécificités de la géométrie inhabituelle du contact tore-plan.

### *Modèle de contact ponctuel elliptique*

Dans un premier temps, on adapte le modèle de contact circulaire Thermo-EHD (TEHD) non-Newtonien aux contacts elliptiques. Ce modèle permet de reproduire un très grand nombre de configurations correspondants à des cas industriels comme à des cas d'étude scientifique. Etant donné que l'essentiel de ce modèle est décrit avec précision par Habchi (4) et Doki-Thonon (5), seules les modifications apportées dans le cadre de ce travail sont exposées ici. On note en particulier sur la Figure 1.1-12 que $R_{x,t}$ peut être différent de $R_{y,t}$, et de même $R_{x,b}$ et $R_{y,b}$ peuvent différer. Ceci donne naissance aux contacts de forme elliptique.

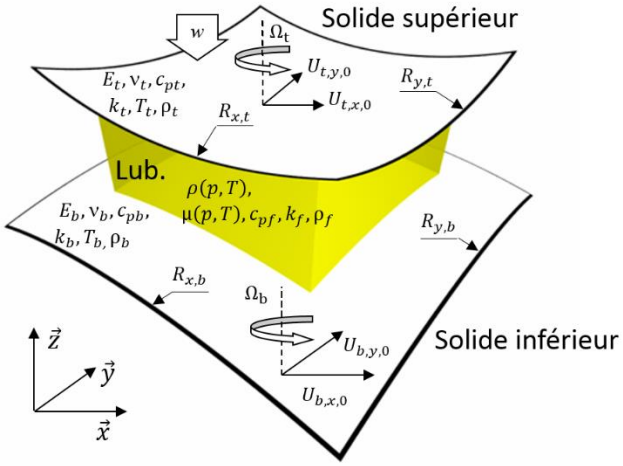


*Figure 1.1-12 – Schéma du confinement d'un lubrifiant entre deux surfaces en mouvement l'une par rapport à l'autre (inspiré de Doki-Thonon (5))*

Afin de traiter le problème EHD, on résout simultanément l'équation de Reynolds, les déformations élastiques dans les solides en contact et l'équilibre de la charge. Ces équations restent inchangées par rapport aux travaux antérieurs. Cependant, l'expression de l'épaisseur de film est enrichie par la possibilité de faire varier les rayons de courbure principaux indépendamment l'un de l'autre.

$$h(x,y) = h_0 + \frac{x^2}{2R_x} + \frac{y^2}{2R_y} + \delta(x,y) \qquad \text{Equation 3}$$

Avec $h_0$ l'écart entre les deux solides rigides et $\delta(x,y)$ les déformations.

Le modèle prend en compte les spécificités du comportement du lubrifiant sous haute pression, à savoir la compressibilité (au travers de l'équation d'état de Murnaghan (6)), la piézo-viscosité (au travers de l'équation de WLF modifié (7)) et la rhéo-fluidification (au travers de l'équation de Carreau-Yasuda (8)). Cette dernière caractéristique n'est cependant pas prise en compte dans le modèle utilisé dans la suite, faute d'avoir pu mettre en évidence le comportement non-Newtonien du lubrifiant avec les rhéomètres haute pression disponibles.

De plus, la compression du lubrifiant ainsi que la cinématique des solides imposent un échauffement au sein du fluide. Ceci se traduit par une modification des propriétés locales du lubrifiant et un modèle thermique est donc couplé au modèle EHD pour prendre en compte ce phénomène.

### *Modèle de contact ponctuel tore-plan*

Dans un deuxième temps, le modèle présenté est complexifié afin de traduire la vraie géométrie du confinement entre les deux solides : en effet, l'un des deux adopte une forme torique et il ne peut potentiellement plus être modélisé par un entrefer de forme parabolique tel que dans l'Equation 3. Cette équation est réécrite de sorte à ce qu'elle intègre la forme de l'entrefer du contact rigide à la place des termes paraboliques :

$$h(x,y) = h_0 + h_{torus}(x,y) + \delta(x,y) \qquad \text{Equation 4}$$

avec $h_{torus}$ la forme de l'entrefer du contact rigide. Pour parvenir à exprimer cet objet géométrique, on fait appel au dessin assisté par ordinateur. L'entrefer est dessiné virtuellement (voir Figure 1.1-13), puis l'expression de la hauteur de cet objet est convertie en une fonction qui dépend de la position dans le plan du contact : il s'agit de $h_{torus}$.

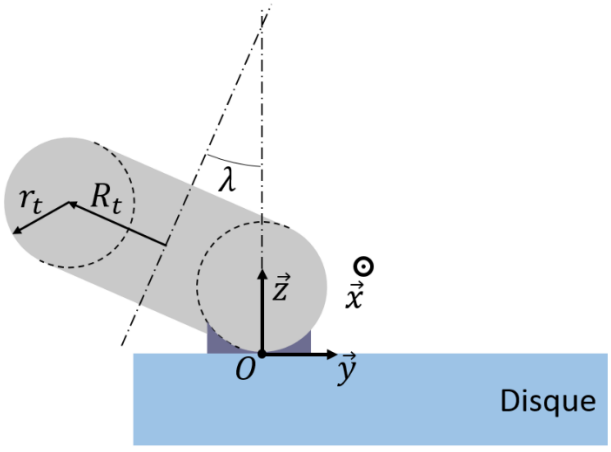


*Figure 1.1-13 – Entrefer rigide entre un tore et un plan*

### Validation du modèle numérique

Après avoir été défini, le modèle numérique est évalué par rapport à des expériences représentatives des conditions industrielles. Le modèle de contact elliptique est le premier à faire l'objet d'une validation, et l'évaluation du modèle tore-plan est présentée ensuite.

#### *Modèle de contact elliptique (Jérotrib)*

Le banc d'essai Jérotrib est utilisé et on juxtapose les résultats d'épaisseur de film de l'expérience et ceux issus du modèle numérique.

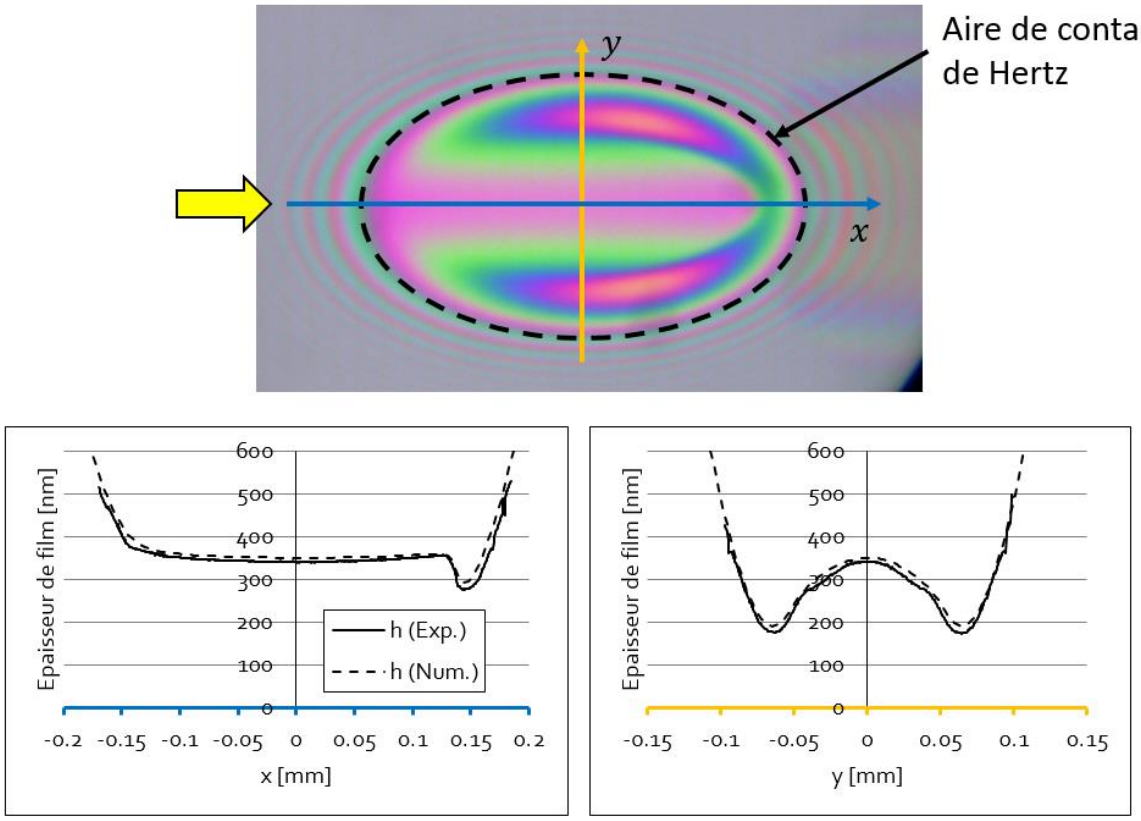


*Figure 1.1-14 – Epaisseur de film le long des axes principaux du contact ($x$ est représenté en bleu et $y$ en orange) d'un contact elliptique étroit chargé à $13\ N$. La vitesse d'entrainement ($u_e = 6.16\ m/s$) est représentée par la flèche jaune.*

La Figure 1.1-14 présente ces résultats, avec l'interférogramme en haut et les comparatifs le long des axes x et y en dessous. A partir de ces comparatifs, on remarque que le modèle est en mesure de prédire avec précision la distribution de l'épaisseur de film dans le contact EHD elliptique étroit.

#### *Modèle de contact tore-plan (Tribogyr)*

Fort de cette comparaison en contact elliptique, une comparaison similaire est effectuée dans le cas du contact tore plan. C'est avec l'aide de Tribogyr que les résultats expérimentaux sont

fournis. La Figure 1.1-15 expose ce comparatif, et on voit à nouveau que la distribution de l'épaisseur de film prédite par le modèle (en haut) et celle mesurée lors de l'expérience (en bas) sont très semblables.

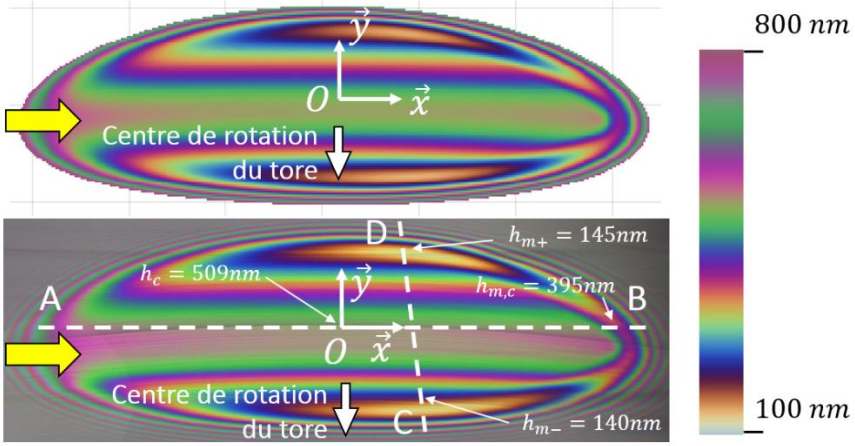


*Figure 1.1-15 – Epaisseur de film dans et autour du contact EHD tore plan – comparaison des résultats numériques (en haut) et expérimentaux (en bas) - $w = 400\ N$ & $u_{ex,0} = 2\ m/s$*

Cependant, avec ce modèle numérique, on cherche aussi à prédire le frottement au sein du contact. Afin d'évaluer les capacités du modèle, on confronte ses prédictions à des mesures effectuées sur le contact tore plan.

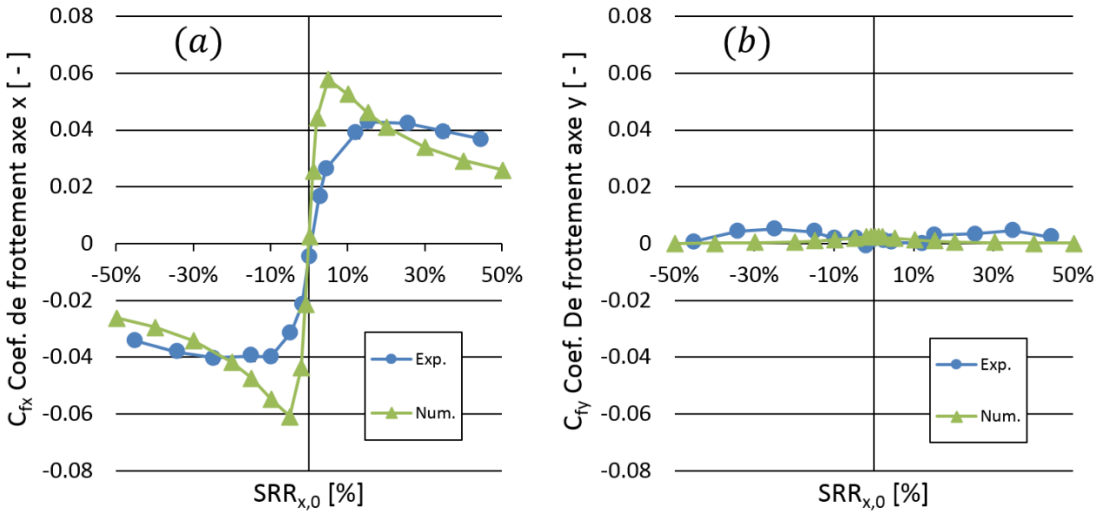


*Figure 1.1-16 – Coefficient de frottement selon l'axe $x$ (a, à gauche) et $y$ (b, à droite): comparaison entre les mesures (Exp.) et les prédictions numériques (Num.) pour $\lambda = -2.5°$*

Dans ce contexte, on montre que les résultats du modèle numérique sont bien moins proches que pour la prédiction d'épaisseur de film. La Figure 1.1-16 présente un comparatif qui souligne le manque de performance du modèle numérique pour prédire le frottement. Les

prédictions ne sont pas quantitatives, et qualitativement, les courbes numériques et expérimentales n'observent pas les mêmes tendances pour $C_{fx}$. On retiendra cependant que les ordres de grandeur du coefficient de frottement sont correctement estimés par le modèle.

En résumé, le modèle numérique présente de bonnes capacités à prédire l'épaisseur de film dans les contacts elliptiques et tore-plan, mais il est peu fiable pour prédire le frottement dans le contact. Pour cela, il faudrait probablement qu'une loi de comportement non-Newtonienne, basée sur une caractérisation indépendante, soit incluse dans le modèle numérique.

### Résultats

Grâce aux évaluations du modèle numérique, il est possible de mener une étude quantitative sur le comportement du contact EHD. En premier lieu, on mène une étude sur l'influence de l'ellipticité sur le comportement du contact EHD. Dans un deuxième temps, on étudie le contact tore-plan et on cherche ensuite à identifier s'il est possible de le modéliser par un contact elliptique équivalent.

#### *Comportement du contact elliptique*

Le contact tore-plan a été traditionnellement modélisé par un contact elliptique étroit (voir Colin et al. (9)). Cependant, ce même contact elliptique étroit reste relativement peu étudié. On consacre donc une étude à cette configuration. Les configurations de contact circulaire et de contact elliptique large sont aussi étudiées.

Dans le but d'isoler l'influence du ratio d'ellipticité $k$, on fait varier ce paramètre sans varier la pression de Hertz du contact ni son aire. Par conséquent, la charge reste constante et on maintient tous les autres paramètres identiques par ailleurs. La Figure 1.1-17 présente l'épaisseur de film en fonction de l'ellipticité. On peut faire plusieurs observations sur ce graphique :

- l'épaisseur de film au centre $h_c$ voit son maximum survenir pour $k \approx 2/3$, un contact elliptique étroit,

- il en va de même pour le minimum d'épaisseur de film sur l'axe central $h_{m,c}$,

- mais à l'opposé, $h_m = \min(h_{m,l+}, h_{m,l-}, h_{m,c})$ le minimum d'épaisseur de film global atteint son maximum pour $k \approx 2.4$, un contact elliptique large.

- Enfin, on constate que le minimum global d'épaisseur de film a lieu sur les côtés du contact pour $k \leq 2.4$ mais qu'il se déplace à la sortie du contact, le long de l'axe central pour $k \geq 2.4$.

La position du maximum de $h_c$ est assez surprenante, car on s'attendrait à ce que le contact elliptique le plus large soit celui qui assure la meilleure séparation des surfaces. Or c'est un contact elliptique plutôt étroit qui voit la meilleure séparation au centre dans le cadre de la variation des paramètres de cette étude.

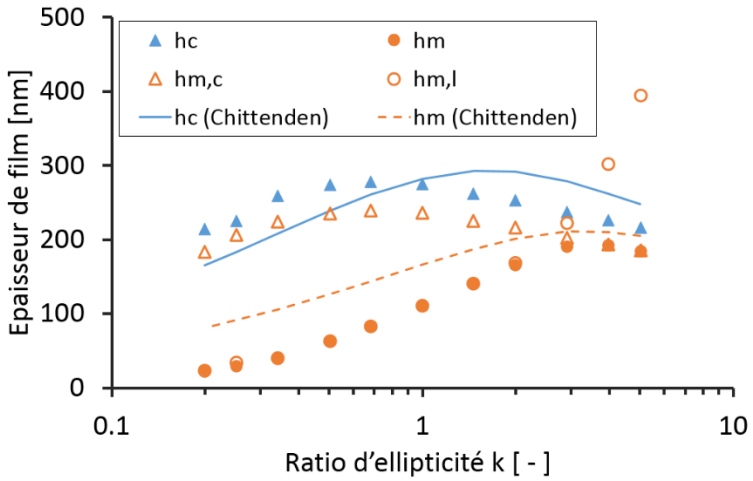


*Figure 1.1-17 – Epaisseur de film pour différents ratio d'ellipticité et pour $w = 800\ N$ et $u_e = 2\ m/s$*

On note par ailleurs que les prédictions effectuées avec la formule de Chittenden et al. (10) sont qualitativement proches des résultats des simulations par la méthode des éléments finis. Au-delà de ça, la prédiction de l'épaisseur de film au centre $h_c$ est juste à $10-20\%$ près, mais est encore meilleure pour le cas circulaire. En ce qui concerne le minimum d'épaisseur de film, les prédictions sont relativement correctes (surestimation de 10 à 30%) pour le contact elliptique large. Par contre, dans le cas du contact elliptique étroit les prédictions de Chittenden et al. (10) surestiment très fortement les résultats numériques, qui sont réputés plus justes. Cette surestimation peut atteindre 300%, ce qui invite à être particulièrement méfiant sur l'usage de la formule.

Les variations de l'épaisseur de film peuvent être reliés d'une certaine manière à la variation de la géométrie du convergent : il s'agit de la zone en amont du contact où le champ de pression se construit. Ce convergent varie en fonction de l'ellipticité.

Pour mieux comprendre les mécanismes à l'œuvre, une analyse des débits de fluide est menée dans la zone amont du contact. On définit la frontière d'étude $\mathcal{F}$ d'après la Figure 1.1-18. Au travers de cette frontière, on étudie les débits de Poiseuille et de Couette qui portent respectivement les indices $p$ et $c$. On distingue par ailleurs les débits latéraux des débits longitudinaux, annotés respectivement par les indices $y$ et $x$. On définit aussi les débits $Q_{in}$ et $Q_{out}$ qui sont respectivement les débits totaux entrant et sortant de $\mathcal{A}$ par la frontière $\mathcal{F}$. Ces derniers débits servent à exprimer des débits de Poiseuille et de Couette relatifs à la somme des débits entrants et sortant, afin de faciliter la comparaison entre les différentes configurations.

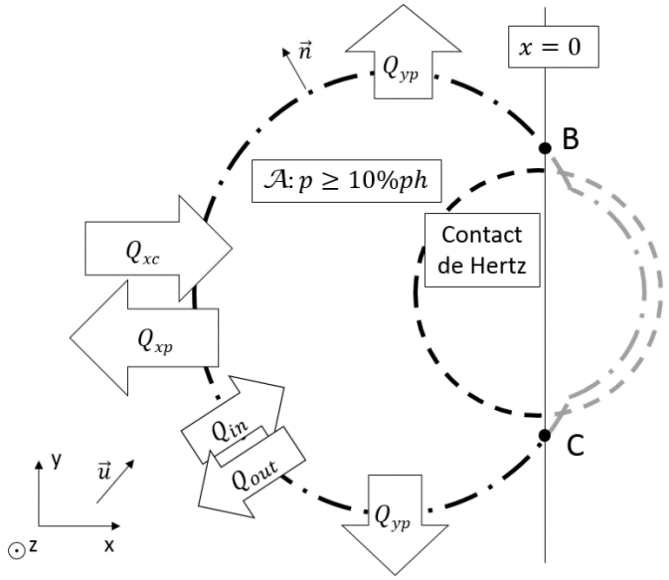


*Figure 1.1-18 – Aire de contact de Hertz (− −) et effective (appelée $\mathcal{A}$, · − ·) avec les débits de fluides traversant la frontière $\mathcal{F}$; $\mathcal{F}$ est la partie gauche (marquée par · − ·) de la frontière de $\mathcal{A}$, entre les points B et C; $\mathcal{A}$ est la surface où $p \geq 10\%p_h$*

Fort de ces grandeurs de débit, on s'attelle à identifier les rôles des différents écoulements, en fonction de l'ellipticité. Les débits relatifs tirés des simulations de la Figure 1.1-17 sont tracés sur la Figure 1.1-19. On remarque en particulier que le débit de Poiseuille longitudinal $Q_{xp}/(Q_{in} + Q_{out})$ représente l'essentiel des écoulements de Poiseuille dans le cas du contact elliptique large. Ceci révèle la présence d'un reflux important à l'entrée du contact. Inversement, on constate que $Q_{yp}/(Q_{in} + Q_{out})$ domine son équivalent longitudinal pour le contact étroit quand $k \leq 0.34$. Ceci indique que le fluide a principalement tendance à fuir le contact par les côtés. De plus, les fuites sont globalement plus importantes pour le contact elliptique étroit. Etant donné que $R_x$ est plus grand pour ce contact, les effets hydrodynamiques y sont plus faibles que pour le contact large. Ceci se cumulant avec les fuites plus importantes, la séparation des surfaces (en termes de minimum global) est moins importante pour le contact étroit.

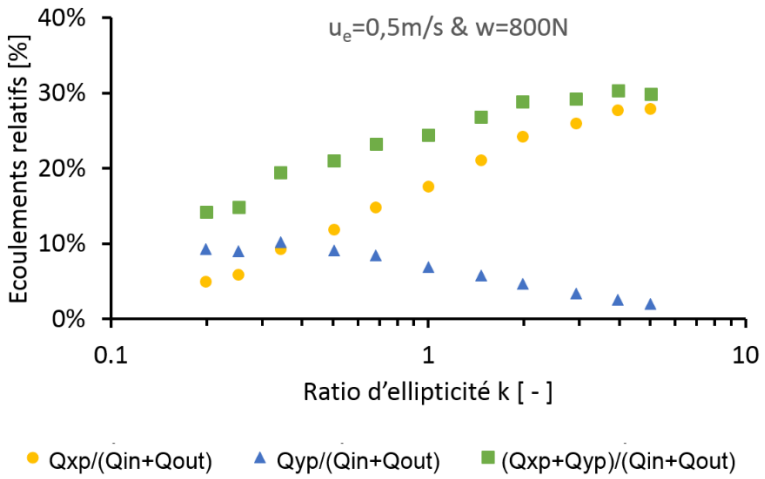


*Figure 1.1-19 – Variation des débits relatifs suite aux variations de l'ellipticité du contact pour $u_e = 2\ m/s$ & $w = 800\ N$*

### *Rôle de l'angle de spin dans le contact tore plan*

A présent, on utilise le modèle de contact tore-plan afin d'étudier cette configuration. En effet, l'influence de cette géométrie particulière sur le comportement du contact n'a encore jamais été étudiée et cela constitue un besoin particulier. On fait varier l'angle de spin, dénommé $\lambda$ dans la Figure 1.1-13. On choisit d'étudier les champs de pression et d'épaisseur de film afin de mieux comprendre le fonctionnement de ce contact atypique.

Sur la Figure 1.1-20 on observe la distribution du champ de pression. On note en particulier qu'une modification de 1.5° de l'angle de spin se traduit par de nombreux changements. Le contact est plus allongé lorsque l'angle est proche de zéro et il est aussi un peu plus étroit. Au bilan, l'airecontact augmente et la pression diminue. De plus, lorsque $\lambda$ se rapproche de zéro la zone pressurisée adopte une courbure caractéristique. L'intérieur de la courbe est tourné vers le centre de rotation de l'éprouvette torique. Malgré tout, la courbure reste ici modérée et

on peut s'interroger sur la nécessité de l'approche qui consiste à modéliser la vraie géométrie du tore.

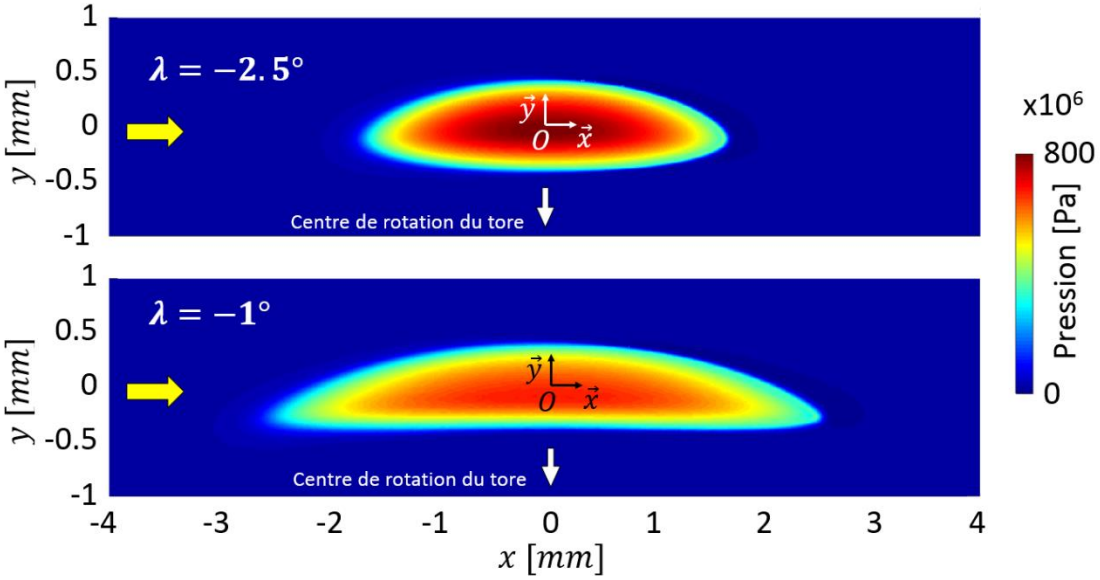


*Figure 1.1-20 – Champ de pression EHD avec un glissement nul au centre et $\lambda = -2.5°$ (haut) et $\lambda = -1°$ (bas)*

Parallèlement, sur la Figure 1.1-21 on observe que le champ d'épaisseur de film adopte les mêmes contours : ils sont assez proche d'un contact elliptique pour $\lambda = -2.5°$ et avec une courbure marquée pour $\lambda = -1°$. On note que les lignes d'iso-épaisseur de film à l'intérieur du contact suivent la courbure. Enfin, on remarque que le long de l'axe $x = 0$, le maximum de l'épaisseur de film se situe à peu près au niveau de $y = 0$ pour $\lambda = -2.5°$ mais qu'il est décalé vers les $y$ négatifs pour $\lambda = -1°$. Une analyse détaillée montre que ce décalage est dû à l'asymétrie du champ de la vitesse d'entrainement (champ comportant du pivotement), mais aussi à l'asymétrie des objets en contact.

Sur cette même figure, on remarque que les minima d'épaisseur de film sont réduits quand $\lambda$ s'approche de 0°.

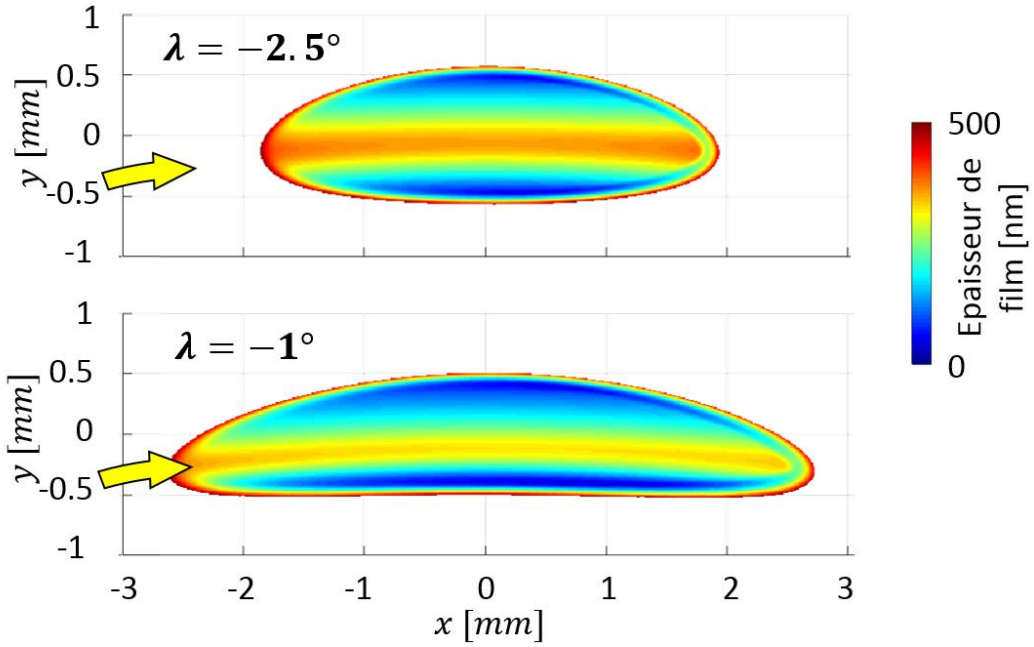


*Figure 1.1-21 – Champ de l'épaisseur de film avec un glissement nul au centre et $\lambda = -2.5°$ (haut) et $\lambda = -1°$ (bas)*

### *Opportunités de simplification du modèle de contact tore-plan*

Il a été montré que le contact tore plan reste relativement proche d'un contact elliptique étroit. Cependant, on souhaite quantifier cette proximité. Ainsi, on définit le contact elliptique équivalent (EE) au contact tore-plan (TOP) : le modèle EE a les mêmes rayons de courbures principaux équivalents que le modèle TOP au centre du contact. On compare ensuite les deux approches d'une manière quantifiée, sur l'épaisseur de film et le maximum de pression. Sur la Figure 1.1-22, on observe que l'épaisseur de film prédite avec les modèles TOP et EE est très semblable pour $h_c$, $h_{m,l+}$ et $h_{m,l-}$. Cependant, on peut observer que pour $\lambda = -0.5°$, l'écart grandit sur les minima d'épaisseur de film. Cela n'est pas très visible sur la Figure 1.1-22, mais le tableau comparatif ci-dessous explicite les choses :

| | **TOP** | **EE** | **Ecart relatif** |
|---|---|---|---|
| $\min(h_{m,l+}, h_{m,l-})\ [nm]$ | 34 | 43 | +27% |

Avec le modèle EE on surestime l'épaisseur de film. En effet, on observe en réalité un désaccord marqué entre la forme du champ de la vitesse d'entrainement et la forme de la zone pressurisée : le lubrifiant qui entre dans la zone du contact et sépare les surfaces est extrait d'une manière anticipée. Or ce phénomène n'est pas pris en compte par le modèle EE. Une quantité de lubrifiant plus faible sépare les surfaces que celle prédite par ce dernier modèle.

En règle générale, un modèle de type EE donnera des résultats satisfaisants, mais dans les cas où $\lambda$ est faible voire très faible, on risque d'effectuer de mauvaises prédictions.

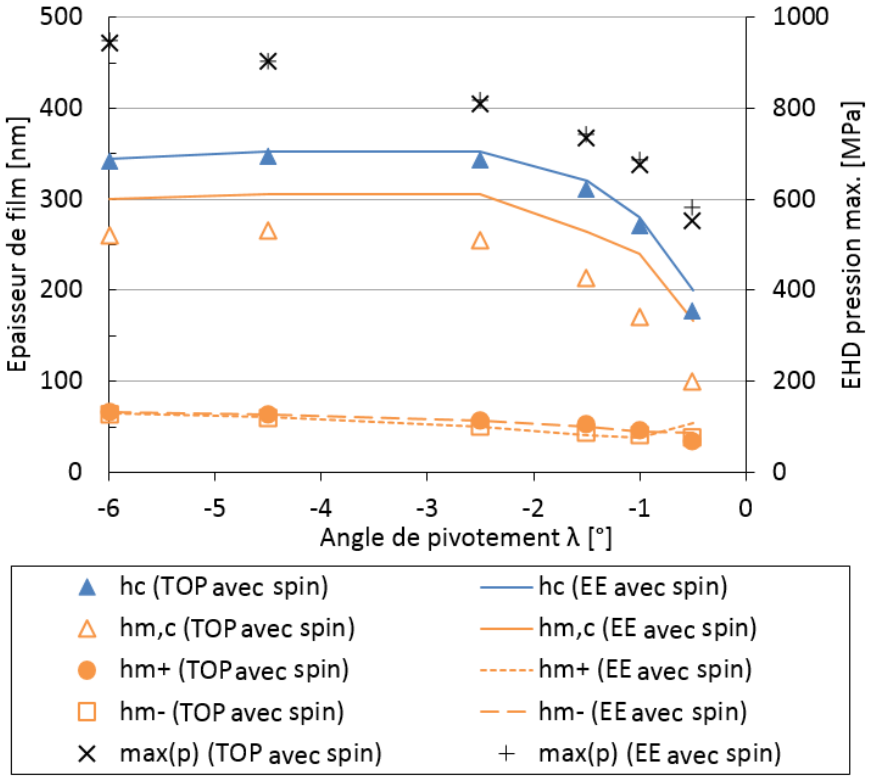


*Figure 1.1-22 – Comparaison de l'épaisseur de film et de la pression EHD maximum pour les modèles TOP et EE*

## Conclusion

Cette thèse portant sur les contacts tore-plan a pu apporter de nouveaux outils expérimentaux et numériques pour l'étude de cette configuration inhabituelle. Les obstacles liés à la présence de géométries particulières ont été levés et l'outil numérique présenté a été validé au travers d'expériences représentatives des conditions opératoires des roulements réels.

En modélisant ce contact collet-rouleau de type tore-plan par une ellipse, on a pu déterminer le rôle de la géométrie sur l'écoulement de fluide ainsi que sur l'épaisseur de film. De plus, en utilisant le modèle représentant la géométrie tore-plan, il a été possible de montrer l'influence de la position du tore par rapport au plan sur le comportement du contact. Enfin, il a été montré que le contact tore-plan peut être modélisé par un contact équivalent elliptique au lieu d'un modèle tore-plan ; néanmoins cette simplification requiert de la prudence car les deux modèles prédisent des résultats qui diffèrent de plus en plus lorsque l'angle de pivotement s'approche de 0°.

Grâce à ces développements, de nouveaux outils et de nouvelles notions sont disponibles pour la conception de roulements à rouleaux plus performants.

# Nomenclature

| Variable | Unit | Description |
|---|---|---|
| | | **Roman characters** |
| $\mathcal{A}$ | $[-]$ | Name of the EHD representative contact area |
| $a$ | $[m]$ | Static contact dimension along x axis (elliptical contact), or along the arc of radius $R = R_t + r_t\ sin(\lambda)$ (torus on plane contact) |
| $A_1, A_2, b_1, b_2, C_1, C_2$ | [various] | Modified WLF constants |
| $a_{CY}$ | $[-]$ | Carreau-Yasuda constant |
| $a_v$ | $[K^{-1}]$ | Murnaghan EOS constant |
| $\vec{B}$ | $[kg.s^{-2}.A^{-1}]$ | Magnetic field vector |
| $b$ | $[m]$ | Static contact dimension along y axis |
| $C$ | $[\ -\ ]$ | Contrast |
| $c$ | $[m.s^{-1}]$ | Light celerity |
| $C_{fx}$ | [%] | Friction coefficient along x direction |
| $C_{fy}$ | [%] | Friction coefficient along y direction |
| $C_{pf}$ | $[J.kg^{-1}.K^{-1}]$ | Lubricant heat capacity |
| $C_{pt}, C_{pb}$ | $[J.kg^{-1}.K^{-1}]$ | Heat capacity of top ($t$) and bottom ($b$) solids |
| $C_x\ , C'_x\ , C_y\ , C'_y$ | [various] | Integration constants |
| $d1$ | $[m]$ | Intermediate distance to measure $R_p$ |
| $d2$ | $[m]$ | Intermediate distance to measure $R_p$ |
| $E$ | $[Pa]$ | Equivalent Young modulus |
| $E'$ | $[Pa]$ | Reduced Young modulus ($2/E' = (1-\nu_t^2)/E_t + (1-\nu_b^2)/E_b$) |
| $E_t, E_b$ | $[Pa]$ | Young moduli of top ($t$) and bottom ($b$) solids |
| $\vec{E}$ | $[kg.m.A^{-1}.s^{-3}$ | Electric field vector |
| $f$ | $[\ -\ ]$ | Calibration function |
| $f$ | $[m]$ | Depth of the torus pin bore |
| $F$ | $[\ -\ ]$ | Modified WLF pressure term |
| $\mathcal{F}$ | $[\ -\ ]$ | Name of the inlet EHD contact frontier |
| $G$ | $[\ -\ ]$ | Dimensionless material parameter ($G = \alpha^* E'$) |
| $G_{CY}$ | $[\ Pa\ ]$ | Carreau-Yasuda constant |
| $h$ | $[m]$ | Film thickness |
| $H$ | $[\ -\ ]$ | Point on the section of the torus |
| $h_0$ | $[m]$ | EHD gap between the rigid bodies at O |
| $h_c$ | $[m]$ | Film thickness at the contact centre, $(x; y) = (0; 0)$ |
| $h_m$ | $[m]$ | Minimum film thickness |
| $h_{m-}$ | $[m]$ | Minimum film thickness on the side of the contact which is the closest to the disc rotation axis |
| $h_{m,c}$ | $[m]$ | Minimum film thickness along the x axis |
| $h_{m,l-}\ , h_{m,l+}$ | $[m]$ | Lateral minimum film thickness (+ stands for the side closest to the rotation centre of the surface, if existing) |

| | | |
|---|---|---|
| $h_{m+}$ | $[m]$ | Minimum film thickness on the side of the contact which is the furthest to the disc rotation axis |
| $h_r$ | $[m]$ | Film thickness in the rigid gap |
| $h_{torus}$ | $[m]$ | Rigid gap between a plane and a torus |
| $I_0, I_1 \dots I_n$ | $[-]$ | Reflected beam names and their light intensity |
| $I_{max}$ | $[-]$ | Maximum of the intensity of the interferences |
| $I_{min}$ | $[-]$ | Minimum of the intensity of the interferences |
| $j$ | [various] | Norm of $\vec{E}$ or $\vec{B}$ |
| $J$ | [various] | Wave amplitude of either $\vec{E}$ *or* $\vec{B}$ |
| $k$ | $[-]$ | Ellipticity ratio |
| $k_f$ | $[W.m^{-1}.K^{-1}]$ | Lubricant conductivity |
| $k_t, k_b$ | $[W.m^{-1}.K^{-1}]$ | Conductivity of top ($t$) and bottom ($b$) solids |
| $K_M$ | $[-]$ | Murnaghan EOS temperature dependant term |
| $K'_M$ | $[-]$ | Murnaghan EOS constant |
| $k_{mc}$ | $[-]$ | Wavenumber |
| $K_{MM}$ | $[-]$ | Murnaghan EOS constant |
| $L_1, L_2$ | $[-]$ | Parameters of the torus on plane static pressure distribution |
| $N_0$ | $none$ | Strait line |
| $N_H$ | $none$ | Strait line |
| $n_{CY}$ | $[-]$ | Carreau-Yasuda constant |
| $n_{mc}$ | $[-]$ | Refractive index of the fluid |
| $O$ | $none$ | Contact centre |
| $p$ | $[Pa]$ | Pressure |
| $p_h$ | $[Pa]$ | Hertz pressure |
| $P$ | $[W]$ | Power dissipated inside of the contact |
| $Q_{comp}$ | $[J]$ | Compression heat source |
| $Q_{shear}$ | $[J]$ | Shearing heat source |
| $Q_{in}$ , $Q_{out}$ | $[kg.s^{-1}]$ | Total flow incomming and outcomming (respectively) through $F$ |
| $Q_{xp}$ , $Q_{yp}$ | $[kg.s^{-1}]$ | Poiseuille mass flow rate in the x and y directions respectively |
| $r$ | $[m]$ | Distance from the contact centre (circular contact only) |
| $r_t$ | $[m]$ | Minor axis of the torus |
| $R, G, B$ | $[-]$ | Light intensity of respectively the red, green and blue colours |
| $R_{app}$ | $[m]$ | Apparent gyration radius of the pin (from a top view) |
| $R_d$ | $[m]$ | Gyration radius on the disc |
| $R_{local}$ | $[m]$ | Local cuvature radius of the rigid torus |
| $R_p$ | $[m]$ | Gyration radius on the pin |
| $R_t$ | $[m]$ | Major radius of the torus |
| $R_r$ | $[m]$ | Bending radius of the torus on plane contact |
| $R_x$ | $[m]$ | Principle curvature radius along x axis |
| $R_{xt}, R_{yt}$, $R_{xb}, R_{yb}$ | $[m]$ | Principal curvature radii of the top ($t$) and bottom ($b$) surfaces, along the x and the y axis |
| $R_y$ | $[m]$ | Principle curvature radius along y axis |
| $S$ | $[m^2]$ | Contact surface |
| $SRR(x, y)$ | [%] | Slide to roll ratio (local description) |
| $SRR_{x,0}$ | [%] | Slide to roll ratio at O |
| $t$ | $[s]$ | Time |

| | | |
|---|---|---|
| $T$ | $[°C]$ | Temperature |
| $T_0$ | $[°C]$ | Environment temperature |
| $T_{boundary}$ | $[°C]$ | Function of the matter temperature at the numerical domain inlet |
| $T_{f0}$ | $[°C]$ | Fluid temperature at the numerical domain inlet |
| $T_g$ | $[K]$ | Glass transition temperature at a given pressure |
| $T_{g,0}$ | $[K]$ | Glass transition temperature at ambient pressure (contact environment condition) |
| $T_R$ | $[K]$ | Reference conditions temperature |
| $T_{s0}$ | $[°C]$ | Solid temperature at the numerical domain inlet |
| $T_t, T_b$ | $[°C]$ | Bulk temperature of the top (t) and bottom (b) solids (generally equal to $T_0$) |
| $T_z$ | $[N.m]$ | Friction torque in the contact |
| $U$ | $[\ -\ ]$ | Dimensionless velocity ($U = \mu_0 u_e/(E'R_x)$ ) |
| $u_e$ | $[m.s^{-1}]$ | Entrainment velocity field |
| $u_{ex,0}$ | $[m.s^{-1}]$ | Entrainment velocity at the contact centre |
| $u_f$ | $[m.s^{-1}]$ | Lubricant velocity field |
| $u_{fx}$ , $u_{fy}$ | $[m.s^{-1}]$ | Lubricant velocity field components, in the x and y directions, respectively |
| $u_t$ , $u_b$ | $[m.s^{-1}]$ | Velocity field at the top ($t$) and bottom ($b$) surfaces |
| $u_{tx,0}, u_{ty,0}$, $u_{bx,0}$ , $u_{by,0}$ | $[m.s^{-1}]$ | Velocity at the contact centre, on the top ($t$) and bottom ($b$) surfaces, along the x and the y axis |
| $u_{tx}$ , $u_{ty}$, $u_{bx}$ , $u_{by}$ | $[m.s^{-1}]$ | Velocity field componants in the x and y direction, for the top ($t$) and bottom ($b$) surfaces |
| $V$ | $[m^-3]$ | Volume |
| $V_0$ | $[m^{-3}]$ | Volume at the contact environment conditions |
| $V_R$ | $[m^3]$ | Volume at the reference conditions |
| $w$ | $[N]$ | Load |
| $W$ | $[\ -\ ]$ | Dimensionless load ($W = w/(E'R_x^2)$ |
| $x, y, z$ | $[\ -\ ]$ | Coordinates of the 3D space |
| $X, Y, Z$ | $[\ -\ ]$ | Coordinates of the dimensionless 3D space |
| $x_{mc}$ | $[m]$ | Position on the light beam trajectory |

## Greek characters

| | | |
|---|---|---|
| $\alpha^*$ | $[\ Pa^{-1}\ ]$ | Piezoviscosity index, as defined by Blok (11): $\frac{1}{\alpha^*} = \int_{0.1}^{+\infty} \frac{\mu_0}{\mu(p)} dp$ |
| $\beta_K$ | $[K^{-1}]$ | Bulk modulus-temperature Murnaghan EOS constant |
| $\Gamma_0$ | none | Strait line |
| $\Gamma_H$ | none | Strait line |
| $\delta$ | $[m]$ | Deformation sum of the mating bodies, in the z direction |
| $\delta_{mc}$ | $[m]$ | Distance delay |
| $\Delta u_{x,0}$ | $[m.s^{-1}]$ | Sliding velocity at the contact centre and along x axis |
| $\Delta u_{y,0}$ | $[m.s^{-1}]$ | Sliding velocity at the contact centre and along y axis |
| $\theta$ | $[°]$ | Intermediate angle to measure $R_p$ |
| $\lambda$ | $[°]$ | Spin angle |
| $\lambda_{mc}$ | $[m]$ | Wavelength of the filter for the monochromatic light |
| $\mu$ / $\eta$ | $[Pa.s]$ | Newtonian viscosity / non-Newtonian viscosity |
| $\mu_e, \eta_e$ | $[Pa.s]$ | Viscosity integral number 1 |
| $\mu'_e, \eta'_e$ | $[Pa.s]$ | Viscosity integral number 2 |

| | | |
|---|---|---|
| $\mu_G$ | $[Pa.s]$ | Viscosity constant of the modified WLF model |
| $\mu_0$ | $[Pa.s]$ | Viscosity at ambient pressure and at $T = T_0$ |
| $\nu$ | $[-]$ | Equivalent Poisson ratio |
| $\nu_t, \nu_b$ | $[-]$ | Poisson ratios of top ($t$) and bottom ($b$) solids |
| $\xi$ | $[-]$ | Phase shift at the reflection on the steel surface |
| $\rho$ | $[kg.m^{-3}]$ | Lubricant density |
| $\rho_0$ | $[kg.m^{-3}]$ | Density at the contact environment conditions |
| $\rho_R$ | $[kg.m^{-3}]$ | Density at the reference conditions |
| $\rho_t, \rho_b$ | $[kg.m^{-3}]$ | Density of the top ($t$) and bottom ($b$) solids |
| $\tau$ | $[Pa]$ | Shear stress |
| $\tau_{zx}$ , $\tau_{zy}$ | $[Pa]$ | z shear stress, in the x and y directions, respectively |
| $\varphi$ | $[-]$ | Phase at the origin of the light beam |
| $\Omega_t, \Omega_b$ | $[rad.s^{-1}]$ | Rotation velocity of the mating top ($t$) and bottom ($b$) surfaces |

## Abbreviations

| | |
|---|---|
| EE | Elliptical Equivalent: it is addressed to the elliptical equivalent of a TOP contact |
| EHD | Elastohydrodynamic |
| FREC | Flange roller-end contact |
| IS | Investigative simulation: it indicates a computation case defined for investigation purposes |
| TOP | Torus on plane |

# General introduction

This document summarises a thesis work dedicated to a specific contact which occurs in roller bearings and tapered roller bearings. It deals with the mating point between the roller ends and the flange of the rings. The mating bodies have unconventional shapes as one of the solids is a torus and the other one is a plane. A deeper understanding of these contact characteristics and behaviour is mandatory for an improvement of bearing designs. In order to develop this knowledge, a scientific approach is adopted. Numerical and experimental tools are used and developed in order to explore this specific subject.

Four chapters constitute this thesis. The first one introduces and details the topic, together with its industrial and scientific context. Readers who have no background in Tribology will be led from general mechanic notions to the specificities of the topic.

Based on the literature review, the second chapter presents a first approach: the torus on plane contact is approximated by an elliptical contact. Conclusions for torus on plane contacts are drawn but the knowledge on elliptical contacts in general is also enriched by a new study philosophy.

At last, the third and fourth chapters investigate the torus on plane contact without the elliptical approximation: the actual bodies' geometry is included in the analysis. Chapter 3 presents the tools that are used in the analysis, whereas chapter 4 presents the investigation itself. Additional conclusions are developed on the torus on plane contact. This chapter also concludes on the strengths and the weaknesses of the elliptical approximation.

Finally, a general conclusion will summarise the results and state the prospects.

# Chapter I. Introduction

# I. Introduction

The present chapter aims to introduce the thesis topic to the reader. It will start with a basic description of the rolling element bearing. Then it will present the main questions that this document addresses together with their origins in the industrial context. Then the literature on the defined topic will be analysed by themes.

## 1.1. Rolling element bearings

A rolling element bearing can be defined as a mechanism which mission is to withstand a moving load by the mean of rolling elements (see Figure 1.1-1). In this figure, the rolling elements are able to accommodate the velocities between the moving mass and a static shelf. Rolling elements introduce a rolling friction instead of a sliding friction which occurs in case of direct shelf-mass contact. The former friction is much smaller than the latter, and therefore rolling element bearings are used to reduce friction losses. Historically, the first rolling element bearing mechanisms might be the well-known tree trunks arranged under heavy loads, as suggested by Figure 1.1-1.

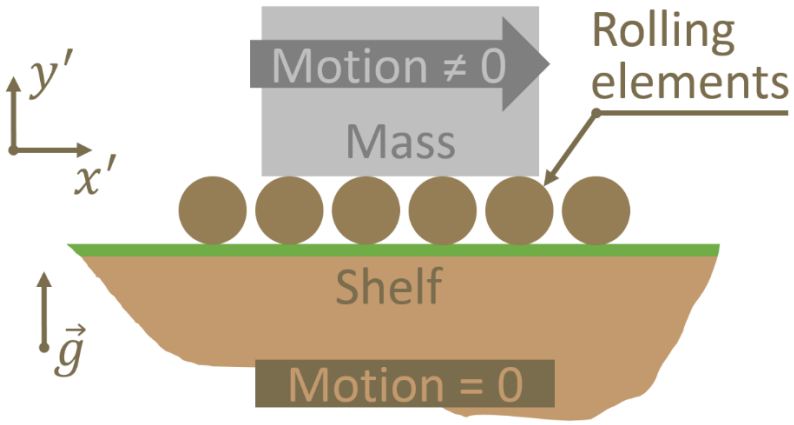


*Figure 1.1-1 – Basic rolling element bearing*

However, the tree trunks were under the mass for a short time during the rolling, and the trunks had to be brought back at the front of the moving mass. It is the reason why modern rolling element bearings include a recirculation system. The most obvious of them is to place the rolling elements between two concentric rings as illustrated in Figure 1.1-2. This schematic rolling element bearing has a clamped inner ring. The mechanism allows the outer ring to bear a radial load while it rotates. Opposing to this rotation, there is a rather weak torque resistance due to the low friction generated at each contact between the rings and the rolling elements. In order to guide the rolling elements, a cage is generally added to the system (not

represented): the cage maintains the rolling elements axis parallel to the rings' axes. However, the sliding contacts between the cage and the rolling elements contribute to the power losses.

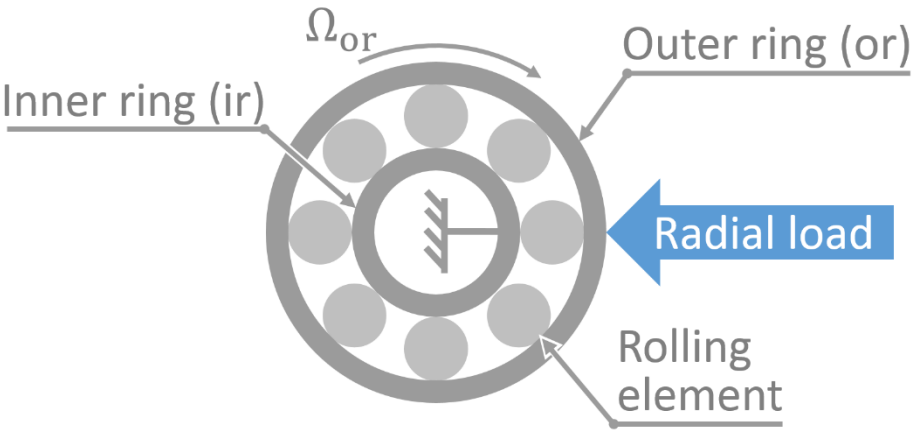


*Figure 1.1-2 - Schematic classic rolling element bearing*

## 1.2. Flange-roller end contact: scientific challenge and industrial motivation

So, after this brief introduction to rolling element bearings, the current section will present the problematic of the thesis and its context. Figure 1.2-1 presents an actual roller bearing which is much more complex than the schemes presented in section 1.1.

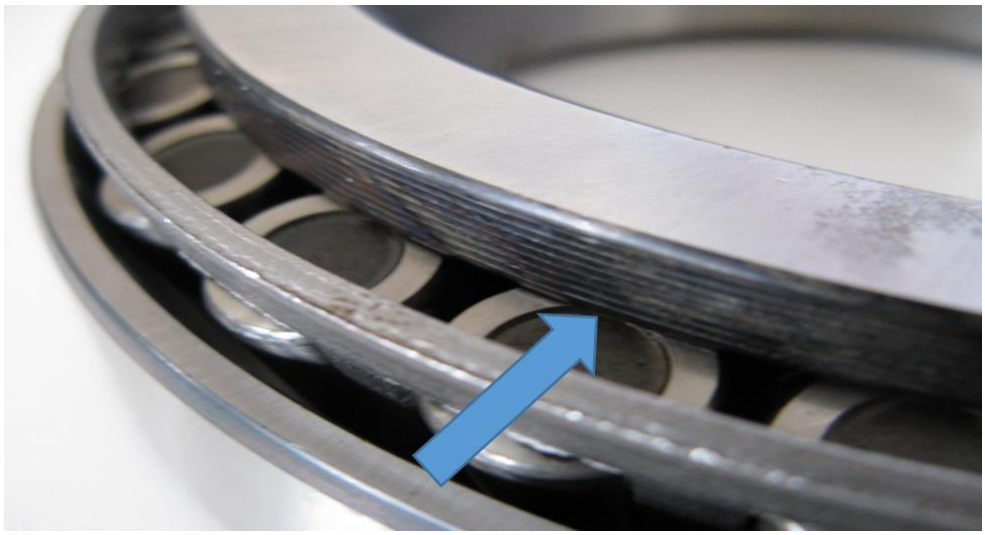

*Figure 1.2-1 - Industrial roller bearing*

Rolling element bearings generally withstand a radial load, yet the load is hardly ever purely radial. This explains the complexity of the rolling element bearing in Figure 1.2-1. A load parallel to the rotation axis is generally present. Therefore, the rings are adapted to bear the axial load and to maintain the rolling elements inside the mechanism. For example, Figure 1.2-2 shows one of the bearings: the roller bearing. Rollers are displayed between the two rings, sharing their rotation axis. Comparing to Figure 1.1-2, Figure 1.2-2 and Figure 1.2-3 show the flanges of the rings. The flanges (also called ribs in some references) are on the side of the rings and they mate the rollers at their end. Thanks to this ring's special shape, the axial load can be transmitted from the outer ring to the clamped inner ring through the flange-roller end contacts (FREC, represented in brown). The reader should note that the FRECs are the focus of the thesis: for now, some aspects of their properties are not mastered. They will be studied in order to understand their behaviour under certain conditions that will be detailed later. For its part, the radial load is transferred through the blue areas.

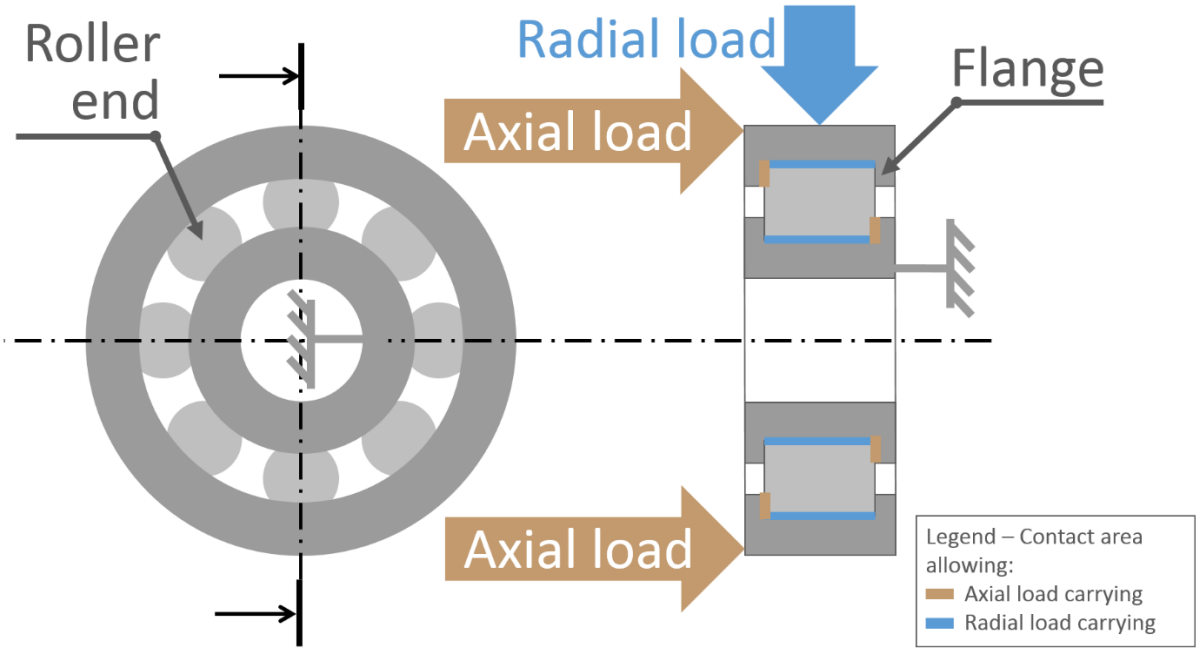


*Figure 1.2-2 – Radial and axial loading of a roller bearing*

### 1.2.1. The flange roller-end contact kinematic

The FREC is quite particular in the rolling element bearing as the roller kinematic involves a high sliding and a high spinning friction. Figure 1.2-3 is a zoom of Figure 1.2-2, and it shows the flange-roller end contact localisation (brown disc) and kinematic. Its area is located at the contacting interface between the end of the roller and the inner part of the flange. One can consider the radial load contact (in blue in Figure 1.2-3) as a non-sliding contact. Consequently, when the roller rotates around the inner ring, the roller instantaneous velocity field is the one represented with red arrows on Figure 1.2-3 (in the inner ring frame, $O', \overrightarrow{x'}, \overrightarrow{y'}, \overrightarrow{z'}$). This shows the high sliding that the FREC may endure. In 1967 H. Korrenn (12) presented one of the

earliest experiments on this contact. He separated the flange from the rest of the ring in order to measure the friction torque that the flange endures. Karna (13) led a similar study and he also found that the FREC generates a low friction coefficient.

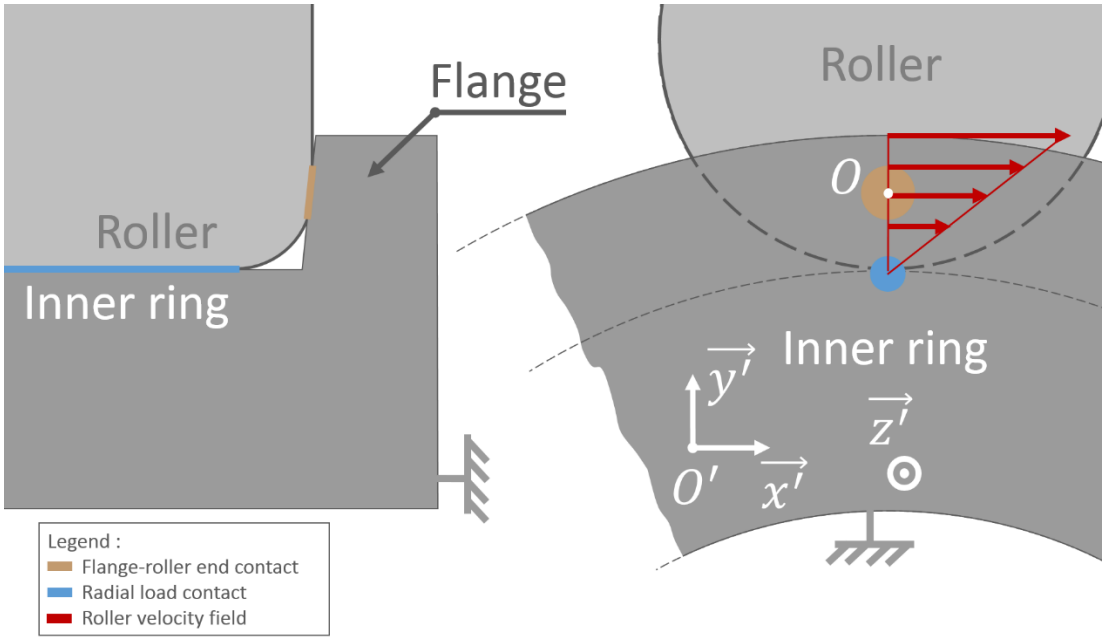


*Figure 1.2-3 - The flange - roller end contact*

To better describe the contact kinematics, one has to consider the velocity field in the contact frame ($O, \vec{x}, \vec{y}, \vec{z}$ with $O$ the contact centre). This frame is moving all around the ring at the same angular speed as the roller axis. Within this frame, the roller and the ring axis can be considered as static and the velocity fields are as presented on Figure 1.2-4 (on $y$ axis only, and along $x$ direction). Because of the frame change (the contact frame is different from the ring frame) there is a change in the aspects of the velocity field between Figure 1.2-3 and Figure 1.2-4. The difference between the ring and the roller velocity fields is composed of both sliding and sliding-spinning components. The sliding and sliding-spinning velocity sum is the total velocity difference. The sliding velocity is constant everywhere, and is equal to the velocity difference at $y = x = 0$ (orange arrows in Figure 1.2-4). The sliding-spinning velocity (which is a sliding, but induced by the rotations of the mating bodies) is the total velocity difference when the sliding velocity is subtracted (blue arrows in Figure 1.2-4); contrary to the sliding velocity, the sliding-spinning velocity varies everywhere.

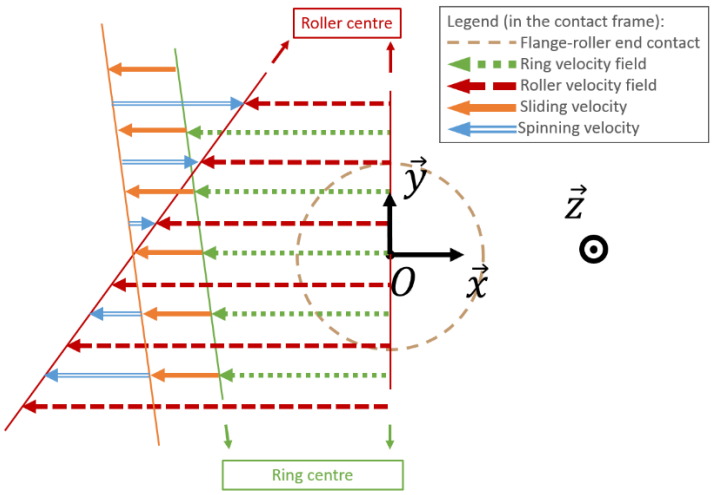


*Figure 1.2-4 - Velocity field in the contact frame*

Another way to represent the velocity fields is to focus on one of the two surfaces. For each of them, the velocity field is composed of the longitudinal and the spinning velocities. Figure 1.2-5 presents these two components in the contact frame, for the roller surface velocity field. With this point of view, the sliding-spinning is the difference between the spinning velocities of the two surfaces, and the sliding is the difference between the two longitudinal velocities.

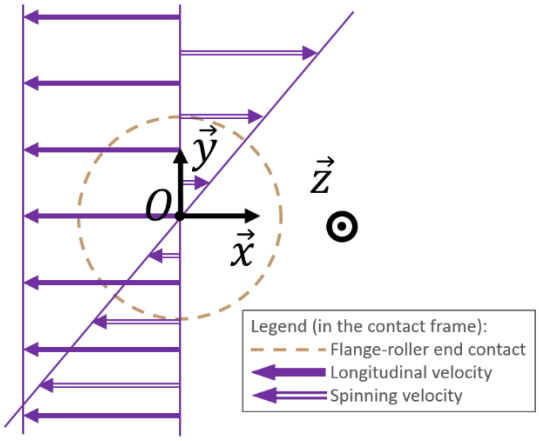


*Figure 1.2-5 - Velocity field composition of the roller surface*

This complex decomposition of the kinematic is characteristic of the FREC, and it is mandatory to take it into account.

### 1.2.2. The bodies' unusual geometry

Another particularity is the geometry that the contacting bodies have. According to Zhang et al. (14) the roller end can be either a sphere or a torus portion whereas the flange can either be

a concave spherical or conical surface. As a result, the area where the two bodies are in contact varies. In previous studies (2,5,15–17) and in section 1.2.1, the contact was schematically represented by a circular shape, but the contact is very likely to be different between a torus and a cone or a sphere. Initially, the contact between the rigid bodies is a point, but as these bodies follow a linear elasticity law, it extends to a non-zero area which has a shape defined by the curvature radii of the bodies. Contrary to usual contacts, the area contour is neither circular nor elliptical: it is a general shape which losses most of its symmetries. Figure 1.2-6 is a schematic diagram of such a contact configuration. The roller end torus is defined by the parameters $r_t$ (the minor torus axis), $R_t$ (the major torus axis) and $\lambda$ (the spin angle), whereas the conical or spherical ring is modelled by a plane. Indeed, the cone and sphere curvature radii are very large at the contact centre. The subsequent contact area is represented in brown. To sum up, modelling the torus on plane FREC requires to take into account the bodies' elastic behaviour (like all EHD contacts) but also to fully represent the unusual bodies' shape.

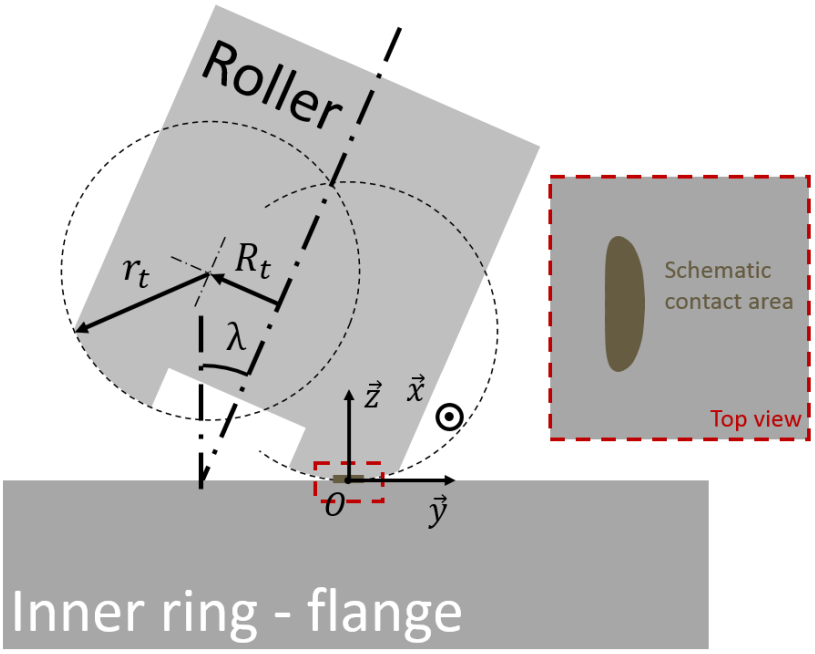


*Figure 1.2-6 – Torus on plane contact*

### 1.2.3. Lubricant role

In addition, a fluid is introduced in the bearings' contacts in order to reduce wear and friction: it is the lubricant. Generally, the lubricant is constituted of an oil or a grease, to which some additives (anti-wear for instance) are added and represent about 5-15% of the lubricant. In the contact vicinity the grease releases oil (see Cann and Lubrecht (18)). So whether the lubricant is oil or grease, one can consider in a first approach that they both behave like an oil at the contact scale. In the following, the lubricant will be treated as a fluid which interacts with the surfaces, the interaction being mainly mechanical and chemical. However here, it is the

mechanical side which is studied. In the present thesis, a standard industrial oil was selected for its low proportion of additives and its properties at room temperature.

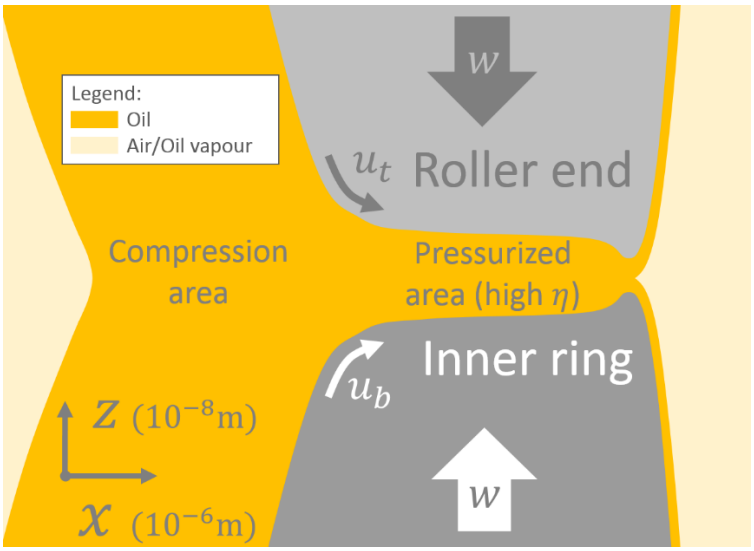


*Figure 1.2-7 - Elastohydrodynamic basics*

### 1.2.4. Elastohydrodynamic phenomenon

As explained before, the contact between two non-conformal rigid bodies is a point. This point extends to a surface when a load is applied and when the solids are not rigid: indeed deformations of the loaded solids occurs in the contact vicinity. In the presence of lubricant and motion, the fluid and the mating solids start to have a significant influence on each other.

To be more precise, the moving surfaces entrain the fluid through Couette flows (entrainment velocities are called $u_t$ and $u_b$ in Figure 1.2-7, where $t$ stands for "top" and $b$ stands for "bottom"). In the contact vicinity, the gap between the solids is drastically reduced, leading to a severe compression of the lubricant (pressure rises up to several GPa in the pressurised area). Under pressure, the lubricant flows away from the contact through Poiseuille flows. However the pressure increases the oil viscosity exponentially (piezoviscous effect) and therefore the Poiseuille flows become much lower at high pressure. Consequently, the piezoviscous fluid is dragged between the surfaces and can literally separate them. This phenomenon is at the origin of the wear and friction reduction as the solid-solid direct interaction disappears (for perfectly smooth surfaces). When the bodies' deformation sum is larger than the surface separation generated by the presence of the fluid, the phenomenon is called elasto-hydrodynamic (EHD) as it adds the elastic behaviour of the solids to the hydrodynamic effects. The hydrodynamic pressure imposes a deformation of the mating bodies, which modifies the contact inlet and influences in return the pressure build up. It is a complex problem with a strong coupling between fluid and solid mechanics. In the context of wear prediction, it is important to specify that the surface separation is not homogenous and that the pressure field generated in EHD contact leads to film thickness minima. It is these gap minima which can lead to solid-solid interaction (for rough surfaces).

In 1972, Wren and Moyer (19) adapted the EHD theory to the FREC and were the first to highlight the existence of a full film lubrication regime. Since then, industry and laboratories collaborated to develop the knowledge on EHD theory in this specific case and enable new products development.

Indeed, the EHD problem is quite complex in itself, even at its basics. At first, it is a multiphysic problem as it gathers fluid mechanics and solid mechanics. Then, one shall add thermal effects due to the fluid compression and the shear-generated heat. Secondly, it is a multiscale problem: the solids are at the centimetre/decimetre scale, the contact surface is at the millimetre scale and the film thickness is at the micrometre/nanometre scale. At last, as it was previously said there are unusual velocity fields and shape of the contacting bodies, which make the problem more complex. As a consequence, any attempt to deepen the understanding on FREC requires dedicated investigations.

### 1.2.5. Industrial needs and scientific challenges

Bearing manufacturers need to predict the contacts behaviour precisely in order to design better and long lasting products. The FREC is one of the bearing critical contacts as it can generate high power losses, and also because it is harder to feed it with oil. Indeed, the flange is narrow and the rolling elements easily dispel the oil on it. Moreover, because of the large radii of the mating bodies, the exact location of the contact is hardly ever at the middle of the flange, but it is regularly on the sides: this leads to contact truncation. The power loss is converted into heat dissipation which changes the lubricant properties and tends to reduce the film thickness. Together with the harsh oil feeding, this film thickness reduction leads to premature wear and surface damage. The damage can even lead to the bearing jamming.

So, for bearing designers, it is mandatory to have adequate models to evaluate the efficiency and the lifetime of their products.

From the scientific point of view, the challenge is slightly different. The behaviour of such an unusual contact remains unknown even if some studies have already pertained to this topic. Due to the specifics of this EHD problem, there are even more parameters and physics to take into account. Experiments will be required to identify and demonstrate the influence of some governing parameters on the results. Moreover, numerical modelling will provide a tool to highlight the role of each parameter and distinguish the driving ones from the negligible ones. The expected results of this scientific analysis will be an improved understanding of the contact physics, and an efficient way to predict its behaviour.

## 1.3. Literature overview

This section presents the previous studies related to the EHD torus on plane FREC. They can be separated in several categories. Some rare works relate to the EHD torus on plane FREC. They will be presented first. Some more studies refer to other general EHD contacts, and it will be interesting to analyse the authors' approach to the problem. This second category will be

used as an inspiration to the present work. Finally, other papers are dedicated to the EHD elliptical contacts. One should take them into account as their shape is often similar to the ones of the two first categories: the narrow elliptical contacts are used as approximation for the general or the torus on plane contacts.

The two main concerns are the friction forces opposed to the motion in the contact, and the thickness of the oil film separating the contacting bodies. The former is of high interest to predict and minimize the power losses in the contact, whereas the latter is more related to wear prevention. Indeed, the more the surfaces are separated, the lower probability there is for the solid-solid damaging contact to occur. Film thickness can be accurately predicted nowadays through numerical models (like in Doki-Thonon et al. (17)). These numerical models gave birth to a few simplified predictive laws which are less accurate but easier to use.

### 1.3.1. EHD Torus on plane flange roller-end contact

Torus roller-end design is not a recent innovation and it can be found in different kind of roller bearings. Together with the industrial use of such a geometry, some studies were led to tackle this specific problem.

In 1984, Gadallah and Dalmaz (20) presented their work on the torus on plane FREC. With a dedicated test rig, they were able to simultaneously measure the traction forces in the two directions of the contact plane and the film thickness by an interferometric method. They compared their film thickness results with three different predictive laws developed by Archard and Cowking (21), Hamrock and Dowson (22–24) and Kapitza (25). They showed rather good agreements with the last one under hydrodynamic conditions. Under EHD conditions, the discrepancy increased. According to the authors, it was mainly due to the starvation occurring at the experimental contact inlet. However, within all conditions, the theoretical results were based on elliptical contact simulations. The predictions did not take into account the actual bodies' geometry.

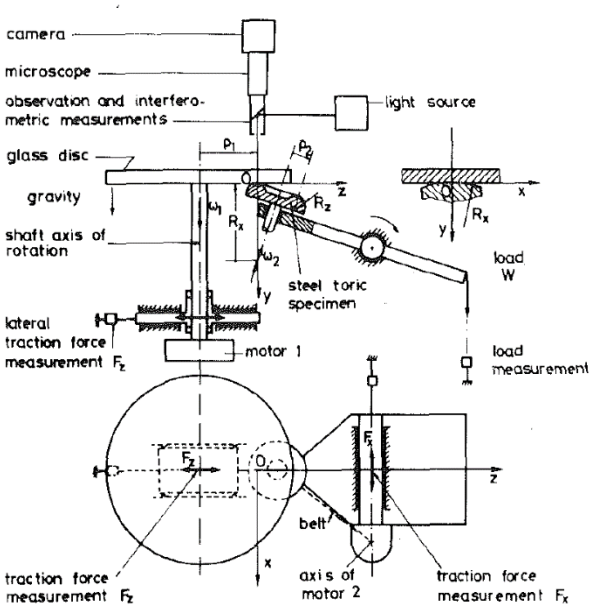


*Figure 1.3-1 - Gadallah and Dalmaz test-rig – from* (20)

In 1988, Zhang et al. (14) led a numerical study on FREC for different geometries, including torus roller end. They made the same geometry assumption: the torus on cone contact can be approximated by an elliptical contact. However, they were able to take into account the solids' deformation: it was an isothermal Newtonian EHD model. They defined optimum radii ratios (for maximum surface separation and minimum friction) and showed that the FREC should be located at the middle of the flange track in order to maximise the surface separation. Nevertheless, more recent studies showed the importance of thermal effects (as Doki-Thonon et al. (5)) in the prediction of friction and, in a lesser extent, film thickness. Consequently, there is a need for thermal EHD studies pertaining to torus on plane FREC.

In 1998, Colin et al. (9) studied the influence of starvation on the flange-roller end EHD lubrication with the same device as Gadallah and Dalmaz (20). They also developed a starved isothermal Newtonian EHD model. They were able to validate the model by their experiments. However, this validation required the choice of the starvation parameter which offered the best fit. The model was considering the toroidal on plane contact as an elliptical contact, and therefore, the actual bodies' geometry influence was not investigated. They showed through the numerical model that the pressure distribution is no more symmetrical: the pressure maximum is shifted towards the side of the contact which is the further from the roller gyration axis.

Apart from these few references, the EHD torus on plane contact was not investigated, to the best of our knowledge. However, this subject belongs to a wider topic: the EHD general shape contact. The torus on plane FREC contact topic is also related with other FREC and spinning contacts. In order to gather more information on the state of the art of the torus on plane FREC, the next section (1.3.2) will relate the works dedicated to FREC and spinning contacts. The two last bibliography sections will present the works allotted to, respectively, the general shape EHD contacts and the elliptical EHD contacts.

### 1.3.2. Flange roller-end and spinning contacts

Spinning kinematic in EHD contacts is not so widespread, but it can be found in FREC and the continuously variable transmissions (CVT) like the toroidal traction drive.

In 1966 Poon et al. (26,27) published their friction results obtained on a test-rig which included spin. It was the very first work on spinning and they showed that the friction coefficient is altered by the presence of spin.

One year later, Korrenn (12) adopted a macroscopic approach by using an apparatus in which the flange was detached from the tapered roller bearing in order to measure the torque between the flange and the inner ring. Therefore, it allowed to deduce the friction in the contacts. Karna (13) used the same kind of test rig (Figure 1.3-2) and they both found that the flange-roller end contact (circular spinning contact) has a low friction coefficient. Moreover, they showed the existence of the hydrodynamic effects in this contact, which occur with increasing rotation speed.

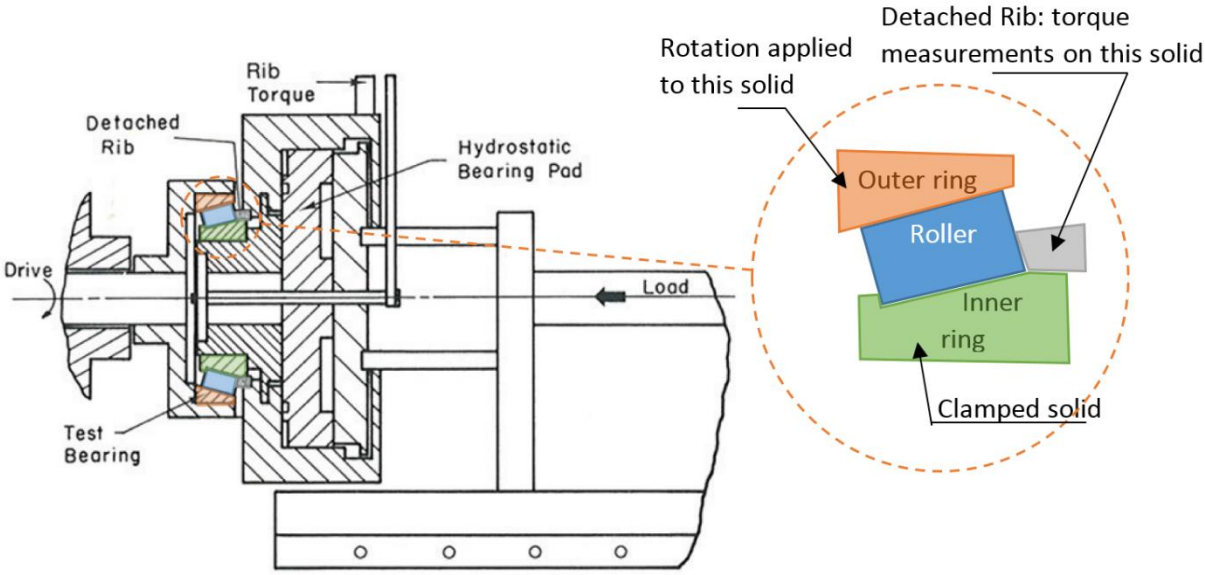


*Figure 1.3-2 - FREC friction measurement test-rig by Korrenn* (12)

Spinning contact can also occur in deep groove ball bearings. In 1969, Snidle and Archard (28) obtained a hydrodynamic solution for a spinning sphere in a groove. In other words, they computed a hydrodynamic spinning elliptical contact. They proposed an analytical formula to predict the maximum pressure.

In 1988, Zhang et al. (14) studied elliptical spinning contacts in order to model the FREC with various contact geometries. They proposed an optimal ellipticity ratio for optimised surface separation.

In 1991, Dowson et al. (29)demonstrated that EHD elliptical contacts are influenced by the presence of spin. The rotation axis was located on the major axis of the ellipse. In this configuration, the pressure distribution was hardly affected whereas the film gap became highly asymmetrical in the presence of spin. Indeed, the entrainment velocity varies locally, and the side which is the furthest from the rotation axis sees a larger entrainment velocity than the other. These results were confirmed later on by Yang and Cui (30).

Within the same configuration, Tanighuchi et al. (31) developed a predictive formula for the minimum film thickness for Newtonian isothermal spinning contacts.

In 1999, Zou et al. (32) proposed a predictive formula for both central and minimum film thickness in elliptical Newtonian isothermal spinning contacts. Though thermal and non-Newtonian effects were ignored, they explained that the central and minimum were reduced under spinning conditions by hydrodynamic effects.

It is in the same period that the thermal effects and the non-Newtonian lubricant behaviour were introduced in EHD models. Indeed, both of them have a great influence on the friction, and in a lesser manner on the surface separation. In 1995, Jiang et al. (33) integrated in an EHD model the pressure and shear stress influence on the lubricant properties. They demonstrated that these rheological effects have a significant influence on friction and they proposed optimised FREC bearing designs. Their design guidelines pertained to the optimum curvature radii of the mating bodies in order to minimise friction and maximise film thickness. When the thermal effects are introduced separately from the non-Newtonian laws, the temperature rise is very likely to be overestimated, according to Ehret et al. (34). Similarly, Liu et al. (35) focused on the introduction of a non-Newtonian Eyring rheological model. They drew the same conclusion: thermal and non-Newtonian effects should be used together to be able to predict the temperature rise in sliding contacts.

Dormois et al. (15) investigated circular spinning contacts through the Tribogyr test-rig and a non-Newtonian isothermal EHD model. They measured friction forces under various operating conditions and underlined the key role of thermal effects. Again, the need for both thermal and non-Newtonian modelling was emphasized.

In 2008, Miyata et al. (36) proposed an experimental approach to obtain the temperature rise inside of the pressurised area in an elliptical spinning contact. Their measure was based on platinum thin film sensors. They showed that under moderate sliding, the spinning contact endure a larger thermal heating than the non-spinning contacts. For larger sliding, the difference diminishes.

Doki-Thonon et al. (16,17) presented their work on circular spinning contacts. With a thermal non-Newtonian EHD model validated through independent experiments, they showed the influence of the spin on the contact behaviour. In particular, they highlighted the recirculation of the spinning body which can generate significant film thickness reductions. Indeed, the body's temperature locally rises in the contact, and before this heated area cools down, it is reintroduced in the contact. At the contact inlet, the lubricant temperature is increased and the film thickness is reduced.

### 1.3.3. General shape EHD contacts

Whereas most tribological applications can be modelled through line and/or elliptical simulations, one may notice that it is sometimes required to get rid of these common formulations to use a more suitable one. Indeed, some contacts have shapes which are too far from the classical line and elliptical configurations and consequently they may require dedicated studies.

General contacts are found in wheel-rail contacts, wheel-rail flange contacts, in some flange-roller end contacts and in some gear meshings. The bibliography about flange-roller end contact was detailed earlier: as it is the main topic of the author researches, it deserved a dedicated part. Moreover, even if the contact shape was general, it was always modelled by an elliptical contact.

The work on wheel-rail contact is the widest, and the goal is generally to get a fast and accurate model as it is often part of a bigger computation, like vehicle system dynamic models. The wheel-rail contact simulations are free from lubricant considerations and are therefore not of the interest of the author. For more information on the several wheel-rail contact models, one may consider the models comparison of Sichani et al. (37) or the methods assessment by Wiest et al. (38).

Worm, helical and hypoid gears are characterized by lubricated general contacts at meshing. The first point contact EHD solutions were developed for circular and elliptical contacts. Based on these previous studies and since the early 80's, Simon has made an extensive numerical work on gear EHD lubrication. In 1981 and through the earliest thermal EHD model for general contacts, he showed (39) the importance to take into account thermal effects in hypoid gear models. No dimensionless parameter was used in this model. The film thickness was defined by the following formula:

$$h(x,y) = h_{min} + d(x,y) + g(x,y)$$

where $h_{min}$ is the minimum film thickness due to hydrodynamic effects, and $d(x,y)$ is the normal elastic displacement of the teeth surfaces (caused by the pressure distribution). The separation due to the rigid geometries of the teeth surfaces is $g(x,y)$. It is obtained by resolving the equations defining the gap between the gear teeth.

In 1985, Simon extended his study to worm gears and in 1988 to helical gears (40). He deduced several recommendations to design these kinds of gears. Simon continued his work on gears since then, but there is no significant numerical improvement after his thermo-EHD model.

In 2001, Evans, Snidle et al. (41–43) published their work on elastohydrodynamic lubrication of worm gears. They developed a non-Newtonian thermal EHD model. This latter is also at the full scale and uses an iterative method to find the pressure distribution and the gap between the worm and the wheel under load in the dry contact. It only requires to know $g(x,y)$, the gap between the two bodies when touching under zero load. $g$ is obtained here by fitting high order polynomials ($10^{th}$ order was chosen) to the numerical results of the separation in order to remove the unwanted local gap fluctuation introduced by the discretized nature of the data. The EHD calculation included a limiting shear stress formula.

They have found that worm gears can be subjected to a severe thinning of the oil film thickness due to the specific kinematics and geometry of the meshing. Indeed, according to Figure 1.3-3 (from (41)), there are several lubricant entrances in the contact. Figure 1.3-4 (from (41)) shows the line where the poor film generation occurs (due to poor alimentation). At the beginning of this line, there is the frontier between an inlet and an outlet area (see Figure 1.3-4), and this means that no entrainment occurs along this line. According to their observation, this line coincides with a low film thickness area. In addition, thermal thinning occurs because of the heat generated by the lubricant shearing. This heat generation leads to make the solids hotter which increases in his turn the lubricant temperature at the entrance of the contact.

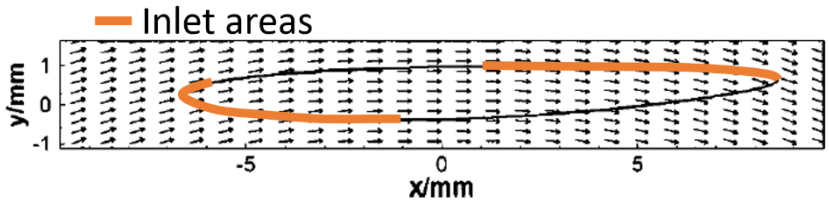


*Figure 1.3-3 - Area of dry elastic contact of a worm gear meshing showing entrainment velocity vectors, from* (41)

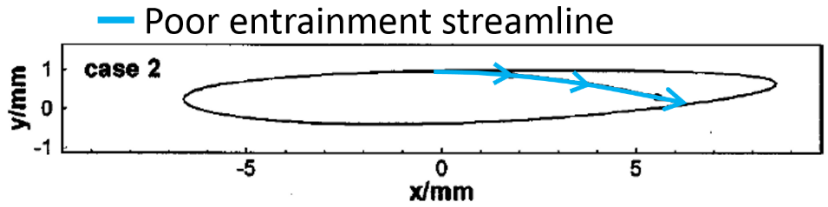


*Figure 1.3-4 - Line of predicted poor film generation for the same worm gear meshing, from* (41)

In (41), the authors compared their numerical results with the predictions of the formulae proposed by Chittenden et al. (10,44). These formulae were developed for elliptical EHD contacts, but they can be used as an approximation (explanation developed in section 1.3.4). They showed a rather good accordance between the formulae estimations and their isothermal numerical results. The discrepancy however reached 100% on central film thickness for some configurations. One shall then conclude that apart from Simon, and the team of Evans and Snidle, the general lubricated contact has not been widely studied with advanced numerical tools. Moreover, no experimental study was identified. Despite this low amount of publications, the different authors managed to obtain models which allowed to improve gear knowledge and performances through thermal non-Newtonian EHD simulations. However none of these models has been validated by comparison with experimental results, and none of them was applied to the torus on plane FREC.

These models will inspire the development of a general contact solver for flange-roller end contacts. Existing models like the one developed by Habchi et al. (45) and improved by Doki-Thonon et al. (16,17) showed really good agreements with experimental works. The work of

Doki-Thonon et al. was dedicated to circular FREC and constitutes a good basis. Even based on reliable approaches, the general contact model should be validated through experiments which include general shape properties.

The EHD general shape contact subject is wider than the one this document deals with, this topic remains rather unexplored. However, as general shape contact was often approximated by an elliptical one, the next section explores this subject.

### 1.3.4. EHD elliptical contacts

As mentioned previously, the general shape contact is often approximated by an elliptical contact. The state of the art on the latter may help to understand the former. And consequently, it may help to analyse into details torus on plane FREC. To strengthen the link between this contact and its approximation, Figure 1.2-6 shows clearly the visual similarities between them: the torus on plane contact shape is analogous to an ellipse. The principal curvature radii are used to make the approximation. They are the curvature radii at the rigid contact point, along the two main directions of the contact. They are called $R_{xt}$, $R_{yt}$, $R_{xb}$ and $R_{yb}$ in Figure 1.3-5 (where $t$ stands for "top body" and $b$ for "bottom body").

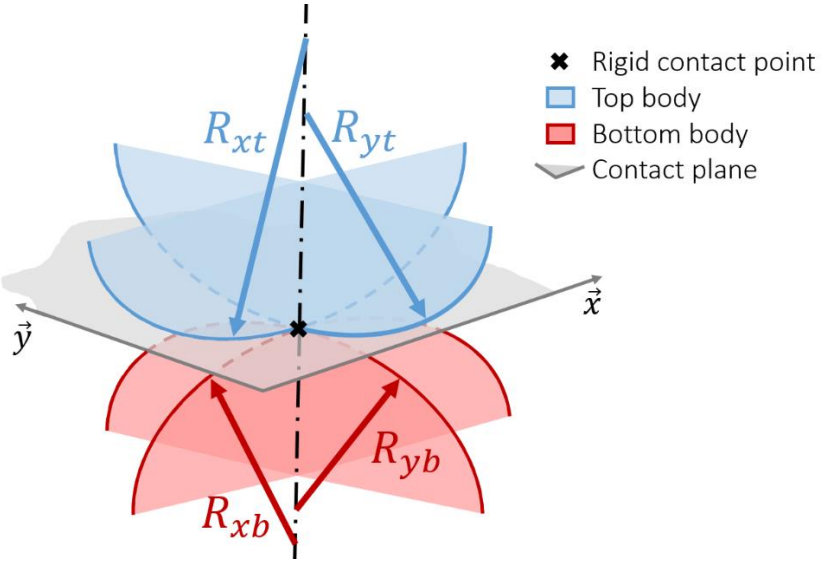


*Figure 1.3-5 - Principal curvature radii of the two contacting bodies*

Based on the principal curvature radii, principal equivalent curvature radii are defined, thanks to the following formulation:

$$\frac{1}{R_x} = \frac{1}{R_{xt}} + \frac{1}{R_{xb}} \;\&\; \frac{1}{R_y} = \frac{1}{R_{yt}} + \frac{1}{R_{yb}}$$

Figure 1.3-6 shows the equivalent body defined by the principal equivalent curvature radii ($R_x$ and $R_y$). This equivalent body is the one which inherits the curvature properties of real both surfaces, whereas the other one is flat and their contacting surface is in the flat plane.

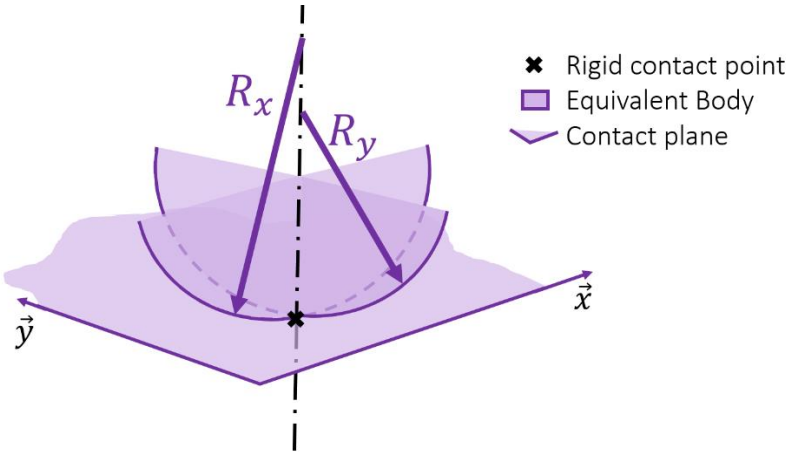


*Figure 1.3-6 - Principal equivalent curvature radii*

Based on these principal radii, one can simplify any non-conformal contact and model it by an elliptical contact. The EHD elliptical contacts have been quite widely studied since the development of numerical solutions. They can be separated into two categories. The first one is the slender or narrow elliptical contact (see Figure 1.3-7, on the left), where the ellipticity ratio is $k = b/a < 1$ (with $a$ and $b$ the contact semi-axis respectively along $\vec{x}$ and $\vec{y}$ directions) and the entrainment direction is oriented along the major axis of the ellipse. This configuration can model, for instance, the FREC for torus roller ends. The second category is the wide elliptical contact (see Figure 1.3-7, at the right), where $k > 1$. The transition between the two categories is of course the circular contact (see Figure 1.3-7, at the middle) where $k = 1$.

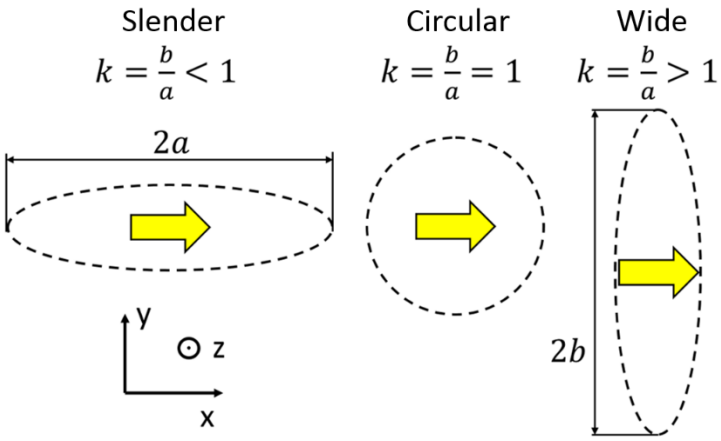


*Figure 1.3-7 - Contact configurations when k varies (entrainment velocity represented by the yellow arrow).*

Since the 70's, several investigations have been conducted on the influence of contacting solids' geometry on point contacts. In 1976, Hamrock and Dowson (22–24) were the first to publish a complete numerical solution of the EHD point contact problem. Based on numerical

simulations, they developed a semi-analytic formula that can predict the minimum film thickness of elliptical contacts but, however, limited to contacts where the lubricant entrainment is along the minor axis of the ellipse ($k > 1$).

In the following years, other works were focused on the slender elliptical contact ($k < 1$). The first numerical study on slender elliptical contacts was probably led by Mostophi and Gohar (46). In 1982, they published a study on elliptical contacts, for low loads and different entrainment velocity directions. Through numerical simulations and experiments, they demonstrated that the film thickness minima are located on both sides of the contact (see Figure 1.3-8). Moreover, they underlined the drastic film thickness reduction which occurs in this configuration compared with the circular case. For wide elliptical contacts ($k > 1$) and low normal load, they also noticed that there is only one minimum, located at the centre of the exit zone. From their numerical simulations, they proposed a minimum film thickness formula for lightly loaded elliptical contacts in a wide range of ellipticity ratios (from slender to wide ellipses).

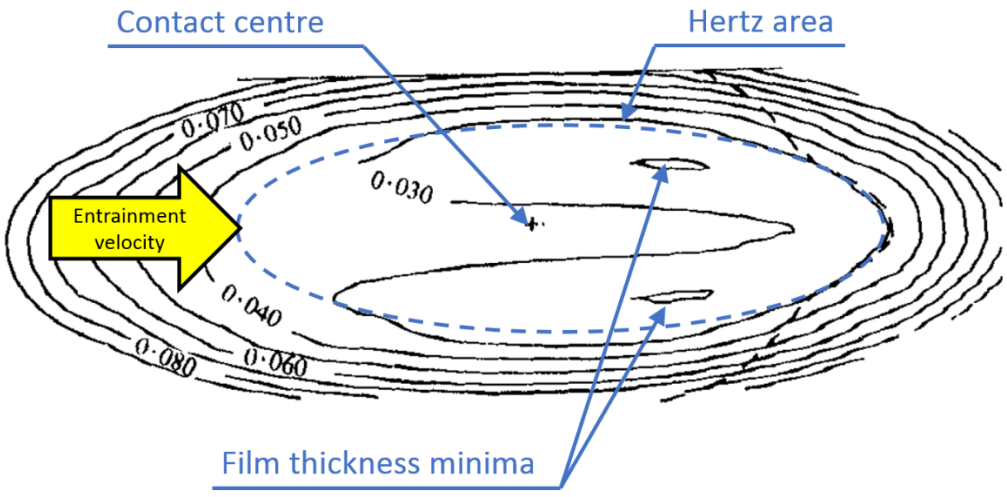


*Figure 1.3-8 - Minimum film thickness on the sides (from Mostophi and Gohar (46), with indications added for clarity)*

The following year, Evans and Snidle (47) published a short note on heavily loaded slender elliptical contacts ($k < 1$). They underlined the severe thinning that occurs on the contact sides, and explicitly blamed this film reduction on the slenderness of the contact.

In 1985, Chittenden et al. (10,44) published new film thickness expressions for central and minimum film thicknesses. These formulae cover a wide range of ellipticity ratios (from slender ($k < 1$) to wide ($k > 1$) elliptical contacts) and are still used nowadays for film thickness prediction. Moreover, they also studied different entrainment directions: the long ellipse axis can be parallel ($k < 1$) or perpendicular ($k > 1$) to the entrainment direction, but it can also be an intermediate configuration.

Chittenden et al. investigated widely elliptical contacts, but varied the ellipticity ratio while keeping constant the dimensionless parameters ($U$, the velocity parameter, $G$ the materials parameter and $W$ the load parameter, as defined in (23)). This choice led to vary the actual load in a large range together with the ellipticity. Chittenden et al. also explained that the minima on the contact sides act as lubricant seals which indeed limit side leakage and preserve the flow continuity.

The numerical results presented above would not have made sense without validation from several experimental studies conducted during the same period. In 1972, Thorp and Gohar (48) published their work on the effect of entrainment direction on the elliptical contact. Thanks to experiments carried out under pure sliding, they concluded that the largest surface separation occurs for the wide elliptical contact ($k > 1$), while the slender one ($k < 1$) endures less favourable conditions. Shortly thereafter, Bahadoran and Gohar (49) studied experimentally the wide elliptical contact ($k > 1$) and compared their results with film thickness formulae. In 1978, Gledhill et al. (50) demonstrated through experimental observations that an EHD regime can take place when the lubricant entrainment direction is parallel to the major axis of the ellipse ($k < 1$). They measured minimum film thicknesses with an interferometric method and compared them favorably with Hamrock and Dowson's predictions (22–24). In 1981, Koye and Winer (51) evaluated experimentally the same formula. They concluded that the Hamrock and Dowson expression could be used to obtain a gross estimation of the minimum film thickness in the slender geometry ($k < 1$). Alongside their model development, Chittenden et al. (52) conducted an experimental study for several elliptical contact configurations which showed a good agreement with their numerical results.

After the determination of film thickness formulae, other studies continued the research on elliptical contacts. In 1993, Evans and Snidle (53) focused on heavily loaded slender elliptical contacts, for Wildhaber-Novikov gears application. One year later, Nijenbanning et al. (54) proposed a film thickness expression and underlined an asymptotic trend: the wide elliptical contact can be considered as a transition case between the circular and the line configurations. This transition between circular and line contact is presented in Figure 1.3-9 with a different ellipticity parameter: $D = R_x/R_y$ (which varies inversely with $k$) as in (54).

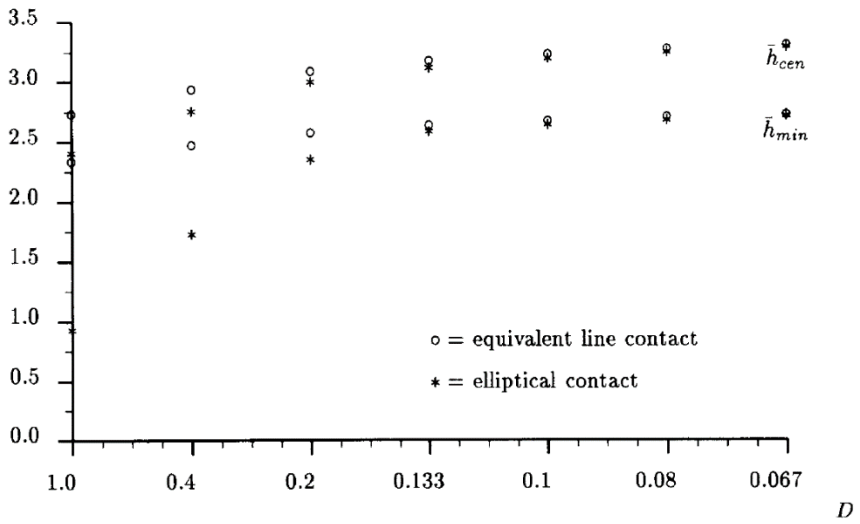


Fig. 8. Dimensionless minimum ($h_{min}$) and central film thickness ($h_{cen}$) as functions of $D$ obtained for the full elliptic contact solution, and the values obtained from solving the equivalent line contact problem ($M = 500$, $L = 5$).

*Figure 1.3-9 – Influence of the ellipticity ratio $D = R_x/R_y$ on the minimum and central film thickness – from Nijenbanning et al.* (54)

As a consequence, when the elliptical contact becomes wider and wider (increasing $k > 1$), its behaviour tends to that of the line contact. This asymptotic behaviour is one strength of their work, but similarly to Chittenden et al. (5,6), Nijenbanning et al. varied the dimensioned load while keeping some dimensionless parameters constant. Therefore, the ellipticity influence was not studied by itself. In 2000, Sharif et al. (55) proposed a comparison of their numerical work with Chittenden formulae (5,6). They showed that a 50% discrepancy can occur between the analytical predictions and the isothermal solutions of the full EHD problem.

In the same period, Kaneta et al. investigated the thermal effects in elliptical contacts with experiments under pure sliding conditions and a thermal Newtonian EHD model. At first with wide elliptical contacts (56), they showed the presence of dimples due to the thermal properties difference of the mating solids. Then, they continued their investigations with the slender elliptical contacts (57) and showed that this dimple can become unstable under certain sliding conditions. At last, they led experiments with different entrainment velocity directions (58), with the entrainment velocity vector which is not necessarily parallel to one of the axis of the ellipse. However, their numerical results only showed qualitative agreement with the experiments. A better lubricant characterisation would have certainly enhanced the correlation. As a confirmation, Kaneta et al. (35) underlined the need for non-Newtonian thermal EHD models in point EHD contacts.

In 2003, Zhu (59) computed about 600 contact cases in order to evaluate Hamrock-Dowson (22–24) and Chittenden (10,44) formulae in extreme conditions (heavy load, high speed, high ellipticity). Zhu ran calculations on a wide range of conditions, however the extreme cases' results were contested (60,61). In the same year, Damiens (62) analysed the influence of Poiseuille flows on starved wide elliptical contacts ($k > 1$). He proposed a model to simulate the starvation in an EHD contact located on a bearing track after several passages of the rolling elements, based on the ejection of lubricant out of the rolling track through Poiseuille flows.

In 2010, Venner and Lubrecht (63) published a paper on slender elliptical contacts ($k < 1$), based on numerical solutions. They contributed to improve the knowledge of the ellipticity effect on the central to minimum film thickness ratio. This may lead to an enhanced film thickness prediction for engineering applications. However, the study is limited to the narrow case only and it is based on dimensionless parameters which makes the analysis of the ellipticity influence not trivial to untangle. The same year, Canzi et al. (64) published a study on the transition between circular and line contacts: the wide elliptical contact being an intermediate case. They proposed a formula to use this relationship for predicting the central film thickness under all wide elliptical conditions.

More recently, Stahl et al. (65) investigated the EHD point contact with different entrainment velocity directions. They ran several experiments and showed a rather good agreement between film thickness measurements and numerical results under several load and entrainment cases. This was especially true for the film thickness minima. However, a non-Newtonian and thermal modelling would have probably improved the correlation at the larger entrainment and sliding velocity conditions. Pu et al. (66) investigated numerically the influence of mixed lubrication in the same contacts.

Moreover, despite the several experimental studies, precise validations of the EHD elliptical contact numerical models are still needed. With lacks in both numerical and experimental aspects, the EHD elliptical contact shall be studied as an unavoidable mean to improve the knowledge on torus on plane FREC.

## 1.4. Outline of the thesis

It was shown that the literature dedicated to flange roller-end contact (FREC) with torus roller end is nearly non-existent. Such a lack of references on the subject underlines the need for a dedicated study.

The literature pertaining to the FREC with torus roller end was extended by other works which were addressed to other general shape contacts. The approach developed in these publications will also inspire the work which will be presented afterwards.

As general shape contacts were often approximated by the elliptical ones, a bibliography pertaining to them was presented. It turned out that further developments are still required for this topic also.

The literature report revealed lacks in the understanding of the FREC with torus roller end. Several questions were raised by Gadallah and Dalmaz (20), Zhang et al. (14) and Colin et al. (9). From a numerical point of view, nobody has computed FREC with the torus roller end actual geometry. Has the actual geometry an influence on the contact modelling? Or is the elliptical approximation sufficient? An advanced modelling should be developed in order to answer these questions. The works on the gear topic will inspire the development of this FREC focused model.

Moreover, the model validations showed differences with experimental results. It was suspected that a starvation occurred and penalized the film forming. But was it not the modelling choices (geometrical assumptions, the use of dimensionless parameters, the rheology hypothesis, thermal effects…) which may have been responsible? Similarly, did the experimental approaches mentioned before really represent the conditions expected? A better control of the experimental environment, more precise measurements and advanced models should be developed in order to provide stronger validations.

As elliptical and general contact understanding are intimately related, the focus will also be drawn on the former in chapter 2. First of all, experimental validation should be furnished to the numerical model. Then, the influence of ellipticity ratio on the film forming capacity will be studied. This ratio should be varied independently from the other operating parameters, in order to complete the existing studies.

Based on these tool improvements, it will be possible to extend and improve the understanding of the torus on plane FREC. In chapter 3, new tools to the study of this contact are presented, and in chapter 4, the influence of entrainment velocity and load on friction forces and film thickness will be investigated. As the kinematics is known to have a key role on FREC, its influence will also be investigated. This chapter will also give conclusions on the validity of the elliptical approximation.

# Chapter 2. The flange roller-end contact as a slender elliptical EHD contact

# II. The flange roller-end contact as a slender elliptical contact

As mentioned in the previous chapter, the torus on plane flange roller-end contact may be considered, as a first approach, as an elliptical contact. In particular, it can be approximated by a slender elliptical contact. However, the literature review underlined the lack of knowledge on elliptical contacts, especially for the slender configuration. This chapter aims to bring further the understanding on both elliptical EHD contacts, by studying the slender ones, together with the other ellipticity ratios and flange roller-end contact. This ratio should be varied independently from the other operating parameters, in order to complete the existing studies. Thus experimental and numerical approaches were run in parallel. Jérotrib, a ball-on-disc test-rig enabling friction and film thickness measurements, will be adapted for elliptical EHD contacts. Besides, a numerical model built on the basis of the ones of Habchi et al. (45) and Doki-Thonon et al. (16) will simulate elliptical EHD contacts. Some improvements were made in order to model the elliptical configurations.

## 2.1. Numerical and experimental tools

### 2.1.1. Jérotrib test-rig

#### *2.1.1.1. The test-rig*

The present bespoke apparatus (see Figure 2.1-1) was built at first to run tests on circular EHD contacts. Its precision and wide possibilities were demonstrated on several occasions for both friction and film thickness measurements. In Jérotrib, a load $w$ which can reach $400\ N$ is applied between a convex sample and a disc. The disc can be made out of glass or sapphire for film thickness measurements and out of steel or tungsten carbide for other applications. Similarly the convex sample can be a steel or a tungsten carbide sample. In any case, both specimen are mirror polished ($R_a \leq 5\ nm$ in general, but $R_a \leq 50\ nm$ for tungsten carbide samples). The different configurations allow for large contact pressures, up to $3\ GPa$ in the context of two tungsten carbide samples. The convex sample has a curvature radius $R_x = 12.7\ mm$ along the entrainment direction. The entrainment velocity can be varied between a few millimetres per second and up to $7\ m/s$. Two independent spindles set the rotation of the samples. The spindles and specimen temperatures are set to the temperature of the experiment (*i.e.* the lubricant temperature) through a circulating heat transfer fluid.

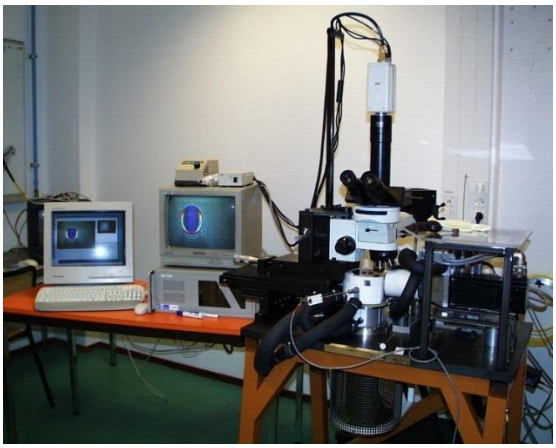

*Figure 2.1-1 – Jérotrib test-rig*

In 1999, Molimard et al. (3) developed an experimental method for film thickness measurement, the differential colorimetric interferometry (DCI), and led the first studies with it. Later on, Chaomleffel et al. (67) showed fair agreements in a wide range of operating conditions between the experimental results stemming from Jérotrib and predictive formulae once the physical properties of the lubricant were correctly accounted for.

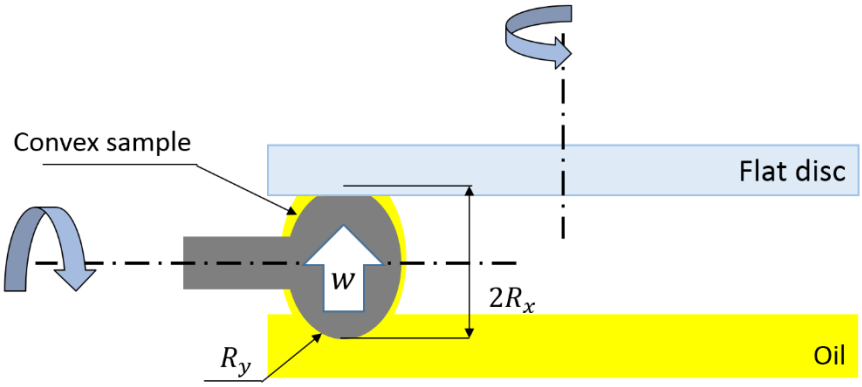


*Figure 2.1-2 - Jérotrib contacting bodies*

Figure 2.1-2 shows the convex sample on which the normal load $w$ is applied in order to put it in contact with the flat disc. The convex sample dips into the tested oil reservoir and drags the lubricant to the contact, insuring fully-flooded conditions. The lubricant is filtered with a $0.47\ \mu m$ polymer filter. Unlike the previous studies on this test-rig, $R_y$ was varied while $R_x$ remained constant. Several steel convex samples were designed and used. Their geometric properties are gathered in Table 2.1-1, whereas their mechanical properties are presented in Table 2.1-2.

| Convex sample | $R_x$ [mm] | $R_y$ [mm] | $k = b/a$ | $a$ [mm] * | $b$ [mm] * |
|---|---|---|---|---|---|
| "Slender Elliptical" | 12.70 | 4.82 | 0.526 | 0.173 | 0.0910 |
| "Circular" | | 12.70 | 1 | 0.149 | 0.149 |
| "Wide Elliptical" | | 84 | 3.46 | 0.105 | 0.364 |

*Table 2.1-1 - Presentation of the different lower sample geometries. They are made of steel ($E_b = 210e9\ Pa, \nu_b = 0.3$) and the ellipse dimensions (*) are computed for a contact with a glass disc ($E_t = 72e9\ Pa, \nu_t = 0.23$) for $w = 20\ N$.*

The flat disc was made of glass (properties displayed in Table 2.1-2). A thin chromium coating was applied to its lower side to improve the film thickness measurements, as the method used is the differential colorimetric interferometry. This layer has no noticeable influence on the disc thermal properties. Another coating was applied on the disc: it is a silica spacer layer. It is an optical tool to enable the measurement of very thin film thickness (down to a few nanometres) and was developed first by Westlake and Cameron (68) and used for instance by Hartl et al. (69).

| Glass disc properties | |
|---|---|
| **Parameter [Unit]** | **Value** |
| $E_t\ [Pa]$ | $72 \times 10^9$ |
| $\nu_t\ [-]$ | 0.23 |
| $\rho_t\ [kg.m^{-3}]$ | 2530 |
| $k_t\ [W.m^{-1}.K^{-1}]$ | 0.937 |
| $C_{pt}\ [J.kg^{-1}.K^{-1}]$ | 880 |

| Steel sample properties | |
|---|---|
| **Parameter [Unit]** | **Value** |
| $E_b\ [Pa]$ | $210 \times 10^9$ |
| $\nu_b\ [-]$ | 0.3 |
| $\rho_b\ [kg.m^{-3}]$ | 7850 |
| $k_b\ [W.m^{-1}.K^{-1}]$ | 50 |
| $C_{pb}\ [J.kg^{-1}.K^{-1}]$ | 470 |

*Table 2.1-2 – Sample properties*

The test rig temperature is set according to the experiment requirement. The temperature regulation is assumed within a precision of 0.1°C thanks to a platinum resistance located at the contact exit and a heat-carrying fluid which circulates around the sample and disc holders but also under the oil container. The aim is to set the whole contact environment to the desired temperature. In this chapter the temperature of the experiment environment is set to $T_0 = 30°C$.

#### *2.1.1.2. Optical interferometry principles*

White light interferometry appears as the most suitable technique to measure film thickness in EHD contacts within a few nanometres precision. A methodology has been defined by Molimard et al. (3), and it is based on a direct treatment of RGB (Red, Green, Blue) intensities of chromatic interferograms. The physic principle is quite widely known: it is this principle that gives their colours to the dirty oily puddles in the streets. Figure 2.1-3 shows one of these

oily puddles, with the colourful fringes that appear on it: the light is reflected at the air-oil interface but also at the oil-water interface. As a thin layer of oil floats on the water, there is an optical path difference between the two reflected light beams. This optical path difference is nothing more than two times the oil layer thickness and the resulting colour depends on this thickness.

*Figure 2.1-3 - Oily puddle*

A mono-chromatic configuration is selected to approach the interferometry phenomenon. Thanks to a mono-chromatic lighting (with $\lambda_{mc}$ the wavelength, the superscript $_{mc}$ stands for monochromatic), it is possible to predict the resulting interference fringes and to relate them to the optical path difference experimentally. Unlike chromatic light, mono-chromatic light interferences can be described more easily with analytical expression. In this thesis, a red filter ($\lambda_{mc} = 635 \pm 4\, nm$) was used to obtain a monochromatic radiation from a white light source. Besides, a Hitachi Kokusai HV-F22 camera and a microscope were used with the DyVa-s software from Alliance Vision in order to obtain digital pictures of the contact.

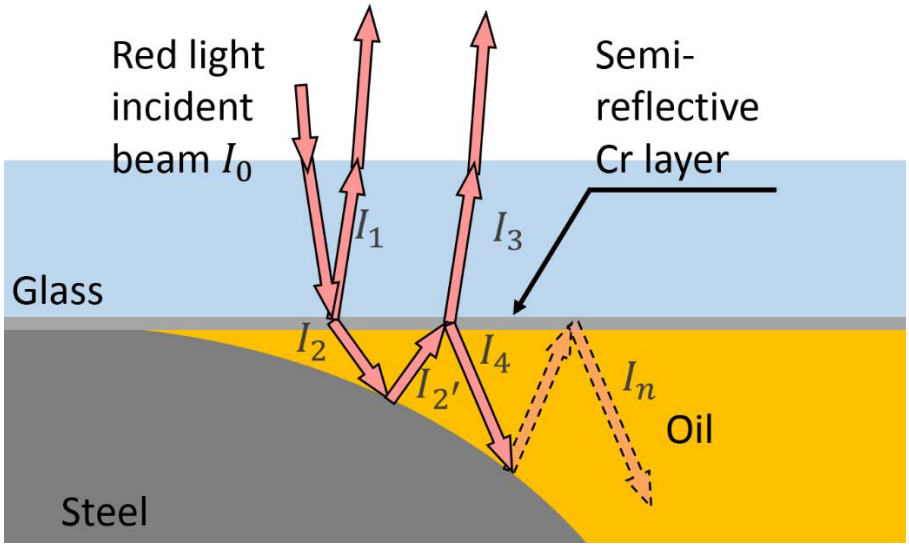


*Figure 2.1-4 - Mono-chromatic interferometry in a static contact vicinity. $I_0$ is the incident beam and $I_1$ to $I_n$ are the reflected beams*

Electromagnetic waves are constituted of an electric field $\vec{E}$ and a magnetic field $\vec{B}$. Their norm can be both described by the following expression:

$$j = J\cos\left(\frac{2\pi}{\lambda_{mc}}(c\,t - n_{mc}\,x_{mc}) - \phi\right) \qquad \textit{Equation 2.1-1}$$

with $J$ the wave amplitude, $\lambda_{mc}$ its wavelength, $c$ the light velocity, $t$ the time, $n_{mc}$ the refractive index of the medium, $x_{mc}$ the position, and $\phi$ the phase at the origin. When two beams of the same wave train meet, they interfere (like $I_1$ and $I_3$ in Figure 2.1-4). When the interfering beams have a path difference (of the length $\delta_{mc}$) the resulting wave is different. The resulting light intensity (the square of $J$) is then:

$$I = I_1 + I_3 + 2\sqrt{I_1 I_3}\cos\left(\frac{2\pi\delta_{mc}}{\lambda_{mc}}\right) \qquad \textit{Equation 2.1-2}$$

This means that $I$ varies between $I_{min} = I_1 + I_3 - 2\sqrt{I_1 I_3}$ and $I_{max} = I_1 + I_3 + 2\sqrt{I_1 I_3}$. In the present description, the reader may have notice that $I_4$ to $I_n$ were neglected. It can be demonstrated that their contribution to $I$ is negligible. The optical path difference $\delta_{mc}$ is twice the distance between the two samples. Indeed, the light beam crossed the $n_{mc}$ index fluid before and after the reflection on the steel sample. Then, it comes that $\delta_{mc} = 2\,h\,n_{mc}$ with $h$ the film thickness. At the reflection on the steel surface, the electromagnetic wave undergoes a phase shift $\xi$ (nota bene: a mirror polishing is applied to the convex sample before each experiment to insure a homogenous reflection on the steel surface). Equation 2.1-2 becomes:

$$I = I_1 + I_3 + 2\sqrt{I_1 I_3}\cos\left(2\pi\left(\frac{2\,n_{mc}\,h}{\lambda_{mc}} + \xi\right)\right) \qquad \textit{Equation 2.1-3}$$

Consequently, the extrema of $I$ occur for $h = (k_{mc} - \xi)\lambda_{mc}/(2n_{mc})$ (the maximum) and $h = (k_{mc} + 1/2 - \xi)\lambda_{mc}/(2n_{mc})$ (the minimum). The former is due to a constructive interference, whereas the latter is due to a destructive interference. The integer $k_{mc}$ is the interference order, and it characterises the number of the interference. Indeed, the interferences fringes are similar to one another and the same pattern is repeated for each of them. The pattern has a period of $\lambda_{mc}/(2n_{mc})$, which means that two consecutive minima are separated by this period.

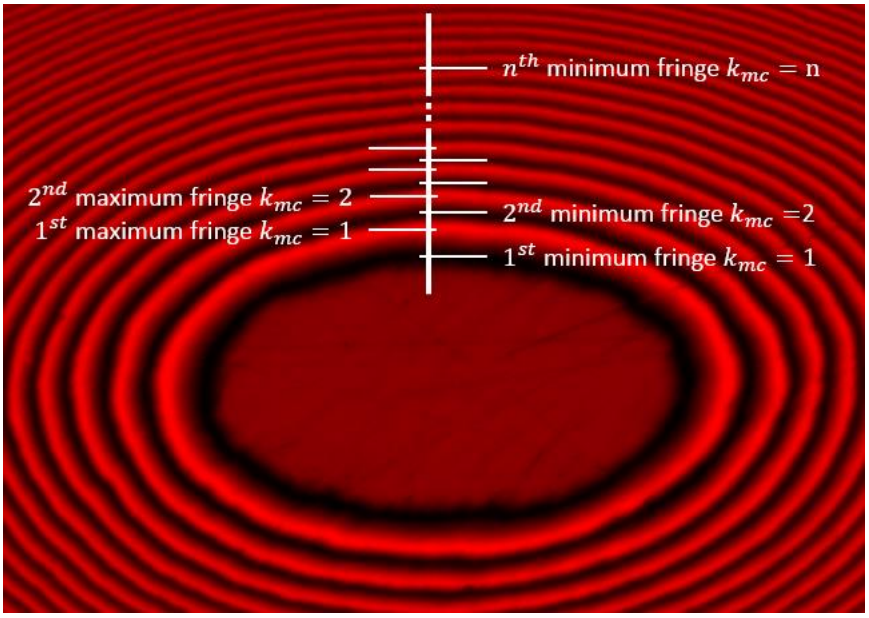


*Figure 2.1-5 – Narrow elliptical convex sample in a static contact with a glass disc illuminated by a $\lambda_{mc} = 635\ nm$ light. The interferences maxima and minima are indicated with their order.*

The mono-chromatic interferences are easy to describe analytically, but there is no bijective relationship between the colour and the optical path difference. Indeed the function is periodical in a wide range of gap. Moreover, Molimard (1) demonstrated that the analytical description of the mono-chromatic interferences is only valid at the black fringes location. These limits exclude the use of mono-chromatic interferometry to measure the EHD film thickness. However, Molimard (1) also explained that in the $0 \leq h \leq 800\ nm$ range, the chromatic interferometry generates a bijective relationship between the interference colour and the optical path difference. This bijection property is very useful as it is the range of film thickness encountered in EHD contacts.

Figure 2.1-6 shows the chromatic interferometry principle, applied to the oil gap between a steel and a glass surface. The white light incident beam $I_0$ crosses the glass and is partially reflected on the semi-reflective chromium layer. This first reflection is $I_1$. $I_3$ is the reflection of $I_0$ on the steel surface. The oil gap introduces an optical path difference between $I_1$ and $I_3$ and the two reflected beams are consequently interfering (as they belong to the same wave train). The colour (defined by its decomposition in the RGB frames captured by a digital 3-CCD camera) resulting from the interference is representative of the optical path difference, and consequently of the thickness $h$ of the oil gap.

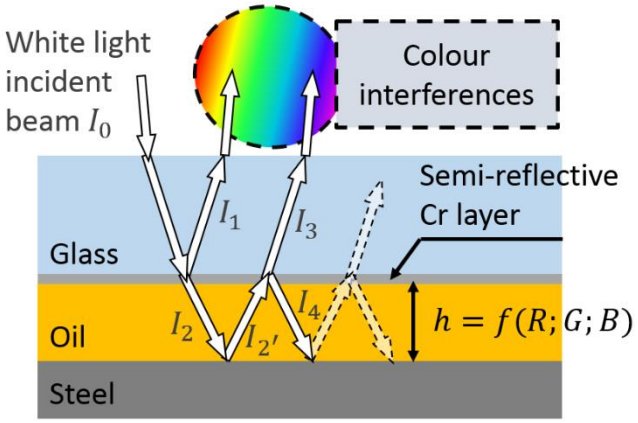


*Figure 2.1-6 – Physical principle of interferences*

Molimard et al. (3) developed a method based on this principle to perform film thickness measurements in EHD contacts. In their method, the function $f$ relating the RGB light intensity triplet and the oil gap has to be determined to enable film thickness measurements. This function depends on a wide range of environment conditions such as, among them, the light source spectrum, the refractive index (and therefore the pressure) of the lubricant, the optical path, the surfaces chemical condition (which influences the light reflections and introduces a phase shift) or the chromium layer thickness. Due to all these complex causal links, each experiment has its own calibration function. Therefore, the determination of $f$ is a mandatory part of the film thickness measurement procedure. However, the method developed by Molimard et al. (3) is limited to the circular contacts, as the calibration step depends on Equation 2.1-4 which is only valid for sphere on plane conjunctions.

The method for sphere on plane contact is based on an analytical formula which gives the gap height at the contact vicinity. Equation 2.1-4 was proposed by Johnson (70), and is presented below. This equation is valid for circular contacts only ($R_x = R_y$ and $a = b$):

$$h(r) = \frac{r^2}{2R_x} - \frac{a^2}{R_x} + \frac{1}{\pi R_x}\left[(2a^2 - r^2)\ \arcsin\left(\frac{a}{r}\right) + r^2\left(\frac{a}{r}\right)\sqrt{1-\left(\frac{a}{r}\right)^2}\right] \quad for\ r \geq a \qquad \textit{Equation 2.1-4}$$

with $r$ the distance from the contact centre (refer to (1) and (71) for more information). In the methodology defined by Molimard et al. (3), Equation 2.1-4 is mandatory. This equation gives the height between the mating bodies independently from the material mechanical properties.

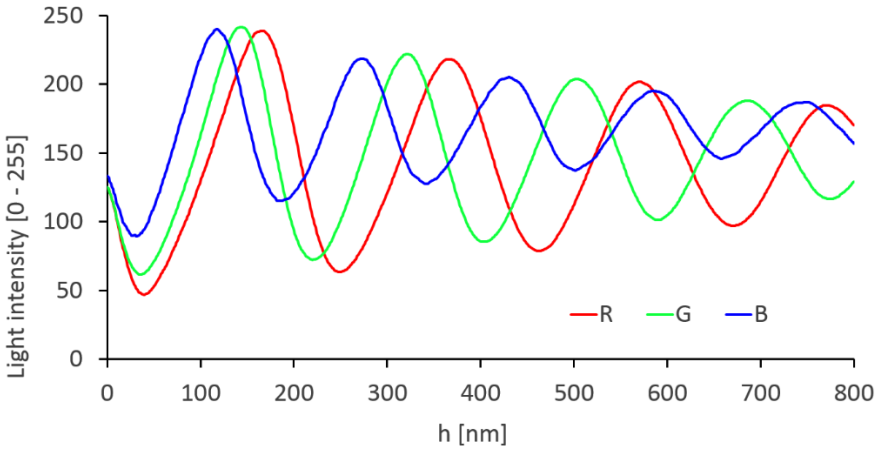


*Figure 2.1-7 – The function $f$, a typical white light interferometry calibration curve in the range $0 < h < 800\ nm$*

Figure 2.1-7 presents the resulting function $f$ which is constituted of three curves. The contrast $C = (I_{max} - I_{min})/(I_{max} + I_{min})$ of the light intensities will determine the measurement resolution of the dynamic oil gap. Consequently, $C$ should be maximized by adjusting the environment conditions. When the contrast has been maximized, one can obtain $f$ from a dedicated procedure. It was demonstrated by Molimard (1) that each RGB light intensity triplet corresponds to a single gap $h$ (bijection property), which avoids the confusions between interference order. Moreover, and apart from the variation of the oil refraction index with pressure, the relationship between the light intensities and the film thickness is considered identical for the static gap and the dynamic gap.

#### *2.1.1.3. The new calibration method*

However, the existing method to establish the calibration curve $f$ required static circular contacts (see Figure 2.1-8 at the centre). During this thesis, the experiments were run with the 3 convex samples presented in Table 2.1-1 and a new method had to be developed.

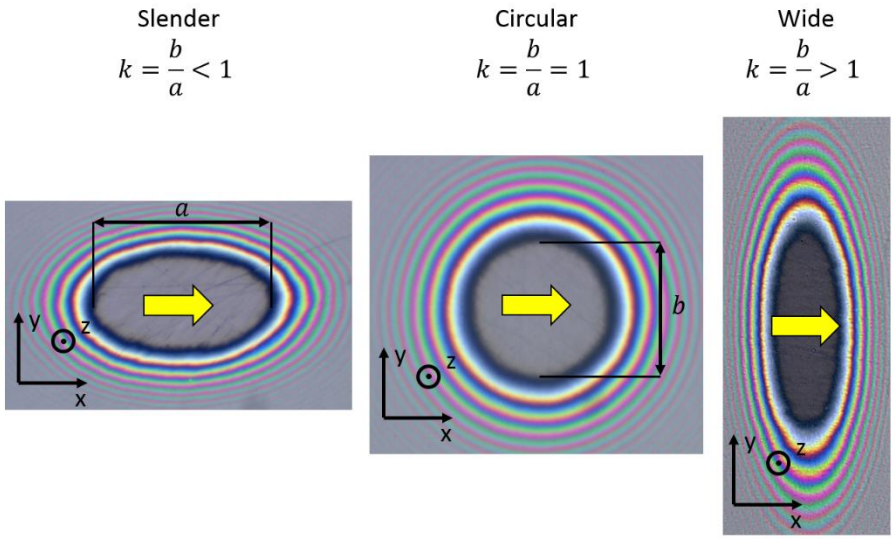


*Figure 2.1-8 - The different static contact for the 3 convex samples. From left to right: Slender Elliptical, Circular and Wide Elliptical static contacts. With $a$ the contact semi-axis along $x$ direction (entrainment velocity direction, when applied) and $b$ the contact semi-axis along $y$ direction.*

Unfortunately, the height expression Equation 2.1-4 has no analytical equivalent for the non-circular contact. It is not possible to predict the deformed gap analytically for all other types of point contacts, and even for the elliptical conjunction, no analytical exact solution is available. Consequently, a new method is required to determine the height between the loaded bodies.

In order to replace the missing height expression, a mono-chromatic interferogram is used. The minima of the interferogram can be used to define contour lines. As said previously, there is a $\lambda_{mc}/(2n_{mc})$ gap between two consecutive minimum contour lines. Thanks to an interpolation between the minima (where the gap is known), it is possible to define the relative shape of the gap at the contact vicinity. However, it is not trivial to define the absolute gap in this area as the very first minimum fringe gap is not known (due to the unknown phase shift $\xi$).

The height at the first minimum contour line is a data which is not obvious to obtain, but a solver which uses interpolations was successfully developed during this thesis. The method was inspired by the demodulation work of Badulescu et al. (72). The solver determines the contact frontier by a detection algorithm which analyses the light intensity extinction at the limit of the mating area. Then, the solver extracts data from the three first black fringes and the contact frontier position: the height at these four positions is supposed to locally follow the function described in Equation 2.1-4. From this the solver computes the gap at the first black fringe via Newton-Raphson iterations. Based on the knowledge of the height at this first fringe, the entire gap can be determined.

To sum-up, it is possible to fully determine the gap in the contact proximity by processing a contact picture illuminated by a well-defined mono-chromatic light.

Then, the same contact is illuminated by a chromatic light under the same conditions, and it will give the RGB interferences at each location of the contact vicinity. The mono-chromatic

and the chromatic interferogram constitute an interferogram pair. The final step towards the calibration curve is to relate the height (coming from the mono-chromatic picture) to the RGB triplets (coming from the chromatic picture). This operation allows for the determination of the calibration curve $f$ (like in Figure 2.1-7) without any hypothesis on the materials or the optical system. The only hypothesis is the shape of the gap interpolation (cubic polynomial order was selected) between the fringes. The method was implemented in a program with a user interface (with MATLAB software). This algorithm allows for fast determination of the calibration curve of an experiment. Moreover, the user does not need a full understanding of the whole process as the program guides the different operations. This program was tested with several users and they obtained relevant and precise results. The different steps followed by the algorithm are summarised in Annexe A.

Practically, in order to establish a calibration curve representative of an experiment, several calibrations are made from several interferogram pairs. These pairs are obtained all along the experiment. Habitually, 5 pairs are made previously to the EHD experiment, 5 pairs at mid-experiment, and 5 at the end of the experiment. Each pair can provide a slightly different calibration curve, and the one which is the most representative of the curve group is selected. The differences between the different curves enable to track some potential variations of the whole experimental set up, and to evaluate if the calibration curve chosen is suitable for the entire experiment.

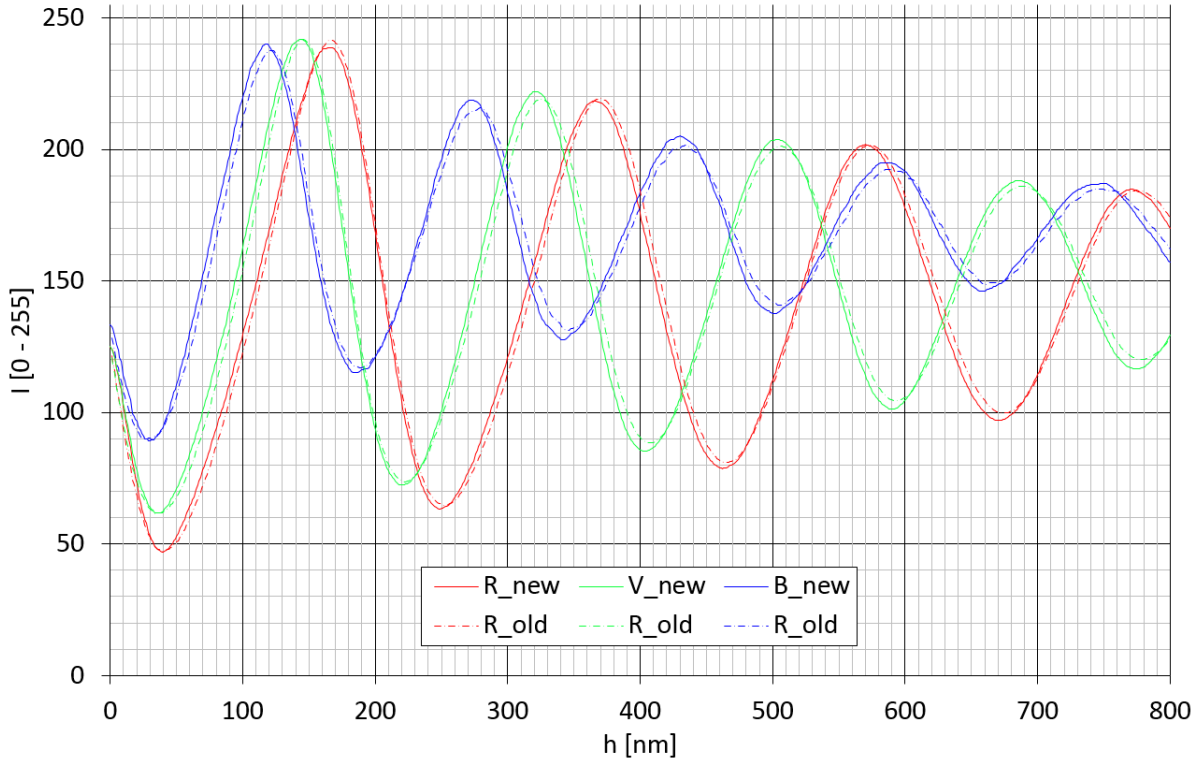


*Figure 2.1-9 – Calibration curve comparison between Molimard et al. (3) ("old") and the present ("new") methodologies. Comparison basis: a static circular contact made with the Jérotrib test-rig*

The new method described was validated as it was able to establish a calibration curve very similar to the one obtained via the previous method for the same circular contact (see Figure 2.1-9). Moreover, it enabled to measure the gap in the vicinity of a Hertzian elliptical contact: these measures agreed very well with the predictions of a numerical static contact model. An additional validation is proposed in Annexe A.

#### *2.1.1.4. Application*

Thanks to this new calibration method, one can measure the film thickness in the contact and its proximity under EHD conditions, for any general contact configuration (smooth surfaces), including the torus on plane contact. Figure 2.1-10 presents such a contact.

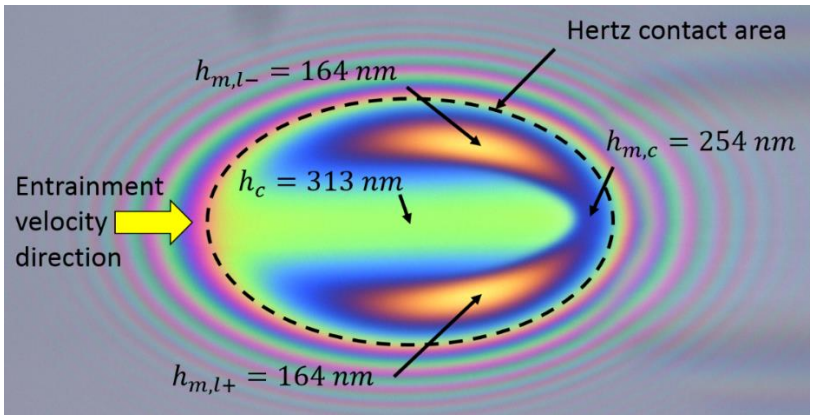


*Figure 2.1-10 - Slender elliptical EHD contact*

The entrainment direction is in the direction of the yellow arrow. According to the classical EHD theory, the contact has a classical horseshoe shape with a constriction occurring at the contact exit and on the sides. Like slender contacts from the literature, the minima are located on the two sides. They are called $h_{m,l+}$ and $h_{m,l-}$ as they are the lateral minima. The + sign indicates the side which is the closest to the rotation axis of the disc whereas the – sign indicates the furthest. The central film thickness $h_c$ is measured by the interference colour in the central region, but a Lorentz-Lorenz correction (73) has to be applied. Indeed, the calibration is made with the lubricant at ambient pressure. However, the lubricant refractive index at the ambient pressure $n_0$ actually varies with pressure, which changes the optical path length. To obtain the actual gap, an adjustment is required:

$$h(p) \times n(p) = n_0 \times h_0 \qquad \textit{Equation 2.1-5}$$

with $h_0$ the apparent film thickness (without correction), $h(p)$ the actual gap and $n(p)$ the refractive index predicted by the Lorentz-Lorenz correction. The index $n(p)$ can be determined from:

$$\frac{1}{\rho_f(p)} \times \frac{n(p)-1}{n(p)+2} = \frac{1}{\rho_0} \times \frac{n_0-1}{n_0+2}$$ *Equation 2.1-6*

where $\rho_f(p)$ is the fluid density at a given pressure and $\rho_0$ at the ambient pressure. Thanks to this adjustment, the relationship between the film thickness and the light intensities is considered unchanged under static and dynamic conditions. The pressure dependence of the fluid density is modelled by the Murnaghan equation of state detailed later in Equation 2.1-7 and Equation 2.1-8. For this operation, the lubricant pressure is supposed to be equal to the Hertzian pressure distribution.

Jérotrib is one of the tools used to study the elliptical contacts, and by extension torus on plane flange roller-end contacts. It enabled to run experiments and obtain precise measurements of the characteristic values of the contact, like film thickness in circular and elliptical configurations. The results were used as powerful means to validate the numerical model.

### 2.1.2. Numerical model

The experimental set-up presented previously was completed with a numerical model. Indeed, the experimental results may not fully correspond to the torus on plane (TOP) flange roller-end contact (FREC) configuration (in terms of load or geometry for instance). Using numerical methods allowed for more flexibility in studying such a complex contact. A thermo-elastohydrodynamic (TEHD) model was based on the work of Habchi et al. (45) and Doki-Thonon et al. (16) and a supplementary component was added. The additional feature is the adaptation to the elliptic contact problem. It will be detailed in the following. Most of the influent parameters involved in the contact could be summarized in Figure 2.1-11. This schematic overview of the model introduces variables which will also be detailed in this section. Among these variables, some were obtained by solving the governing equation, while some others were defined by constitutive laws and depend on the other ones. The constitutive laws will be presented at first, and the rest of the model (equations, domains and solver) will be introduced afterwards.

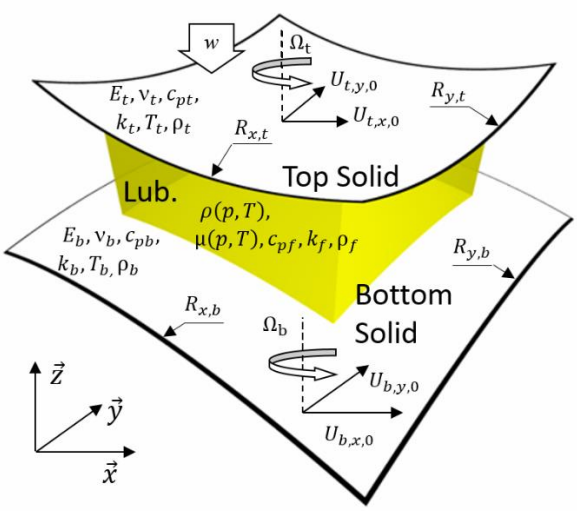


*Figure 2.1-11 – Schematic view of a lubricant trapped between two rolling-sliding-spinning solids (inspired from T. Doki-Thonon thesis)*

#### *2.1.2.1. The constitutive laws*

The aim of the present numerical model is to predict the behaviour of an actual EHD contact. To do so, the lubricant physics had to be known and described by constitutive laws. The density and the viscosity of the lubricant are influenced by the large pressure occurring inside the contact. Besides, the temperature rise in the lubricant also had an influence on its density and viscosity. At last, the shear stress can also have a significant influence on viscosity.

In order to generate results independently from the Jérotrib experimental results, other test-rigs such as rheometers and viscometers were used to characterise the lubricant. The lubricant selected for this thesis is a standard mineral based turbine oil. Two different batches were used: lubricant 2 and lubricant 3, where lubricant 2 corresponds to the fluid called lubricant 2 in Doki-Thonon's thesis (5). Lubricant 1 used by Doki-Thonon is not used here. In the present thesis, lubricant 3 is used when not otherwise specified. Lubricant 3 was characterized and its properties are displayed in Tables 2.1-4, whereas Lubricant 2 and its characteristics are displayed in Tables 2.1-3.

**Lubricant density**

A Murnaghan equation of state (EOS) (based on the work of Murnaghan (6)) was chosen (similarly to Doki-Thonon et al. (16)) to fit the density dependence on pressure and temperature:

$$\frac{V}{V_0} = \frac{\rho_0}{\rho_f} = \left(1 + \frac{K'_M}{K_M} p\right)^{-\frac{1}{K'_M}} \qquad \textit{Equation 2.1-7}$$

where $V$ and $\rho_f$ are respectively the lubricant volume and density, $K'_M$ a constant. The superscript $(\ )_0$ stands for the environment conditions ($T = T_0, p = 0$).

$$K_M = K_{MM} e^{-\beta_K T}$$

is a temperature related parameter, with $K_{MM}$ a constant, $\beta_K$ the bulk modulus-temperature coefficient and $T$ the temperature. When $T_0$ (at $p = 0$ ), the environment temperature and $T_R$ (at $p = 0$ ), the reference temperature (at which the lubricant was characterized) are different, the density variation writes:

$$\frac{V_0}{V_R} = \frac{\rho_R}{\rho_0} = 1 + a_v(T_0 - T_R) \qquad \textit{Equation 2.1-8}$$

This EOS was initially developed for geologic conditions, but was adapted to lubricant application. It suits to the pressure and temperature range encountered in the EHD conditions, and the parameters determined by experimental work are in Tables 2.1-3 and Tables 2.1-4.

### Lubricant viscosity

Another lubricant parameter varies with temperature and pressure: the viscosity. For its part, the pressure is the most influent parameter: an important pressure rise occurs in EHD contacts, but an even larger rise of viscosity (several orders of magnitude) happens as a consequence. An independent characterisation was made at the LaMCoS with bespoke rheometers. The lubricant was tested in a wide range of temperature ($0 \leq T_0 \leq 150°C$) and pressure ($0.1 \leq p \leq 800\ MPa$) conditions. A modified Williams-Landel-Ferry (WLF) correlation (as defined by Bair et al. (7)) was selected (similarly to Raisin et al. (74)) to fit the results of the characterisation. It reads:

$$\mu(p,T) = \mu_G\ exp\left[\frac{-2.303\ C_1\ (T - T_g)F}{C_2 + (T - T_g)F}\right] \qquad \textit{Equation 2.1-9}$$

with $T_g(p) = T_{g0} + A_1 \ln(1 + A_2 p)$ and $F(p) = (1 + b_1 p)^{b2}$

with $C_1, C_2, A_1, A_2, b_1$ and $b_2$ constants of the WLF law, $T_g$ the glass transition temperature at a given pressure, and $T_{g0}$ the glass transition temperature at ambient pressure. These parameters are displayed in Tables 2.1-3 and Tables 2.1-4.

| Murnaghan EOS – Lubricant 2 | |
|---|---|
| **Parameter [Unit]** | **Value** |
| $a_v\ [K^{-1}]$ | $7.734 \times 10^{-4}$ |
| $\beta_K\ [K^{-1}]$ | $6.090 \times 10^{-3}$ |
| $K_{00}\ [Pa]$ | $9.234 \times 10^{9}$ |
| $K_0'\ [-]$ | 10.545 |
| $T_R\ [K]$ | 298 |
| $\rho_R\ [kg.m^{-3}]$ | 872 |

| Modified WLF – Lubricant 2 | |
|---|---|
| **Parameter [Unit]** | **Value** |
| $A_1\ [°C]^*$ | 188.86 |
| $A_2\ [Pa^{-1}]$ | $0.7190 \times 10^{-9}$ |
| $b_1\ [Pa^{-1}]$ | $8.200 \times 10^{-9}$ |
| $b_2\ [-]$ | $-0.5278$ |
| $C_1\ [-]$ | 16.09 |
| $C_2\ [°C]^*$ | 17.38 |
| $T_{g,0}\ [°C]$ | $-83.2$ |
| $\mu_G\ [Pa.s]$ | $10^{12}$ |

*Tables 2.1-3 - Lubricant 2 laws parameters (*implies to write T in °C)*

| Murnaghan EOS – Lubricant 3 | |
|---|---|
| **Parameter [Unit]** | **Value** |
| $a_v\ [K^{-1}]$ | $7.734\ \times\ 10^{-4}$ |
| $\beta_K\ [K^{-1}]$ | $6.090 \times 10^{-3}$ |
| $K_{MM}\ [Pa]$ | $9.234 \times 10^{9}$ |
| $K_M'\ [-]$ | 10.545 |
| $T_R\ [K]$ | 298 |
| $\rho_R\ [kg.m^{-3}]$ | 872 |

| Thermal properties – Lubricant 3 | |
|---|---|
| **Parameter [Unit]** | **Value** |
| $C_{pf}\ [J.kg^{-1}.K^{-1}]$ | 1901 |
| $k_f\ [W.m^{-1}.K^{-1}]$ | 0.118 |

| Modified WLF – Lubricant 3 | |
|---|---|
| **Parameter [Unit]** | **Value** |
| $A_1\ [°C]^*$ | 188.951 |
| $A_2\ [Pa^{-1}]$ | $0.53321 \times 10^{-9}$ |
| $b_1\ [Pa^{-1}]$ | $7.373 \times 10^{-9}$ |
| $b_2\ [-]$ | $-0.6171$ |
| $C_1\ [-]$ | 15.9035 |
| $C_2\ [°C]^*$ | 14.1596 |
| $T_{g,0}\ [°C]^*$ | $-68.4697$ |
| $\mu_G\ [Pa.s]$ | $10^{12}$ |

*Tables 2.1-4 - Lubricant 3 laws parameters (*implies to write T in °C)*

The influence of the shearing on viscosity was investigated via a rheometer. Figure 2.1-12 presents the results of this characterisation under various conditions, such as pressure, temperature and sheared gap. Despite the rather wide range of the operating conditions (shear stress up to 3 $MPa$), the results are not obtained in the same conditions as the EHD contacts reproduced during this thesis in tribometers. Additionally, it is suspected that the non-Newtonian effects have an important influence on friction in sliding contacts: this was demonstrated for lubricant 2 in Doki-Thonon thesis (5). As it was not possible to determine a Carreau law for lubricant 3 from Figure 2.1-12, the Carreau fit of another similar lubricant was used for a short study on non-Newtonian effects. This study is presented in Annexe C, and it demonstrated that this other lubricant was not similar enough to lubricant 3. The Carreau fit used did not correspond to behaviour of lubricant 3. Therefore, in the absence of a suitable model for non-Newtonian effects, the rest of the document will consider Lubricant 3 as Newtonian.

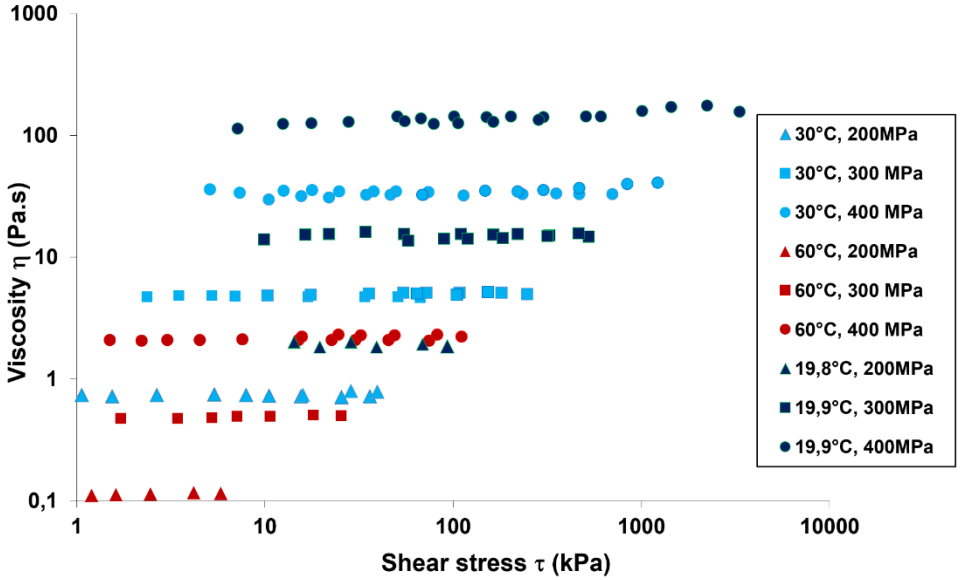


*Figure 2.1-12 - Lubricant 3 viscosity dependence on shear stress, under various pressure and temperature conditions.*

#### *2.1.2.2. The EHD problem*

As presented in chapter 1, the EHD problem requires the solving of different systems of equations.

**The generalised Reynolds equation**

The Navier-Stokes equations represent the mechanical equilibrium of the fluid medium. One can consider the fluid as continuous and the flow not time dependent. Moreover, the inertia forces and the surface tension are considered negligible in comparison with viscous forces. The fluid flow occurs in a confined domain where the film thickness is small compared to the other dimensions of the contact. Moreover, this flow is considered as laminar. Under these conditions, the simplified Navier-Stokes equations read:

$$\begin{cases} \dfrac{\partial p}{\partial x} = \dfrac{\partial}{\partial z}\tau_{zx} \\ \dfrac{\partial p}{\partial y} = \dfrac{\partial}{\partial z}\tau_{zy} \\ \dfrac{\partial p}{\partial z} = 0 \end{cases}$$

*Equation 2.1-10*

$(x, y, z)$ being the 3 space coordinates, with $z$ oriented along the film thickness, $p$ the pressure and $\tau_{ij}$ the $i$ shear stress in the $j$ direction. As one considers the fluid as viscous, these equations become:

$$\begin{cases} \dfrac{\partial p}{\partial x} = \dfrac{\partial}{\partial z}\left(\mu \dfrac{\partial u_{f,x}}{\partial z}\right) \\ \dfrac{\partial p}{\partial y} = \dfrac{\partial}{\partial z}\left(\mu \dfrac{\partial u_{f,y}}{\partial z}\right) \\ \dfrac{\partial p}{\partial z} = 0 \end{cases}$$

*Equation 2.1-11*

where $u_{f,i}$ is the velocity field of the lubricant in the direction $i$. The variable $\mu$ is the viscosity of the lubricant. After integrations along $z$, and considering that the viscosity may vary across the film thickness, the Navier-Stokes equations read:

$$\begin{cases} u_{f,x} = \dfrac{\partial p}{\partial x}\displaystyle\int_0^z \frac{z}{\mu} dz + C_x \int_0^z \frac{1}{\mu} dz + C'_x \\ u_{f,y} = \dfrac{\partial p}{\partial y}\displaystyle\int_0^z \frac{z}{\mu} dz + C_y \int_0^z \frac{1}{\mu} dz + C'_y \end{cases}$$

*Equation 2.1-12*

with $C_x$, $C'_x$, $C_y$ and $C'_y$ the integration constants. One considers no-slip at the fluid-structure interface:

$$\begin{aligned} \vec{u}_{f|z=0} &= \vec{u}_b \\ u_{f|z=h(x,y)} &= \vec{u}_t \end{aligned}$$

*Equation 2.1-13*

with $h(x,y)$ the film thickness at the point $(x,y)$, $u_t$ and $u_b$ the velocity fields at the top (t) and bottom (b) surfaces. The boundary conditions presented previously enable to define the four integration constants:

$$C_x = -\frac{\partial p}{\partial x}\frac{\int_0^h \frac{z}{\mu} dz}{\int_0^h \frac{1}{\mu} dz} + \frac{u_{t,x} - u_{b,x}}{\int_0^h \frac{1}{\mu} dz} \quad C_y = -\frac{\partial p}{\partial y}\frac{\int_0^h \frac{z}{\mu} dz}{\int_0^h \frac{1}{\mu} dz} + \frac{u_{t,y} - u_{b,y}}{\int_0^h \frac{1}{\mu} dz}$$
$$C'_x = u_{b,x} \qquad C'_y = u_{b,y}$$

*Equation 2.1-14*

Then one inserts these constants into Equation 2.1-12 (with the notations: $\frac{1}{\mu_e} = \int_0^h \frac{1}{\mu} dz$ and $\frac{1}{\mu'_e} = \int_0^h \frac{z}{\mu} dz$):

$$u_{f,i} = \frac{\partial p}{\partial i}\left(\int_0^z \frac{z}{\mu} dz - \frac{\mu_e}{\mu'_e}\int_0^z \frac{1}{\mu} dz\right) + \mu_e\left(u_{t,i} - u_{b,i}\right)\int_0^z \frac{1}{\mu} dz + u_{b,i} \text{ for } i = \{x, y\}$$

*Equation 2.1-15*

This expression describes the momentum. The following equation describes the mass conservation:

$$\frac{\partial m_x}{\partial x} + \frac{\partial m_y}{\partial y} = 0 \text{ with } m_x = \int_0^h \rho u_{f,x} dz \text{ and } m_y = \int_0^h \rho u_{f,y} dz$$

*Equation 2.1-16*

By introducing Equation 2.1-15 into the mass flow expressions (Equation 2.1-16), one obtains:

$$m_i = \int_0^h \left( \rho \frac{\partial p}{\partial i} \left( \int_0^z \frac{z'}{\mu} dz' - \frac{\mu_e}{\mu'_e} \int_0^z \frac{1}{\mu} dz' \right) + \mu_e \left( u_{t,i} - u_{b,i} \right) \int_0^z \frac{1}{\mu} dz' + u'_{b,i} \right) dz \quad \text{for } i = \{x, y\} \qquad \textit{Equation 2.1-17}$$

Under this form, this expression is at the basis of the generalised Reynolds equation as defined by Najji et al. (75) and used by Habchi et al. (4) and Doki-Thonon et al. (16). Indeed, with the notations detailed below:

$$\rho_e = \int_0^h \rho \, dz, \quad \rho'_e = \int_0^h \left( \rho \int_0^z \frac{1}{\mu} dz' \right) dz, \quad \rho''_e = \int_0^h \left( \rho \int_0^z \frac{z'}{\mu} dz' \right) dz,$$
$$\bar{\varepsilon} = \frac{\mu_e}{\mu'_e} \rho'_e - \rho''_e, \qquad \rho_i^* = \rho'_e \mu_e \left( u_{t,i} - u_{b,i} \right) - \rho_e u_{b,i} \qquad \textit{Equation 2.1-18}$$

Equation 2.1-17 can be reformulated. When differentiated, it becomes:

$$\frac{\partial m_i}{\partial i} = -\frac{\partial}{\partial i} \left( \bar{\varepsilon} \frac{\partial p}{\partial i} \right) + \frac{\partial}{\partial i} (\rho_i^*) \qquad \textit{Equation 2.1-19}$$

When Equation 2.1-19 is inserted into Equation 2.1-16, one obtains the generalised Reynolds equation:

$$\vec{\nabla} . \left( \bar{\varepsilon} \, \vec{\nabla} p \right) - \vec{\nabla} . \overrightarrow{\rho^*} = 0 \qquad \textit{Equation 2.1-20}$$

This expression is a mass conservation equation and it takes into account the viscosity and density variations along the $z$ axis.

In Equation 2.1-20, the film thickness $h$ has a key role, even if it does not appear explicitly. The common choice to express it is to consider the rigid bodies as parabolic in the contact vicinity. The gap between the surfaces is then:

$$\mathrm{h}(\mathrm{x}, \mathrm{y}) = \mathrm{h}_0 + \frac{x^2}{2R_x} + \frac{y^2}{2R_y} + \delta(x, y) \qquad \textit{Equation 2.1-21}$$

with $\delta(x, y)$ the deformation sum of the bodies along $z$ under load, and $h_0$ the gap between the rigid bodies, at the contact centre.

### The elastic deformations

The deformation term in Equation 2.1-21 is computed using linear elasticity equations. They are the second equation system of the EHD problem. Under the pressure generated by the hydrodynamic effects (described in the generalised Reynolds equation), the bodies are deformed, leading to a shape change of the fluid flow confinement. The solid mechanics side of this fluid-structure interaction is quite easily described by the classical elasticity equations.

However, it should be noticed that the equivalent body theory was applied to this problem. It is a common choice in the EHD domain (see Habchi (4) and Habchi et al. (45)). With this theory, one considers that the two mating solids can be reduced to a unique equivalent solid to compute the deformations. Its Young modulus $E$ and Poisson ratio $\nu$ are obtained from the ones of the original solids:

$$E = \frac{E_b^2 E_t (1+\nu_t)^2 + E_t^2 E_b (1+\nu_b)^2}{\left(E_b(1+\nu_t) + E_t(1+\nu_b)\right)^2}$$
$$\nu = \frac{E_b \nu_t (1+\nu_t) + E_t \nu_b (1+\nu_b)}{E_b(1+\nu_t) + E_t(1+\nu_b)}$$

*Equation 2.1-22*

with $E_b$ and $\nu_b$ the Young modulus and the Poisson ratio of the bottom solid, and $E_t$ and $\nu_t$ the ones of the top solid. As a result, only one equivalent deformable solid has to be modelled. It is of great use to reduce the computational time.

### The load equilibrium equation

The third and last equation which describes the EHD problem is the equilibrium of the load. One has to insure that the pressure sum generated over the EHD contact area is equal to the load applied on the solids. It simply writes:

$$\mathrm{w} = \iint_S p \, dxdy$$

*Equation 2.1-23*

with $w$ the contact load and $S$ and the pressurized surface area.

### Computation domains

The three equation systems presented above are solved simultaneously on two domains. Elastic deformations are solved on a cuboid (represented in grey in Figure 2.1-13). Its dimensions are chosen according to the literature (see Habchi (4)): they are much larger than the contact, and they model a semi-infinite body. Indeed, when they are large enough, their variation does not affect the results of the Reynolds equation. This equivalent body is clamped at its lower face, and a part of the upper face (represented in blue in Figure 2.1-13) undergoes the pressure generated in the contact. The other faces are free.

This pressure is the result of the Reynolds equation. The domain on which this equation is solved is defined much larger than the contact area. In such a way, its dimensions do not affect the results of the Reynolds equation. In Figure 2.1-13, the Reynolds domain dimensions are $8a$ along $x$ direction and $8b$ along $y$ direction, with $a$ and $b$ the Hertzian contact dimension respectively along the entrainment direction and perpendicular to it. These values are set according to the literature: Doki-Thonon (5) selected $9a$ for both directions (circular contacts) and Habchi selected (4) $6a$. The present study requires a smaller domain than Doki-Thonon's,

as the spinning kinematic is less severe, but it was decided to use a wider domain than Habchi's, because the ellipticity ratio varies and the pressure build up at the contact inlet varies with it. The selected dimensions were tested with success. At the limit of the Reynolds computation domain, the boundary $p = 0$ is set (it sets that the ambient pressure is the reference of the relative pressure). The free boundary problem occurring at the contact exit is solved using a penalty method (Wu (76), Habchi (4)). Indeed, at the contact exit the oil film rupture occurs and at this place $p = 0$.

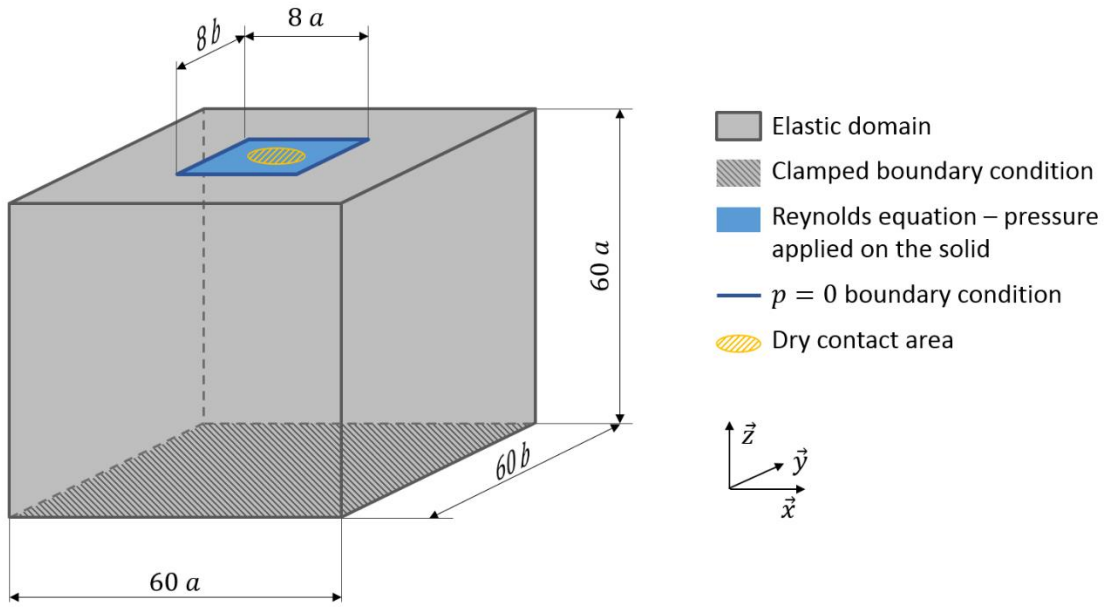


*Figure 2.1-13 - Computation domain*

### 2.1.2.3. *Thermal model*

Solving the EHD basic equations enables a good understanding of the contact behaviour. However, the equations previously presented do not permit to take into account more complex effects. Indeed, under EHD conditions, the lubricant endures a severe compression at the contact inlet, and a sudden pressure drop at its exit. These pressure variations constitute a heat source that writes:

$$Q_{comp} = -\frac{T}{\rho}\frac{\partial \rho}{\partial T}\left(\overrightarrow{u_f}.\vec{\nabla}p\right) \qquad \textit{Equation 2.1-24}$$

Moreover, due to the kinematic conditions, the lubricant experiences a moderate to high shear rate. The relative sliding of the mating surfaces imposes a shearing which induces thermal dissipation. This second heat source can be expressed as follows:

$$Q_{shear} = \mu\left(\left(\frac{\partial u_{f,x}}{\partial z}\right)^2 + \left(\frac{\partial u_{f,y}}{\partial z}\right)^2\right) \qquad \textit{Equation 2.1-25}$$

These heat sources operate in the lubricant film, and the temperature rise has a major influence on the lubricant properties. To be able to take into account these dependences, the following energy equation should be solved in the lubricant:

$$-\nabla.(\mathrm{k_f}\nabla T) + \rho_f c_{pf} \overrightarrow{U_f}.\nabla T = Q_{comp} + Q_{shear} \qquad \textit{Equation 2.1-26}$$

and in the top ($t$) and bottom ($b$) solids:

$$-\nabla.(\mathrm{k_i}\nabla T) + \rho_i c_{pi} \overrightarrow{u_i}.\nabla T = 0 \text{ with } i = \{t, b\} \qquad \textit{Equation 2.1-27}$$

The variable $T$ is the temperature, $k_f$ is the lubricant thermal conductivity and $c_f$ is its heat capacity.

As the heat sources and the material parameters vary in the lubricant thickness, the computation domain should be in the three dimensions as mentioned in Figure 2.1-14. Moreover, because the two solids may be of different nature, they should be both represented and no symmetry assumption can be made.

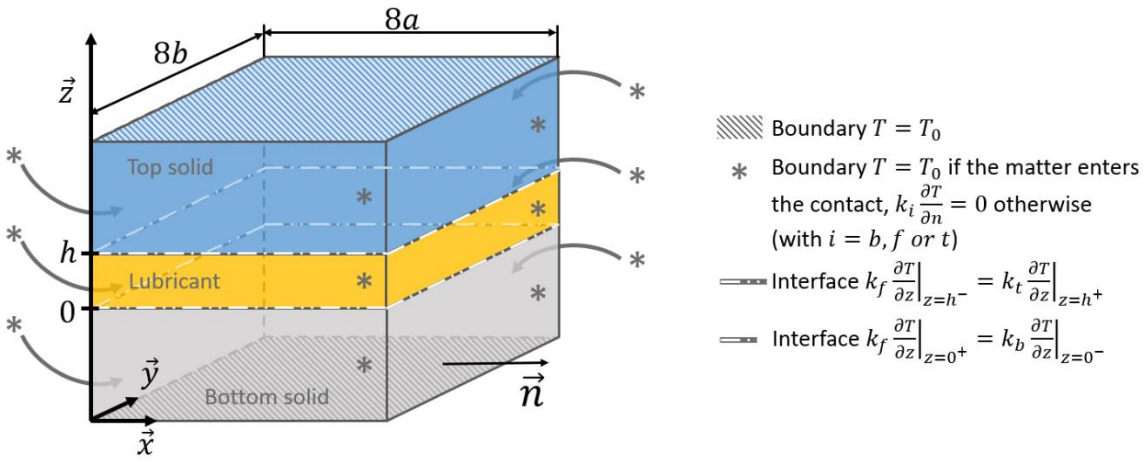


*Figure 2.1-14 - Thermal model computation domain*

At the top and bottom boundaries, the temperature is set at $T_0$ (the environment temperature), and the computation domain is defined so that the solids are infinitely thick comparing to the lubricant film thickness. The aim of this choice is to maintain a zero temperature gradient at the top and bottom boundaries. The lateral boundary conditions are set to the temperature $T_0$ as well, if the matter is entering the domain. Otherwise, a free-flux boundary condition is applied. Moreover, at the solid-liquid interfaces, the flux continuity is insured.

#### 2.1.2.4. *Solver*

The multiphysics aspects of this simulation, together with the complexity of the solution, make the fully-coupled solving within one step arduous. Each model equation must be initialised with a first guess which is as close as possible to the final solution. At first, the solid deformations are computed for a static Hertzian pressure distribution (a step called "Initialisation" in Figure 2.1-15). This deformation field is then used as an initial solution to the linear elasticity equations in the isothermal EHD fully coupled problem ("Isothermal EHD solver" in Figure 2.1-15), which means that the different equation systems are solved simultaneously. In this problem, the Reynolds pressure is initialised with the same static Hertzian pressure distribution. In parallel with this isothermal EHD computation, the thermal model is initialised by a one direction coupling with the EHD model: it is a loose coupling. The thermal model initialisation step solves the energy equation in isothermal EHD conditions, as if the thermal effects had no influence on these conditions. Finally the EHD model and the Thermal model are solved together in a fully coupled way. Such a process is similar to the stationary steps methodology chosen by Raisin et al. (77). The software used to compute all the equations described previously is COMSOL Multiphysics 4.4.

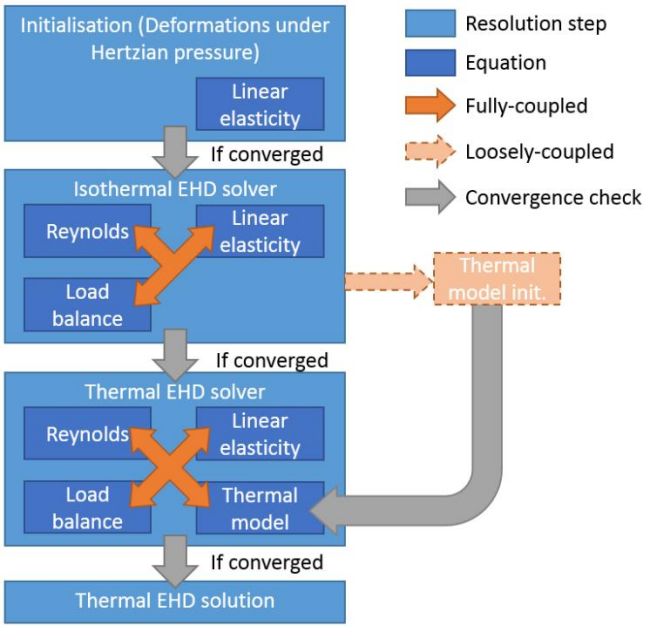


*Figure 2.1-15 – Resolution successive steps*

Despite the successive initialisation steps, the problem is highly non-linear: consequently several Newton-Raphson iterations are required to get the convergence at each step. The algorithm requires about 2h to converge on a classical computation (650 000 degrees of freedom) with a 3.5 GHz processor but without parallelisation. Moreover, the solution of one case can be used as an initial guess for other computations in order to save time.

The choice of the relative discrepancy criterion was made thanks to a numerical analysis, and the relative discrepancy is computed on the variation of $h_c$. The results are presented in Table 2.1-5, and it was decided to select the 0.001 relative discrepancy criterion.

| **Relative discrepancy** | **0.005** | **0.003** | **0.0015** | **0.001** | **0.0002** |
|---|---|---|---|---|---|
| $h_c\ [nm]$ | 245.6 | 274.3 | 310.8 | 315.5 | 316.7 |
| $h_m\ [nm]$ | 182.9 | 180 | 180.5 | 180.9 | 181.6 |

*Table 2.1-5 – Influence of the relative discrepancy (convergence criterion) on the central and minimum film thicknesses for the Case 1 described in section 2.2.1*

The typical dimensionless mesh size inside the pressurized area is selected to be 0.02 according to Figure 2.1-16 which gathers the results of the numerical analysis on mesh convergence. This graphs shows that it is necessary to have a mesh size inside the Hertz zone of the Reynolds domain which is inferior or equal to 0.02 in order to reach a numerical accuracy below 0.1%. It corresponds to a numerical problem with approximately $10^6$ degrees of freedom (DOF) for all the EHD isothermal Newtonian equations. A finer mesh does not contribute significantly to reduce the discretization error, but it increases the computation time.

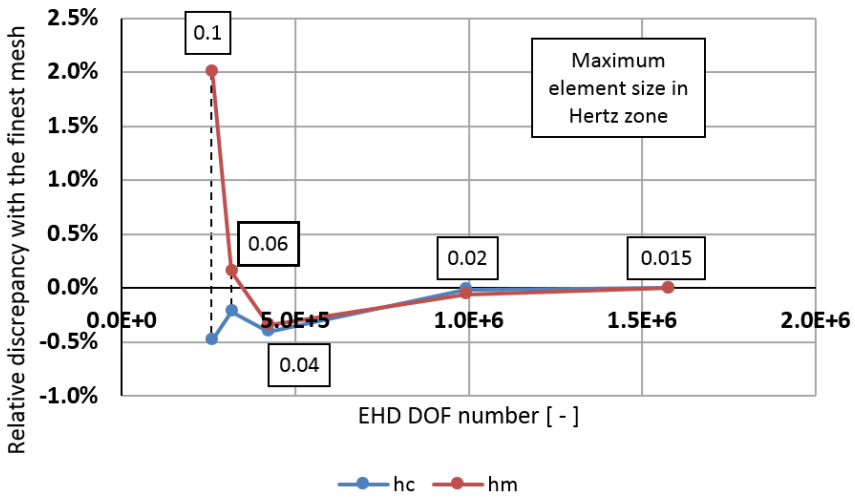


*Figure 2.1-16 – Relative discrepancy on film thickness according to the mesh refinement which is specified in terms of degrees of freedom (DOF) number and mesh size for case 3 presented in section 2.2.1*

Even though the model was inspired by a rich and reliable literature, and in spite of the physics based constitution laws, the solution cannot be considered as correct without an experimental validation.

### 2.1.3. Model validation

The model presented previously aims to predict accurately the EHD contact specifics in wide ranges of ellipticity ratios and velocity-load encountered under real EHD conditions. To evaluate its abilities, several experiments are considered. As this model was extensively validated for the $k = 1$ (circular contact) configuration (in the work of Habchi et al. (78) or Doki-Thonon et al (17)), it is decided to present numerical-experimental comparisons for $k \neq 1$ only. The first case considered is a slender configuration (as this one is in line with the torus on plane FREC), and a wide elliptical contact is presented after.

A validation based on film thickness comparison is used here: indeed, it is possible to obtain a map of data from the experiment and to compare it with the numerical results. Because of the thin film conditions, an optical spacer layer is used in the experiments of this section. However, no friction study is proposed in this chapter. Further assessments of the model are presented in section 3.3 with friction comparisons between the model predictions and the measurements.

#### *2.1.3.1. Slender elliptical contact*

The "Slender elliptical" sample presented in Table 2.1-1 is used together with a glass disc, leading to a $k = 0.526$ contact. The two specimen's properties are detailed in Table 2.1-2. The oil used for the experiment is lubricant 3 and is presented in Tables 2.1-4. The operating conditions are presented in Table 2.1-6.

| **Operating conditions** | |
|---|---|
| **Parameter [Unit]** | **Value** |
| $k\ [-]$ | 0.526 |
| $w\ [N]$ | 13 |
| $T_0\ [K]$ | 303 |
| $u_e\ [m/s]$ | $0.35 \leq u_e \leq 6.16\ m/s$ |
| $p_h\ [Pa]$ | $525 \times 10^6$ |

*Table 2.1-6 – Operating conditions of the slender elliptical EHD experiment*

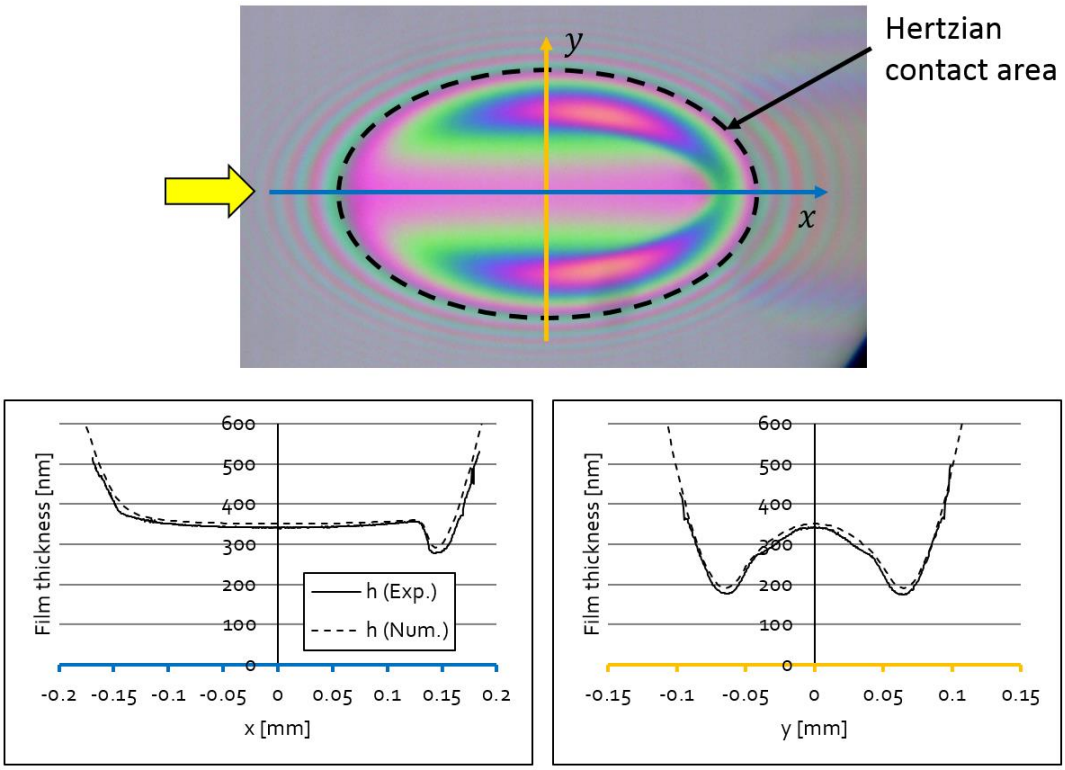


*Figure 2.1-17 - Film thickness along the main axes ($x$ is represented in blue and $y$ is in orange) of a slender elliptical contact. The entrainment velocity $u_e = 6.16\ m/s$ is represented by the yellow arrow*

For each entrainment condition, 10 interferograms are recorded in order to obtain an averaged result and its standard deviation. One of these interferograms is reported at the upper row of Figure 2.1-17. This picture is chosen as it is representative of the average values of the 10 pictures of the same entrainment velocity.

The maximum standard deviation is smaller than 5 $nm$ for both central ($h_c$) and minimum film thickness ($h_m$) under all operating conditions. For its part, the relative standard deviation on the experimental data is smaller than 5% (for $h_c$) and than 16% (for $h_m$)..

The numerical study is performed for the same conditions as the experiments for comparison. The graphs displayed in Figure 2.1-17 gather the experimental and numerical film thicknesses along the contact main axes ($x$ and $y$ according to the colour code) for one entrainment condition. Experimental and numerical results show good agreement all along these axes. To be more specific, there is a maximum difference of about 10 $nm$ only on the film thickness inside the Hertzian contact area. Another positive aspect is the ability to predict the position of the minima of this field: they are generally not easy to locate precisely. These encouraging results shows that the model is able to predict the gap between two bodies for slender elliptical EHD contacts.

A similar comparison was made for the whole entrainment velocity range. The film thickness characteristic values ($h_c$ and $h_m = (h_{m,l+} + h_{m,l-})/2$ as presented in Figure 2.1-10) are measured for each condition and the average values were reported in Figure 2.1-18. A good agreement is shown between experimental and numerical results. The average relative

difference is 8.9% for $h_c$ and 9.5% for $h_m$: besides, the maximum is 16.9% on $h_c$ (or 12 $nm$) and 15.1% on $h_m$ (or 10 $nm$). Differential colorimetric interferometry generally enables more precise results, but in this case the applied load corresponds to the minimum possible with this test-rig, leading to visible contact fluctuations. There is a slight reduction of the film thickness for the larger entrainment velocities. It is observable on the results from Jérotrib and on those from the model. It is also important to notice that the convex sample surface had a roughness $R_a \approx 10\ nm$ which contributed to the dispersion of the results. One can notice this on Figure 2.1-18: the isothermal trend is the linear extrapolation of the film thickness variation with $u_e$ in the $u_e < 2\ m/s$ area, which is not influenced by thermal effects according to the thermal film thickness reduction coefficient $\varphi_t$ proposed by Cheng (79). Moreover, the good agreement of Figure 2.1-17 (at the largest entrainment velocity and k< 1 configuration) also testifies of the model capabilities about thermal effects prediction. So even though there are some differences, the experiment confirms the accuracy of the model over a wide range of entrainment conditions.

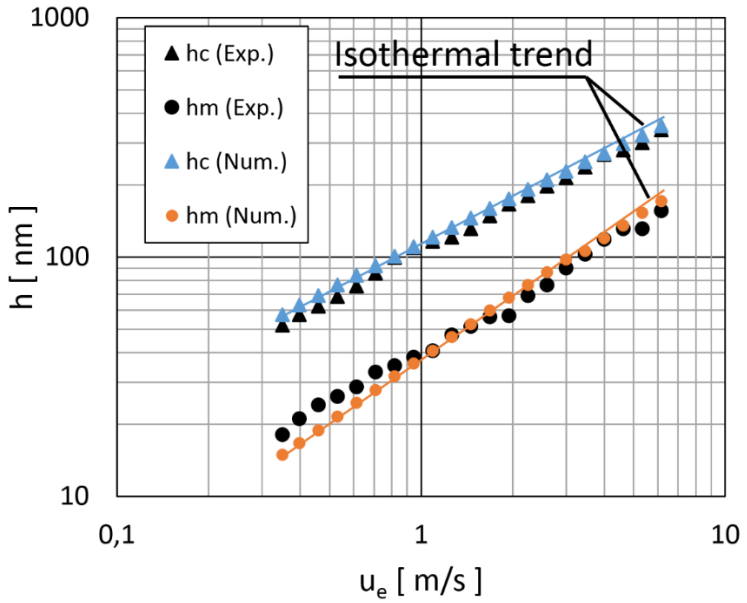


*Figure 2.1-18 – Film thickness for a slender elliptical contact (k=0.526) and for various entrainment conditions*

### 2.1.3.2. *Wide elliptical configuration*

When $k > 1$, the contact becomes a wide ellipse, with the entrainment velocity perpendicular to the large axis of the ellipse. The "wide elliptical" sample, with an ellipticity ratio $k = 3.46$ presented in Table 2.1-1 was used. The operating conditions are presented in Table 2.1-7.

| Operating conditions | |
|---|---|
| **Parameter [Unit]** | **Value** |
| $w\ [N]$ | 150 |
| $k\ [-]$ | 3.46 |
| $T_0\ [K]$ | 303 |
| $u_e\ [m/s]$ | $0.05 \leq u_e \leq 6.46\ m/s$ |
| $p_h\ [Pa]$ | $489 \times 10^6$ |

*Table 2.1-7 – Operating conditions of the wide elliptical EHD experiment*

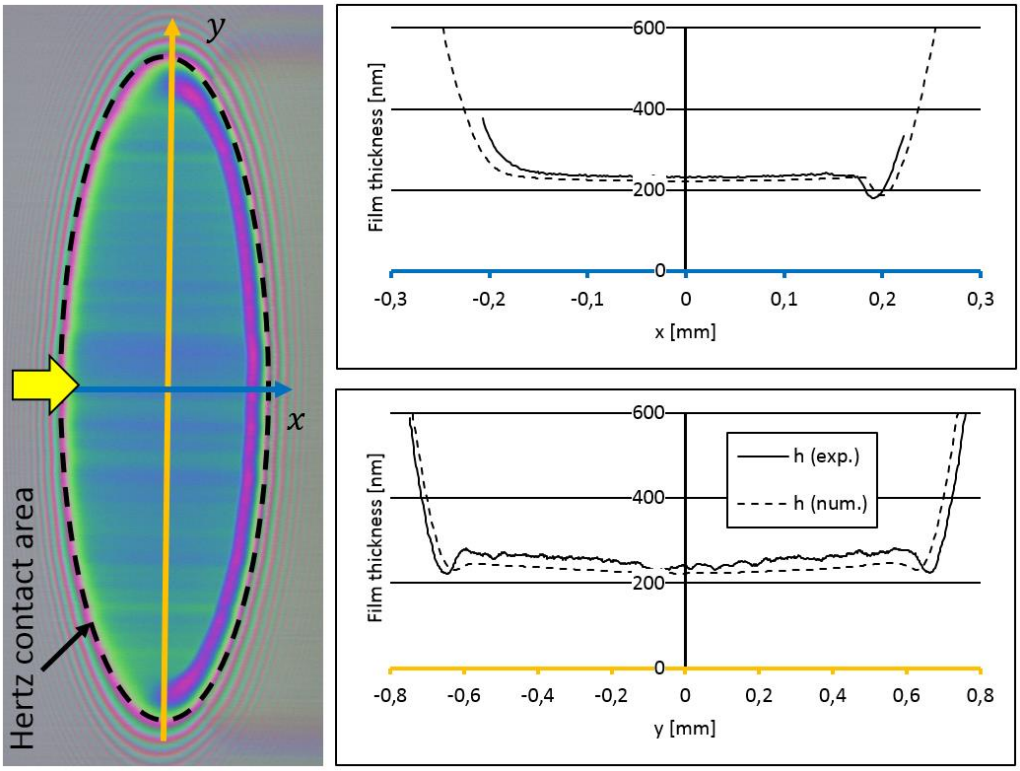


*Figure 2.1-19 - Film thickness along the main axes ($x$ is represented in blue and $y$ is in orange) on a wide elliptical contact (at $u_e = 1.79\ m/s$). The entrainment velocity is represented by the yellow arrow*

The same experimental procedure was applied here. For each entrainment condition, 10 interferograms of each EHD contact and its vicinity were taken. Through post-treatment, the averaged central and minimum film thickness is obtained, together with their standard deviations. In all the operating conditions, the maximum standard deviation was smaller than

4 $nm$ for the central film thickness and smaller than 8 $nm$ (ie. smaller than 4% of the corresponding case) for the minimum film thickness.

A focus is made on the $u_e = 1.79\ m/s$ condition. An interferogram was selected as it represents well the characteristic film thickness values observed on the 10 interferograms in this entrainment condition. This picture is displayed in Figure 2.1-19 together with its film thickness evaluation along the main axes of the contact. Through a numerical analysis with the model presented in section 2.1.2, the film gap is computed along the same axes. A comparison of the results shows a good agreement between the two approaches though some roughness is visible on the experimental curve. The simulation is able to predict the shape of the gap, but also the position of local phenomena such as the constriction at the exit and on the sides.

For all entrainment velocities, the numerical and experimental results show a good accordance, as presented in Figure 2.1-20. The average relative difference is 5.5%. The maximum relative deviation is 12.6% for the central film thickness (corresponding to 3 $nm$) and 17.9% for the minimum film thickness (corresponding to 3.3 $nm$). Similarly to the slender elliptical contact of section 0, a bigger difference is found at lower entrainment velocities and thus at low film thickness. It is accountable to the absolute uncertainty of the measurement method and also the roughness of the convex sample. At larger film thicknesses, this uncertainty has a negligible role. Figure 2.1-19 and Figure 2.1-20 show that the model is able to predict the wide elliptical EHD contact physics and principle characteristics.

Figure 2.1-20 gives a general overview of the film thickness results. The entrainment velocity is varied, both experimentally and numerically, and both central and minimum film thickness are gathered in the graph. The standard deviations are not reported as their representation is always smaller than the geometric symbol representing the mean values. Moreover, the isothermal trend is not reported either, as no significant deviation from it was observed at the largest velocities.

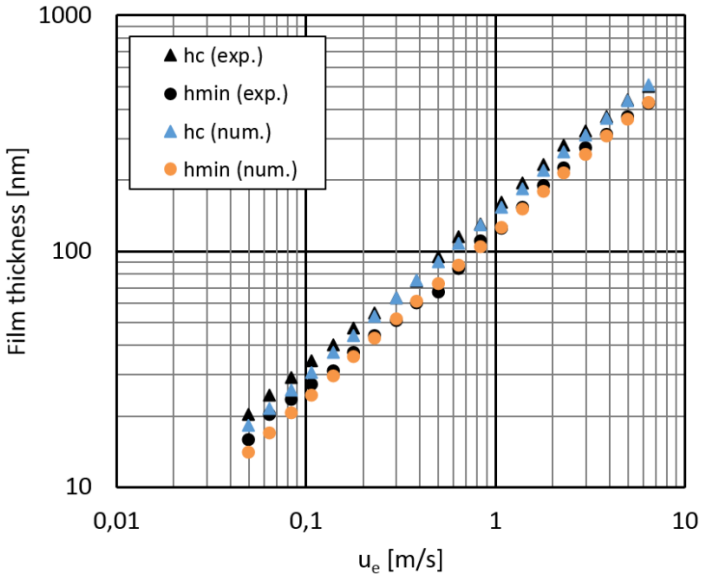


*Figure 2.1-20 - Comparison between experimental and numerical TEHD results for a wide elliptical contact ($k = 3.46$)*

Thanks to the two experiments presented (for wide and slender elliptical contacts), one can consider the model presented in section 2.1.2 as valid for film thickness predictions. The demonstration was made over a quite wide range of entrainment velocities and under a pressure typically encountered in flange roller-end contacts. It confirms and extends the validity domain of the model which was previously tested on circular contacts only. The model can now be used with confidence to explore the influence of operating conditions (including ellipticity) on the contact behaviour.

## 2.2. Ellipticity ratio influence

### 2.2.1. Study philosophy

With this validated model for film thickness predictions, the aim is now to extend the knowledge pertaining to the elliptical contacts, especially the slender ones which were less studied in the literature. The underlying idea is to develop the understanding of the slender contacts in order to use it as an approach to the torus on plane FREC.

The thermal effects were not computed in order to simplify the identification of the physical mechanisms driven by the ellipticity. As a consequence, the terms of the generalized Reynolds equation (Equation 2.1-18 and the generalized viscosities $\mu_e$ and $\mu'_e$) become:

$$\rho_e = \rho_f * h \qquad \rho'_e = \frac{\rho_f h^2}{2\mu} \qquad \rho''_e = \frac{\rho_f h^3}{6\mu} \qquad \frac{1}{\mu_e} = \frac{h}{\mu} \qquad \frac{1}{\mu'_e} = \frac{h^2}{2\mu}$$

$$\left(\frac{\rho}{\mu_e}\right) = \frac{\mu_e}{\mu'_e}\rho'_e - \rho''_e = \frac{h^3\rho_f}{4\mu} - \frac{\rho_f h^3}{6\mu} = \frac{\rho_f h^3}{12\mu} \qquad \text{Equation 2.2-1}$$

$$\rho_i^* = \rho'_e\mu_e(u_{t,i} - u_{b,i}) - \rho_e u_{b,i} = \frac{\rho h}{2}(u_{t,i} - u_{b,i}) - \rho_f h u_{b,i} = \rho_f h u_e$$

These simplifications transform the generalized Reynolds equation (Equation 2.1-20) into the classical Reynolds equation:

$$\frac{\partial}{\partial x}\left(\frac{\rho_f h^3}{\mu}\frac{\partial p}{\partial x}\right)+\frac{\partial}{\partial y}\left(\frac{\rho_f h^3}{\mu}\frac{\partial p}{\partial y}\right)-12u_e\frac{\partial(\rho_f h)}{\partial x}=0 \qquad \textit{Equation 2.2-2}$$

The lubricant 2 was used in this section. Its properties are presented in Tables 2.1-3. One may notice that the Murnaghan EOS parameters are the same but that the modified WLF parameters are slightly different. The model evaluations presented in section 2.1.3 are still valid with this different batch: the same characterisation process was used for the two lubricants.

To explore the different entrainment conditions existing in FREC, five velocity-load reference cases (fully described in Table 2.2-1) were studied, with $u_e = 0.5, 2, 10\ m/s$, and $w = 120, 800, 2500\ N$. Table 2.2-1 also includes the corresponding Hertzian pressures and contact areas.

The temperature of the contact is set to $T_0 = 313\ K$. For each entrainment velocity-load case, different configurations were computed keeping the contact surface $S$ constant whereas the ellipticity was varied from $k = 0.2$ to $k = 5$. The corresponding values of $R_x$ and $R_y$ are reported in Table 2.2-2. Because the ellipse surface, defined by $S = \pi ab$, was kept constant for a given load $w$, the Hertzian pressure, $p_h$, also remains constant when $k$ varies.

$$p_h = \frac{3w}{2\pi ab} \Rightarrow p_h = \frac{3w}{2S} = \text{constant for a given } w \qquad \textit{Equation 2.2-3}$$

| | | $u_e$ [ $m/s$ ] | | |
|---|---|---|---|---|
| | | *0.5* | *2* | *10* |
| $w$ [$N$] ($p_h$ [$MPa$]; $S$ [$mm^2$]) | ***120*** *(*364; 0.49*)* | - | *case 1* | - |
| | ***800*** *(*686; 1.75*)* | *case 2* | *case 3* | *case 4* |
| | *2500* *(*1002; 3.74*)* | - | *case 5* | - |

*Table 2.2-1 - Load, pressure and velocity of the five reference cases computed. In each case, k varies by a change of both $R_x$ and $R_y$ ($E = 210\ GPa$, $\nu = 0.3$, $T_0 = 313\ K$, $\mu_0 = 0.00795\ Pa.s$, $\rho_0 = 863\ kg.m^{-3}$ and $\alpha^* = 20.2\ GPa^{-1}$ constant).*

| $k$ [$-$] | $R_x$ [$mm$] | $R_y$ [$mm$] |
|---|---|---|
| 5.03 | 28.92 | 345.00 |
| 3.96 | 33.00 | 270.00 |
| 2.92 | 39.32 | 200.00 |
| 1.98 | 49.84 | 140.00 |
| 1.46 | 60.90 | 108.00 |
| 1.00 | 80.00 | 80.00 |
| 0.68 | 108.00 | 60.90 |
| 0.50 | 140.00 | 49.84 |
| 0.34 | 200.00 | 39.32 |
| 0.25 | 270.00 | 33.00 |
| 0.20 | 345.00 | 28.92 |

*Table 2.2-2 - $k, R_x$ and $R_y$ values for the different ellipticity configurations*

As the load $w$ and the Hertzian pressure $p_h$ remain constant, each case may correspond to a single industrial application in which the bodies' geometry still has to be defined. The geometry is varied so that its influence is isolated from the influence of other parameters. The configurations in which $k < 1$ correspond the most to the torus on plane FREC (see Colin et al. (9) for instance), but the $k \geq 1$ configurations are studied together to enable a more global view on elliptical contacts.

Figure 2.2-1 shows a representation of the five reference cases described in Table 2.2-1. They are plotted on a $M - L$ diagram and on a $k - L$ diagram in order to give an overview of the various computed cases, $M$ and $L$ being the dimensionless parameters defined by Moes (80). The same data are plotted on the two graphs: they are the projection of data which are initially in a 3D space defined by $M$, $L$ and $k$. Each red line represents one of the five reference cases. The tabulated values of film thickness together with the dimensionless parameters are available in Annexe D. The Chittenden et al. (10,44) and the Hamrock and Dowson (22–24) computation cases were also reported on the graphs. These results enabled the development of useful prediction formulae. Chittenden et al. formulae were based on the results of Hamrock and Dowson but they added other computations dedicated to slender elliptical contacts. Like most EHD numerical studies, they were based on dimensionless parameter variation. In the present study, the choices explained previously were made, in order to make quantitative comparisons between the ellipticity configurations and to draw new conclusions. Thus, the current work is more in line with an engineering approach, when an optimum contact geometry for given (i.e. dimensioned) entrainment speed and normal load is being sought.

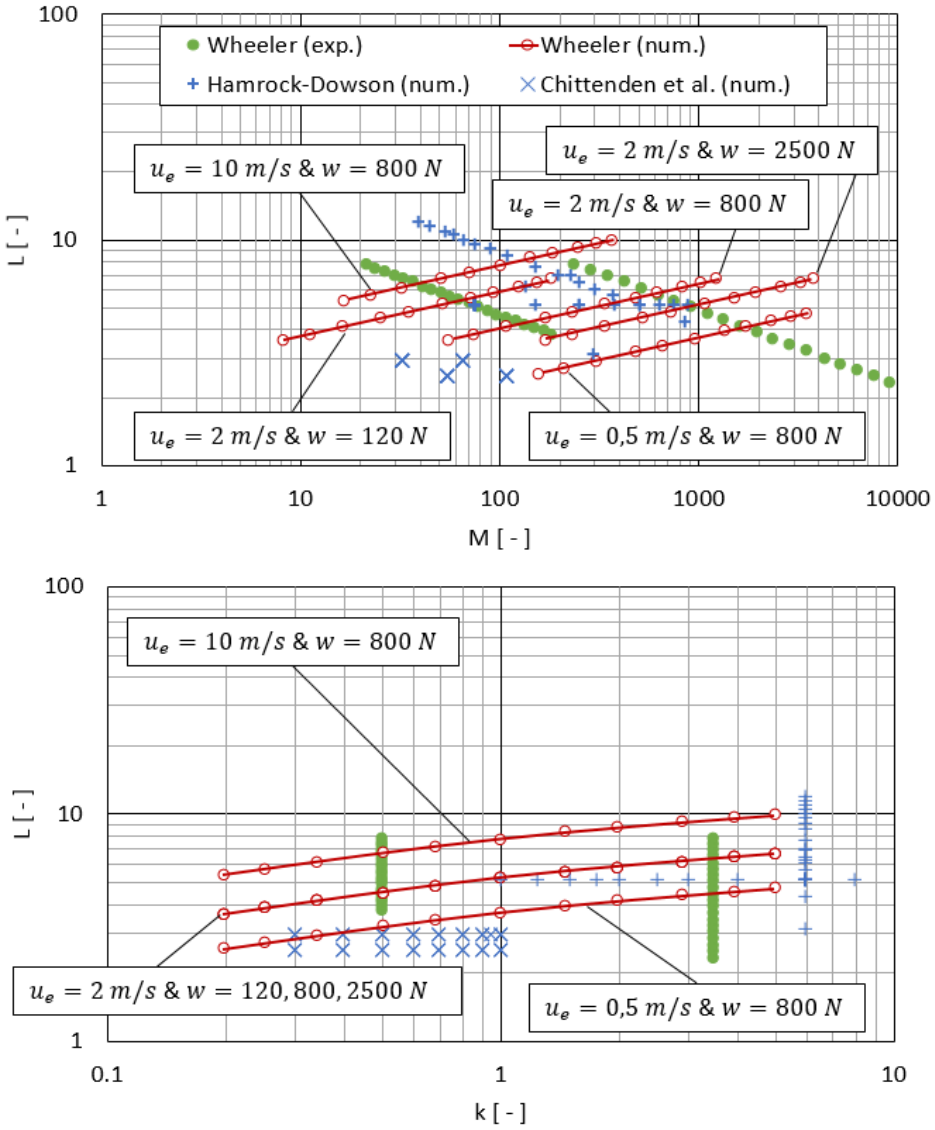


*Figure 2.2-1 – Sum-up diagram: five velocity-load reference cases (red circles) together with the experimental validations cases presented in section 2.1.3 (green discs). The Chittenden et al.* (10,44) *and Hamrock-Dowson* (22–24) *computation configurations are also represented.*

### 2.2.2. Film thickness results

Figure 2.2-2 shows the film thickness results for $u_e = 2\ m/s$ and $w = 800\ N$. While entrainment velocity and load remain constant, the ellipticity ratio varies between $k = 0.2$ and $k = 5$, from the slender to the wide elliptical contact and including the circular configuration. For comparison purposes, the central and minimum film thicknesses computed in this study are plotted together with the prediction from Chittenden *et al.* (10,44) given by the semi-analytical formulae below:

$$h_{c\ (Chittenden)} = 4.31\ U^{0.68}\ G^{0.49}\ W^{-0.073}\ R_x \left(1 - e^{-1.23(R_y/R_x)^{2/3}}\right)$$
$$h_{m\ (Chittenden)} = 3.68\ U^{0.68}\ G^{0.49}\ W^{-0.073}\ R_x \left(1 - e^{-0.67(R_y/R_x)^{2/3}}\right)$$

*Equation 2.2-4*

with $G = \alpha^* E'$ the dimensionless material parameter, $W$ the dimensionless load parameter, and $U$ the dimensionless speed parameter, as defined by Hamrock and Dowson (22). The piezo-viscous coefficient $\alpha^*$, known as the reciprocal asymptotic isoviscous pressure and defined by Blok (11) was used here. The well-known predictive formulae developed by Hamrock and Dowson (22–24) are not used here as they are addressed to $k \geq 1$ contacts only (circular and wide elliptical). At the temperature $T_0 = 313K$ considered in this study, $\alpha^* = 20.2\ GPa^{-1}$.

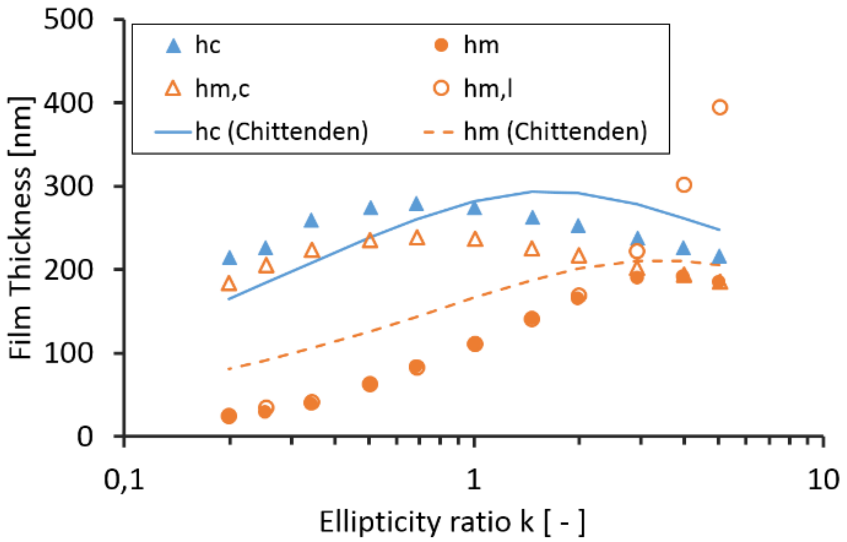


*Figure 2.2-2 - Film thickness for varying ellipticity ratio for $w = 800\ N$ and $u_e = 2\ m/s$*

Figure 2.2-1 includes the $M - L$ configurations from which Chittenden *et al*. derived their formulae. These configurations are mainly corresponding to the cases of both low velocity and low load, but also the circular contact at the $w = 800\ N$ load.

Figure 2.2-2 shows $h_c$, the central film thickness, variations with a maximum occurring for $k \approx 2/3$. For $k < 2/3$, when the ellipse becomes narrower and for $k > 2/3$, when the ellipse becomes wider, $h_c$ clearly decreases. The overall minimum film thickness, $h_m$, plotted in Figure 2.2-2 actually represents the minimum of two different physical quantities: the minimum film thickness on the contact central line, $h_{m,c}$, and the minimum film thickness on the contact sides $h_{m,l}$ (lateral position), according to the observations made by Hamrock and Dowson (23). To be more precise, $h_m = \min(h_{m,l}\,; h_{m,c})$. For the wide elliptical contact, $h_{m,c}$ becomes the smallest and $h_{m,l}$ is a local minimum. One may notice that $h_{m,c}$ is smaller than $h_c$ but follows its trend, whatever the ellipticity ratio. Yet, $h_{m,l}$ has a totally different variation from $h_c$ and even if it drastically decreases for low $k$, it becomes larger than $h_c$ for $k \geq 3.2$. The two minima $h_{m,l}$ and $h_{m,c}$ are equal for $k \approx 2.4$ and in the following, $h_{m,l}$ and $h_{m,c}$ will not be represented anymore for the sake of clarity. The tabulated values of film thickness presented in this graph are reported in Annexe D.

In this EHD contact range, the central film thickness computed with Chittenden formula matches the computations of this study with a deviation of less than 7% (see Figure 2.2-3, case $w = 120\ N$). However the minimum film thickness difference can rise up to 30% at $120N$ and much more at higher loads: this highlights the validity of the analytical models published in 1985 but also asks questions on the relevance of these formulae today. They also provide acceptable trends outside of the domain used to establish them, however they do not allow for quantitative considerations (see Figure 2.2-3, for $w = 800N$ *or* $2500\ N$). Given their precision limitations and their rather restricted range of application, the need for advanced film thickness prediction in EHD elliptical contacts is underlined here.

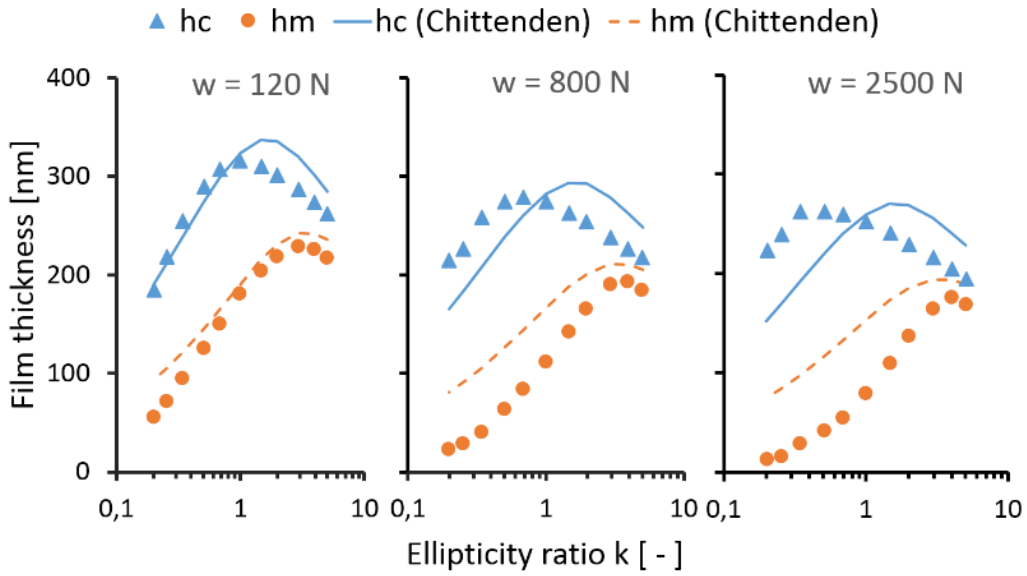


*Figure 2.2-3 - Film thickness for varying ellipticity ratios for three different normal loads and a constant entrainment velocity $u_e = 2\ m/s$*

Figure 2.2-3 shows the film thickness variations with ellipticity for the different load cases, while $u_e = 2\ m/s$ remained constant. The same trends are observed for the three configurations. Namely, $h_c$ maximum does not occur for the wider elliptical contact but for $k \approx 1$ at low load, $k \approx 2/3$ for intermediate load and $k \approx 0.34$ for the largest load. Moreover, the largest $h_m$ is found for $3 \leq k \leq 4$ whatever the load value. For slender elliptical contacts, when $k$ decreases and especially at high load and low velocity, $h_m$ decreases drastically and approaches zero film thickness. $h_c$ globally decreases as well, but it can be noticed that, at the lowest $k$ values, the load influence on $h_c$ is opposite to the intuitive trend. For instance at $k = 0.20$ and $k = 0.25$, $h_c$ is higher for $w = 2500\ N$ than for $w = 800\ N$ or $w = 120\ N$. As a consequence, in those conditions the $h_c/h_m$ ratio can take values as large as 10 or even 20, thus very far from those found in circular EHD contacts that rarely exceed 3. Also, for the wide elliptical contact, increasing $k$ does not lead to an asymptotic value for $h_c$ or $h_m$. However $h_c$ and $h_m$ become closer and closer and thus follow the same tendency at high $k$. This unusual result is simply due to the choice to maintain $w$, $S$ and $u_e$ constant, instead of dimensionless load and velocity.

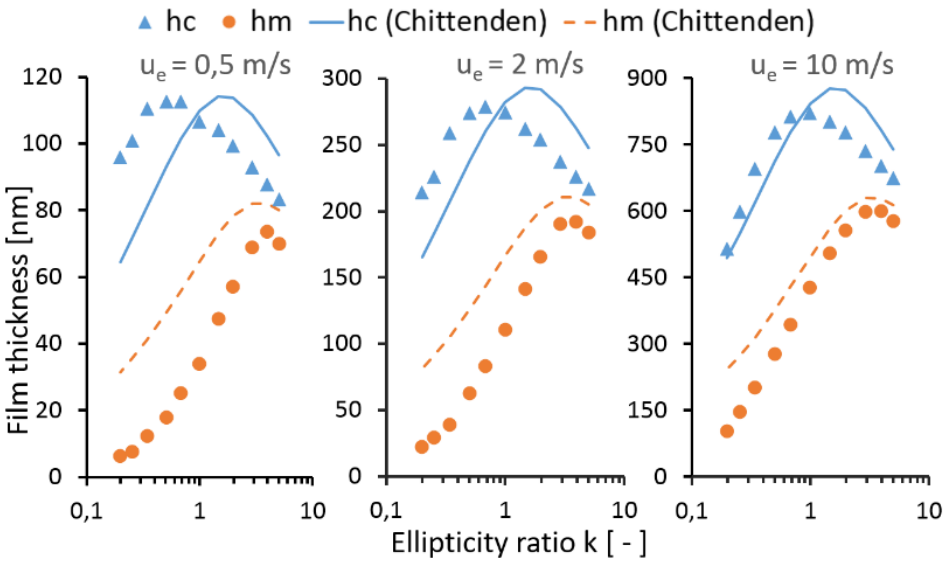


*Figure 2.2-4 - Film thickness for varying ellipticity ratios for three different entrainment velocity and a constant normal load $w = 800\ N$*

Likewise, three different entrainment velocities were simulated for $w = 800\ N$. Because $u_e$ has a greater influence than $w$ on film thickness, the scaling is not the same between the graphs reported in Figure 2.2-4. In the three entrainment velocity cases, $h_c$ and $h_m$ exhibit similar trends. $h_c$ maximum occurs for $k \approx 1$ at high entrainment velocity, $k \approx 2/3$ at intermediate velocity and $k \approx 0.5$ for the lowest velocity. Similarly to the results presented in Figure 2.2-3, $h_m$ is the largest for $3 \leq k \leq 4$, whatever the entrainment velocity. Again, extremely low $h_m$ values are obtained for $u_e = 2$ and $0.5\ m/s$, leading to unconventional $h_c/h_m$ ratio values close to 10 and even 20, respectively. Nevertheless, compared to more classical (e.g. circular) EHD configurations, no counterintuitive trend of the entrainment velocity influence on film thickness was detected.

Figure 2.2-3 and Figure 2.2-4 provide one last remarkable point concerning this time the central film thickness in circular contacts ($k = 1$). A quantitative good agreement is found between the values predicted by the numerical model, and those obtained with the Chittenden *et al.* (10,44) formula, even though here the $M - L$ area exceeds the domain on which Equation 2.2-4 was established. At this stage, it is noteworthy that van Leeuwen (81) obtained a similar accordance, but by comparing his experimental $h_c$ results with the analytical predictions from the same equation. Moreover, he also found that the validity of Equation 2.2-4 transcended the area where it was originally designed for.

So as film thickness varies according to ellipticity, load and velocity, hydrodynamic effects must be analyzed together with the fluid flow rates in order to understand more about the ellipticity influence. For this purpose, the inlet and lateral characteristics will be described together with their influence on flow rates and pressure gradients in Section 2.3.

## 2.3. Discussion

The film thickness variations can be influenced by several parameters. When considering Reynolds classical equation, one may distinguish the Poiseuille terms (the two first terms of Equation 2.2-2) and the wedge effect due to the lubricant entrainment in a converging gap (coming from the second term of Equation 2.2-2).

The wedge term, $\partial(u_e \rho h)/\partial x$, generates pressure and is directly influenced by $R_x$, the radius of curvature along the entrainment direction. Indeed, when $R_x$ decreases, $\partial h/\partial x$ increases and the pressure gradient increases. This phenomenon is at the basis of the hydrodynamic effect and contributes to the surfaces' separation. When the ellipse becomes wider, $R_y$ is increased and $R_x$ is reduced. Consequently, the film thickness should monotonously increase as the wedge term is increased. However here, for $k > 2/3$ (see case $u_e = 2\ m/s$ in Figure 2.2-4) the central film thickness decreases when $k$ increases (or when $R_x$ is decreased). Thus the hydrodynamic effect cannot explain by itself the film thickness variations reported in this work.

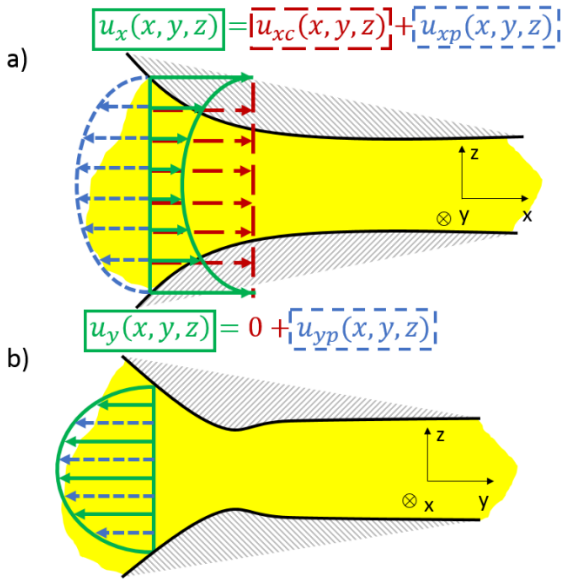


*Figure 2.3-1 - a) Velocity fields at the contact inlet, in the $y = 0$ plane; b) Side flow represented by the velocity field at the contact side, in the $x = 0$ plane.*

In the EHD contact, one also needs to consider the Poiseuille flow rates due to the pressure terms in the Reynolds equation. To discuss into detail the film forming mechanisms occurring in elliptical contacts, the relative values of the different (incoming and outgoing) flow rates must be computed over a representative frontier. Figure 2.3-1 presents schematically the lubricant's flows at the contact inlet (Figure 2.3-1 a, Poiseuille and Couette contributions) and at the contact side (Figure 2.3-1 b, Poiseuille flow). Whereas the Hertzian area of any dry contact is well defined by an ellipse on which the Hertzian pressure distribution applies, the pressurized zone of an elastohydrodynamically lubricated contact requires another definition.

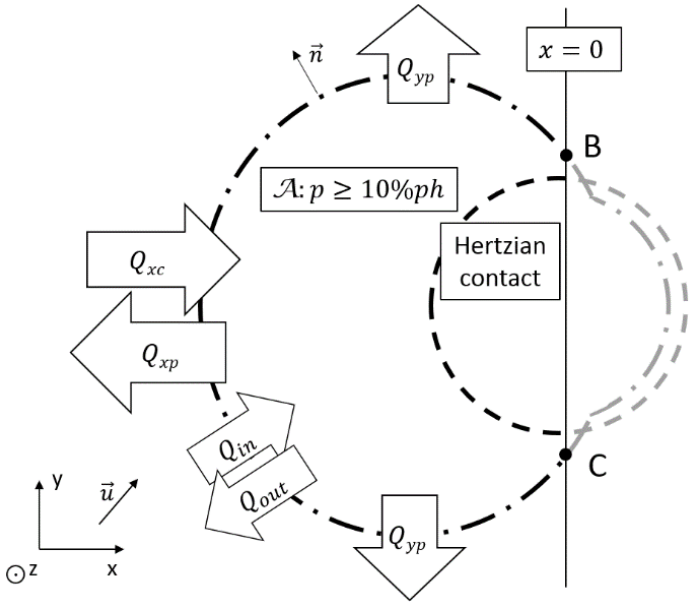


*Figure 2.3-2 - Hertzian (− −) & effective (called $\mathcal{A}$, · − ·) areas together with fluid flows crossing the $\mathcal{F}$ frontier; $\mathcal{F}$ is the left part (denoted by · − ·) of $\mathcal{A}$ frontier between the points B and C; $\mathcal{A}$ is defined as the surface where $p \geq 10\%p_h$*

A representative area $\mathcal{A}$ of the lubricated contact is arbitrarily defined here as the surface where $p \geq 10\%\, p_h$ (see a schematic representation in Figure 2.3-2). This area $\mathcal{A}$ will be considered as the effective EHD contact surface on the two solids. The flow rates crossing the frontier between the two representative areas will be investigated in order to explain film thickness variations. The frontier $\mathcal{F}$ used for the fluid flows analysis corresponds to the left side of $\mathcal{A}$ (as illustrated schematically in Figure 2.3-2), represented by the dotted-dashed line between the points B and C in the $(\vec{x}, \vec{y}, 0)$ plane. For mass conservation verification purposes, the frontier $\mathcal{F}$ was closed by a straight line between the points $B$ and $C$: it was found that conservation was insured within less than 1%. Figure 2.3-2 also represents the fluid flows which will be considered in the following. The Couette flow rate along $\vec{x}$ in pure rolling is:

$$Q_{xc} = \iiint_{\mathcal{F}} \rho(x,y,z) * u_e \; dx\, dy\, dz \qquad \textit{Equation 2.3-1}$$

Moreover, Poiseuille flow rate along $\vec{x}$ is defined by:

$$Q_{xp} = \iiint_{\mathcal{F}} \rho(x,y,z) * [(\overrightarrow{u_f} \cdot \vec{x} - u_e) * \vec{x}] \cdot \vec{n} \; dx\, dy\, dz \qquad \textit{Equation 2.3-2}$$

with $\vec{u}$ is the fluid velocity at point $(x, y, z)$ and $\vec{n}$ the outgoing vector normal to $\mathcal{F}$. $Q_{xp}$ is the flow rate that limits the oil feeding of the contact due to the pressure gradient $\partial p/\partial x$ at the inlet. It is also called backflow rate.

There is another Poiseuille flow rate, along $\vec{y}$:

$$Q_{yp} = \iiint_{\mathcal{F}} \rho(x,y,z) * [(\overrightarrow{u_f} \cdot \vec{y}) * \vec{y}] \cdot \vec{n}\, dx\, dy\, dz \qquad \textit{Equation 2.3-3}$$

This flow rate is due to the pressure gradients $dp/dy$ occurring on the contact sides and it evacuates the lubricant laterally. It is often known as side leakage.

In Figure 2.3-2, $Q_{in}$ and $Q_{out}$ are also reported: they represent the total flow rates going into the contact through $\mathcal{F}$ and going out of the contact through $\mathcal{F}$, respectively. They are defined by:

$$Q_{in} = \iiint_{\mathcal{F}} \rho(x,y,z) * [\overrightarrow{u_f} \cdot \overrightarrow{-n}] * [(\vec{u} \cdot \vec{n}) < 0]\, dx\, dy\, dz \qquad \textit{Equation 2.3-4}$$

$$Q_{out} = \iiint_{\mathcal{F}} \rho(x,y,z) * [\overrightarrow{u_f} \cdot \vec{n}] * [(\vec{u} \cdot \vec{n}) > 0]\, dx\, dy\, dz \qquad \textit{Equation 2.3-5}$$

with $[(\vec{u} \cdot \vec{n}) < 0] = 1$ if the condition is true and 0 otherwise, and $[(\vec{u} \cdot \vec{n}) > 0] = 1$ if the condition is true and 0 otherwise.

$Q_{in} + Q_{out}$ will be used as a reference value to quantify the lubricant amounts that flow through $\mathcal{F}$, driven by longitudinal and transverse gradients. Due to the various contact configurations simulated here and in particular the resulting very different contact widths $b$, the amount of lubricant to consider is different from one contact to another. However, the mass conservation leads the expressions given by Equation 2.3-1 to Equation 2.3-5 to verify $Q_{in} + Q_{out} = Q_{xc} + Q_{xp} + Q_{yp}$ over the frontier $\mathcal{F}$.

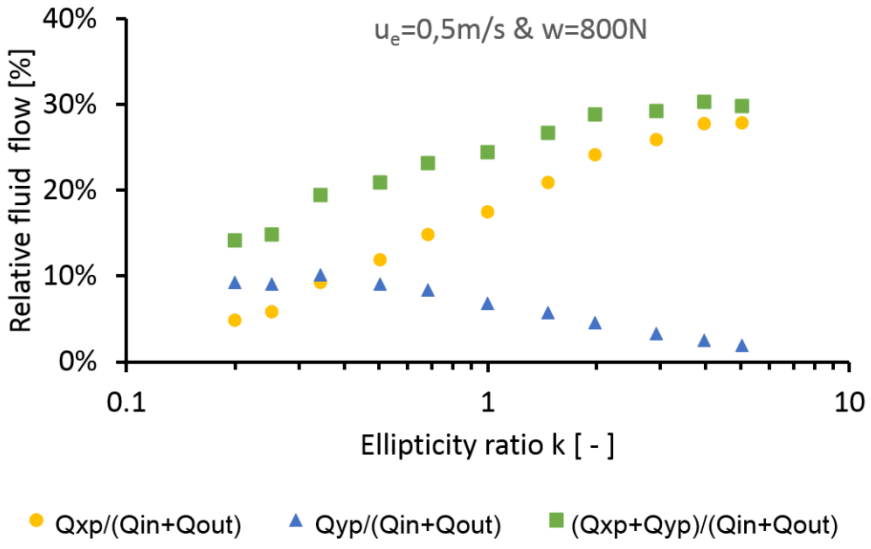


*Figure 2.3-3 -Relative fluid flows variations due to ellipticity ratio for $u_e = 2\ m/s$ & $w = 800\ N$*

In a similar manner to Damiens (62), the fluid flows are investigated for various ellipticity ratios. However, in the present case, it is their influence on film thickness which is analyzed. Figure 2.3-3 shows the relative fluid flow variations when the ellipticity varies, for $w = 800\ N$ and $u_e = 2\ m/s$. The reference flow for each ellipticity is $Q_{in} + Q_{out}$ and the other flows are expressed relatively to this sum. The relative Poiseuille flow along $\vec{x}$ is small for the slender configuration and increases for wider elliptical contacts. On the contrary, the relative Poiseuille flow along $\vec{y}$ is high for the slender contacts and becomes lower for wider ones. This means that the relative backflow has a great influence on the wide elliptical contacts whereas the relative side flow is dominant in the slender configuration. Nonetheless, the graph in Figure 2.3-3 underlines the low variation of total relative leakage: its maximum is $\approx 60\%$ larger than its minimum. Indeed, when $k$ increases, the backflow increase is almost compensated by the side leakage reduction. However the two Poiseuille flows do not have the same effect on film thickness. The side flow contributes to decrease the film thickness on the sides: according to Evans and Snidle (47), the minima act as seals toward the contact area forcing the minimum to occur on the sides. When the side flow is high enough, $h_m$ can be dramatically reduced. For its part, the backflow competes against the Couette flow and reduces the lubricant flow rate entering the contact. Moreover, for slender elliptical contacts, the high side leakage and the low hydrodynamic effects (a large $R_x$ reduces the wedge effect) are cumulated and, consequently, the resulting film thickness will be thinner, especially on the contact lateral edges. This certainly explains, to a large extent, the very thin or even extremely thin $h_m$ values reported for low k in Figure 2.2-3 and Figure 2.2-4. On the contrary for the wide elliptical contact, the backflow influence on film thickness is balanced by the strong hydrodynamic effect (a small $R_x$ increases the wedge effect) and therefore the fluid film in this kind of contact remains rather thick. Simultaneously the typical minimum film thickness feature appearing onto the two contact lobes is gradually lost in favor to a single minimum occurring at the exit along the contact centerline. Figure 2.3-3 also shows that the backflow curve crosses the side leakage curve for $k \approx 0.4$ whereas in Figure 2.2-2, the maximum central film thickness occurs for $k \approx 2/3$. Thus, in the competition between Couette and Poiseuille flows, the former dominates the latter as it takes advantage of the low side leakage and low backflow. Consequently, as the hydrodynamic effect is less limited by the Poiseuille flows, the central film thickness optimum is reached for this ellipticity ratio range. When $k$ is becoming larger, the backflow contributes to decrease the surface separation, whereas when $k$ is smaller, the side flow reduces it as well, but in a different way. In addition, one may notice that the maximum of $h_c$ does not occur for the same ellipticity range as the maximum of $h_m$. The former happens where the Couette flow dominates the Poiseuille flow, whereas the latter happens where the position of the film thickness minimum changes.

When the load or the velocity are varied, the conclusions remain similar (see Figure 2.3-4 and Figure 2.3-5). The Poiseuille flow sum varies slightly with ellipticity comparing to the turnaround observed between backflow and side leakage. Again, the backflow is weak for slender contacts and strong for wide ones whereas an opposite variation is observed for the side leakage.

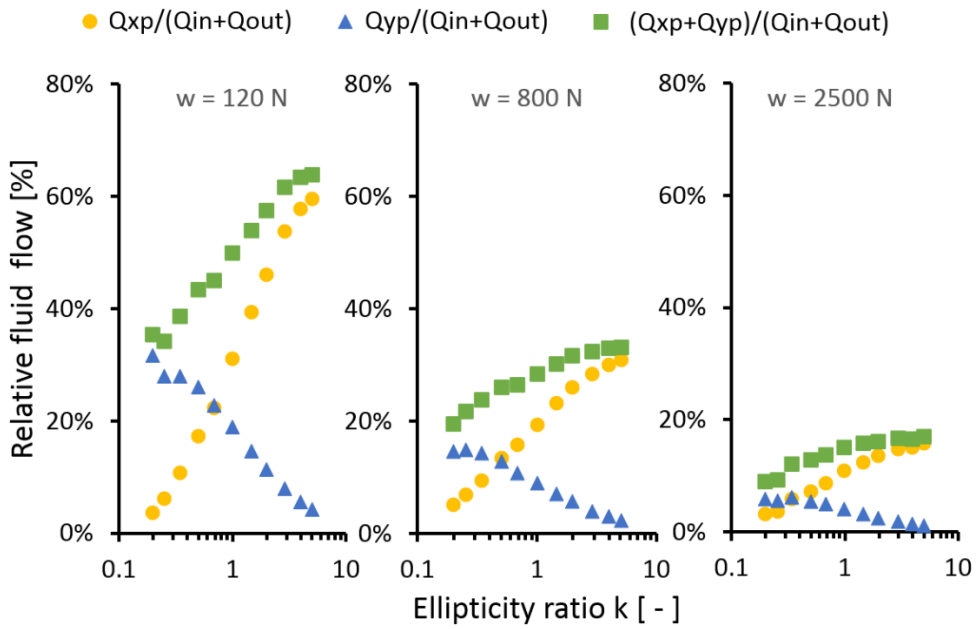


*Figure 2.3-4 - Relative fluid flow variations due to ellipticity ratio for $u_e = 2\ m/s$ & various loads*

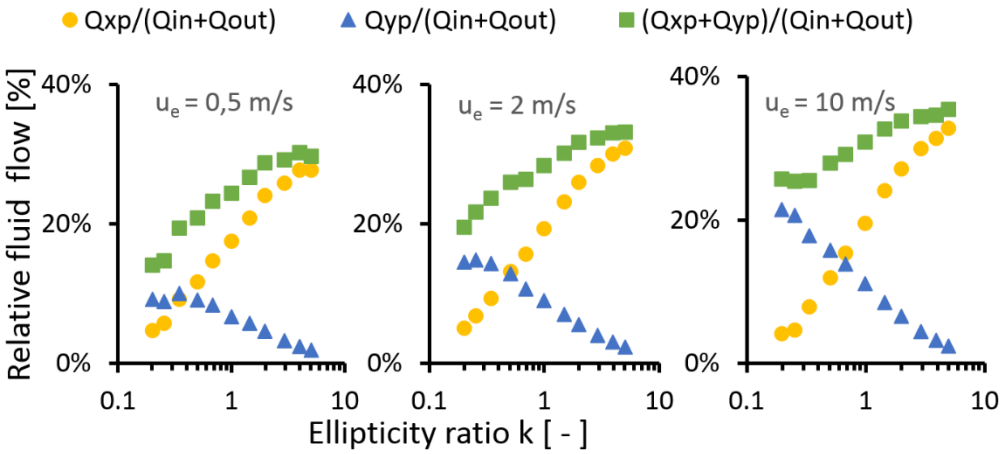


*Figure 2.3-5 - Relative fluid flow variations due to ellipticity ratio for $w = 800\ N$ and various entrainment velocities*

Finally, in order to understand fluid flow rates variations, one must consider the pressure gradients $\partial p/\partial x$ and $\partial p/\partial y$. Indeed, the Poiseuille flows are pressure gradient driven. These pressure gradients are ruled through the Reynolds equation (Equation 2.2-2) by the film thickness gradient which is influenced by the ellipticity ratio $k$.

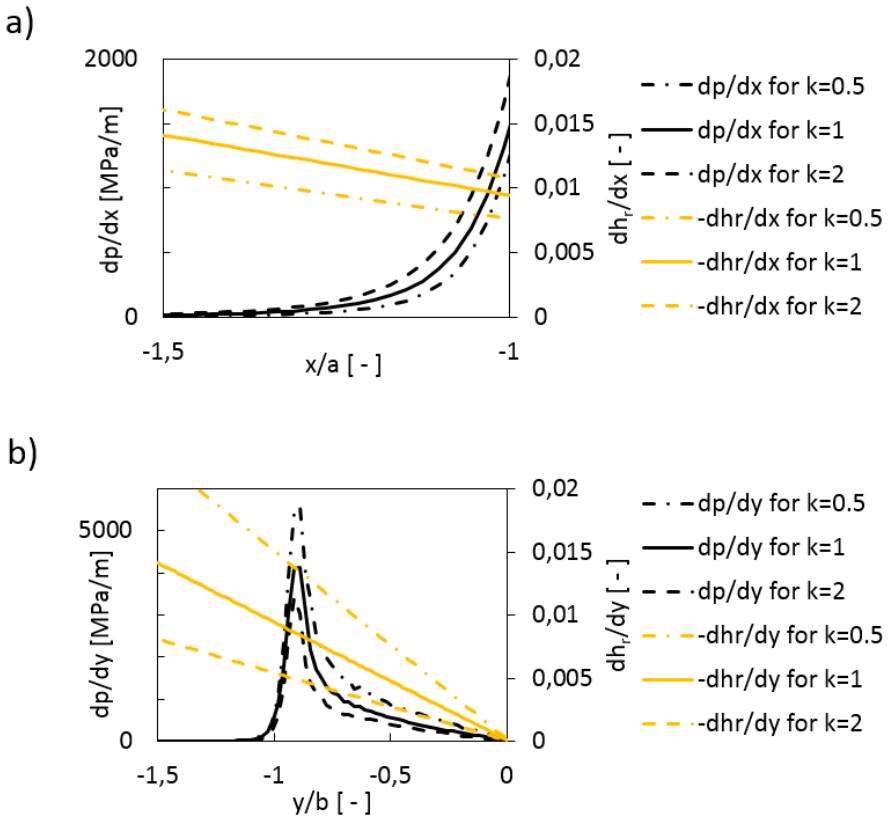


*Figure 2.3-6 - Convergent shape influence on pressure gradients, a) along the $\vec{x}$ axis and b) along the $\vec{y}$ axis for $w = 800\ N$ & $u_e = 2\ m/s$*

Figure 2.3-6 represents the film thickness gradients $\partial h_r/\partial x$ and $\partial h_r/\partial y$ together with the pressure gradients for the case $w = 800\ N, u_e = 2\ m/s,$ and the configurations $k = 0.5, 1, 2$. Along the $\vec{x}$ axis (Figure 2.3-1 a) and upstream from the contact, the pressure gradients are different depending on the ellipticity ratio:

$$\left.\frac{\partial p}{\partial x}\right|_{k=0.5} < \left.\frac{\partial p}{\partial x}\right|_{k=1} < \left.\frac{\partial p}{\partial x}\right|_{k=2} \qquad \textit{Inequation 2.3-6}$$

Similarly for the film thickness gradients:

$$-\left.\frac{\partial h_r}{\partial x}\right|_{k=0.5} < -\left.\frac{\partial h_r}{\partial x}\right|_{k=1} < -\left.\frac{\partial h_r}{\partial x}\right|_{k=2} \qquad \textit{Inequation 2.3-7}$$

Inequation 2.3-6 and Inequation 2.3-7 underline the well-known result that the thickness gradient drives the pressure gradient. Thereafter, the pressure gradient along the $\vec{x}$ direction leads the backflow to vary in the way described hereinbefore.

As for the mechanisms occurring along the $\vec{y}$ axis, the same observations are made from Figure 2.3-1 b:

$$\left.\frac{\partial p}{\partial y}\right|_{k=0.5} > \left.\frac{\partial p}{\partial y}\right|_{k=1} > \left.\frac{\partial p}{\partial y}\right|_{k=2} \qquad \textit{Inequation 2.3-8}$$

However, the configuration $k = 0.5$ gives now the largest pressure gradient. As these pressure gradients are directly responsible for the side flow, Inequation 2.3-8 correlates well with the ellipticity influence on side flow presented previously. Moreover the film thickness gradients, responsible for the pressure gradients, are ranked in the same order (see Inequation 2.3-9 below).

$$-\left.\frac{\partial h_r}{\partial y}\right|_{k=0.5} > -\left.\frac{\partial h_r}{\partial y}\right|_{k=1} > -\left.\frac{\partial h_r}{\partial y}\right|_{k=2} \qquad \textit{Inequation 2.3-9}$$

Through the pressure and film thickness gradients analysis, the link is made between ellipticity and film thickness. Indeed, in our approach the ellipticity ratio determines the convergent shape through the radii of curvature of the solids. These latter characterize the thickness gradients which drive the pressure gradients. Finally, the pressure gradients determine the fluid flows, which in turn determine the film thickness.

These results are key to the understanding of the torus on plane FREC. Even if the spinning kinematic was not studied here, the ellipticity role was underlined. The extremely narrow contacts will lead to a drastic reduction of the minimum film thickness. The central film thickness will remain rather large. Moreover, the use of the Chittenden prediction laws may be hazardous for $k < 1$ outside of the range they were designed for. It is particularly on the minimum film thickness that the results are the most hazardous.

It was demonstrated that the ellipticity drives the film thickness characteristics through the gap geometry.

## 2.4. Conclusion

In this chapter, the elliptical EHD contact was explored via experiments and numerical simulations. The Jérotrib test-rig was used to run tests under realistic flange roller-end contact (FREC) conditions. With the new calibration method, it was possible to investigate the film thickness variations with the entrainment velocity and the ellipticity. Two ellipticity ratios $k$ were tested: a slender elliptical contact (which corresponds the most to the torus on plane FREC) and a wide elliptical contact.

The numerical model presented consistent predictions of the film thickness under all experimental operating conditions, and it constitutes a new contribution to the literature. These operating conditions were in line with the numerical study introduced in this chapter. With an attempt to isolate the ellipticity influence on the EHD contact from the other parameters, it has been possible to explore the influence of $k$ on the film forming capacity. The ellipticity ratio affects the gap shape, which in turn drives the pressure gradients. The different

Poiseuille flows variations are influenced by these pressure gradient and they alter the film gap. The large lateral Poiseuille flows were quantified and related to the very thin lateral minimum film thickness.

However, the convergent of the torus on plane contact is more complex than the one of an elliptical contact. The question consequently rises: is this complexity able to influence significantly the EHD contact behavior or is it possible to simplify it by a simple elliptical contact convergent?

The actual shape modelling is a supplementary challenge to the quite complex EHD models. If the elliptical approximation appears sufficient for friction and film thickness condition, it would be very helpful for the different industrial applications which need better predictions.

It is with these questions in mind that the next chapters will be presented.

# Chapter 3. Torus on Plane Contact - Tools

# III. Torus on plane contact - Tools

Whereas chapter 2 presented tools to the study of torus-on-plane (TOP) flange-roller end contact (FREC) with the elliptical approximation, this third chapter presents new tools which include the real gap shape of the TOP FREC. For this purpose, a test-rig designed to reproduce FREC, Tribogyr, was adapted to run tests on torus on plane contacts. Concurrently, the numerical model presented in chapter 2 was modified to take into account the real gap of the TOP contacts. A comparison is also presented to evaluate the model capacity to predict friction and film thickness in this unusual contact.

## 3.1. Tribogyr test-rig

Tribogyr (for TRIBOlogy and GYRation), is a unique test-rig, built at LaMCoS to study large size spinning lubricated contacts. Figure 3.1-1 is a picture of the test machine. It has already delivered some exclusive results for circular contacts, by Dormois et al. (15) and Doki-Thonon et al. (17). In this thesis, the test-rig was adapted to the TOP contact.

*Figure 3.1-1 - Tribogyr test-rig*

Tribogyr simulates at the full scale the behaviour of the spinning contacts in large-size bearing elements. Therefore, it is a large test-rig (3 $m$ high, 1.5 $m$ wide and long) which is able to impose a large load (up to 3000 $N$) on the contact. In order to reproduce spinning contacts in their actual conditions, it is able to operate at rotation speeds of up to 22,000 rpm. The curvature radii of the mating bodies are also large, and therefore the contact pressures are generally moderate, that is to say $< 1\ GPa$. The kinematic is also representative of the FREC conditions and will be described in section 3.1.1. Film thickness and forces measurements can be performed simultaneously thanks to dedicated facilities. The force sensors are located in the plane of the top body, which is also the plane of the contact. This allows for direct measurement of the forces themselves. The methods and principles related to these measurements will be presented in section 3.1.3 and 3.1.4.

### 3.1.1. Tribogyr kinematics – the TOP case

The test-rig enables a contact between a disc (either made of glass or steel) and a steel torus-end, similarly to the experiment of Gadallah and Dalmaz (20). Figure 3.1-2 presents the torus specimen which was designed for this thesis work and the way it was defined. $R_t = 11\ mm$ defines the major radius of the torus, whereas $r_t = 40\ mm$ is the minor radius.

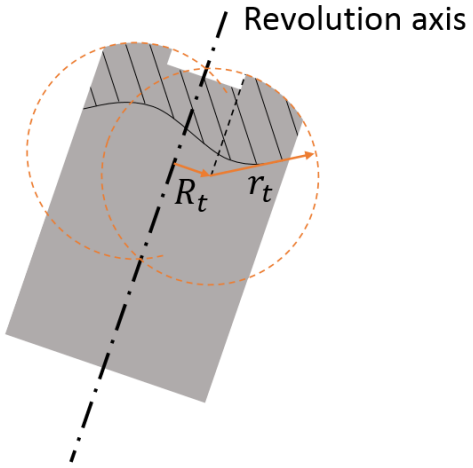


*Figure 3.1-2 – Torus specimen*

As $R_t < r_t$ it is not the familiar ring torus, it is the spindle torus (self-intersecting at two points). A bore is applied at the top of the specimen for machining reasons. This bore has a radius which is equal to $R_t$. The rest of the specimen is a cylinder which enables to clamp the specimen on the Tribogyr lower motor's spindle.

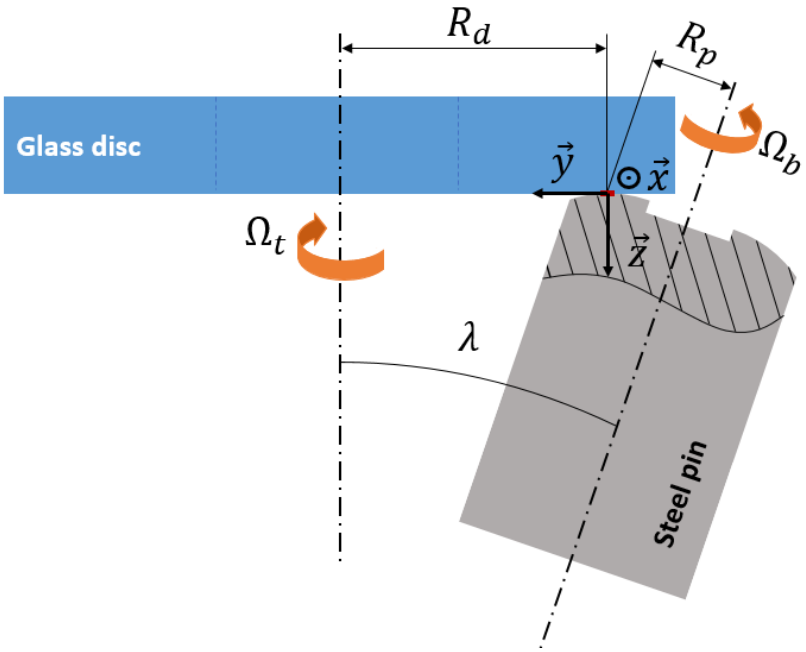


*Figure 3.1-3 - kinematic of the Tribogyr pin and disc*

Figure 3.1-3 presents the two contacting bodies, together with the rotation axes they have when they are installed on Tribogyr on their respective spindle. The gyration radii are $R_d$ (on the disc) and $R_p$ (on the pin): they are the shortest distance between the contact centre and their respective rotation axes. When it comes to TOP contact, its shape is neither circular nor elliptical: it is more complex. Its contact centre is defined as the contact point $O$ between the rigid lower and upper bodies. This point $O$ is also the frame centre. Unless otherwise specified, it is in this frame that the equations are written. The disc rotates at the velocity $\Omega_t < 0$ and the pin $\Omega_b > 0$ (where $t$ stands for "top" and $b$ stands for "bottom). A significant parameter is here $\lambda$, the angle between the two rotation axes. It is called the "spin angle". Within the considered frame, $\lambda < 0$. This geometrical construction results from the definition of the input physical parameters of the Tribogyr test-rig.

Before the experiment, the spin angle is applied to the lower specimen through a well-defined process: the spinning angle $\lambda$ is applied at first by tilting the spindle and its sample. Then, a shift in the contact plane is applied to the assembly supporting the top spindle so that the future contact will occur at the Tribogyr frame origin. Figure 3.1-3 presents the Tribogyr contact frame relatively to the mating bodies. It enables a precise positioning of the lower body relatively to the top one. The linear velocities of the top and bottom solids, respectively are then, along the $x$ axis:

$$u_{tx} = +(R_d - y)\,\Omega_t \approx R_d\,\Omega_t \text{ as } R_d \gg y$$
$$u_{bx} = -(R_p + y\cos(\lambda))\,\Omega_b \qquad \textit{Equation 3.1-1}$$

Consequently, the velocity field varies all over the contact area and its vicinity. Similarly, along the $y$ axis:

$$u_{ty} = x\,\Omega_t \approx 0 \text{ as } x\,\Omega_t \ll x\,cos\lambda\,\Omega_b$$
$$u_{by} = x\cos(\lambda)\,\Omega_b$$

*Equation 3.1-2*

The top solid velocity vector is $\overrightarrow{U_t}(x,y) = (u_{tx};\, u_{ty})$ and the bottom solid velocity vector is $\overrightarrow{U_b}(x,y) = (u_{bx};\, u_{by})$. Thus the entrainment velocity vector is $\overrightarrow{U_e}(x,y) = \frac{1}{2}\left(\overrightarrow{U_t}(x,y) + \overrightarrow{U_b}(x,y)\right)$. With Equation 3.1-1 and Equation 3.1-2, $\lambda$ close to 0 means that the spinning kinematic becomes more important.

During the experiments, the radii $R_d$ and $R_p$ are determined through optical measurement with different actuators and optical devices including a microscope. A precise determination is absolutely mandatory to master the kinematic conditions. Whereas the $R_d$ measurement is quite straightforward, $R_p$ requires more attention. Indeed, $R_d$ is obtained by finding the positions of the contact centre and the one of the disc rotation centre. The distance between these two points is $R_d$, as they are in the same plane $(O, x, y)$, which is perpendicular to the microscope optical axis. For its part, the pin rotation centre (called $I$ in Figure 3.1-4) visible through the microscope is not in the same plane $(O, x, y)$ as the contact.

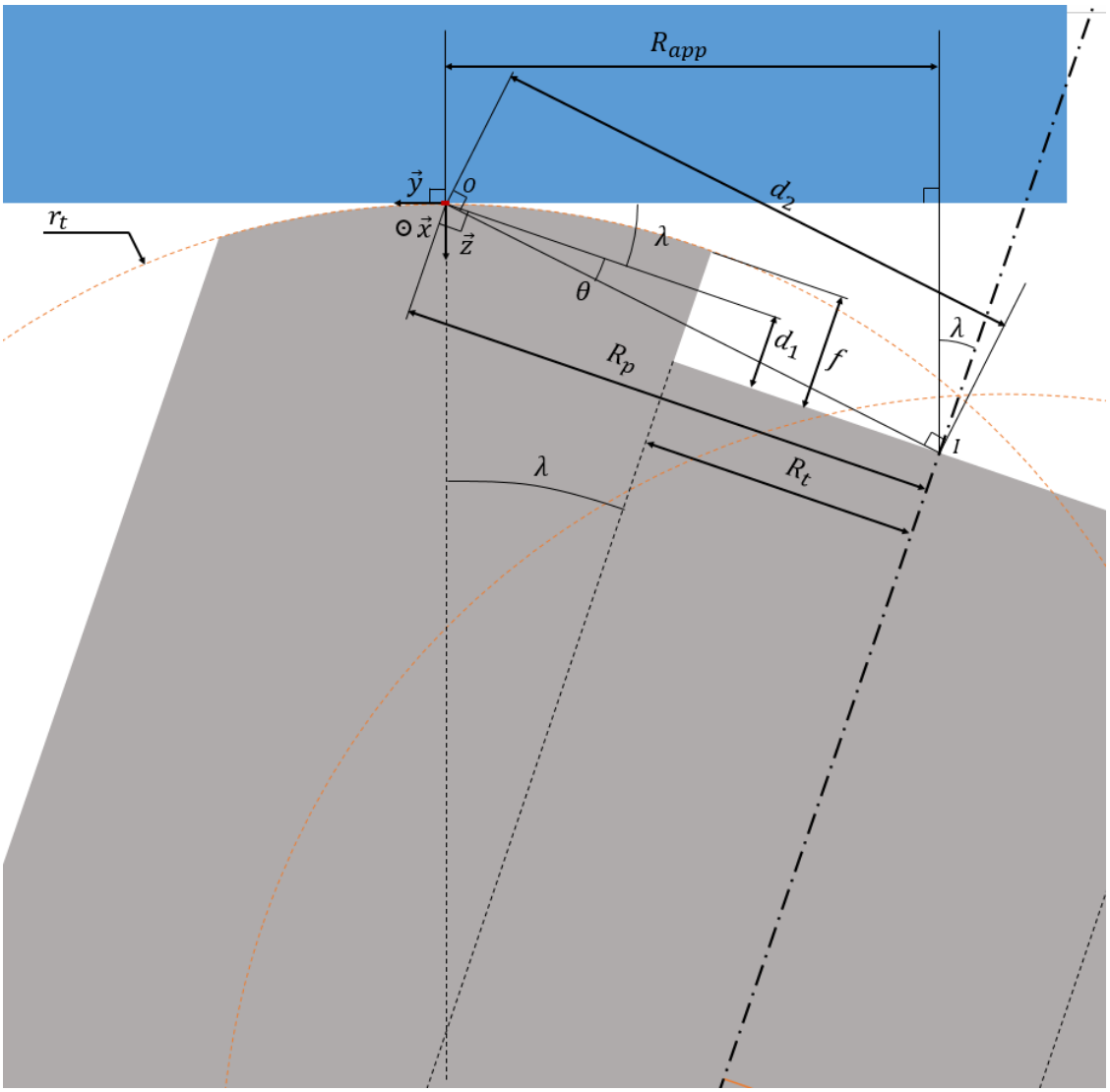


*Figure 3.1-4 - Determination of the effective pin gyration radius from the apparent gyration radius*

Figure 3.1-4 presents the diagram of the contacting bodies together with the different parameters measured to obtain the effective gyration radius: $R_p$. The depth $f$ of the bore is measured with a depth gauge while the apparent gyration radius $R_{app}$ is measured with the microscope from the top: it is the distance between the pin apparent gyration centre and the contact centre, along the $y$ axis. From this diagram, one writes:

$$d_1 = f - (r_t - r_t\cos(\lambda)) = f + r_t(\cos(\lambda) - 1)$$
$$d_2 = \sqrt{R_p^2 + d_1^2}$$
$$R_{app} = d_2\cos(\theta + \lambda), \text{ with } tan(\theta) = \frac{d_1}{R_p}$$

*Equation 3.1-3*

So, by reformulating the apparent gyration radius expression:

$$R_{app} = \sqrt{R_p^2 + (f + r_t(\cos(\lambda) - 1))^2}\cos\left(arctan\left(\frac{f + r_t(\cos(\lambda) - 1)}{R_p}\right) + \lambda\right) \qquad \textit{Equation 3.1-4}$$

From Equation 3.1-4, the experimenter has to extract $R_p$. For this purpose, a Newton algorithm is used. The value of $R_p$ is initialised at the first step of the resolution by the value of $R_{app}$. This method supposes that the minor axis of the torus $r_t$ is known. As this dimension is not easy to machine, a variation of about 10% on $r_t$ may be encountered. However, with this method $r_t$ has a negligible influence: $R_p$ varies only by about $1.4 \cdot 10^{-3}$%.

A second method could be to consider that $R_p = R_t + r_t\, sin(\lambda)$, but then, a variation of 10% on $r_t$ implies a variation of 1.4% on $R_p$. Moreover, this second method requires to know $R_t$ precisely, even if it is not a measurable value. Finally, the fist method requires less hypothesis on the torus geometry (no need for $R_t$ and less influence of $r_t$) and introduces measurable values instead (like $R_{app}$ and $f$). Therefore this method provides reliable and precise results for the kinematic measurement needs. The gyration radius on the disc is typically about $R_d \approx 45\ mm$ and it can be determined within a $0.01\ mm$ precision. For its part, the gyration radius on the torus is about $R_p \approx 12\ mm$ and it can be determined within a $0.1\ mm$ precision as well. The spin angle $\lambda$ is determined within a precision of 0.01°.

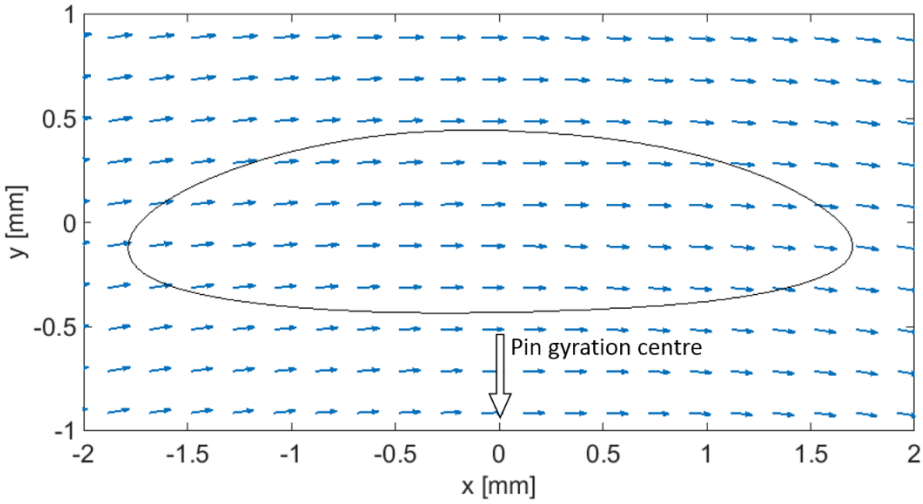


*Figure 3.1-5 - Velocity field of the pin surface, together with the EHD pressurised contact area (for the friction reference case presented in section 3.3.1 with $\lambda = -2.5°$) represented by its iso-pressure line for $p = 10\%p_h$*

As $u_{tx}$ and $u_{bx}$ can be known precisely, the kinematic conditions can be well defined from Equation 3.1-1 and Equation 3.1-2. The velocity field of the pin is represented together with the pressurised area contour on Figure 3.1-5. This contour is the same as in Figure 3.1-6 and is not an ellipse, because one of the two mating solids is a torus; this is presented later, in Figure 3.1-8 for instance. Due to the differences between the top and the bottom velocity fields, a sliding occurs. It is characterised by the local slide-to-roll ratio:

$$SRR(x,y) = \frac{\left|\overrightarrow{U_t}(x,y) - \overrightarrow{U_b}(x,y)\right|}{\left|\overrightarrow{U_e}(x,y)\right|} = \frac{\sqrt{(u_{tx}-u_{bx})^2 + \left(u_{ty}-u_{by}\right)^2}}{\left|\overrightarrow{U_e}(x,y)\right|}$$

$$\text{with } \overrightarrow{U_e}(x,y) = \frac{1}{2}\left(\overrightarrow{U_t}(x,y) + \overrightarrow{U_b}(x,y)\right) = \frac{1}{2}\sqrt{(u_{tx}+u_{bx})^2 + \left(u_{ty}+u_{by}\right)^2}$$

then it comes that:

$$SRR(x,y) = 2\frac{\sqrt{(u_{tx}-u_{bx})^2 + \left(u_{ty}-u_{by}\right)^2}}{\sqrt{(u_{tx}+u_{bx})^2 + \left(u_{ty}+u_{by}\right)^2}} \qquad \textit{Equation 3.1-5}$$

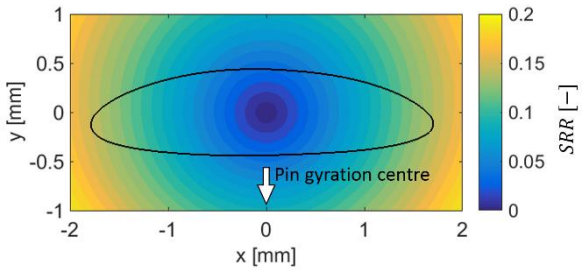


*Figure 3.1-6 - $SRR(x,y)$ plotted in the contact area and its vicinity (for the friction reference case presented in section 3.3.1 with $SRR_{x,0} = 0\%$) - the black contour is the pressurised contact area*

The slide-to-roll ratio introduced by the spinning velocity varies all over the contact area, as shown in Figure 3.1-6. It is also possible to define the slide-to-roll ratio in the *x*-direction as a parameter to quantify the relative sliding at the centre of the contact. It may be expressed as follows:

$$SRR_{x,0} = 2\frac{u_{tx,0} - u_{bx,0}}{u_{tx,0} + u_{bx,0}} \qquad \textit{Equation 3.1-6}$$

with $u_{tx,0}$ and $u_{bx,0}$ which are respectively the velocities $u_{tx}$ and $u_{bx}$ at the contact centre.

Similarly the local entrainment velocity writes:

$$u_e(x,y) = \frac{\sqrt{(u_{tx}+u_{bx})^2 + \left(u_{ty}+u_{by}\right)^2}}{2} \qquad \textit{Equation 3.1-7}$$

Whereas the entrainment velocity at the contact centre is:

$$u_{ex,0}(x,y) = \frac{u_{tx,0} + u_{bx,0}}{2} \qquad \textit{Equation 3.1-8}$$

Comparing to the work of Doki-Thonon (5), the influence of the spinning kinematic on sliding is reduced as $R_p$ the gyration radius on the pin is much larger in the TOP case. Figure 3.1-7 presents a case which is similar to the one in Figure 3.1-6. The former is a circular spinning contact with moderate spin. The spinning induced slide-to-roll ratio occurring in this contact is clearly larger than the one in the latter. Whereas in Doki-Thonon, an average slide-to-roll ratio was defined to express this large spinning induced sliding, $SRR_{x,0}$ is used to define the whole sliding condition of the contact: indeed, the spinning induced sliding in TOP FREC contact is relatively small.

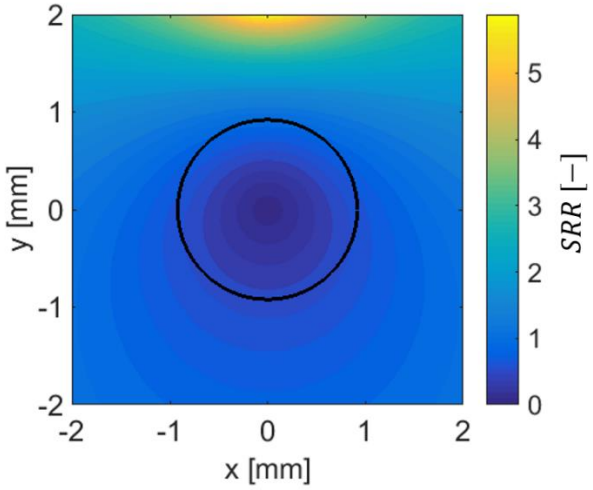


*Figure 3.1-7 - $SRR(x,y)$ plotted in the contact area and its vicinity (according to Doki-Thonon's thesis* (5) *friction case with moderate spin (p. 80) and $SRR_{x,0} = 0$) - the black contour is the Hertz contact area*

This section introduced the Tribogyr test-rig and its specifics, with a focus on the kinematic occurring in the contact. There is another detail of the TOP FREC contact which still has to be presented: the contact shape itself. It is the topic of the next section.

### 3.1.2. The torus on plane (TOP) contact

As the TOP contact shape is not easy to comprehend, the torus defined previously is used in a static contact experiment. A contact between a glass disc and the defined pin is established in order to observe an actual TOP contact.

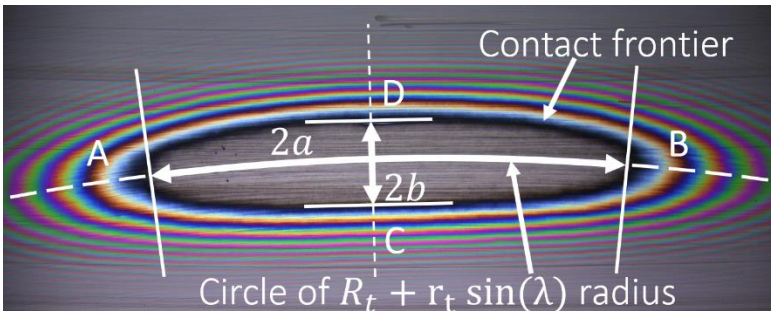


*Figure 3.1-8 – White light interferometry static contact between a glass disc and the steel toroidal pin*

Figure 3.1-8 shows one of these TOP contacts, the first black line being the contact frontier. The contact is similar to an ellipse, however one may notice that this ellipse-like shape is bent along its larger dimension. It is characteristic of the TOP contact.

The two samples have the properties defined in Table 3.1-1 and Table 3.1-2. Tribogyr test-rig enabled an angular positioning within 0.01° and linear positioning of the torus within 0.1°. However, even with well-known geometries and materials, it is not possible at this stage to obtain an approximation of the static contact dimensions.

| Parameter [Unit] | Value |
|---|---|
| $E_t\ [Pa]$ | $62.8 \times 10^9$ |
| $\nu_t\ [-]$ | 0.2 |
| $\rho_t\ [kg.m^{-3}]$ | 2230 |
| $k_t\ [W.m^{-1}.K^{-1}]$ | 1.14 |
| $C_{pt}\ [J.kg^{-1}.K^{-1}]$ | 749 |

*Table 3.1-1 - Glass disc properties*

| Parameter [Unit] | Value |
|---|---|
| $E_t\ [Pa]$ | $210 \times 10^9$ |
| $\nu_t\ [-]$ | 0.3 |
| $\rho_t\ [kg.m^{-3}]$ | 7850 |
| $k_t\ [W.m^{-1}.K^{-1}]$ | 50 |
| $C_{pt}\ [J.kg^{-1}.K^{-1}]$ | 470 |

*Table 3.1-2 - Steel torus pin and steel disc properties*

A method consists in using the Hertz theory and the principal curvature radii presented in section 1.3.4. Figure 3.1-9 presents a TOP (torus on plane) contact, and from the scheme on the left, one deduces that $R_y = r_t$ (with $R_y$ the principal curvature radius in $y$ direction). The other principal curvature radius, $R_x$, requires more attention: it is the curvature radius along the $x$ direction at the contact centre $O$. As the curvature of the torus in the $(O, z, x)$ plane (see Figure 3.1-9) varies all along the torus section, a dedicated calculation is mandatory.

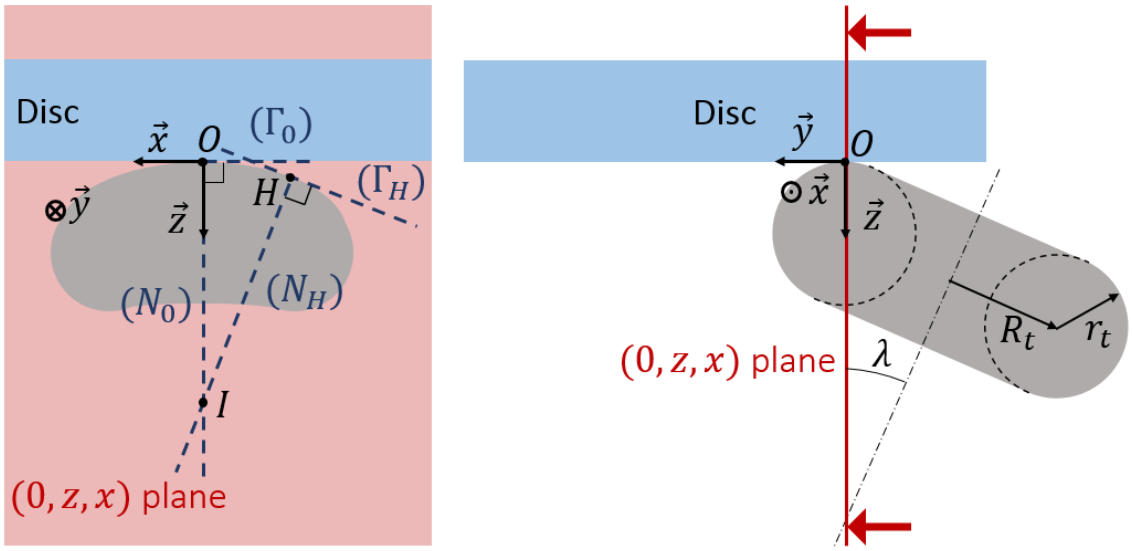


*Figure 3.1-9 - TOP contact (left) and a cut view of the contact (right)*

The straight line $\Gamma_0$ is tangent to the torus section at the point $O$, and $\Gamma_H$ is tangent at $H$. $N_0$ is the perpendicular line of $\Gamma_0$ and they cross at $O$. Similarly, $N_H$ is perpendicular to $\Gamma_H$ and they intersect at $H$. The intersection of $N_H$ and $N_O$ is $I$. The equation of these straight lines ($\Gamma_0, \Gamma_H, N_0$ and $N_H$) can be determined analytically but the details are not presented here. When $H \to O$, the intersection $I$ defines the centre of the local curvature of the torus section at $(x, y, z) = (0,0,0)$. Then, it comes that: $R_x = \lim_{H \to O} OI = \lim_{H \to O} HI$. The analytical development leads to:

$$R_x = \left| R_t \cdot \frac{\cos(2\lambda)}{sin(\lambda)} \right| + r_t \qquad \textit{Equation 3.1-9}$$

As a consequence, one can precisely estimate the contact dimensions and pressure (see Annexe B). The principal curvature radii $R_x$ and $R_y$ can be used with confidence in the Hertz theory: the contact maximum pressure and the contact dimensions $a$ and $b$ are predicted with success (see Annexe B). There is only one difference with the classical elliptical contacts: the longest dimension of the ellipse adopts a curved shape (see Figure 3.1-8). Consequently, the value of $2a$ does not correspond to the segment $AB$ (in Figure 3.1-8) between the contact extremities: it is the arc distance $\widehat{AB}$ between the contact extremities, along the arc of radius $R_t + r_t \sin(\lambda)$. However, when the load is moderate and $|\lambda| \geq -1°$, the chord of the arc does not differ significantly from the arc.

The actual shape of the contact can be obtained more precisely through a finite element analysis which includes a contact law. Annexe B presents the work done in this area which enabled to determine that the Hertz theory was reliable here. The finite element analysis was validated with experimental results and they show together that the Hertz theory is sufficient for precise predictions.

### 3.1.3. Film thickness measurement

The film thickness measurement method is the same as the one presented in sections 2.1.1.3 and 2.1.1.4. Indeed, the calibration does not require hypothesis on the contact shape, unlike the method of Molimard et al. (3). Based on this calibration, the film thickness measurement in EHD contacts can be done easily.

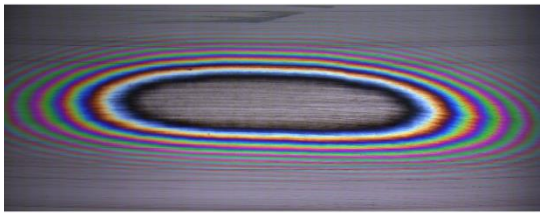

*Figure 3.1-10 - TOP contact under a chromatic light, for calibration*

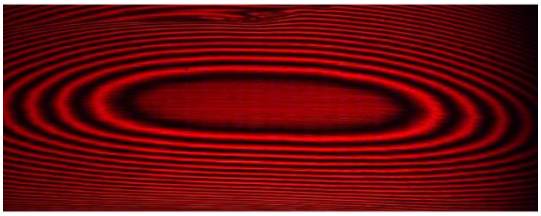

*Figure 3.1-11 – TOP contact under a monochromatic light, for calibration*

Figure 3.1-10 and Figure 3.1-11 show a pair of interferograms that were used to establish a calibration curve. Again, several pairs of pictures are used to determine a group of calibration curves. Among these curves, the one which represents the average value of the curve group is selected to measure film thickness in the whole dynamic experiment. This curve is very similar to the one in Figure 2.1-9.

Based on this calibration curve, one can analyse the EHD contact pictures. Figure 3.1-12 presents such a contact, together with the considerations made to obtain the characteristics of the film thickness field. At first, the contact centre is defined as the middle of the contact principal directions. There is no reason for it to correspond exactly to the rigid bodies' contact point, but it is not too different and would have made less sense than the value obtained in dynamic conditions due to the large uncertainty in its localisation. The film thickness at the contact centre is $h_c$, the central film thickness. The minimum film thickness on the $y = 0$ axis is the central minimum film thickness $h_{m,c}$. The minimum thickness on the $y < 0$ side it the furthest from the disc rotation centre: it is called $h_{m-}$. On the contrary, the minimum thickness on the other side is the closest from the disc gyration centre and is called $h_{m+}$.

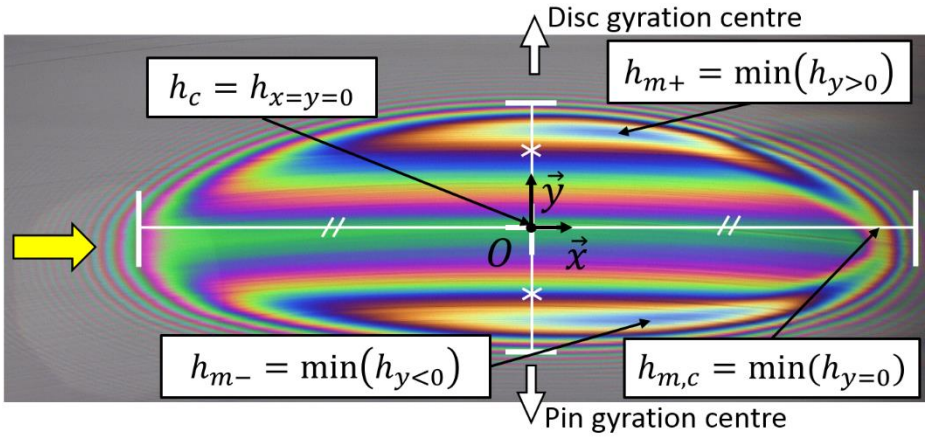


*Figure 3.1-12 White light interferometric TOP EHD contact with film thickness values at some points of interest.*

### 3.1.4. Friction forces measurement

Besides the film thickness, the Tribogyr test-rig enables the measurement of the friction forces. The two specimens (pin and disc) are held and set in rotation by two different spindles. In their turn, the spindles are supported by two independent assemblies.

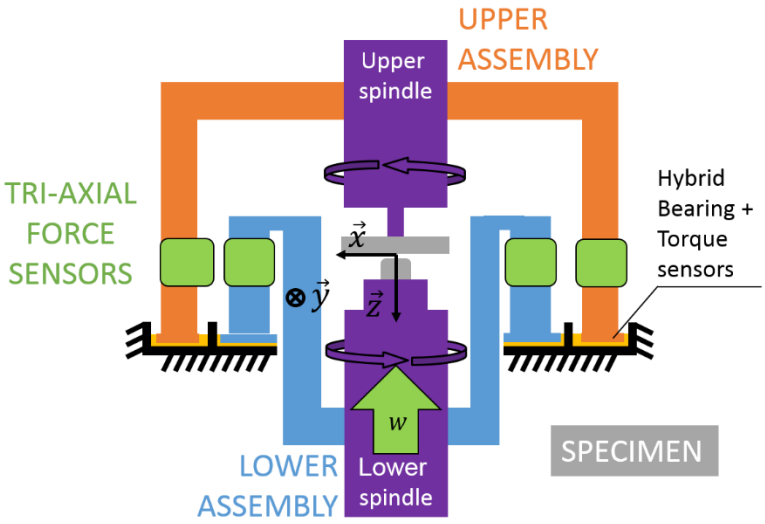


*Figure 3.1-13 - The two Tribogyr assemblies, together with their respective spindles and samples*

Figure 3.1-13 presents these two assemblies. They are each sustained by hybrid bearings, combining a hydrostatic thrust bearing together with a circular hydrostatic one. This bearing pair supports the dead-weight of each assembly and enables their free rotation in the $(O, x, y)$ plane, around the contact centre. It allows for the measurement of the friction torque generated in the contact.

The assemblies are both connected to the hydrostatic bearings by tri-axial piezoelectric force sensors. They are located in the contact plane to measure directly the friction forces ($F_x$ and $F_y$), the normal load (w). Moreover, the torque (Tz,0) generated in the contact plane on each specimen contacting surface is directly obtained with the help of a lever and a very sensitive force sensor secured to the Tribogyr main frame. The torque and forces measurements are carried out on the two assemblies.

### 3.1.5. Temperature measurements

Mastering the experimental thermal conditions is certainly one of the main challenges of this work. Indeed, the thermal effects are one of the keys to understand spinning-sliding EHD contacts (see (5)). They drive contact friction, power losses and film thickness. It is mandatory to be able to predict their importance with precision.

In the experimental context, rather large and unknown variations can occur if the experimental conditions are not set carefully. At this stage, it is important to describe the oil feeding system. An oil bath contains the lubricant that will be delivered to the contact with the help of a peristaltic pump and a hydrodynamic slider bearing. The temperature is controlled in this oil reservoir which is set so that $T_{f0} = 30°C$. $T_{f0}$ is the temperature of the oil just before being spread on the lower surface of the glass or steel disc, and in this work $T_0 = T_{f0}$, with $T_0$ the temperature of the experiment environment. However, in section 3.3.2, $T_0$ will be replaced by more detailed boundary conditions.

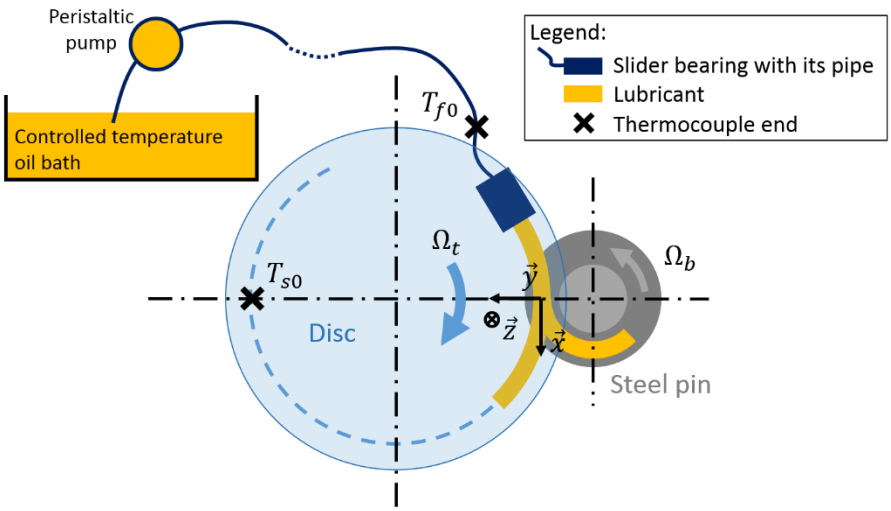


*Figure 3.1-14 - Oil feeding of the contact and the measurement points*

The temperature measurements are made thanks to thermocouples. The first thermocouple is located inside of the pipe which brings the oil towards the hydrodynamic slider bearing. Then the lubricant is spread on the glass disc lower surface, on the same track than the contact. The amount of oil delivered to the contact is set so that the contact occurs under fully flooded

conditions. Another temperature measurement is performed, on the disc surface, at the opposite of the contact, but on its track. This temperature is $T_{s0}$ and will be considered as the temperature of the solids at the contact inlet in section 3.3.2. Indeed, $T_{s0}$ represents the disc global heating in the region of the contact track. Unless otherwise specified, $T_{f0} = T_{s0} = T_0$ is applied. The measurement precision of the two thermocouples is $0.2°C$.

## 3.2. Numerical model

### 3.2.1. Film thickness expression

In the past, Gadallah and Dalmaz (20) compared their experimental measurement with elliptical film thickness prediction formulae, and Colin et al. (9) and Zhang et al. (14) modelled such a gap by an elliptical contact gap. However, in the present study, the new geometry of the torus specimen leads to a new gap shape, for application to the study of flange roller-end contacts.

This new geometry is introduced in Equation 2.1-21 and replaces the parabolic terms. It corresponds to a change of the rigid gap expression. Indeed, $h_0$ and $\delta$ remain unchanged.

$$h(x,y) = h_0 + h_{torus}(x,y) + \delta(x,y) \qquad \textit{Equation 3.2-1}$$

However, no analytical expression is known for $h_{torus}$ in the contact frame. A novel method to obtain $h_{torus}$ was then developed. This method is based on CAD (Computer Assisted Design) considerations: the adequate torus is drawn in the $(O,x,y,z)$ 3D frame and its position is arranged in accordance to the needs of the simulation (rigid contact point at $O$, the frame origin, and $\lambda$ angle applied to the torus). This torus is plotted in Figure 3.2-1 where it is in the appropriate position.

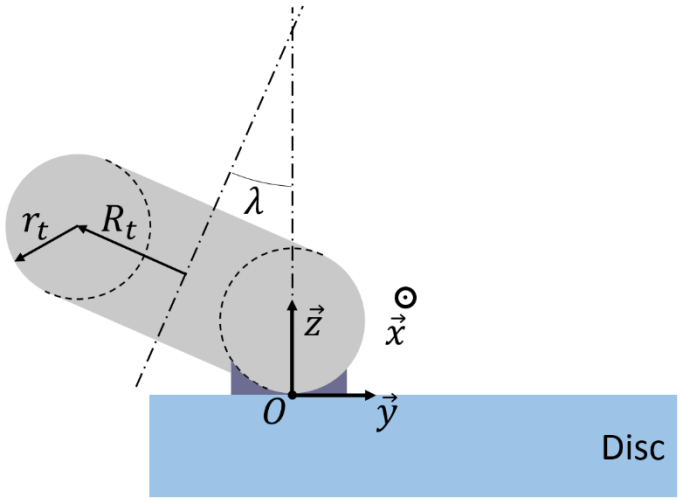


*Figure 3.2-1 – Rigid gap between a torus and a plane in the $(O,x,y,z)$ Cartesian frame*

The rigid gap is then simply the distance between the plane and the torus. This gap is represented in purple in Figure 3.2-1 and Figure 3.2-2.

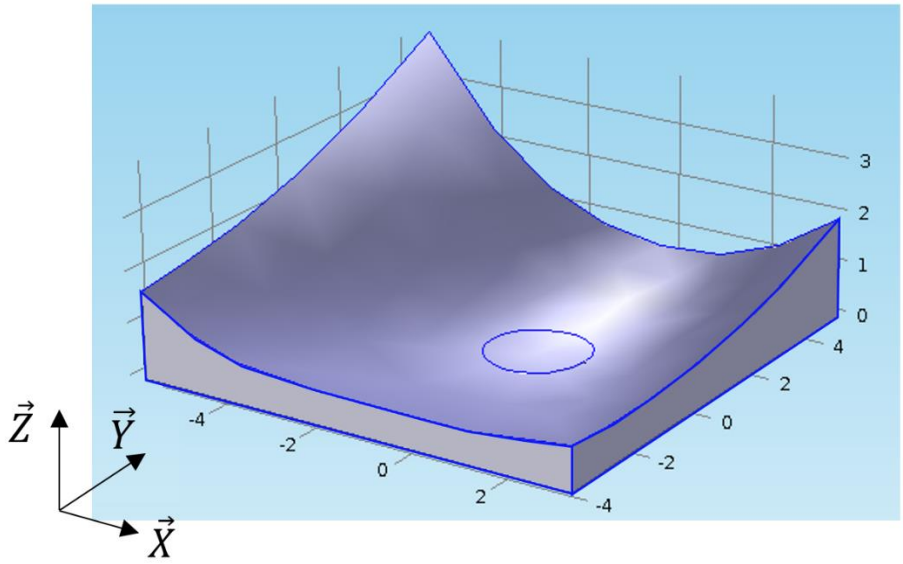


*Figure 3.2-2 - Rigid gap between a torus and a plane in the $(O, X, Y, Z)$ dimensionless Cartesian frame*

Figure 3.2-2 presents a focus on the solid formed by the TOP rigid contact gap, in the contact vicinity. It was set in its dimensionless frame ($X = x/a\,; Y = y/b\,; Z = z \times R_x/a^2$); in the real frame, the gap would look flat due to the large scale differences between the thickness and the in-plane dimensions of the contact. One may notice that the gap is not symmetrical relatively to the $xOz$ plane: it is due to the asymmetry between the two sides of the contact. Moreover, on the $y < 0$ side, the curvature of the gap appears not constant.

This model which includes the real gap geometry was used to run TOP EHD simulations, for various spin angle $\lambda$, various loads and sliding.

Besides, the elliptical point contact model as presented in section 2.1.2 was also used to model the TOP contact under the same conditions as in the model presented hereinabove (apart from the rigid gap shape). The simplified elliptical modelling is called an "Elliptical Equivalent" (EE) of the real TOP simulation. Comparisons were made between the two approaches, in order to conclude on the relevance of this actual gap model.

### 3.2.2. Thermal boundary conditions (film thickness validation only)

The thermal boundary conditions were modified in order to adapt to the conditions of the experiments. Indeed, because of the sliding that occurs in the contact, the disc and the pin temperature can increase significantly, together with the whole test-rig. It is not possible to

control this heating. However, it is possible to measure the global heating of the pin and of the disc.

Film thickness predictions can be very precise, but the temperature of the lubricant and the bodies around the contact have to be known. A variation of about $0.5°C$ of the solids temperature can lead to a 5 $nm$ difference on $h_c$: it is important to run simulations in the same thermal conditions as the experiments. For this purpose, and in the case of the film thickness validation only, the bodies' temperature and the lubricant temperature are distinguished: $T_{f0}$ addresses to the fluid's boundary conditions, and $T_{s0}$ to the solids' boundary conditions. Indeed, the solids encounter a heating all along the experiment due to the energy dissipated in the contact, whereas the lubricant's temperature is more stable because it is regulated at the inlet of the contact. The measurements of $T_{s0}$ and $T_{f0}$ in the Tribogyr test-rig were described in section 3.1.5. Despite the efforts to record the heating of the system, it was not possible to measure the pin surface temperature. Consequently, a rough hypothesis is made: the pin temperature rise is considered equal to the one of the disc.

In order to apply consistent thermal boundary conditions, a function $T_{boundary}$ was defined in order to further develop the thermal model proposed in section 2.1.2.3. Indeed, as the solids' and the lubricant temperatures on the boundary are not constant anymore, one shall define the temperature at the interfaces, in order to define coherent Dirichlet boundary conditions. For this purpose, $T_{boundary}$ is based on an $arctan$ function and verifies the conditions: $T_{boundary} = \frac{T_{s0}+T_{f0}}{2}$ at the interface, $T_{boundary} = T_{s0}$ at the solids boundaries, and $T_{boundary} = T_{f0}$ at the lubricant boundary. The function $T_{boundary}$ is then presented in Figure 3.2-3.

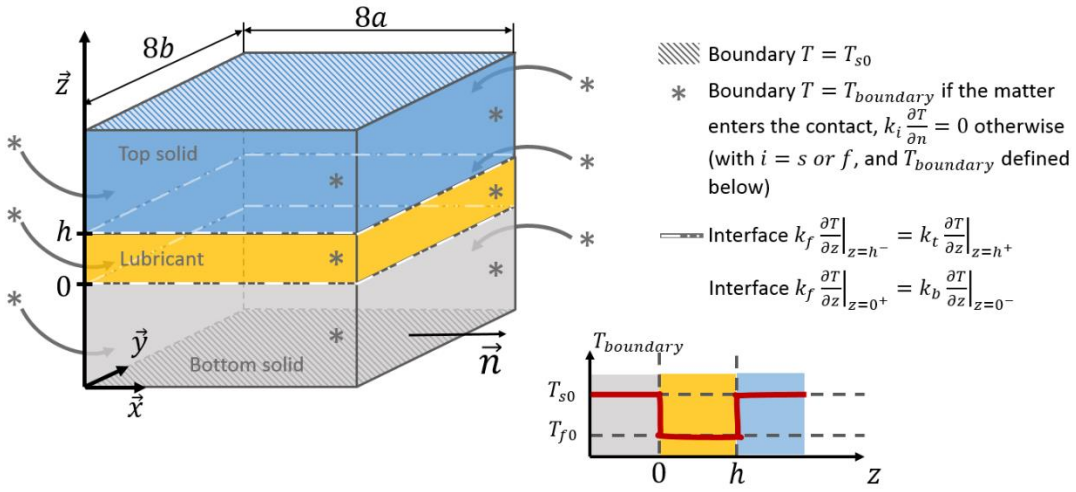


*Figure 3.2-3 - Modified thermal model to reproduce the film thickness reference case experimental conditions*

It is important to mention that the use of experimental measurements in the numerical model is not a fitting of the results to the expected trend. Indeed, the numerical model is only addressed to the contact and its close vicinity: the further environment may vary in a large

extent. The experimental environment thermal conditions are measured, and are expressed by the boundary conditions.

### 3.2.3. Lubricant characterisation limits

At this stage, it becomes necessary to present with more details the lubricant characterisation. As presented in section 2.1.2.1, independent measurement were made on the fluid in order to define its properties under pressure and shearing for different temperatures. For this purpose, a viscometer and Couette rheometer were used. In spite of their advanced performances, they have not been able to run tests under all the conditions encountered in EHD sliding contacts.

The viscometer is limited as it can apply a maximum pressure of $800\,MPa$ on the fluid. Moreover, as it is a falling body viscometer, it is not possible to apply a large shear stress to the fluid: as a consequence, the moving part may not fall down in a reasonable amount of time above a certain viscosity limit, which is generally around $10^{+2} - 10^{+5}\,Pa.s$, according to the nature of the lubricant. At such a large viscosity, the lubricant is too viscous for the apparatus used in this study. As a consequence, and for the lower temperatures, the lubricant cannot be investigated at the full pressure range available. There are also limits in terms of temperature: the lubricant was characterised between $30°C$ and $150°C$. When the WLF model is used outside of these limits, it is an extrapolation of the experimental data that were used to establish the model, which suits for such extrapolations in the range $T_g(0) + 300\,°C$. However, the extrapolation in pressure can be hazardous. Indeed, above a certain viscosity, the influence of pressure on viscosity may increase significantly comparing to the influence it has inside of the range used for the characterisation. This means that the behaviour of the lubricant outside of the characterisation domain is not predictable from the data obtained inside of this domain but within a limited range of typically 500 to 900 MPa, for low to high temperatures respectively. Figure 3.2-4 summarises the characterisation range of the lubricant 3, and what is a reasonable use of extrapolation.

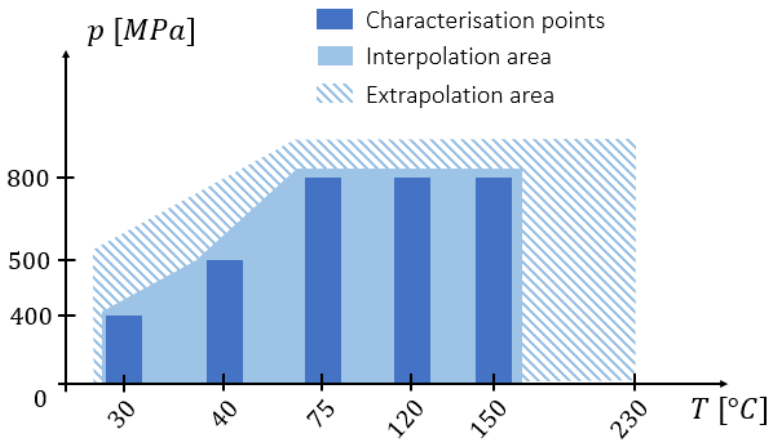


*Figure 3.2-4 – Characterisation domain, interpolation and extrapolation of the pressure and temperature dependence of the T9V3 viscosity*

Similarly, the shear stress influence on viscosity was investigated. The Couette rheometer enabled characterisations between $20°C$ and $60°C$ for shear stresses up to 5 $MPa$, see Figure 2.1-12. Under the whole range of $(p,T)$ conditions represented in Figure 3.2-5, the lubricant 3 showed a Newtonian behaviour. No shear-dependence was observed and consequently the lubricant was considered as Newtonian in the model.

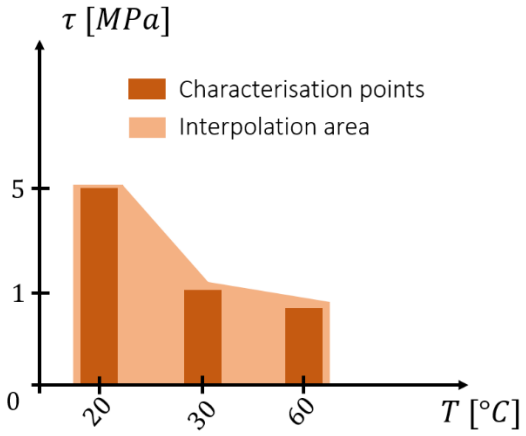


*Figure 3.2-5 - Characterisation domain of the pressure and temperature dependence of the T9V3 viscosity*

In the tribometers, and in particular with Tribogyr, the shear stress that the lubricant withstands was much larger, especially during friction tests. In order to compare numerical predictions and experimental results, the lubricant was considered purely Newtonian under all conditions. However this was a necessarily extrapolation but which is not reliable from a certain point, as the lubricant is very likely to adopt a non-Newtonian behaviour outside of the shear range explored. Consequently, the interpretation of the simulation results had to be done with care.

## 3.3. Experimental validation

This section is dedicated to the validation of the model by the comparison of numerical solutions with results obtained from the Tribogyr test-rig. Numerical simulations were run on the model presented in chapter 2 and adapted for TOP contact with the new film thickness expression (Equation 3.2-1). At first, correlations on friction coefficient were performed. Experiments were run under realistic industrial conditions, presented in Table 3.3-1. The case presented in this table is the friction reference case: other entrainment velocities, loads and spin angles were applied to the contact but the reference one is chosen as the basis for validation. Its conditions are medium in terms of velocity and spin angle, but its load is the largest. The large load condition enables more accurate friction measurements on the test rig.

Secondly, a film thickness reference case was also defined to evaluate the model ability to predict film thickness. This second reference case is presented in Table 3.3-2.

The oil used in this chapter is exclusively the lubricant 3, which was described previously in section 2.1.2.1.

### 3.3.1. Friction prediction evaluation

The conditions presented in Table 3.3-1 were applied to the numerical model and the test rig. The pin used in this thesis enables experiments with $\lambda = -4.5°$ as well, but the $\lambda = -2.5°$ leads to a contact shape which is more representative of the TOP contact specifics. The results for the other angle will be presented in the following.

| Parameter [Unit] | Value |
|---|---|
| $u_{ex,0}\ [m/s]$ | 2 |
| $SRR_{x,0}\ [\%]$ | $[-45, 45]$ |
| $w\ [N]$ | 1500 |
| $R_t\ [m]$ | 0.011 |
| $r_t\ [m]$ | 0.040 |
| $\lambda[°]$ | $-2.5$ |
| $T_0\ [K]$ | 303 |
| $\Omega_b\ [rad/s]$ | Adjusted to the $SRR_{x,0}$ |
| $\Omega_t\ [rad/s]$ | |

| Parameter [Unit] | Value |
|---|---|
| $R_p\ [mm]$ | 12.54 |
| $R_d\ [mm]$ | 40.34 |
| $p_h\ [MPa]$ | 765 |
| $a\ [mm]$ | 1.19 |
| $b\ [mm]$ | 0.32 |
| $k\ [-]$ | 0.272 |
| Disc material | steel |
| Pin material | steel |

*Table 3.3-1 – Friction reference case – Industrial like experimental conditions*

The slide-to-roll ratio was varied and the friction forces were measured in the two contact plane directions. The results are plotted in Figure 3.3-1. In Equation 3.3-1, the force $F_x$ is the friction force in the $x$ direction, and $F_y$ in the $y$ direction:

$$C_{fx} = \frac{F_x}{w};\ C_{fy} = \frac{F_y}{w} \qquad \textit{Equation 3.3-1}$$

In Figure 3.3-1a, experimental and numerical results only corroborate in terms of order of magnitude. This is verified for the longitudinal friction coefficient, where three regions can be distinguished (82):

· For low $SRR_{x,0}$ (i.e. smaller than 5%), the longitudinal friction coefficient increases drastically and linearly. This is known as the linear region. In this region, the slope at the origin is not the same in the numerical and the experimental approaches. It is apparent from this that two effects can be evoked. The thermal EHD model only is not able to predict friction under low shear. Moreover, the lack of a non-Newtonian behaviour in the model might be accountable for the discrepancy in this region.

· For $SRR_{x,0}$ between 5 and 20%, the friction coefficient rate of increase is slowed down until a plateau value is reached. This decrease is mainly due to the non-Newtonian effects that lower the viscosity. In this second region, the $C_{fx}$ discrepancy is very large too, and the lack of non-Newtonian model is critically underlined. A Carreau law, together with a limiting shear stress response model could decrease the difference of the numerical results comparing to the experimental curve.

· At high $SRR_{x,0}$ (i.e. $SRR_{x,0}$ larger than 20%) and after reaching the maximal plateau value, the friction coefficient drops gently. This region is known as the thermal region where thermal-thinning of the lubricant is predominant due to higher shear rates. These thermal effects lower the viscosity and thus decrease the friction despite the increasing sliding. This regime sees the best accordance between the curves, even if the difference is still about 40%, for very low friction values however. The slope of the curve is now very similar, though the numerical model overestimates the thermal thinning of the lubricant.

The transverse friction coefficient $C_{fy}$ is below 1% for both experimental and numerical results. However, the experiment shows a non-zero friction in the range $5 \leq |SRR_{x,0}| \leq 35\%$, whereas the numerical model predicts a nearly zero friction.

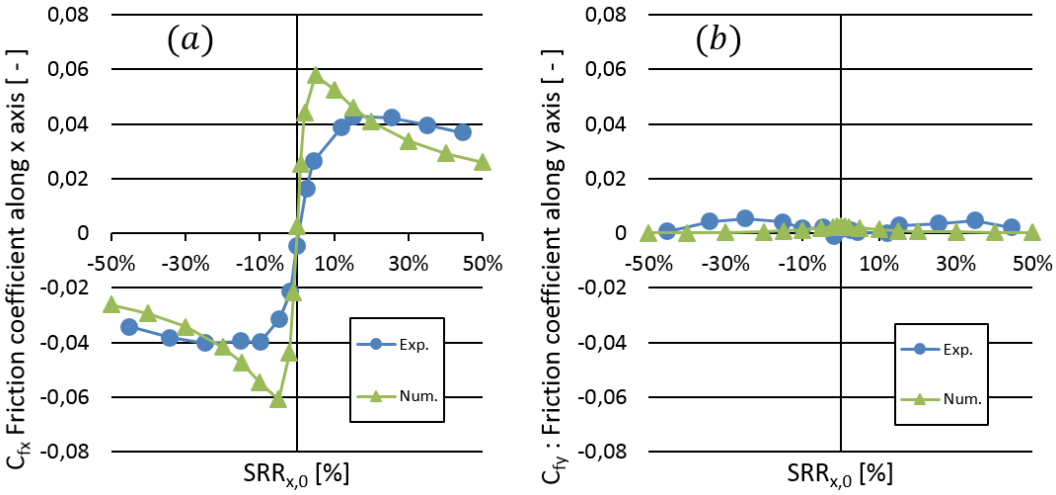


*Figure 3.3-1 - Friction coefficient along x direction (a, left) and y direction (b, right): comparison between experimental measurements (Exp.) and numerical model (Num.) results – reference case presented in Table 3.3-1*

To summarise, the numerical model is neither able to predict the friction quantitatively, nor qualitatively. Yet, a simple order of magnitude estimation is possible.

This result is in accordance with the literature: the friction coefficient in highly-loaded EHD contacts cannot be predicted quantitatively (see (82)). There is a lack of knowledge on lubricant behaviour under very high shear stress: at first, the rheometers are not yet able to measure the viscosity under extreme shear stress. Secondly, the phenomenon commonly called "limiting

shear stress" is for now not well understood, and as a consequence it is not possible to model it either (if it is involved).

There is still one case where the rheology models were sufficient: under high spinning conditions, the friction forces along the entrainment direction was successfully predicted by Doki-Thonon (5) through the same model as the one presented here. In the specific kinematic case he used, it appears that only a non-Newtonian Carreau law, together with thermal effects were required to forecast quantitatively the friction coefficient.

### 3.3.2. Film thickness validation

Thanks to the differential colorimetric interferometry, it was possible to perform film thickness measurement in TOP EHD contacts. Molimard et al. (3) developed an experimental procedure enabling measurements in circular EHD contacts, and this method was further developed in this thesis and made suitable for elliptical and general shape EHD contacts. Sections 2.1.1.3 and 2.1.1.4 and present this newly adapted method.

For the film thickness validation, the conditions differ slightly from the ones of the friction reference case: the film thickness reference case is presented in Table 3.3-2.

| Parameter [Unit] | Value |
|---|---|
| $u_{ex,0}\ [m/s]$ | 3 |
| $SRR_{x,0}\ [\%]$ | 0 |
| $w\ [N]$ | 400 |
| $R_t\ [m]$ | 0.011 |
| $r_t\ [m]$ | 0.040 |
| $\lambda[°]$ | $-2.5$ |
| $T_{f0}\ [K]$ | 304.1 |
| $T_{s0}\ [K]$ | 302.1 |
| $\Omega_b\ [rad/s]$ | 236.01 |
| $\Omega_t\ [rad/s]$ | 65.25 |

| Parameter [Unit] | Value |
|---|---|
| $R_p\ [mm]$ | 12.71 |
| $R_d\ [mm]$ | 45.98 |
| $p_h\ [MPa]$ | 285 |
| $a\ [mm]$ | 1.57 |
| $b\ [mm]$ | 0.43 |
| $k\ [-]$ | 0.272 |
| Disc material | glass |
| Pin material | steel |

*Table 3.3-2 – Film thickness reference case – Industrial like experimental conditions*

Now, a glass disc has replaced the steel disc, and a lower load was applied in order to preserve the disc integrity. Nevertheless, this light load leads to a contact pressure which is still representative of FREC. For the case presented here, 10 interferogram pictures of the contact were taken. Thanks to this relatively large number of data for only one condition, means value of $h_c$, $h_{m,c}$, $h_{m+}$ and $h_{m-}$ were determined. The picture which represented at best these mean values is presented in Figure 3.3-2, at the bottom.

Equivalent simulations were ran with the appropriate temperatures and the real TOP gap shape. A plot was realized using the experimental calibration curve as a scale bar. This scale bar enabled to compare on the same basis, see Figure 3.3-2, the film thickness distributions

obtained from the numerical and experimental approaches, over the whole contact area and its close vicinity. At first glance, there are only slight differences between the two results. The model predicts the whole TOP EHD gap with a good precision.

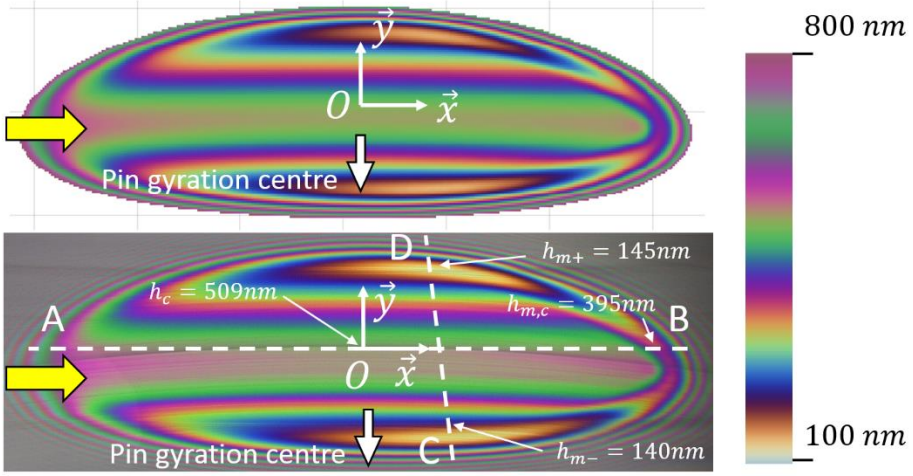


*Figure 3.3-2 - Film thickness in and around a TOP EHD contact – numerical (top) and experimental (bottom) comparison*

A quantitative comparison is proposed in Table 3.3-3, at the characteristic points of the EHD gap. These points are defined in section 3.1.3. Both central and minimum film thickness along the central line show a very good agreement: the numerical results slightly overestimate the experimental values, with a relative error less than 2%. Even under spinning conditions and for an unusual contact geometry, the numerical model presents a good ability to quantitatively predict film thickness. The minimum film thickness shows a slightly bigger deviation, but it is still a rather good agreement. The difference between the two minima is also well predicted. Similarly to the elliptical results, the experimental values in Table 3.3-3 are not stemming from a single picture, but they are the average value of about 10 interferograms taken in the same operating conditions.

There is a rather large $h_c/h_m$ ratio (with $h_m = (h_{m+} + h_{m-})/2$) on both numerical and experimental results. Here, this ratio is larger than 3, which is consistent with the film thickness analysis developed in chapter 2: it was demonstrated that for slender elliptical contacts (TOP FREC are similar to this category), the $h_c/h_m$ ratio is large.

| | **Experimental** | **Numerical** | **Relative gap difference** |
|---|---|---|---|
| $h_c\ [nm]$ | 509 | 516 | 1.3% |
| $h_{m,c}\ [nm]$ | 395 | 402 | 1.6% |
| $h_{m+}\ [nm]$ | 145 | 152 | 4.7% |
| $h_{m-}\ [nm]$ | 140 | 149 | 6.0% |

*Table 3.3-3 - Film thickness comparison at characteristic points*

Figure 3.3-3 presents the film thickness profiles, along the line AB (Figure 3.3-2) which is actually the x axis, and along the line CD, which connects the two minima. Again, the experimental measurement and the numerical results show a good agreement. There is a dissymmetry on the film thickness variation along the CD line: the $dh/d(CD) = 0$ does not occur at the origin of the axis, but it is shifted towards the side of $h_{m-}$. Again, this behaviour of the TOP EHD gap is the same in the experiment and in the model results.

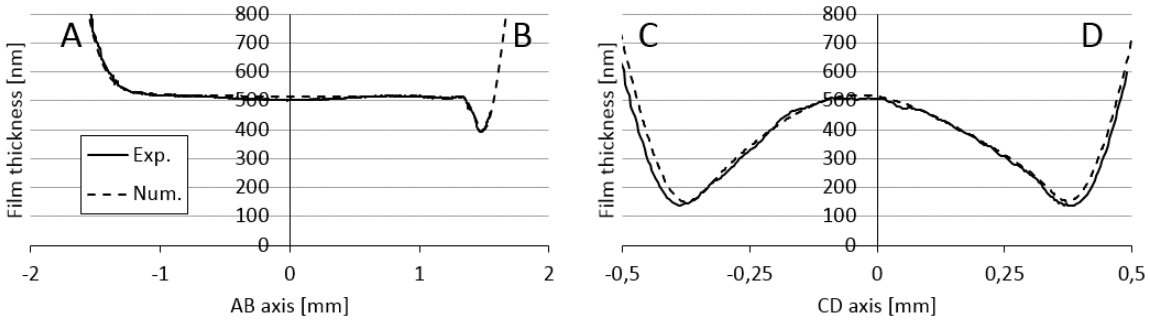


*Figure 3.3-3 - Film thickness along the AB and CD axis as defined in Figure 3.3-2 – numerical and experimental comparison*

The model was evaluated in terms of film thickness and friction for 2 experimental reference cases. The comparison with experiments proved that the model cannot accurately predict the friction: it can only estimate an order of magnitude. However, the model is very relevant with regard to film thickness.

Now, as the tools are defined in sections 3.1 and 3.2, and as their abilities and limits are known from section 3.3, it makes possible the investigation into details of the TOP EHD contact. The numerical model constitutes a helpful complementary mean to go further in the investigation of spinning TOP contacts. Indeed, for a given TOP geometry, Tribogyr does not have the capability to test a wide range of conditions, in particular the spin angle λ, whereas the model does.

## 3.4. Conclusion

In this chapter, several tools were used such as the Tribogyr test-rig and a numerical model. Both were dedicated to the study of torus on plane (TOP) flange roller-end contacts (FREC).

As a consequence, a special pin with a torus end was machined. The new method developed to allow for interferometry measurements on non-circular contacts enabled precise measurements of the film thickness. Moreover, the friction forces, the friction torque, and the temperature were measured in some critical places in the test rig and on the samples.

Thanks to this test-rig, the model built to predict the FREC contact has shown its reliability. However, this TOP model (with the real torus geometry at the contact end) is not able to predict the contact friction with precision, but it can still be used as a prediction of the friction order of magnitude. The film thickness predictions are very faithful, and it is probably the first time that an experimental validation is applied to a non-elliptical point contact model.

Thanks to evaluations and validations, it is possible to use the numerical model as a proper tool to study with more flexibility the TOP FREC contact. It is the topic of chapter 4.

# Chapter 4. Torus on Plane Contact - Results

# IV. Torus on plane contact – Results

Thanks to dedicated numerical and experimental tools presented in chapter 3, an investigation on the torus on plane (TOP) EHD contact is lead. It aims to identify the role of the operating conditions on the contact behaviour. The attention is drawn to the particularities of this unusual EHD conjunction, where neither the gap nor the kinematic is symmetrical.

At first, the influence of the spin angle $\lambda$ on contact pressure, film thickness and friction is investigated. Then, the role of the sliding is explored, in order to identify its effect on friction and film thickness. At last, a comparison between the full torus on plane (TOP) model and a simplified elliptical equivalent (EE) one is performed. This comparison aims to identify the cases in which the torus on plane (TOP) modelling is mandatory, and the cases in which its elliptical equivalent (EE) is sufficient.

## 4.1. Influence of the spin angle

In this section, the effect of the spin angle, $\lambda$, on the pressure distribution, film thickness and friction will be discussed. For this, the influence of the spin angle, a key parameter, will be studied with the experimental and numerical tools developed in this thesis.

The $\lambda$ angle drives the curvature radii in the x direction, in agreement with Equation 3.1-9. It also has an influence on the contact kinematic, according to Equation 2.1-4 and Equation 3.1-2. When $\lambda$ varies, both the bodies' geometry and the entrainment velocity field vary in the contact vicinity. This section investigates the consequences of these relationships between $\lambda$ and the TOP EHD contact behaviour. For the reader's convenience, a part of Figure 3.1-9 is presented here again in Figure 4.1-1, in order to remind the way the torus is defined. As previously said, within the considered frame, $\lambda < 0$.

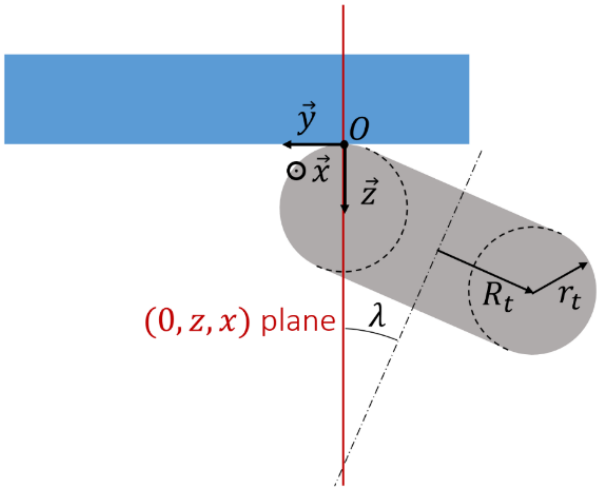


*Figure 4.1-1 - The TOP contact and the spin angle $\lambda$*

### 4.1.1. Influence on EHD pressure

At first, the contact pressure is investigated. As the model was validated through experimental film thickness comparisons, it is possible to study the numerical pressure results with confidence. Indeed, the gap distribution is validated by the interferometry experimental measurements: one can deduce that the Reynolds equation used to compute it is correctly solved. As a consequence, the pressure distribution is also correctly predicted by the model. The incapacity of the model to quantitatively predict friction does not invalidate the capacity to quantitatively predict pressure distribution: the rheology models hardly influence the pressure distribution.

As the bodies' geometry makes the situation more complex, a preliminary study under static conditions is proposed: the spin angle influence on the dry static contact dimensions and Hertzian pressure is briefly presented here. More details can be found in Annexe B. In this annexe, it was demonstrated that the dry static TOP contact characteristics (dimensions and pressure) can be well modelled by an elliptical equivalent (EE) contact if it has the same principal curvature radii. The dry static results are simply the results of this EE with the Hertz theory.

The friction reference case is used here as a basis, but the spin angle is varied as follows:

$$\lambda = [-6°;\ -4.5°;\ -2.5°;\ -1.5°;\ -1°] \qquad \textit{Equation 4.1-1}$$

Figure 4.1-2 presents the variations of the contact dimensions $a$ and $b$ together with the resulting Hertz pressure according to the spin angle. For low $|\lambda|$, the $R_x$ curvature radius is rising up to about 670 $mm$. As a result, the contact dimension increases along the $x$ direction: at $\lambda = -1°$, the contact is $2 * a \approx 5.5\ mm$ long. The contact becomes a little thinner along the other direction, but still, the contact pressure decreases when $|\lambda|$ becomes smaller. It reduces down to about 630 $MPa$. The result of the contact dimension variation is also a variation of the ellipticity ratio $k$. This ratio varies between $k = 0.43$ for the largest $|\lambda|$ and $k = 0.161$ for the smallest. This means that all TOP contacts presented here are slender contacts, and that the smaller $|\lambda|$ is, the smaller $k$.

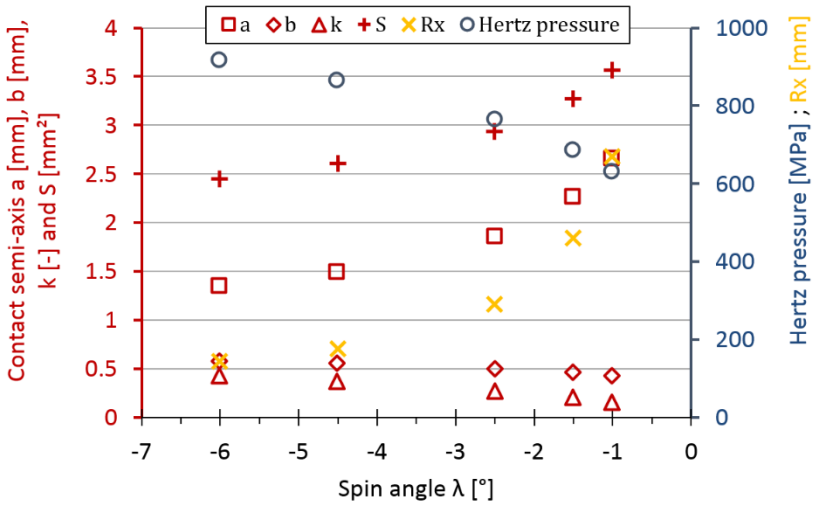


*Figure 4.1-2 – Curvature radius, contact dimensions, ellipticity ratio, contact surface and Hertzian pressure of the friction reference case but for various spin angles λ*

The results presented above on TOP dry static contact are preliminary results to the TOP EHD contacts. It was demonstrated how the spin angle drives the Hertz pressure, the contact dimensions and thus the contact surface. As the bodies' geometry make the study more complex, this analysis under static conditions will help to understand the physics which is involved in the following.

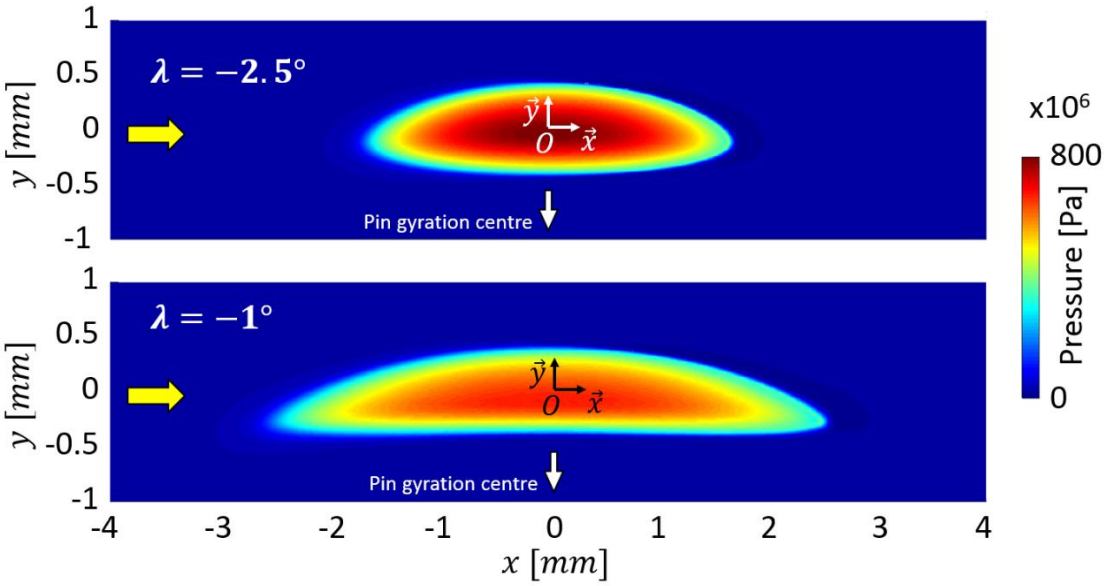


*Figure 4.1-3 - EHD pressure fields for $SRR_{x,0} = 0\%$ and $\lambda = -2.5°$ (top) and $\lambda = -1°$ (bottom) - all other parameters are the ones of the friction reference case*

When a piezoviscous lubricant and an entrainment velocity are involved in these contacts, a hydrodynamic pressure replaces the solid-solid contact pressure. Figure 4.1-3 shows the

pressure distribution in two TOP EHD contacts. At the larger values of $|\lambda|$, the pressurised area has a similar shape to the one of the dry static EHD contact (see Annexe B) similar to an ellipse: it becomes similar to a bent ellipse for the lower values of $|\lambda|$. Moreover, the pressure maximum is larger for the larger values of $|\lambda|$.

To investigate with more details the pressure fields, Figure 4.1-4 presents pressure profiles along the x-direction and y-direction for different TOP contacts. In the left graph of this figure, the global shape of the pressure fields is classical, with a gradually increasing pressure at the inlet (left) and a pressures spike occurring just before the outlet (right) and its sudden pressure drop.

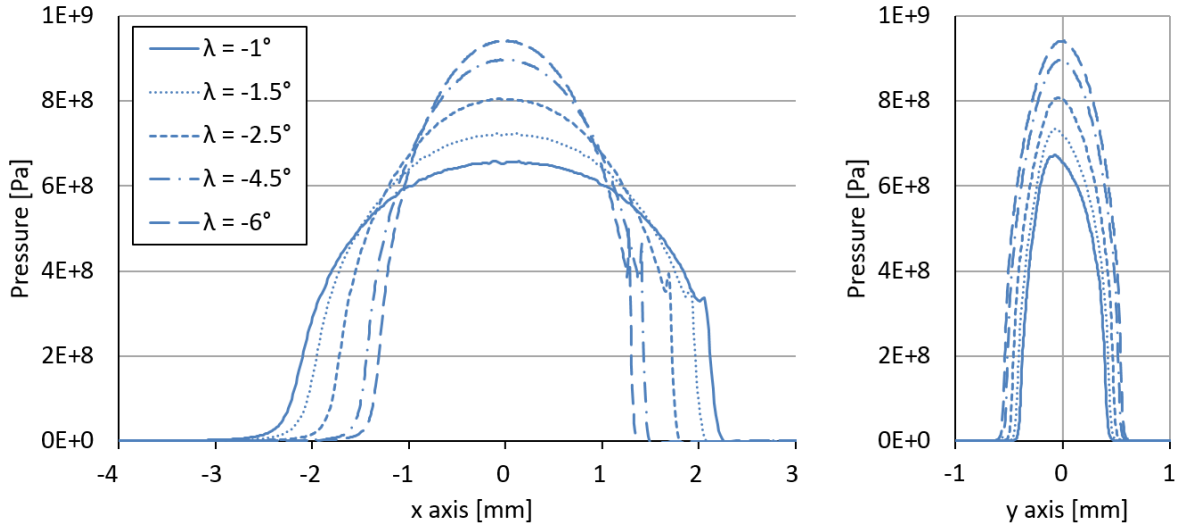


*Figure 4.1-4 - EHD contact pressure profiles along x axis (left) and y axis (right), for the friction reference case (with $\lambda = -2.5°$) and its declinations for other spin angles*

Similarly to the Hertz pressure, the EHD pressure varies when the spin angle changes. The EHD pressure is larger for the large values of $|\lambda|$, as the same load is transmitted from one solid to another through a smaller surface (see Figure 4.1-2). The pressure sum is unchanged for the 5 configurations presented in Figure 4.1-4: Equation 2.1-23 insures this. Because the curvature of the gap changes with $\lambda$, the pressure field changes as a consequence.

Figure 4.1-4 also presents a dissymmetry of the pressure field for the low $|\lambda|$ configurations. Indeed, along the $y$ axis (right graph), the pressure field is not symmetrical relatively to the $y = 0$ point on the $x = 0$ line when $|\lambda|<4.5$. This unusual behaviour obviously finds its origin in the asymmetry of one or more driving EHD parameters, which are here non-symmetrically distributed:

- the entrainment velocity field,
- and the rigid gap shape.

The entrainment velocity is modified by the spin (as shown in Figure 1.1-5). However, it is known that the pressure field is hardly affected by the spin in both circular spinning contacts

(see Doki-Thonon's thesis (5)) and elliptical spinning contacts (see Dowson et al. (29) and also Yang and Cui (30)) when the rotation axis is set along the major axis of the ellipse. In TOP for FREC case, the rotation axis is set along the minor axis of the TOP contact. The spin may have an influence in this case. Colin et al. (9) studied the TOP FREC contact but they used an EE contact to model it: they stated that the pressure field became asymmetrical because of the spin.

Likewise, the rigid gap between the solids is not symmetrical. It is not possible to identify this on the rigid gap along the $y$ axis: the curvature radius in the $y$ direction is constant and equal to the principal curvature radius, that is to say $R_y = r_t$. There is no asymmetry along this axis. However, the principal curvature radius $R_x$ in the other direction is a very local value: it is the curvature of the gap along the $x$ direction, at the $(x, y) = (0,0)$ point. But the curvature of the gap in the $x$ direction varies all over the contact area. For the $\lambda = -1°$ case, the local curvature radius in the $x$ direction, $R_{local}$, was plotted over the contact area in Figure 4.1-5. This radius can be defined by:

$$\frac{1}{R_{local}} = \frac{\partial^2 h_{rigid}}{\partial x^2} \qquad \textit{Equation 4.1-2}$$

with $h_{rigid}$ the rigid gap between the torus and the plane.

The plot of $R_{local}$ shows that the curvature varies in the range $0.3 \leq R_{local} \leq 1.6\, m$ inside of the contact area. Besides, on the $(x; y) = (0; 0.42)$ point, the curvature ratio $R_{local}/R_y$ is four times smaller than on the $(x; y) = (0; -0.42)$ point. These two points are located at the limits of the contact along the $y$ axis. This variation of $R_{local}$ may have an influence on the pressure: it is known from Lubrecht and Venner (63) that when $k < 1$ decreases (that is to say $R_y$ decreases and/or $R_x$ increases), a higher pressure can occur.

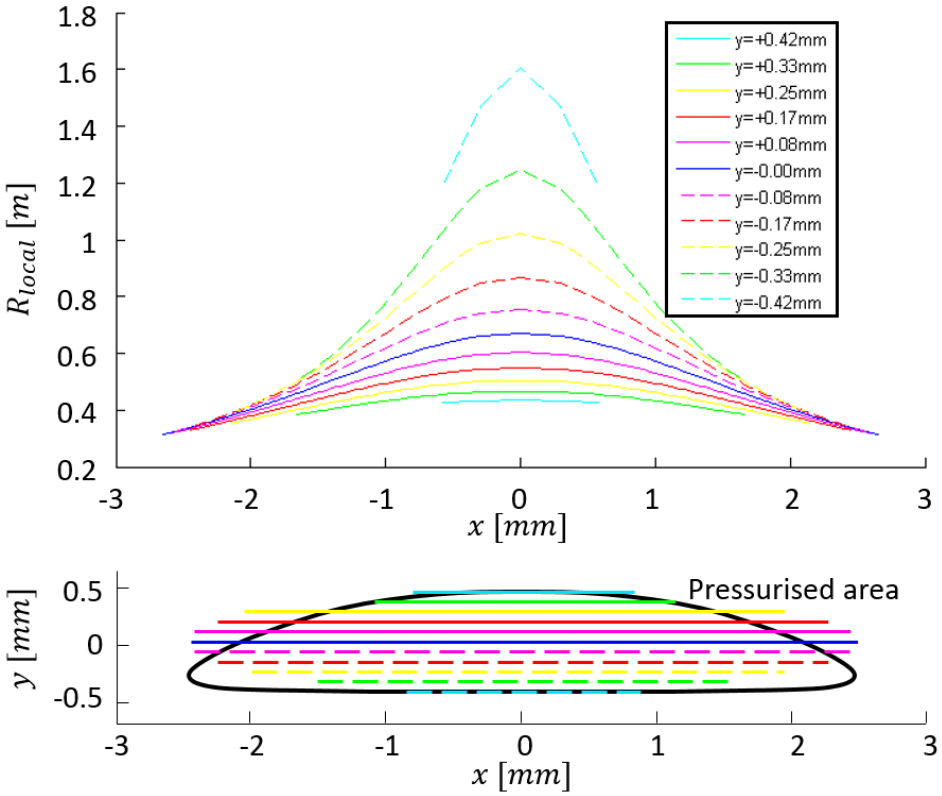


*Figure 4.1-5 – Top: Local curvature radius in the x direction and along several lines, from one side of the contact ($y = 0.42\ mm$) to the opposite side ($y = -0.42\ mm$) – Bottom: Representation of the lines along which the curvature radius is obtained – For the friction reference case but with $\lambda = -1°$*

It is now established that both the spinning kinematic and the bodies' geometry are likely to influence the TOP pressure field. In order to identify and distinguish the role of each of them, the numerical model was used to run virtual investigative simulations: with and without the spinning component of the velocity field, and also with the real TOP gap and with the EE one. These simulations did not aim to reproduce a possible experiment: as inherent components of the actual contact are numerically activated and deactivated, they should allow for uncoupling the mechanical effects and assessing their respective influence.

Based on the friction reference case with $\lambda = -1°$ and $SRR_{x,0} = 0\%$ (Table 3.3-1), four investigative simulations (IS) were run. The first one is the realistic case, "TOP with spin": the real TOP gap is represented and the spinning kinematic is activated. The second is similar to the first one, but the spinning kinematic is deactivated ($\Omega_b = 0$); it is called "TOP without spin". The third one corresponds to the EE of the first case, with the same spinning kinematic

("EE with spin"). The last one is the EE in which the spinning kinematic is not activated ("EE without spin"). A summary of these IS is presented in Table 4.1-1.

| | **Real TOP gap** | **EE gap** |
|---|---|---|
| **With spinning kinematic** | IS1: TOP with spin | IS3: EE with spin |
| **Without spinning kinematic** | IS2: TOP without spin | IS4: EE without spin |

*Table 4.1-1 - The four investigative simulations, IS1 to IS4*

The computation of the four IS did not present any particular problem. In Figure 4.1-6, the pressure fields are plotted together with the entrainment velocity streamlines that enter the pressurised area at first. Both IS1 and IS2 pressurised areas have the curved ellipse shape, whereas IS3 and IS4 have an elliptical shape. The streamline which enters the pressurised area at first is plotted on each graph: because the contact shape changes, the position of this streamline is different. The streamlines are curved when the spinning kinematic is activated (IS1 and IS3) but they are straight when it is deactivated. This streamline has a specific influence on the pressure distribution that will be explored. It also has and influence on the film thickness that will be detailed in section 4.1.2.

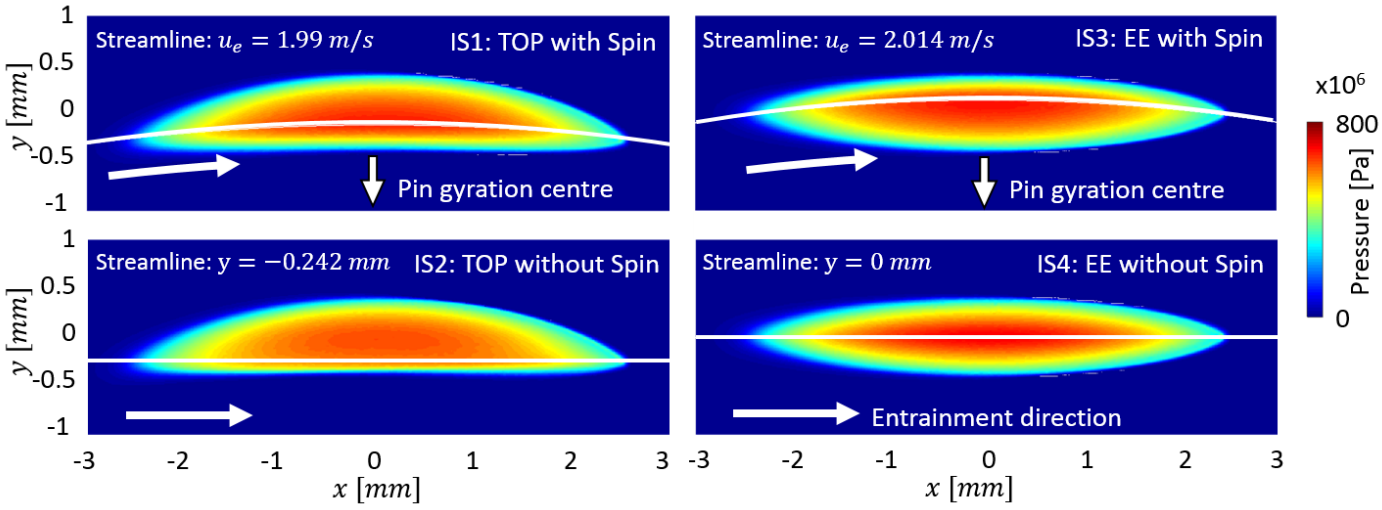


*Figure 4.1-6 - The four investigative simulations: pressure fields and their inlet streamlines, friction reference case with λ=-1° and SRR_(x,0)=0%*

Even if the bodies' shape is identical in the IS1 and IS2 configurations, the pressure distributions are not the same: the spinning kinematic has a role in the pressure distribution. Similarly, even if the entrainment velocity field is the same in IS1 and IS3, the pressure distribution is different: the pressurised area shape is different, and also the maximum pressure is in the $y < 0$ side for IS1 but in the $y > 0$ side for IS3 (see Figure 4.1-7 for more

details). At this stage, it is demonstrated that both the spinning kinematic and the bodies' shape influence the pressure distribution.

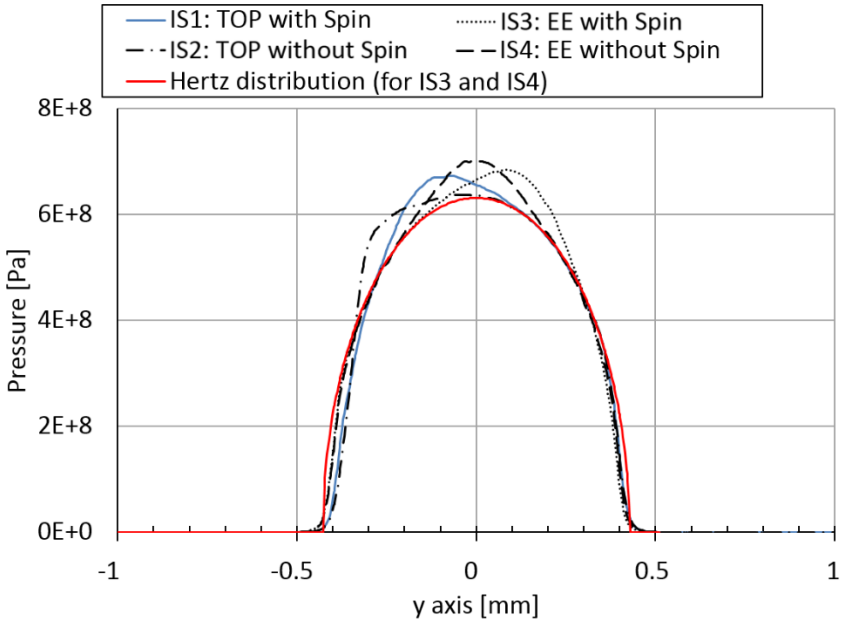


*Figure 4.1-7 - Comparison of the pressure profiles along the $y$ axis and x=0 for the four IS, the Hertz distribution was calculated for the elliptical configurations*

In Figure 4.1-7, the pressure profiles are plotted at x=0 along the $y$ axis. The IS1 curve is the same than in the Figure 4.1-4 (for $\lambda = -1°$). The four curves are all different from one another, and apart from the symmetrical case IS4, there is no obvious reason to attribute one distribution to a specific IS configuration. Indeed, IS4 has a symmetrical entrainment velocity field and a symmetrical gap: the resulting pressure field has to be symmetrical. It presents a prominence relatively to the Hertz distribution which is symmetrical.

It is noticeable that IS1 and IS2 distributions are non-symmetrical: they present a prominence relatively to the Hertz distribution which is located on the $y < 0$ side. The IS2 prominence is more shifted towards $y$ negative values than the IS1 one. The two contacts have in common the same non-symmetrical distribution of $R_{local}$ (local curvature radius of the gap, along the $x$ direction) presented in Figure 4.1-5: $R_{local}$ is larger in the $y < 0$ side than in the $y > 0$ side. According to Venner and Lubrecht (63), in slender elliptical contacts, when the principal curvature radii ratio $R_y/R_x$ becomes small, the maximum pressure rises. Moreover, they showed that the pressure distribution along the $y$ axis adopts a triangular-like shape which is detectable for IS4 in Figure 4.1-7. In the configurations of their study, the curvature radii were constant all over the contact area. Here, it is not the case for IS1 and IS2. But still, the pressure distribution seems influenced by the curvature variation of the gap, and the pressure prominence observed by Venner and Lubrecht in slender elliptical contacts was somehow transferred from the central position to the side where the ratio $R_y/R_{local}$ was the smallest ($y < 0$). To summarise this paragraph: the gap curvature of the TOP contact has an influence on the

pressure distribution, it shifts the pressure prominence toward the side where $R_y/R_{local}$ is the smallest. **This shift is called here the asymmetric gap curvature shift**.

Despite their common gap shape and their prominence in the $y < 0$ side, IS1 and IS2 do not have the same pressure profile. IS1 has a larger maximum pressure, which is quite local, whereas IS2 pressure field is more regularly allocated and its prominence is more shifted. This means that the spinning kinematic also has a role in the pressure distribution of the TOP EHD contact: it contributes to define the location of the prominence. In order to identify this role, a comparison is made between IS3 and IS4. The former also has a prominence, located in the $y > 0$ region, whereas the prominence of the latter is located at $y = 0$. However, they both have constant curvature radii. This means that the entrainment velocity field tends to shift the prominence. The shift due to the kinematic field is toward the lateral contact boundary which is the closest from the inlet streamline. IS3 shows a prominence shift toward the positive values of $y$ comparing to IS4 which has no spin. Similarly, IS1 has a prominence which is shifted toward $y > 0$ relatively to the IS2 prominence. **This shift is called here the asymmetric kinematic shift.**

The origin of this kinematic shift can be found in the entrainment velocity field. The streamline that crosses the inlet at first is plotted in Figure 4.1-6. It is called here the inlet streamline whereby the firstly pressurised lubricant is conveyed. Indeed, as soon as the lubricant enters the EHD pressurised area, the fluid Poiseuille flows are annihilated by the fluid colossal viscosity and its sub-micrometric confinement. Without any opportunity to escape the compression it endures, the highly viscous fluid follows the Couette flows, which are entrainment velocity driven. The only possibilities for the fluid to get away from the confinement before the outlet are towards the contact sides: the closer the sides are from the inlet streamline, the easier for the lubricant to flow away. When this lubricant escapes, the film thickness locally decreases and the pressure on the sides is smaller. Therefore the pressurised area neighbouring the contact outside carries a smaller load. As a consequence, the total load is mainly transmitted through the central pressurised region, where the pressure rises. This is the origin of the prominence.

Additionally, when the spinning kinematic is introduced in slender contacts (cases IS1 and IS3), the inlet streamline is curved and becomes closer to the side which is located far from the pin rotation axis. On this side the lubricant will flow out more easily as the conveyed lubricant is closer to the contact side. The pressurised area then diminishes on this side, and the remaining lubricant endures a larger pressure. On the other side, the pressure decrease between the prominence and the exit happens on a larger distance and the pressurised area diminishes less. Consequently, the prominence does not happen on this side. This asymmetry of the flow is the origin of the prominence shifted position called the **asymmetric kinematic shift**.

For its part the asymmetric gap curvature shift has another origin. A prominence is observed in slender elliptical EHD contacts. Lubrecht and Venner (63) showed that the more the contact is slender the more the prominence is obvious. In other words, the more $k \sim R_y/R_x$, the ellipticity ratio is low, the more the pressure prominence is large. Yet, in TOP contact, this ratio locally varies as $R_x$ varies, as presented in Figure 4.1-5. This ratio is lower on the $y < 0$ side of

the contact than on the other side: consequently the $y < 0$ side has a favourable context for a larger prominence than the other side. Therefore, the prominence observed by Lubrecht and Venner (63) appears on this $y < 0$ side: it is the cause of the **asymmetric gap curvature shift**.

With the **asymmetric gap curvature shift** and the **asymmetric kinematic shift**, the pressure prominence (relatively to the Hertz distribution) location changes. It is particularly visible in Figure 4.1-7. This location explains the values of the pressure maxima: in IS4, the prominence is located at $y = 0$. It is exactly where the classical EHD pressure maximum usually is and it represents the largest value among the four IS. For IS1 and IS3, the prominence is shifted respectively at $y = -0.1\ mm$ and $y = 0.1\ mm$. On these locations the prominence is less large than for IS4. At last for IS2, the shift is hard to locate on the pressure distribution, but according to its inlet streamline, the prominence should be at $y = -0.24\ mm$. At such a distance from the contact centre, the pressure prominence is rather small and is not even able to form a local maximum. At this point, it is important to notice that IS1 and the other IS do not produce identical results even if these results are similar. For instance, it is not possible to use an EE (as in Colin et al. (9)) to model the detailed behaviour of this TOP spinning contact.

According to the idea that the inlet streamline influences the contact, it is interesting to check whether the pressure distributions of the four IS show a similar shape or not along these streamlines. These distributions are plotted in Figure 4.1-8. The main difference between them is their maxima: this difference is also visible in Figure 4.1-7. The four IS curves show a similar trend. The IS3 profile is slightly different: it starts and finishes closer from the contact centre, due to the slightly smaller length of its inlet streamline inside the pressurised area.

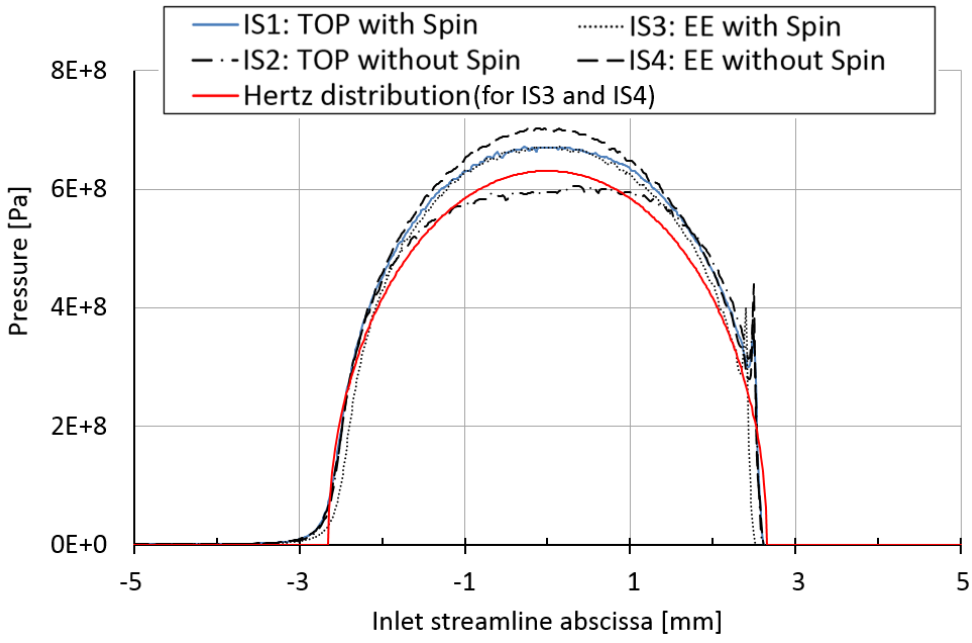


*Figure 4.1-8 - Comparison of the pressure field in the four IS, along their respective inlet streamlines.*

From these four IS, one can deduce that the pressure prominence of the classical slender elliptical contact was shifted toward the $y < 0$ region by the larger curvature radii $R_{local}$ which are present on this side. The same prominence was deviated toward the $y > 0$ side by the presence of spinning kinematic because the inlet streamline was closer to the contact side in this region.

It is now established that the spin angle $\lambda$ has an influence on both the EHD pressure distribution and its maximum. As the pressure gradients drive film thickness, the relationship between $\lambda$, the pressure field, and the film thickness will be investigated in the next section.

### 4.1.2. Influence on film thickness

Similarly to the previous section, when the spin angle is varied, one expects variations of the film gap. Indeed, the velocity field, the gap shape and the pressure distribution are influenced by $\lambda$. In Figure 4.1-9, two variations of the friction reference case are presented: the one at the top is the exact friction reference case for $SRR_{x,0} = 0\%$ (and $\lambda = -2.5°$) and the one at the bottom is the same, but for $\lambda = -1°$. Other simulations were run: the spin angle range was the same than in Equation 4.1-1.

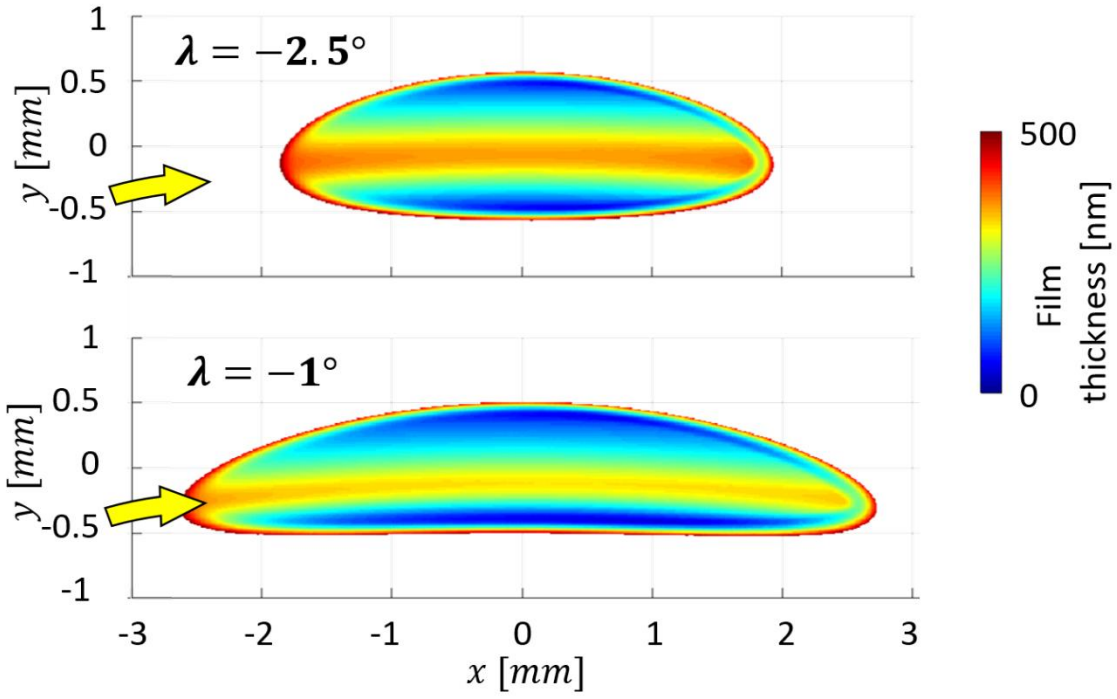


*Figure 4.1-9 - Film thickness distribution of the friction reference case, at $\lambda = -2.5°$ (top) and $\lambda = -1°$ (bottom) and for $SRR_{x,0} = 0\%$*

Several parameters change when $\lambda$ changes. When $|\lambda|$ diminishes, $R_x$ (the curvature radius along the $x$ direction) increases together with $a$, but $b$ decreases. As a consequence, the ellipticity ratio, $k = b/a$, decreases as shown in Figure 4.1-2. These parameters are addressed

at first to the dry static contact, but they also apply to the EHD contact. In Figure 4.1-9, the film thickness distribution is more elongated for $\lambda = -1°$ than for $\lambda = -2.5°$, and both are very characteristic of the slender contacts (see chapter 2). Moreover, the bending of the TOP gap is more visible in the $\lambda = -1°$ case.

When $\lambda$ varies, one expects the film thickness to vary widely as the ellipticity ratio has a significant influence on minimum film thickness (see chapter 2). Figure 4.1-10 presents the variations of $h_c$, $h_{m,c}$, $h_{m+}$ and $h_{m-}$ according to $\lambda$. The numerical values presented here are the ones of the $SRR_{x,0} = 0\%$ case.

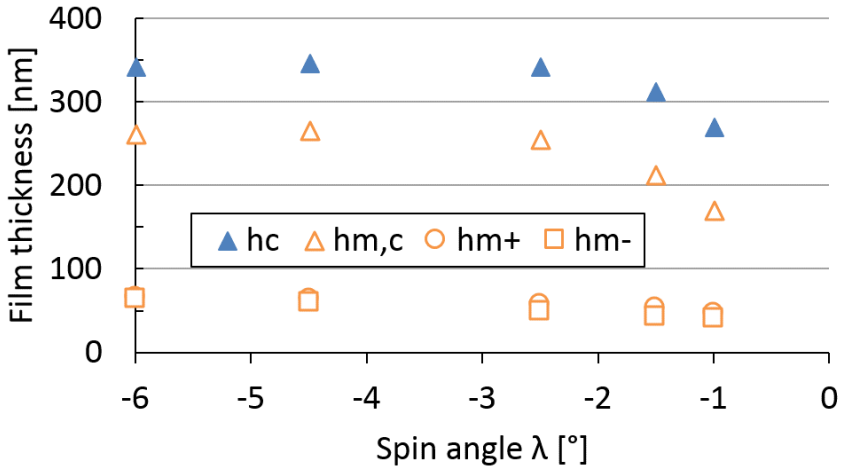


*Figure 4.1-10 –Film thicknesses for the friction reference case, with varying spin angle and $SRR_{x,0} = 0\%$ – numerical results*

The variations of the film thickness are not very large in Figure 4.1-10, but the main change occurs for low $|\lambda|$. When the spin angle is close to 0°, film thickness clearly decreases. Between $\lambda = -6°$ and $\lambda = -1°$, the central film thickness $h_c$ decreases by 21%, the minimum film thickness along central line $h_{m,c}$ by 35% and $h_{m+}$ and $h_{m-}$ by respectively 31% and 36%. The film thickness drop can be explained by the contact geometry change. When $|\lambda|$ decreases, the TOP contact becomes more slender ($k = 0.43$ for $\lambda = -6°$ and $k = 0.161$ for $\lambda = -1°$), and the film thickness decreases.

A comparison can be made between these EHD conditions and the ones presented in chapter 2, in the slender elliptical configurations of the $u_e = 2\ m/s$ and $w = 800\ N$ case. The curvature radii and the entrainment conditions are very similar but the load and the viscosity at ambient conditions differ. In the case of purely elliptical contacts, when $k < 1$ decreases, the film thickness decreases as well: between $k = 0.5$ and 0.2, $h_c$ and $h_{m,c}$ decrease by 22% and $h_{m,l}$ by 65%. Note that the minimum film thickness reduction on the sides is very large in the purely elliptical case because the $R_y$ radius was reduced together with the increase of $R_x$, which is not the case for the TOP contacts. In the elliptical case, it was demonstrated that the

side flow increase is responsible for the minimum film thickness reduction when $k < 0$ decreases. The same mechanism is involved in the TOP case.

Similarly to the pressure field, the film thickness has no $y = 0$ symmetry axis as there is a difference between $h_{m+}$ and $h_{m-}$. For all spin angles represented in Figure 4.1-10, $h_{m+}$ is between 20% and 6% larger than $h_{m-}$. This relative difference is larger than the relative error which is about 6% according to the difference between experimental and numerical results presented in section 3.3.2. This is a characteristic result of the spinning contact in which the kinematic is not symmetrical. The entrainment velocity is higher on the $h_{m+}$ contact side than on the $h_{m-}$ border (by about +5 to +10%), and a larger film thickness on the $h_{m+}$ side is expected. Indeed, the $h_{m+}$ side is the closest from the disc rotation axis, but the furthest from the pin rotation axis (see Figure 3.1-5). However, this entrainment velocity difference is not very large, which explains the relatively low deviation between the minima.

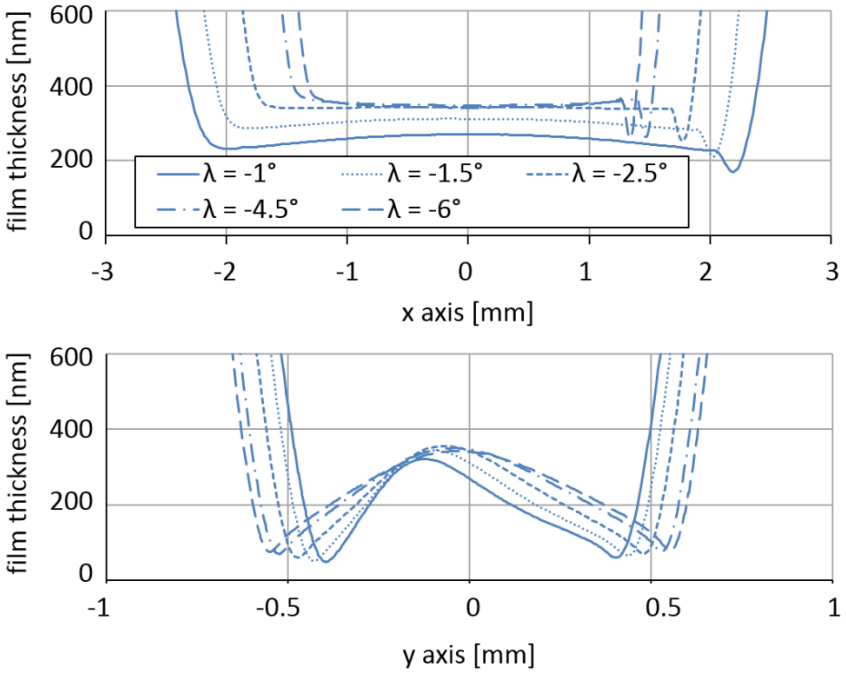


*Figure 4.1-11 - Film thickness along the main axes of the EHD TOP friction reference case and for various values of the spin angle and for $SRR_{x,0} = 0\%$*

However, the film thickness asymmetry that was observed in Figure 4.1-9 and Figure 4.1-10 is presented with more details in Figure 4.1-11. In the bottom graph, when $|\lambda|$ decreases, it is visible that the film minima decrease, that their position is shifted toward $x$ axis, but also that the film thickness in between is also asymmetrical. The film thickness maximum is located at $y = -0.15\ mm$ for $\lambda = -1°$ and at $y = 0\ mm$ for $\lambda = -6°$, and monotonously moves from one position to the other for the intermediate spin angles. Nevertheless, this maximum observed in Figure 4.1-11 (at the bottom) does not vary as much as $h_c$: they are located in different places of the contact and the $h_c$ reduction in Figure 4.1-10 is more due to the shift of the gap maximum than to an actual global decrease of the film thickness.

Similarly to section 4.1.1, the origin of such a film thickness maximum shift (visible in Figure 4.1-11, at the bottom) is investigated. As the strongest shift occurs for $\lambda = -1°$, this case will be studied: the role of the spinning kinematic and the TOP gap curvature will be highlighted. The same four IS are used here, but it is now their film separation which is analysed. Figure 4.1-12 presents IS1 to IS4 film thickness distributions together with the inlet streamlines. These streamlines are the same than in Figure 4.1-6, and they do enter the pressurised area at first.

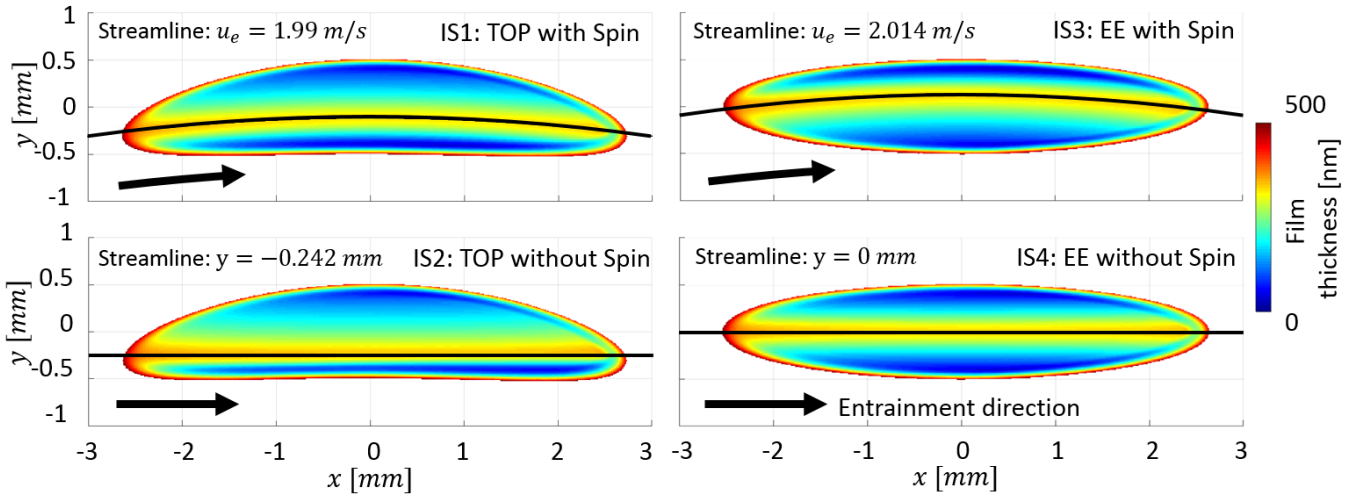


*Figure 4.1-12 - The four investigative simulations IS ($\lambda = -1°$): the film thickness distributions at $SRR_{x,0} = 0\%$ and their inlet streamlines*

The outline of the EHD contact area is elliptical and a curved ellipse for respectively the EE and the TOP cases, as in Figure 4.1-6. When there is no spin, the iso-thickness lines located in the pressurised area follow the inlet streamline (see IS2 and IS4 in Figure 4.1-12): indeed, the lubricant which enters the pressurised area only flows according to the entrainment velocity until it exits the pressurised area. Therefore, when spin is activated, the spinning kinematic tends to bend the iso-thickness lines according to the entrainment velocity field bending (see IS1 and IS3 in Figure 4.1-12). Whether the spinning kinematic is activated or not, whether the gap is the one of a TOP contact or an EE, the lubricant follows the inlet streamline.

In the four IS, the same scenario is repeated. The top graph in Figure 4.1-13 represents the film thickness along the respective inlet streamlines of the different IS configurations. They have the same slope at the inlet and they have nearly the same value in the central region: there is just IS3 which is a little shorter along the $x$ direction. The similarities between the different curves draw again the attention toward the key role of the inlet streamline. It is clearly along the inlet streamlines that the highly viscous fluid is mainly conveyed. Whatever the contact shape or the kinematic, the streamline has the same role toward the lubricant. This affirmation can be, however, tempered by the heat or shear thinning effects which are driven by the kinematic and may have an influence and counterbalance the streamline role. These effects will be introduced later, in section 4.2. There is also another limit to this statement: if the inlet streamline exits the contact before having crossed the whole contact length, the consequences

can be dramatic on film thickness: the inlet streamline will stop conveying the lubricant in the contact and accelerate its premature exit. Section 4.3.2 explains this case with more details.

Along the transverse direction, the film thickness profile is quite different in the four IS. IS4 is the only one which is symmetrical: indeed, none of its driving parameters introduces an asymmetry. In particular, the inlet streamline is superposed with the $x$ axis. The other film thickness curves are shifted similarly to their respective pressure profiles, showed in Figure 4.1-7. Indeed, in section 4.1.1, it was demonstrated that the TOP gap tends to shift the maximum pressure towards the negative values of $y$ in the present configuration. This is also the case for IS1 and IS2 film thickness maxima which are on the left side of the IS3 and IS4 maxima. Besides, it was also demonstrated that the spinning kinematic tends to shift the maximum pressure towards the positive values of $y$ (in the present kinematic configuration). In terms of film thickness, this trend is also verified: IS1 and IS3 film maxima are on the right of, respectively, IS2 and IS4 ones.

The positions of the inlet streamlines along the $y$ axis are also represented. The orange marks show that the inlet streamline of each IS is very close to the maximum thickness region. These two graphs show the key role played by the inlet streamlines. It also strongly demonstrates the role of the principal curvature radius $R_x$ which is the only gap shape common denominator between the four IS. Indeed, the IS3 and IS4 have a single curvature radius along the $x$ direction (see Equation 2.1-21), whereas the IS1 and IS2 cases have a continuously varying rigid gap curvature (see Figure 4.1-5). Moreover, the presence or the absence of spinning kinematic changes the rigid gap curvature along the inlet streamline. However, even if the kinematic changes and even if the gap curvature varies strongly, the key radius that drives the film forming is still a very local value: $R_x$ (together with $R_y$).

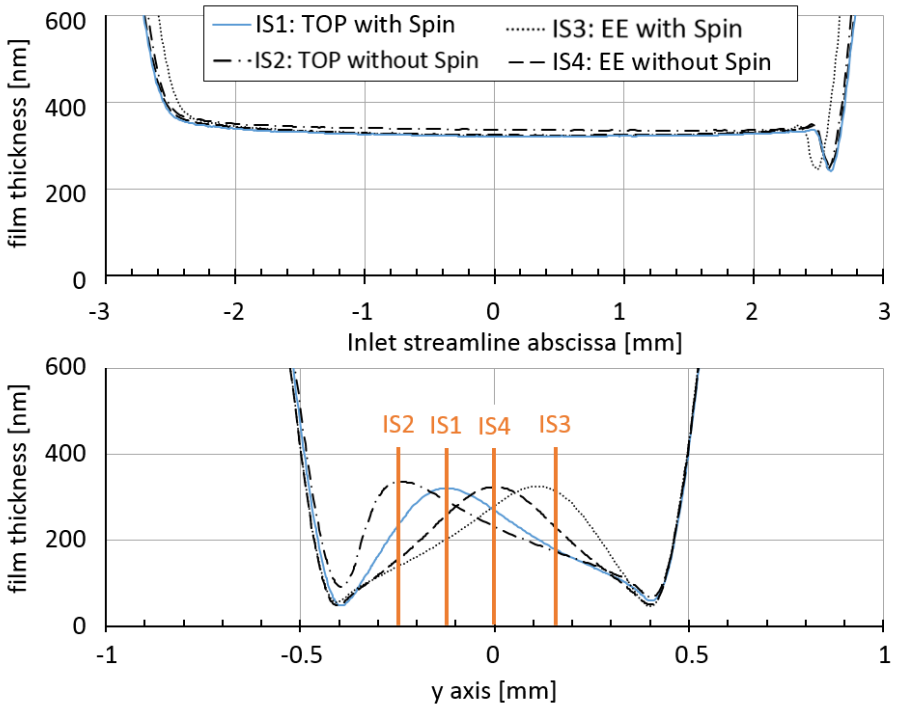


*Figure 4.1-13 - Film thickness profiles for the four IS ($\lambda = -1°$), along their inlet streamlines (top) and along the y axis at x=0 (bottom). The orange marks show the position of the streamlines.*

In the bottom graph of Figure 4.1-13, the minima and the maximum inside the contact are very similar between the curves. There is only the IS2 minimum at the $y < 0$ side which differs from the other minima. This might be explained by the proximity of its maximum film thickness with the contact side. Apart from this specific case, the similarity of the gap minima underlines the key role of $R_y$ in the lateral minimum film thickness. Even if the kinematic changes, even if the gap curvature changes in the $x$ direction, the principal curvature $R_y$ still drives the minima and the maximum of the film thickness together with $R_x$.

In this section, it was demonstrated that the spin angle has an influence on the film thickness distribution. When $|\lambda|$ becomes smaller, the minima of the film thickness decrease together with $h_c$ and $h_{m,c}$. However, the maximum of the film thickness along the $y$ axis (and between the two minima) remains rather constant. Comparing to the other IS, IS1 gives similar results on the characteristic values of the film thickness: it is mainly the location of these characteristic values which changes. This means that the TOP spinning contact can be modelled by a simplified model, but the actual behaviour of the contact would be partially predicted.

### 4.1.3. Influence on friction

The friction reference case described in Table 3.3-1 is used here again. The experimental and numerical friction results will be compared to the ones of other contacts, with various spin angles. Experimental data are here more representative of the industrial conditions, but the spin angle range of the specimen is limited to $\lambda = [-4.5°; -2.5°]$.The numerical friction

coefficient was computed for various $\lambda$ values, but the values obtained are only orders of magnitude.

In Figure 4.1-14, the friction coefficients ($C_{fx}$) are presented according to $SRR_{x,0}$, and the numerical and experimental data are gathered. The numerical results show that, under any sliding condition, the larger $|\lambda|$, the larger $C_{fx}$. This trend is confirmed in Figure 4.1-15, under various entrainment ($u_e = 1, 2$ or $4\ m/s$) and sliding conditions.

In Figure 4.1-14, and for large sliding conditions ($|SRR_{x,0}| > 30\%$), the numerical friction coefficient computed for $\lambda = -6°$ becomes slightly smaller than the one for $\lambda = -4.5°$. However, as these results are only orders of magnitude and can, at best, reveal trends, this particularity will not be investigated. A similar trend can be nevertheless observed in experimental results: the graph at $u_{ex,0} = 4\ m/s$ in Figure 4.1-15 shows the friction coefficients for $\lambda = -2.5°$ and $-4.5°$ becoming identical.

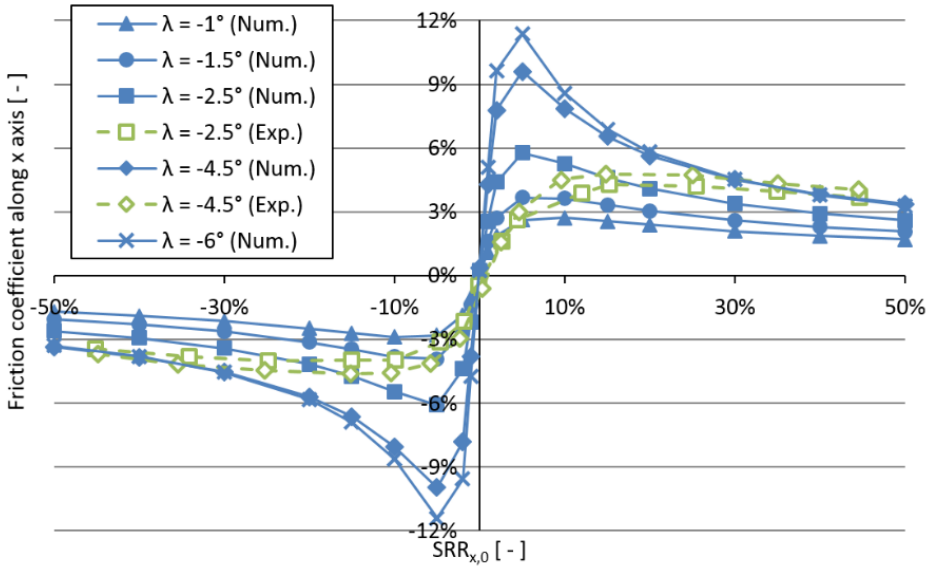


*Figure 4.1-14 - Spin angle influence on friction: experimental (Exp.) and numerical (Num.) analysis for $u_{ex,0} = 2\ m/s$, $p_h = 600\ MPa$ for $\lambda = -1°$ and $p_h = 900\ MPa$ for $\lambda = -6°$*

To understand the causal link between the spin angle $\lambda$ and the friction coefficient, one shall refer to Figure 4.1-2. As presented, $\lambda$ drives the Hertz pressure but it drives the EHD pressure. Table 4.1-2 presents the different contact parameters including the Hertzian and EHD pressures for each spin angle case. Contradictory effects intervene and the numerical values involved are summarised in Table 4.1-2. Firstly, when $|\lambda|$ decreases, the Hertzian and the EHD pressure decrease. This should lead to a decrease of the friction coefficient. Secondly, the contact surface increases when $|\lambda|$ decreases. Consequently, the sheared surface increases which may increase $C_{fx}$ with the decrease of $|\lambda|$. Among these two potential effects, it is not straightforward to identify the parameters which actually drive the friction.

However, to conclude on the different phenomenon that may influence friction, the viscosity integral over the contact area was computed and presented in Table 4.1-2. This calculation presents the viscosity sum for the $SRR_{x,0} = 5\%$ case. It clearly shows that the outcome of the different contradictory effects is a $C_{fx}$ rise when $|\lambda|$ increases.

| $\boldsymbol{\lambda}$ [°] | Hertz pressure [MPa] | EHD max. pressure [MPa] | Contact ellipticity $\boldsymbol{k}$ [ − ] | Contact surface $[mm^2]$ | $\iint_S \mu\, dS$ [Pa.s.m²] for $SRR_{x,0} = 5\%$ |
|---|---|---|---|---|---|
| −1 | 631 | 675 | 0.161 | 3.6 | 0.0038 |
| −1.5 | 687 | 735 | 0.204 | 3.3 | 0.0091 |
| −2.5 | 765 | 808 | 0.272 | 2.9 | 0.0251 |
| −4.5 | 864 | 903 | 0.372 | 2.6 | 0.0720 |
| −6 | 916 | 942 | 0.43 | 2.5 | 0.1131 |

*Table 4.1-2 - Friction key parameter variations with the spin angle, for $u_{ex,0} = 2\ m/s$ and $SRR_{x,0} = 0\%$*

To summarise, in our conditions the spin angle has an important influence on friction as it drives the contact pressure and consequently the lubricant viscosity. When $|\lambda|$ decreases the pressure decreases as well, and the friction coefficient is smaller.

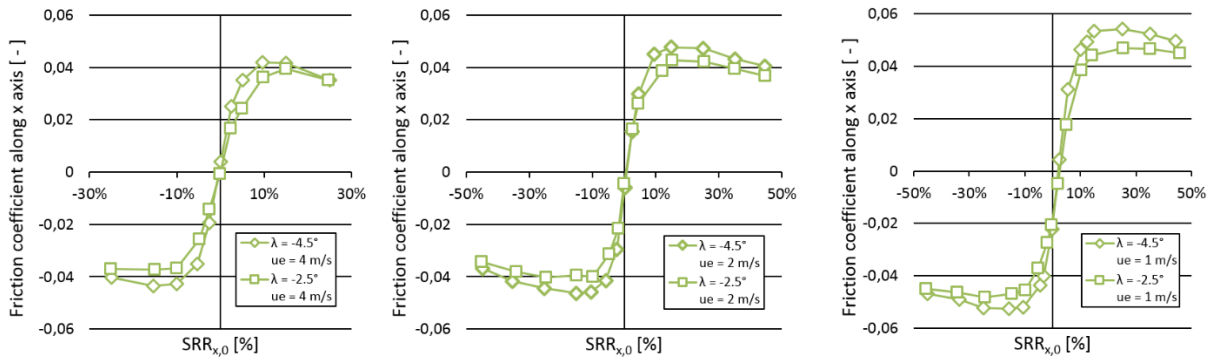


*Figure 4.1-15 - Entrainment velocity influence on friction: experimental results for two spin angles*

However, when $|SRR_{x,0}|$ increases, the friction coefficients of the different $\lambda$ configurations become closer and closer. This result is valid for all entrainment velocities and for both numerical and experimental results. This can be attributed to the thermal effects. Because of the high sliding, more energy is dissipated into heat. This temperature rise decreases the lubricant viscosity and decreases the friction as a consequence. The sliding heating will be investigated in details in the next section.

In the effort to design optimised bodies' geometry and kinematic, the engineer must take into account the influence of the parameter $\lambda$ on pressure, friction and film thickness. For all other parameters kept constant, when $|\lambda|$ is decreased, the pressure maximum decreases, the

pressure distribution is modified, the fully flooded EHD friction is reduced and the film thickness decreases as well.

## 4.2. Influence of the sliding

In real FREC, the sliding is an omnipresent and constituent part of the contact. This section deals with the different physical mechanisms which are involved in the sliding. First of all, the sliding is the result of a velocity difference between two mating surfaces. An accommodation occurs through the lubricant shearing in the pressurised area. Despite the sliding, the surfaces are still fully separated in the conditions that will be described here.

The sliding produces friction, which is a force opposed to the relative motion: the product of this force by the sliding velocity is the power dissipated $P$ (or lost) in the contact. As a first approach, one writes:

$$P = w * C_{fx} * \Delta u_{x,0} + w * C_{fy} * \Delta u_{y,0} + T_z * (\Omega_t - \Omega_b) \qquad \textit{Equation 4.2-1}$$

with $\Delta u_{x,0} = u_{bx,0} - u_{tx,0}$ the sliding velocity along $x$ axis at the contact centre, $\Delta u_{y,0} = u_{by,0} - u_{ty,0}$ the sliding velocity along $y$ axis at the contact centre, and $T_z$ the friction torque in the contact.

The transverse dissipated power ($w * C_{fy} * \Delta u_{y,0}$) is non-existent in this formulation as $\Delta u_{y,0} = 0$. The local transverse friction is however included in the torque contribution to the power losses. In the Tribogyr contacts, the dissipated power can reach about $50\ W$ or more. This energy is transformed into heat, which has an influence on friction and film thickness.

### 4.2.1. Influence on friction

In order to investigate the effect of sliding on friction, the friction reference case was used here again. Other similar configurations were also experimentally explored: the entrainment velocity ($u_{ex,0} = 1; 2; 4\ m/s$), the load ($w = 400; 1500\ N$) and the spin angle ($\lambda = -2.5°; -4.5°$) were varied, resulting in 12 different configurations.

The friction coefficients of these 12 configurations are plotted against the $SRR_{x,0}$ in Figure 4.2-1. The graphs at the top correspond to $w = 1500\ N$ whereas the ones at the bottom to $w = 400\ N$. Similarly, the graphs on the left are at $\lambda = -2.5°$ and the ones on the right are at $\lambda = -4.5°$. On each graph, three entrainment velocities are plotted: $u_{ex,0} = 1; 2; 4\ m/s$.

According to what was explained in section 4.1.3 for $w = 1500\ N$, when $|\lambda|$ increases, the friction coefficient $C_{fx}$ increases. This is also valid at $w = 400\ N$, even if here the error bars are much larger than the ones at $w = 1500\ N$: at lower loads, the Tribogyr test-rig is more sensitive

to the parasitic oscillations induced by both the macro and micro flaws and imperfections of the many parts involved, including the two specimen. Despite the large error bars, the trend is clear: when $|\lambda|$ increases, the friction coefficient $C_{fx}$ increases: in the right graphs, $|C_{fx}|$ reaches larger values than in the left graphs, for the two loads considered, even if the friction is low comparing to EHD friction in general. The reasons are the same for the two load configurations; at larger $|\lambda|$, the contact pressure is larger, and therefore viscosity increases. In its turn, the friction is larger.

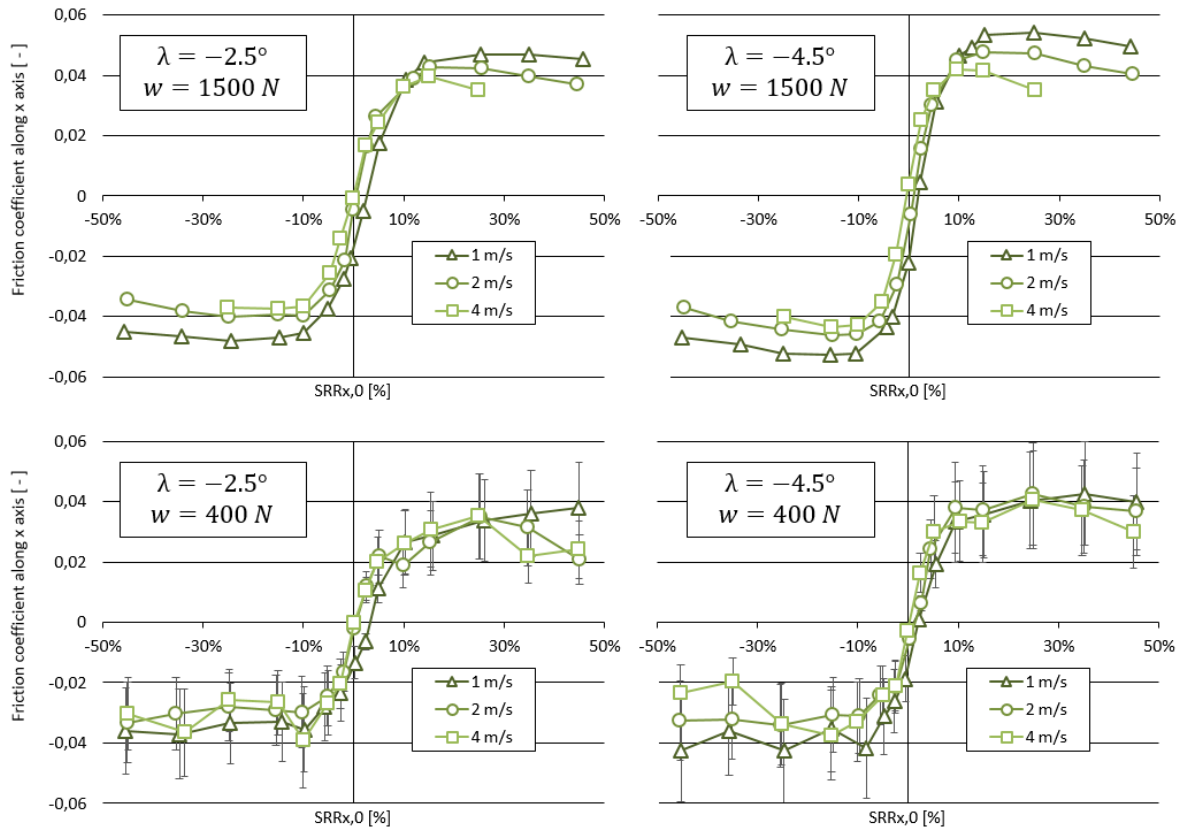


*Figure 4.2-1 – Experimental friction curves at various entrainment velocities: at $w = 1500\ N$ & $\lambda = -2.5°$ (top left); $w = 1500\ N$ & $\lambda = -4.5°$ (top right); $w = 400\ N$ & $\lambda = -2.5°$ (bottom left); $w = 400\ N$ & $\lambda = -4.5°$ (bottom right).*

For similar causes, the friction is larger at the largest load when the other parameters are kept constant: at larger load, the contact pressure is larger and the piezoviscous effects increase the viscosity. In its turn, the friction is increased. Indeed, in the bottom graphs, $|C_{fx}|$ remains inferior to 0.04, but in the top graphs, the $|C_{fx}|$ plateaus (*i.e.* the parts of the friction curves where the friction coefficient slope is close to zero) are all above 0.04.

Within the four graphs of Figure 4.2-1, the slope at the origin seems similar, independently from the entrainment velocity. However, it is not possible to ensure that they are equal: there are only a few experimental points in this so-called linear area, the error bars are quite large and allow a non-negligible variation of the slopes, even at $w = 1500\ N$, where the error bars

are about the size of the graph symbols. At last, it is not sure that the points are located close enough to the origin to actually represent the initial slope. However, even if they are probably not equal, they are similar. Surprisingly, it is not yet possible to fully explain the similarities between the different slopes at the origin.

In the $w = 1500\ N$ graphs and further from the origin (when $|SRR| > 15\%$), the curves show a significant difference. At this stage, the sliding is strong and the power dissipated within the few nanolitres of the contact becomes important. As it is a function of the sliding velocity $\Delta u_{x,0}$, this power and the friction coefficient are plotted against $\Delta u_{x,0}$ in Figure 4.2-2. With this way of plotting the friction coefficient, the different curves become closer after $|\Delta u_{x,0}| > 0.4\ m/s$. Whether the configuration is $\lambda = -2.5°$ or $-4.5°$, the friction curves tend to the same slope and value.

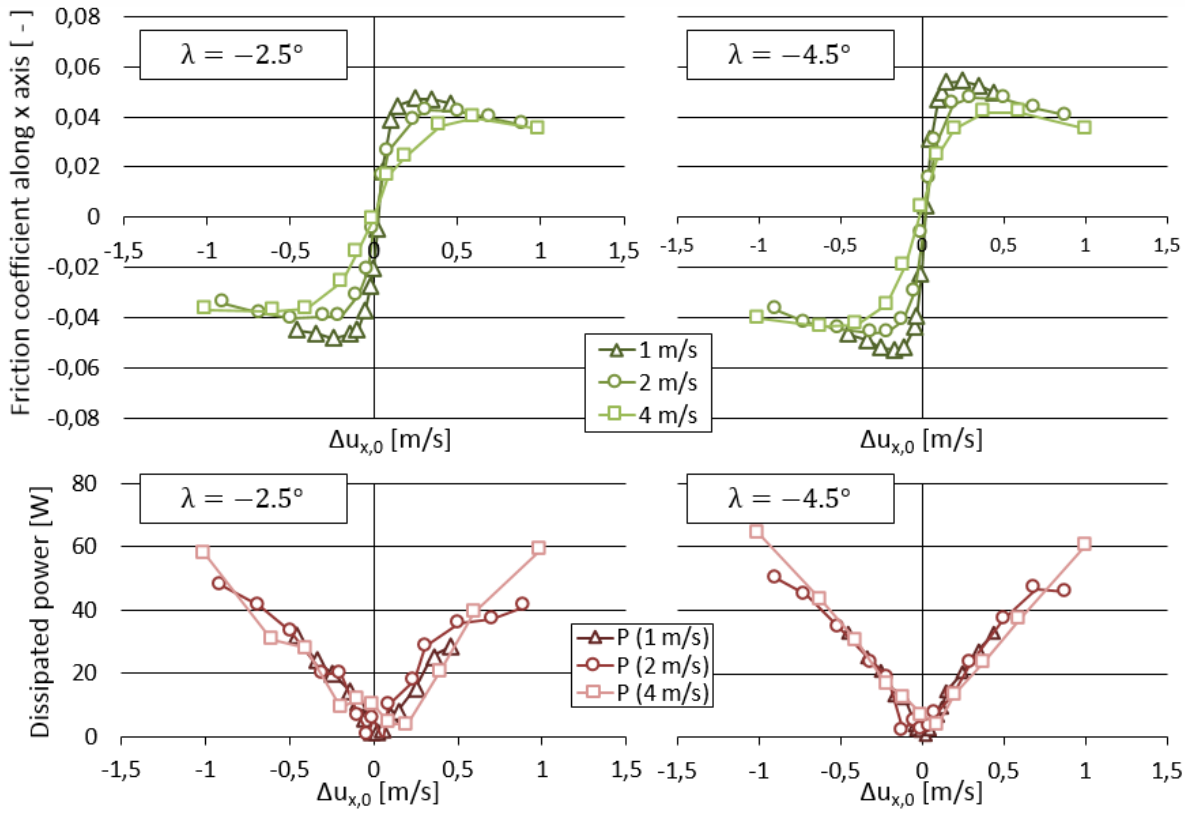


*Figure 4.2-2 – Experimental friction curves and dissipated power according to $\Delta u_{x,0}$ at $w = 1500\ N$ & $\lambda = -2.5°$ (left), $\lambda = -4.5°$ (right)*

The dissipated power curves, denoted by the letter $P$, are very similar within each graph of Figure 4.2-2. They represent the total dissipated power $P$ which is the sum of the sliding and the spinning losses. The lost power curves mainly depend linearly on the sliding velocity as it is visible on the graphs, whatever the entrainment velocity

In Figure 4.2-2, the friction reductions at large sliding are explained by the larger power dissipated in the contact. As the latter remains very similar for the different entrainment

velocity configurations, the friction also remains almost constant. This accordance between the friction curves and the power losses curve underlines a known result: this area of the friction curve is driven by the thermal effects (82).

This analysis shows the importance of the thermal effects. It also underlines the need for simulations that take into account the thermal effects but also the other lubricant thinning mechanisms, as its non-Newtonian behaviour.

As thermal effects have a large responsibility on the friction through the variation on the viscosity, it is possible that they have a significant influence on film thickness.

### 4.2.2. Influence on film thickness

Whereas the friction variations are important for the power losses predictions in real systems, the film thickness reduction is more related to wear prediction or prevention. This section evaluates the model ability to predict the consequences on film thickness of the large power dissipated in the contact and the solids. Indeed, with large power losses transformed into heat, the lubricant viscosity may decrease significantly. This viscosity decrease should imply a film thickness decrease.

In order to model the real contact conditions, the Tribogyr test-rig was used. In the following numerical and experimental analysis the film thickness reference case (described in section 3.3.2) was used again, but the spin angle was varied: in the present section $\lambda = -4.5°$. The sliding was varied in two consecutive steps: the first step was an increase of $|SRR_{x,0}|$, and the second was the $SRR_{x,0} = 0\%$ configuration, right after the first step:

$$\begin{gathered}\text{First step: from } SRR_{x,0} = 0\% \text{ to } SRR_{x,0} = -45\% \\ \text{Second step: } SRR_{x,0} = 0\%\end{gathered} \qquad \textit{Equation 4.2-2}$$

The two steps were done consecutively to isolate the global heating by comparing the $SRR_{x,0} = 0\%$ cases of the first and the second step. Within both steps, a time interval separated each measurement point. Indeed, for each sliding configuration, the entrainment velocity was applied as the upper and the bottom samples were not in contact. Then the load was progressively applied on the two bodies and they were both mating during a couple of minutes before the actual load was reached. When the target load was obtained, the temperature was measured in the incoming oil pipe and on the disc (see section 3.1.5): several contact interferograms were made during approximatively 20 $s$. Note that during the load adjustments and the related measurements, heat was already generated in the contact and the temperature of the bodies globally increased. Between two consecutive film thickness measurements, the temperature of the bodies decreased slowly when they were not mating (as the room temperature was approximately 25°C). These experimental details have to be taken into account for further discussions.

The mean film thicknesses obtained from the different interferograms under each sliding condition are plotted in Figure 4.2-3, together with the disc track temperatures. The incoming lubricant temperature remained stable at about 30°C. As two experimental steps are plotted together in the same graph, the coloured symbols represent the first step, while the black symbols represent the last step. To help the reader, arrows were plotted to indicate on the main curves the chronology.

The minimum film thickness is still plotted here, but as the measurements are below 100 $nm$, the interferometry results are much less accurate: they were performed without any spacer layer unlike in section 2.1.3. They are still plotted as they give qualitative results.

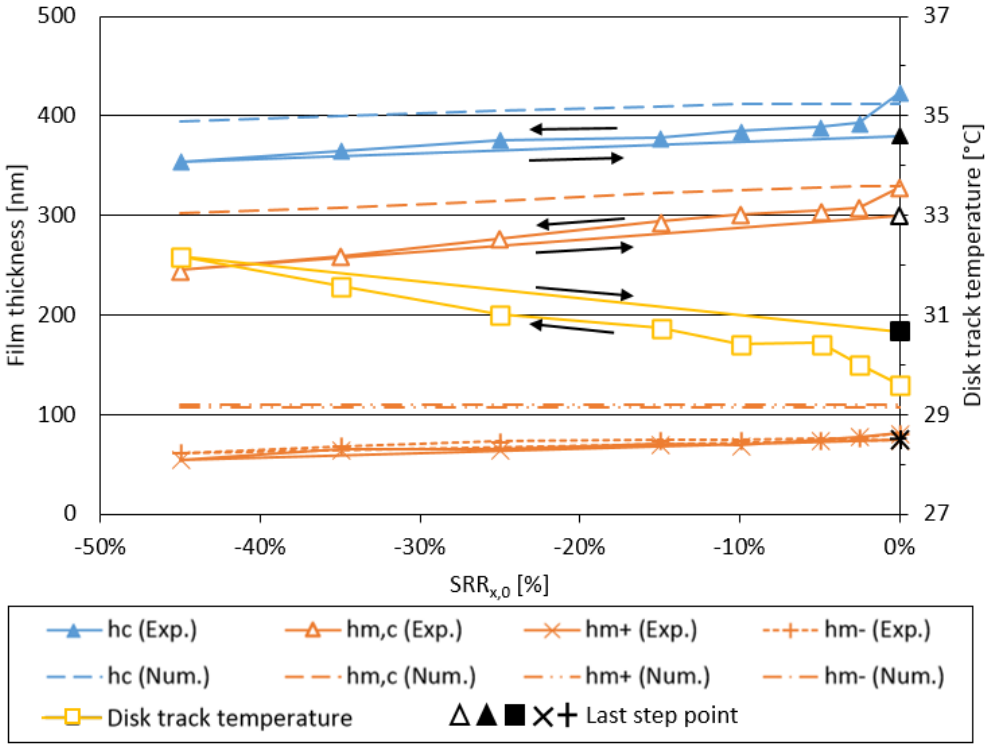


*Figure 4.2-3 - Experimental (Exp.) and numerical (Num.) film thickness results with various $SRR_{x,0}$ for the film thickness reference case, but with $\lambda = -4.5°$. For the experimental results the chronology is given by Equation 3.5 2.*

During the first step, when $|SRR_{x,0}|$ increases, the experimental film thickness globally decreases. Between the extreme sliding configurations, $h_c$ decreased by 16% and $h_{m,c}$ by ≈ 25%. The minima of the film thickness decreased both by more than 20%: because their measurement is not so precise, it is not the exact value which is underlined, but the decreasing trend. On its side, the temperature of the contact track on the disc increased by $2.6°C$. Unfortunately, the temperature of the contact track on the pin was not measured: the presence of the thermocouple tends to degrade its surface. Qualitatively, it is very likely that the temperature on the pin surface was larger than the one on the disc. Indeed:

- the steel conductivity is about 40 times larger than the glass conductivity,

- the disc requires about twice more energy than the pin to rise its temperature by $1°C$,
- and the track length on the pin is 3 times smaller than that on the disc. As a consequence, a portion of the pin track passes more frequently in the contact than for the disc track.

In the second step, the kinematic configuration was the same than at the beginning of the first step. However, between the $SRR_{x,0} = 0\%$ configurations of the first and second steps, $h_c$ decreased by 10% and $h_{m,c}$ by ≈ 9%. On its side, the disc track temperature is $1.1°C$ larger in the second step than at the beginning of the first one.

Besides, the numerical film thickness did not decrease significantly with the sliding increase. The central film thickness only decreased by 4% and $h_{m,c}$ by 8% (decreases between 3 and 4 times less than in the experiments). In the model, the incoming lubricant temperature and the solid's temperature at the computation domain boundaries are constant and set to $T_0 = 30°C$. As the temperature rise due to friction mainly happens inside of the contact, the contact inlet area is nearly at $T_0$ in the simulations. Because the film thickness is ruled by the conditions found in the inlet, the numerical model cannot predict a large film thickness decrease due to the sliding.

To experimentally evaluate the global warming of the two specimens, it would be interesting to measure the temperature on the contact track for both of them. However, in Tribogyr, the oil is spread on the disc. Consequently, the torus is not continuously fed with lubricant and the thermocouple-torus contact may be starved during the adjustment of the rotation velocity of the specimen. Wear may occur fast and invalidate any film thickness measurement via interferograms.

With Figure 4.2-3, it is possible to show that even a short running period with a single contact can lead to a film thickness reduction. This reduction is hard to predict as it depends on a global warming of the mating solids. A solution lies in the coupling with a global warming numerical model, at the scale of the solids dimensions. This model should be transient, and would be able to predict the track temperature from the knowledge of the power dissipated in the EHD contact. In its turn, the EHD model should be coupled with the global warming model by the temperature of the tracks at the inlet.

The sliding influences film thickness and friction in different ways. The friction is driven by the lubricant rheology and thermal behaviour inside the contact: as a result, the mating surface temperatures increase. The TOP FREC contact has a behaviour which is very similar to any other EHD contact about this. For its part, the film thickness is mainly determined by the lubricant rheology and thermal behaviour at the contact inlet. Consequently, the surface temperatures increase tends to thin the lubricant in the inlet. As the dissipated power is rather large, this temperature rise has a noticeable influence even after a few hundreds of cycles. As a prospect, it would be fruitful to develop a global warming model to predict the temperature rise of the specimens. It would also be useful to measure the temperature on the two specimen during the experiment, even if some minor challenges are to be expected.

So far in chapter 3, the TOP contact was modelled with its real gap geometry. In sections 4.1.1 and 4.1.2, the EE models were used in order to identify the role of the torus gap in the contact

behaviour. These sections did not conclude on the relevance of the torus gap modelling: is it mandatory to model the gap by the real geometry, or is it possible to proceed to simplifications? Direct comparisons are proposed in the next section to offer some answers.

## 4.3. Comparisons with equivalent elliptical (EE) contacts

According to the hypothesis made by Hamrock and Dowson (22) and others since then, the principal curvature radii of the contact can be used to model the bodies' geometry in the contact vicinity. However, with the large variations of the curvature radius in the TOP contact and the distorted kinematic fields, the principal curvature radii assumption (PCRA) may not be valid in all cases. This section aims to present the configurations in which the PCRA is valid and those in which the contact behaviour cannot be properly predicted. In these last cases, an alternative modelling is proposed.

For this purpose, the TOP EHD contact model and its EE model will be used. They were validated respectively in section 2.1.3 and section 3.3. The comparison will be made in terms of film thickness and friction. Because the film thickness prediction abilities of the model were proved with strength, this kind of comparison will be reliable. Friction comparisons will only be considered as relative indications between two models: indeed, it was demonstrated that they are not able to predict quantitatively the actual EHD friction.

### 4.3.1. Accordance of the models

#### *4.3.1.1. Film thickness and pressure*

The two models (TOP and EE) are compared in terms of ability to predict the characteristic values of the lubricant film thickness. In sections 4.1.1 and 4.1.2, a comparison was already established for one angular value of $\lambda$ and with the aim to understand the behaviour of the contact. Here, the comparison aims to inform the reader on the reliability of the EE model. Indeed, in the context of an engineer approach, the simplifications of the EE model would be of great help.

For the comparison, the friction reference case described in section 3.3.1 was used. The spin angle $\lambda$ was varied between $-6°$ and $-1°$. The film thickness characteristic values ($h_c$, $h_{m,c}$, $h_{m+}$ and $h_{m-}$) were obtained according to the description of section 3.1.3. The results for the two models are plotted in Figure 4.3-1.

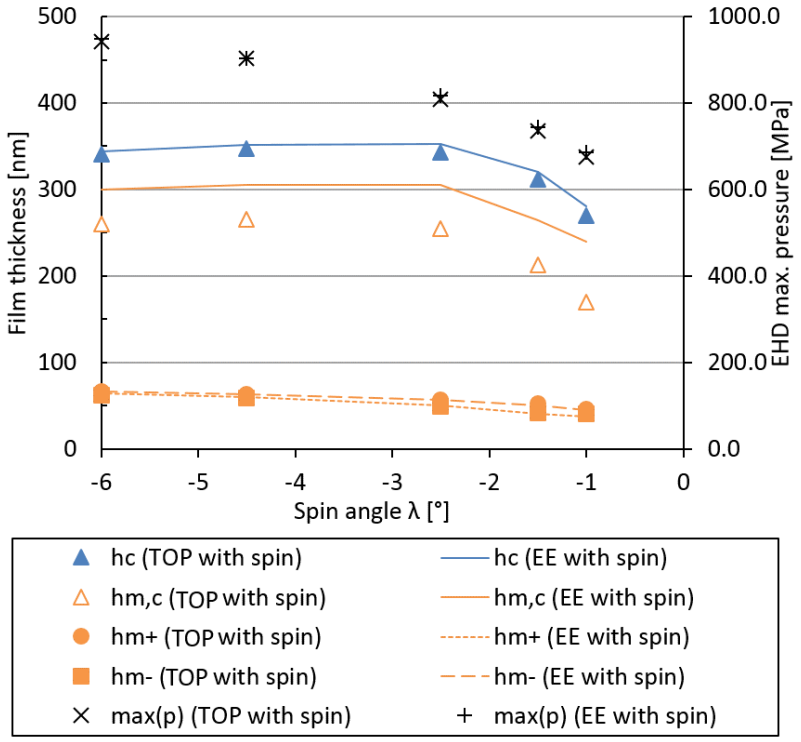


*Figure 4.3-1 - Comparison between TOP and EE film thickness characteristic values and maximum EHD pressure (numerical results) for the friction reference case ($u_{ex,0} = 2\ m/s$ and $w = 1500\ N$) with $SRR_{x,0} = 0\%$*

The reader may notice than in this figure, the trends are very similar between the two models: when $|\lambda|$ decrease, the global film thickness decreases. However, there are some minor distinctions between the TOP and the EE models. The central minimum film thickness $h_{m,c}$ is about 50 $nm$ larger in EE results than in the TOP results: this is mainly due to a change of the localisation of the contact exit. According to the inlet streamline concept, the EE contact exit is located close the $x$ axis, whereas in the TOP gap, it clearly occurs on the $y < 0$ side of the contact. Consequently $h_{m,c}$ (which is the minimum film thickness along the $x$ axis) from the EE model cannot correspond to the one from the TOP model. Another definition of $h_{m,c}$ may show closer results but would be sensitive to apply at the measurement stage.

Besides, there are minor discrepancies in terms of central film thickness: according to the inlet streamline concept, the film thickness maxima do not occur at the same place of the contacts. However, the difference is less than 4%. At last, there is a difference at the film minima $h_{m+}$ and $h_{m-}$. In line with the literature (Dowson et al. (29), Taniguchi et al. (31), Doki-Thonon (5)) pertaining to spinning contact $h_{m+}$ and $h_{m-}$ are different. In the present cases, the difference is negligible for $\lambda = -6°$ but it is of about 10 $nm$ for $\lambda = -1.5°$. However, there is a significant difference between the results of the TOP and the EE models. Indeed, $h_{m+}$ and $h_{m-}$ in the EE results follow respectively the values of $h_{m-}$ and $h_{m+}$ in the TOP results. This means that the global minimum of the gap changed its position. It also means that the global minimum is located on the side of the contact where the inlet streamline is closer to the limit of the pressurised area. When the inlet streamline is close to a contact border, the lubricant is more likely to flow toward this border, to escape the contact and to reduce the film thickness locally.

However, the changes between the TOP and the EE results in terms of film thickness are not very important and it seems that the EE model can be used to predict within a reasonable confidence the TOP contact behaviour.

The maximum pressure is very similar in the two models, as showed in Figure 4.3-1. There is a maximum deviation of about 1.5%. The EE model appears sufficient to predict the EHD contact pressure.

With these rather good concordances in terms of maximum pressure (used in rolling contact fatigue prediction, for example) and film thickness (used to distinguish the mixed and the full film lubrication), the EE seems able to model the behaviour of the TOP contact with a good precision.

#### *4.3.1.2. Friction*

The friction results of the TOP and the EE model are compared in this sub-section. The cases computed here are the same than in the last sub-section 4.3.1, but the sliding was varied. Friction coefficient curves are plotted in Figure 4.3-2

.

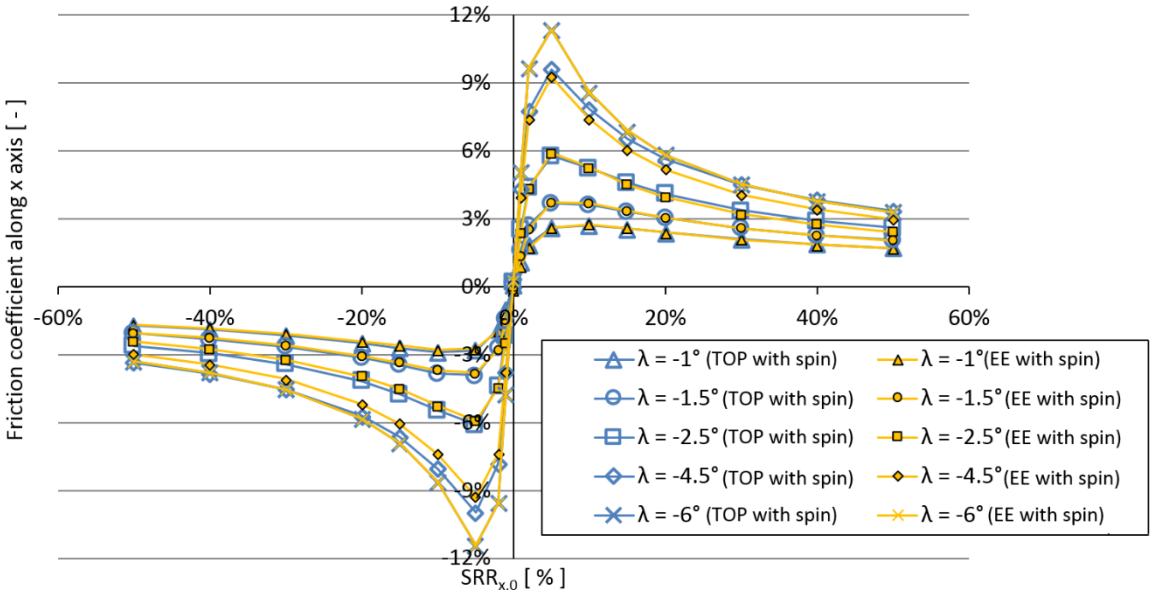


*Figure 4.3-2 - Friction curve comparison: TOP and EE model results for the friction reference case ($u_{ex,0} = 2\ m/s$ and $w = 1500\ N$)*

It clearly appears that the two models agree very well. It was demonstrated that their predictions are not quantitative but rather good orders of magnitude. Despite this weakness in terms of modelling, the results are the same in the two models: the unusual bodies' geometry in the TOP configuration did not affect the friction forces compared with the elliptical case. Whether the gap has the actual shape or an approximation, the shear stress integral in the pressurised lubricant did not change significantly.

Again, in the cases presented, the EE model seems sufficient to predict the behaviour of the contact. However, the role of the inlet streamline enables to consider a limit to the EE approximation: if this inlet streamline exits the contact before the end of the dry contact area, what happens to the entrapped lubricant?

### 4.3.2. The limits of the EE model

The EE model finds it limits when the TOP contact is too curved along the $x$ axis. Indeed, the kinematic is the same in the two models, but as the TOP contact shape changes significantly, there is a risk that the relation between the gap shape and the kinematic differs strongly between the two models. It is the case when $\lambda$ becomes very close to 0, like $\lambda = -0.5°$ for instance. It is a very small angle, but such a curved contact can be seen in the FREC but also in other applications, like in worm gears (see Kong et al. (41)).

The contact characteristics are given in Table 4.3-1. It is a very elongated and very narrow contact. Consequently, as it follows the curvature of the torus shape, the curvature is easily visible.

| Parameter [Unit] | Value |
|---|---|
| $a\ [mm]$ | 3.49 |
| $b\ [mm]$ | 0.375 |
| $k\ [-]$ | 0.11 |
| $p_h\ [MPa]$ | 547 |

*Table 4.3-1 - Dry contact characteristics for the friction reference case with $\lambda = -0.5°$*

EHD pressure distribution is plotted in Figure 4.3-3, together with the inlet streamline. From this figure, it clearly appears that the latter, along which the lubricant compression occurs, exits the pressurised area very early. The lubricant which should be carrying the load tends to exit the contact very quickly, in the abscissa range $-2 < x < -1\ mm$. The load is reported on the part of the lubricant which does not escape, but the film forming should be disturbed.

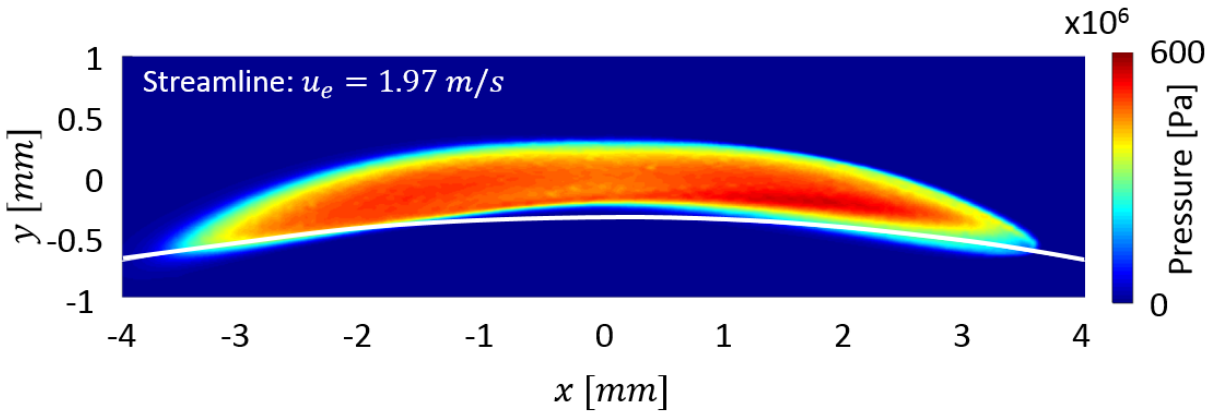


*Figure 4.3-3 - Friction reference case ($u_{ex,0} = 2\ m/s$ and $w = 1500\ N$) with λ=-0.5° and $SRR_{x,0} = 0\%$: pressure distribution for the TOP model*

Moreover, after its exit, the inlet streamline drives some part of the lubricant back in the contact area. However, this second entrance in the contact may be of a poor quality: as a film separation has already happened, the second feeding may not be fully-flooded but starved. The model described in section 2.1.2, and section 3.2 does not describe the air-lubricant biphasic flow at the film separation. As a consequence, the lubrication of the contact at the second entrance of the inlet streamline is probably not well described by the model. Because starvation and diphasic flow were note taken into account, the present model may not be sufficient to fully describe the $\lambda = -0.5°$ configuration, especially on the $x > 0$ side.

Despite these model insufficiencies, it still appears that the pressure distribution is very unusual. In Figure 4.3-3, in the central part of the contact along the x axis (the area where the inlet streamline is outside of the contact) the pressure is reduced. Indeed, because of the exiting flow, the pressure cannot be maintained locally. This pressure is reported on other places of the contact, where the lubricant cannot flow away. It appears that the kinematic field and the contact shape have lost their coherence. This lack of coherence leads to exiting lubricant and a degraded pressure distribution.

Figure 4.3-4 shows the film thickness distribution for the same case: the same elongated shape is observed. The inlet streamline has indeed crossed the local film thickness minimum on the side of the contact. It has entrained some lubricant out of the pressurised area. At the point $A$, the film thickness is approximately $h = 300\ nm$ but at the point $B$, $h = 250\ nm$. These two points are at the middle of the contact width and in another contact there would correspond to a very similar film thickness. But in the present case, some lubricant was lost before the exit, leading to a film thickness reduction.

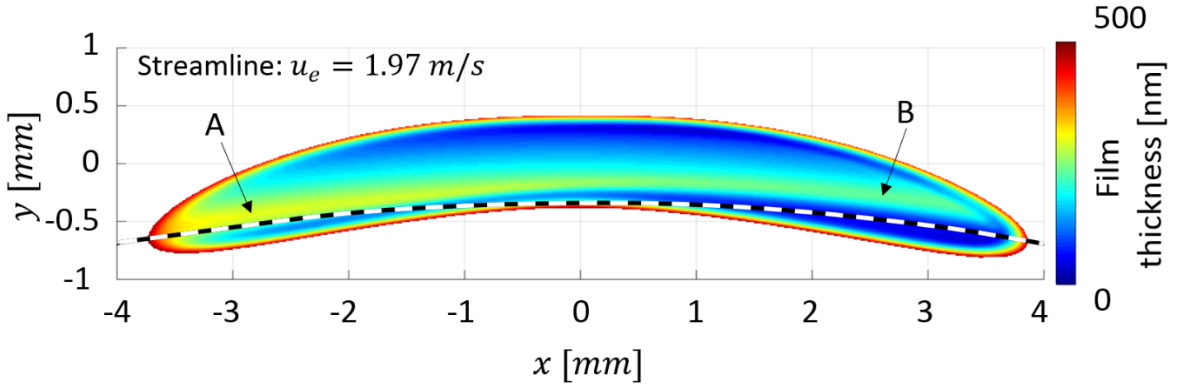


*Figure 4.3-4 - Friction reference case ($u_{ex,0} = 2\ m/s$ and $w = 1500\ N$) with λ=-0.5° and $SRR_{x,0} = 0\%$: film gap for the TOP model*

The summary of the characteristic values of the film thickness is showed in Figure 4.3-5 together with the results of the larger $|\lambda|$ configurations. The global film thickness minimum is 34 $nm$ for $\lambda = -0.5°$, which corresponds to the dark blue area in the right bottom side in Figure 3.6-4: it is nearly twice smaller than the minimum in the same contact but with $\lambda = -6°$. However, this film minimum may be even smaller, as in the present model, the diphasic flow and the starvation are not represented.

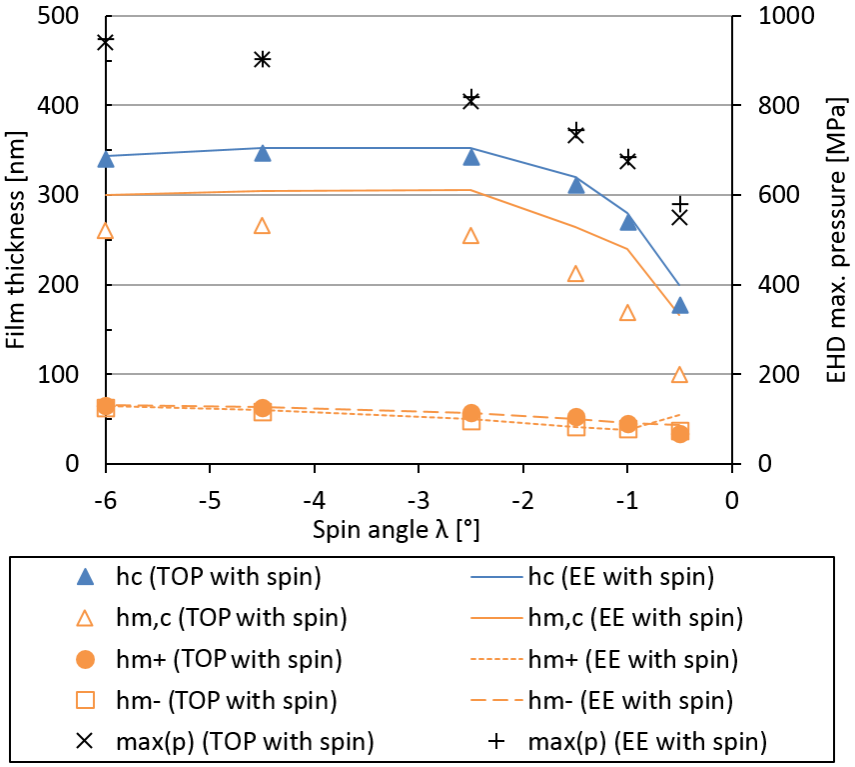


*Figure 4.3-5 - Comparison between TOP and EE film thickness characteristic values and maximum EHD pressure (like in Figure 4.3-1 but with the $\lambda = -0.5°$ case).*

On its side, the EE model also predicts an elongated contact. In Figure 4.3-6, the pressure distribution is represented together with the inlet streamline. In the EE results, the inlet streamline does not exit the pressurised area. This has a significant influence on the quality of the surface separation. Indeed, there is no pressure drop at the middle of the contact, as there is no unusual leakage due to the lack of coherence between the kinematic and the contact shape. This means that the EE model fails, in some situations, to predict the TOP FREC behaviour.

However, the EE model was reasonably correct in its prediction of the TOP maximum EHD pressure: it is only 5% larger in the EE model than in the TOP model.

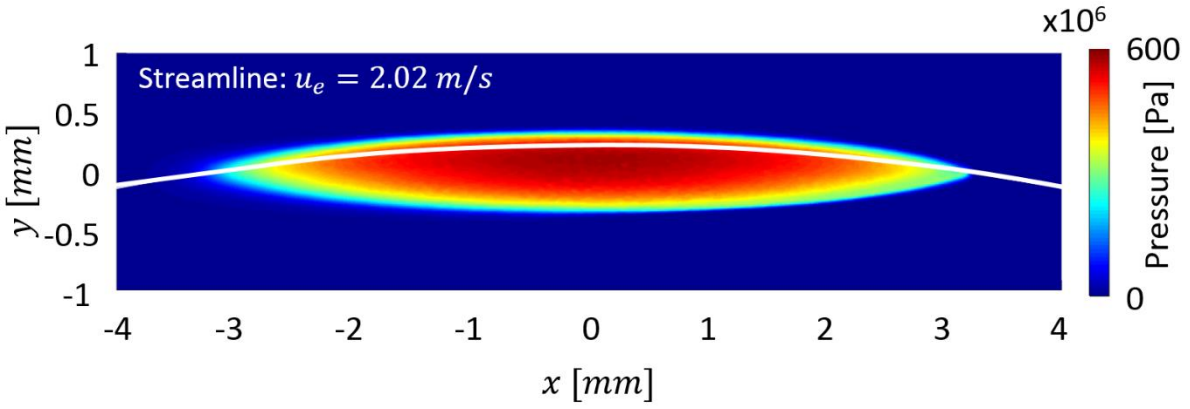


*Figure 4.3-6 - Friction reference case ($u_{ex,0} = 2\ m/s$ and $w = 1500\ N$) with λ=-0.5° and $SRR_{x,0} = 0\%$: pressure distribution for the EE model*

Though asymmetric, the pressure distribution of the EE model is more conventional than in the TOP model. As a result, the film thickness is also more conventional (see Figure 4.3-7): the lubricant does not exit prematurely the contact and the surface separation is better. In Figure 4.3-7, the iso-thickness lines follow the inlet streamline. This means that the lubricant which enters the pressurised area at the inlet, is driven throughout the contact area by the entrainment velocity, and finally exits the contact at its classical outlet, on the opposite side. All along the contact, the lubricant is able to separate the surfaces. At the $A$ point of the contact (see Figure 4.3-7), the film thickness is equal to 300 $nm$, and it is still of 290 $nm$ at the point $B$.

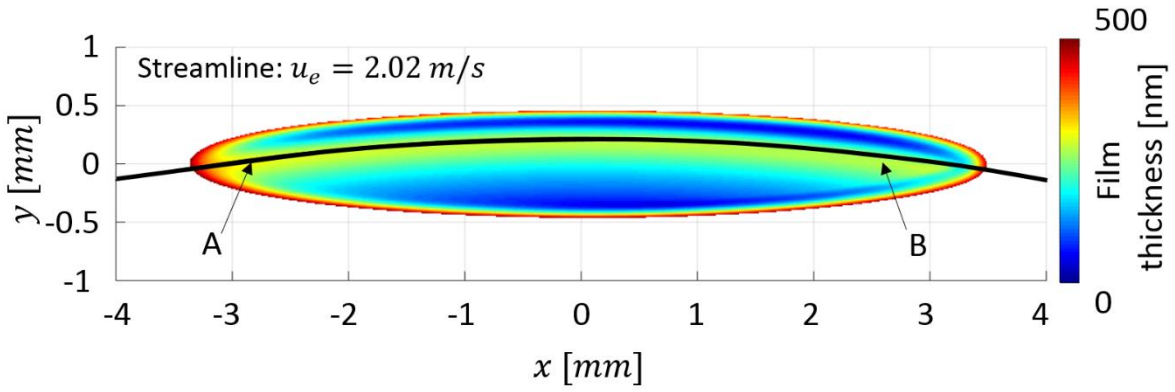


*Figure 4.3-7 - Friction reference case ($u_{ex,0} = 2\ m/s$ and $w = 1500\ N$) with λ=-0.5° and $SRR_{x,0} = 0\%$: film gap for the EE model*

Figure 4.3-5 presents the film thickness comparison between the TOP model results, and the ones stemming from the EE simulations. The EE model now predicts a $23\ nm$ larger film thickness than the TOP model on $h_c$. The difference in the model predictions is more particularly true at the global minimum: even if it is not very visible on this global graph, it is actually 30% larger in the EE model than in the TOP configuration. Moreover, the global minimum was $h_{m+}$ in all configurations of the EE model, but it is $h_{m-}$ in the $\lambda = -0.5°$ configuration. In terms of film thickness prediction, the EE model also has some limits and it cannot predict with confidence the behaviour of all TOP contacts studied here, especially if the TOP contact it is supposed to model has lost its kinematic-shape coherence.

To summarise, the EE model generally models well a TOP contact gap in the context of EHD lubrication. However, if the TOP contact loses its kinematic-shape coherence, the EE model may predict wrong results. It is very likely that it would over-estimate the film thickness. To detect this limit of the EE model, a simulation is not mandatory: indeed, the inlet streamline can be predicted without computation, together with the shape of the contact. So by gathering the information from the kinematic and the bodies' geometry, it is possible to anticipate the modelling risk and to model the TOP gap in an appropriate way.

## 4.4. Conclusion

This last chapter investigated the torus on plane (TOP) EHD conjunction in order to identify the role of the different operating conditions and to propose a simplification of the numerical model.

The spin angle $\lambda$ appeared as the key parameter in the analysis of the TOP EHD contact: the spin angle drives the size, the surface, the shape of the contact but also its pressure (both EHD and Hertz pressures). With the same sample, the contact dimensions can be very different, whether the spin angle is close to zero or not. The larger spin angle configurations are quite similar to an elliptical contact, whereas small spin angle configurations are so elongated along the torus that it is strongly curved by the bodies' geometry. Because the spin angle drives the maximum pressure, it also influences the viscosity increase in the contact and, ultimately, the spin angle drives the friction.

This spinning contact can exhibit a significant power dissipation. A sliding occurs even when the sliding at the contact centre is zero, and the mating bodies' temperature rises, leading to an interaction between the thermal aspects of the contact at its own scale, and the thermal behaviour of the whole solids, at their scale. For better predictions, it appeared mandatory to couple these two scales.

For the present torus pin and both moderate and large spin angle, it is possible to predict the torus on plane contact behaviour by the elliptical equivalent model. Indeed, under such conditions, the torus on plane contact is very similar to an elliptical one.

When the spin angle is small, the behaviour of the torus on plane contacts is less conventional and differs to the one of an elliptical contact. In this context, the concept of "inlet streamline" was developed: it is the streamline that enters the pressurised area at first, and it is the one along which the pressure generally is the largest. In non-spinning contacts, this streamline remains on the symmetry axis of the contact and the distance between the streamline and the contact borders is the same on both sides. However, when the spinning kinematic is introduced together with the curved contact, this inlet streamline is not located on the symmetry axis anymore. It becomes closer to one frontier, and the whole contact is then disturbed in terms of pressure and film separation.

When the spin angle becomes very small, the inlet streamline may exit the pressurised area much before the end of the contact. In this case, the predictions of the elliptical equivalent model significantly differ from the ones of the torus on plane model. It is also very likely that the torus on plane numerical model presented in this thesis may not be able to describe its actual behaviour, which may include diphasic flows and possibly starvation. It would be interesting to improve the current numerical model with these features that may occur for the configurations with the smallest values of the spin angle.

# Conclusions and Prospects

# Conclusions and prospects

## General conclusion

After a general introduction to the flange roller-end and the EHD contacts, the torus on plane flange roller-end contact problem was introduced in chapter 1. Following this introduction, the literature pertaining to this topic was presented. This bibliography analysis underlined the need for more investigations on elliptical contacts and more specifically slender elliptical contacts, which are similar to the torus on plane flange roller-end contact. Moreover, it evidenced the lack of torus on plane flange roller-end contact study which included the real mating bodies' geometry.

Following the literature review, chapter 2 addressed the investigations of the elliptical contacts, as a first approach to the torus on plane flange roller-end contact. This analysis was made with a test-rig, Jérotrib, which enabled reliable film thickness measurements. Thanks to the experimental results, a numerical model was evaluated and a good film thickness prediction capacity was demonstrated. This validation constitutes a progress in the elliptical EHD model literature. This model was used to investigate the influence of the ellipticity on the contact behaviour. A focus on the fluid flow was presented in order to understand the causal links between the upstream gap shape – which are driven by the ellipticity – and the film forming capacity.

Chapter 3 and 4 were dedicated to the study of the torus on plane flange roller-end contacts with the actual bodies' geometry. Chapter 3 presented the numerical model, the Tribogyr test-rig and a validation of the model via the experimental measurements of the test-rig. It is very likely that such an experimental-numerical comparison is proposed for the first time to a non-elliptical point contact. Then chapter 4 provides an analysis of the torus on plane contact. It was demonstrated that the spin angle is the key parameter. It defined the contact pressure, the contact shape and the contact kinematic. As the pin end was a torus, the local curvature radii varied significantly and it influenced the whole contact. In most cases, the torus on plane flange roller-end contact could be approached by an elliptical equivalent flange roller-end contact. The film gap was well predicted by this simplified model. Indeed, the inlet streamline did remain inside the pressurised area in the two models. However, when the spin angle became very small, the inlet streamline exited the torus on plane model pressurised area but it did not in the elliptical equivalent model. This difference led to differences in the results of the two models. However, the torus on plane model was probably not able to predict the actual contact case behaviour as diphasic flow and starvation probably occurred due to the inlet streamline unusual trajectory. Besides, the torus on plane flange roller-end contact is a spinning and sliding contact: rather large power losses are evidenced. They have a large influence on the mating surface temperatures and consequently on film thickness. It was however not possible to predict the global heating of the solids.

To summarise, a model was developed in this thesis to predict the elliptical and general shape EHD contact behaviour. The model ability to predict film thickness was validated through two

different test rigs with two different contact types. This model failed to predict precisely the friction but better lubricant characterisation may enhance the prediction reliability. Thanks to this model, new conclusions were presented for the elliptical contact and the torus on plane contact.

Thanks to improved understanding and advanced numerical models, the film thickness in non-conventional EHD contact may be predicted with great confidence. As a better knowledge of the surface separation allows for better predictions, the future rolling bearings will be designed with an improved precision. This will lead to an advanced prognosis of the wear occurring in this poorly lubricated flange roller-end contact. Moreover, the prediction of film thickness can also be made with a simplified elliptical equivalent model in some well-defined cases. Indeed, as long as the inlet streamline remains inside of the torus on plane contact area, the film thickness can be predicted by both the torus on plane model and its elliptical equivalent.

## Recommendations for future work

Many aspects of the torus on plane contacts were extensively investigated in this work and a new understanding of these unusual contacts was presented. However, new questions were raised: they will be a good basis for future investigations.

At first, the model developed in this study showed very good film thickness prediction abilities but was not able to predict precisely the friction. It was demonstrated that this lack of precision came from the limits of the lubricant characterisation: though covering several physical parameters and a wide range of conditions for all of them, some restrictions penalised the model. Indeed, the shear dependence of the lubricant was evaluated in conditions that did not activate non-Newtonian behaviour. For further works, a wider characterisation of the lubricant may be required. This requirement is a call for progress in the development of new high-pressure rheometers.

It was established that for low spin angle cases (very elongated and curved contacts, similar to the flange roller-end contact in cylindrical roller bearings), the inlet streamline can exit the pressurised area before the end of the contact. Moreover, this streamline then enters the pressurised area again, but with less lubricant: a starvation may occur together with a diphasic flow. A diminution of the film thickness was exhibited. However, this configuration was not observed in the experiments, and the model may find some of its limits as it is not able to predict starvation and diphasic flows. New experiments and a more advanced model would be required to conclude on the film thickness reduction occurring in low spin angle cases.

Thermal effects were observed in this large sliding contact. The Tribogyr test-rig enabled to underline the global heating of the specimens which occurs during the experiment. However, the model was not built to be able to predict these thermal evolutions: indeed the global heating occurs at a time scale which is much longer than the characteristic heating time in the contact vicinity. Future models should include this longer time scale: indeed, the EHD contact dissipates power which heat the mating specimen. However, the specimen temperature has a

great influence on the contact behaviour itself. This reciprocal influence pleads for a full coupling between the two time scales.

In the introduction, the concave conical and spherical flanges were approximated by a plane as the curvature radii of the cone and the sphere are large at the contact. However, in some cases the finite curvature radius of the cone and the sphere may be of the same order of magnitude than the torus larger curvature radius at the contact centre. Moreover, it may be equal and even smaller than the torus larger curvature radius.

# Bibliography

# Bibliography


1. Molimard J. Etude expérimentale du régime de lubrification en film mince - Application aux fluides de laminage [Internet] [phdthesis]. INSA de Lyon; 1999. Available from: 1999ISAL0121

2. Dormois H. Frottement dans les contacts EHD de grandes dimensions, rôle du pivotement [phdthesis]. Institut National des Sciences Appliquées de Lyon, INSA; 2008.

3. Molimard J, Querry M, Vergne P. New tools for the experimental study of EHD and limit lubrications. Proc 25th Leeds-Lyon Symposium. 1999. p. 717–26.

4. Habchi W. A full-system finite element approach to elastohydrodynamic lubrication problems: application to ultra-low-viscosity fluids [Internet] [phdthesis]. Institut National des Sciences Appliquées de Lyon, INSA; 2008. Available from: http://theses.insa-lyon.fr/publication/2008ISAL0038/these.pdf

5. Doki-Thonon T. Thermal effects in elastohydrodynamic spinning circular contacts [phdthesis]. Institut National des Sciences Appliquées de Lyon, INSA; 2012.

6. Murnaghan FD. The compressibility of Media under Extreme Pressures. Proc Natl Acad Sci U S A. 1944;30(9):244–7.

7. Bair S, Mary C, Bouscharain N, Vergne P. An improved Yasutomi correlation for viscosity at high pressure. Inst Mech Eng. 2012;227:1056–60.

8. Bair S. A Rough Shear-Thinning Correction For EHD Film Thickness. Tribol Trans. 2004;47:361–5.

9. Colin F, Chevalier F, Chaomleffel J-P, de Mul J, Dalmaz G. Starved elastohydrodynamic lubrication of the rib-roller end contact in tapered roller bearings: film thickness, traction and moments. Tribology Series, Proceedings of the 24th Leeds-Lyon Symposium on Tribology. Elsevier; 1998. p. 253–63.

10. Chittenden RJ, Dowson D, Dunn JF, Taylor CM. A Theoretical Analysis of the Isothermal Elastohydrodynamic Lubrication of Concentrated Contacts - Part 2: General Case, with Lubricant Entrainment along Either Principal Axis of the Hertzian Contact Ellipse or at Some Intermediate Angle. Proc R Soc London. 1985;A397:271–94.

11. Blok H. Inverse problems in hydrodynamic lubrication and design directives for lubricated flexible surfaces. Proc Int Symp Lubr Wear. 1963;1–151.

12. Korrenn H. Gleitreibung und Grenzbelastung an den Bordflachen von Kegelrollenlagern. Fortschritte Berichte VD I Zeitschrift, Ser 1. 1967;11.

13. Karna CL. Performance characteristics at the rib-roller end contact in tapered roller bearing. Trans ASLE. 1974;17:14–21.

14. Zhang Z, Qiu Z, Hong Y. EHL analysis of rib-roller end contact in tapered roller bearings. Tribol Trans. 1988;31:461–7.

15. Dormois H, Fillot N, Vergne P, Dalmaz G, Querry M, Ioannides E, et al. First traction results of high spinning large-size circular EHD contacts from a new test rig: Tribogyr. Tribol Trans. 2009;52:2:171–9.

16. Doki-Thonon T, Fillot N, Vergne P, Morales-Espejel GE. Numerical insight into heat transfer and power losses in spinning EHD non-Newtonian point contacts. J Eng Tribol. 2012;226:23–35.

17. Doki-Thonon T, Fillot N, Morales-Espejel GE, Querry M, Philippon D, Devaux N, et al. A Dual Experimental Numerical Approach for Film Thickness Analysis in TEHL Spinning Skewing Circular Contacts. Tribol Lett. 2013;50:115–26.

18. Cann P, Lubrecht AA. An analysis of the mechanisms of grease lubrication in rolling element bearings. Lubr Sci. 1999;11–3:228–45.

19. Wren F, Moyer C. Understanding friction and EHL films in concentrated contacts of a tapered roller bearing. 1972 EHL Symposium. Institution of Mechanical Engineers; 1972. p. 55–60.

20. Gadallah N, Dalmaz G. Hydrodynamic lubrication of the rib-roller end contact of a tapered roller bearing. J Tribol. 1984;106:265–74.

21. Archard JF, Cowking EW. Elastohydrodynamic Lubrication at Point Contacts. Proc Inst Mech Engr. 1965;180:47–56.

22. Hamrock BJ, Dowson D. Isothermal elastohydrodynamic lubrication of point contacts - Part 1 - Theoretical Formulation. J Lubr Technol. 1976;98:223–8.

23. Hamrock BJ, Dowson D. Isothermal elastohydrodynamic lubrication of point contacts - Part 2 - Ellipticity parameter results. J Lubr Technol. 1976;98:375–83.

24. Hamrock BJ, Dowson D. Isothermal elastohydrodynamic lubrication of point contacts - Part 3 - Fully Flooded Results. J Lubr Technol. 1977;99:264–76.

25. Kapitza PL. Lubrication of rollers and spheres. Zhurn Tekh Fiz. 1955;25:747–62.

26. Poon SY, Haines DJ. Frictional behaviour of lubricated rolling-contact elements. Proc Instn Mech Engrs Part J J Eng Tribol. 1966;181:363–76.

27. Poon SY. Some Calculations to Assess the Effect of Spin on the Tractive Capacity of Rolling Contact Drives. Proc Inst Mech Eng Part J J Eng Tribol. 1970;185:1015–22.

28. Snidle RW, Archard JF. Theory of Hydrodynamic Lubrication for a Spinning Sphere. Proc Inst Mech Eng. 1969;184:839–48.

29. Dowson D, Taylor CM, Xu H. Elastohydrodynamic Lubrication of Elliptical Contacts with Spin and Rolling. Proc Inst Mech Eng Part C J Mech Eng Sci. 1991;205:165–74.

30. Yang P, Cui J. The influence of spinning on the performance of EHL in elliptical contacts. In: Evans HP, Snidle R, editors. Proceedings of the IUTAM Symposium on Elastohydrodynamics and Micro-elastohydrodynamics. Cardiff: Springer; 2006. p. 81–92.

31. Taniguchi M, Dowson D, Taylor CM. The effect of spin motion upon elastohydrodynamic elliptical contacts. Proceedings of the 23rd Leeds-Lyon Symposium on Tribology. Elsevier; 1997. p. 599–610.

32. Zou Q, Huang C, Wen S. Elastohvdrodvnamic Film Thickness in Elliptical Contacts with Spinning and Rolling. J Tribol. 1999;121(4):686–92.

33. Jiang X, Wong PL, Zhang Z. Thermal non-newtonian EHL analysis of rib-roller end contact in tapered roller bearings. J Tribol. 1995;117:646–54.

34. Ehret P, Dowson D, Taylor CM. Thermal Effects in Elliptical Contacts with Spin Conditions. Proceedings of the 25th Leeds-Lyon Symposium on Tribology. Elsevier; 1999. p. 685–703.

35. Liu X, Jiang M, Yang P, Kaneta M. Non-Newtonian Thermal Analyses of Point EHL Contacts Using the Eyring model. Trans ASME. 2005;127:70–81.

36. Miyata S, Hohn B-R, Michaelis K, Kreil O. Experimental investigation of temperature rise in elliptical EHL contacts related to rolling, sliding and spin motion. Proc 34th Leeds-Lyon Symp Tribol. 2008;41:1074–82.

37. Sichani MS, Enblom R, Berg M. Comparison of non-elliptic contact models: towards fast and accurate modelling of wheel-rail contact. 9th International Conference on Contact Mechanics and Wear of Rail/Wheel Systems. Chengdu, China; 2012. p. 120–8.

38. Wiest M, Kassa E, Daves W, Nielsen JCO, Ossberger H. Assessment of methods for calculating contact pressure in wheel-rail/switch contact. Wear. 2008;265:1439–45.

39. Simon V. Elastohydrodynamic lubrication of hypoid gears. J Mech Des. 1981;103:195–203.

40. Simon V. Thermo-EHD analysis of lubrication of helical gears. Jounal Mech Transm Autom Des. 1988;110:330–6.

41. Kong S, Sharif K, Evans HP, Snidle RW. Elastohydrodynamics of a worm gear contact. J Tribol. 2001;123:268–75.

42. Sharif KJ, Kong S, Evans HP, Snidle RW. Contact and elastohydrodynamic analysis of worm gears Part:1 Theoretical formulation. Proc Inst Mech Eng Part C J Mech Eng Sci. 2001;215:817–30.

43. Sharif KJ, Kong S, Evans HP, Snidle RW. Contact and elastohydrodynamic analysis of worm gears Part:2 Results. Proc Inst Mech Eng Part C J Mech Eng Sci. 2001;215:831–46.

44. Chittenden RJ, Dowson D, Dunn JF, Taylor CM. A Theoretical Analysis of the Isothermal Elastohydrodynamic Lubrication of Concentrated Contacts - Part 1: Direction of Lubricant Entrainment Coincident with the Major Axis of the Hertzian Contact Ellipse. Proc R Soc London. 1985;A397:245–69.

45. Habchi W, Eyheramendy D, Vergne P, Morales-Espejel GE. A full-system approach to the elastohydrodynamic line/point contact problem. J Tribol. 2008;130(2):21501–10.

46. Mostophi A, Gohar R. Oil film thickness and pressure distribution in elastohydrodynamic point contacts. Proc Instn Mech Engrs, Part C J Mech Eng Sci. 1982;24:173–82.

47. Evans HP, Snidle RW. Analysis of Elastohydrodynamic Lubrication of Elliptical Contacts with Rolling along the Major Axis. Proc Inst Mech Eng Part C J Mech Eng Sci. 1983;197(3):209–11.

48. Thorp N, Gohar R. Oil film thickness and shape for a ball sliding in a grooved raceway. J Lubr Tribol. 1972;94(3):199–208.

49. Bahadoran H, Gohar R. The oil film in elasto-hydrodynamic elliptical contacts. Wear. 1974;29:264–70.

50. Gledhill RH, Jackson A, Cameron A. An interferometric study of the EHL of elliptical

contacts aligned in the direction of rolling. Proceedings of the 5th Leeds-Lyon Symposium on Tribology. 1978. p. 116–20.

51. Koye KA, Winer WO. An Experimental Evaluation of the Hamrock and Dowson Minimum Film Thickness Equation for Fully Flooded EHD Point Contacts. J Lubr Technol. 1981;103:284–94.

52. Chittenden RJ, Dowson D, Taylor CM. Elastohydrodynamic Film Thickness in Concentrated Contacts: Part 1: Experimental Investigation for Lubricant Entrainment Aligned with the Major Axis of the Contact Ellipse. Proc Inst Mech Eng Part C J Mech Eng Sci. 1986;200:207–17.

53. Evans HP, Snidle RW. Wildhaber–Novikov circular arc gears: elastohydrodynamics. ASME J Tribol. 1993;115:487–92.

54. Nijenbanning G, Venner CH, Moes H. Film thickness in elastohydrodynamically lubricated elliptic contacts. Wear. 1994;176:217–29.

55. Sharif KJ, de Ling FB, Alanou MJ, Evans MP, Snidle RW. Film thickness predictions for elastohydrodynamic elliptical contacts over a wide range of radius ratios with consideration of side starvation. Proc IMechE, Part J J Eng Tribol. 2000;214:63–78.

56. Yang P, Qu S, Kaneta M, Nishikawa H. Formation of Steady Dimples in Point TEHL Contacts. Trans ASME. 2001;123:42–9.

57. Kaneta M, Kawashima R, Masuda S, Nishikawa H, Yang P, Wang J. Thermal Effects on the Film Thickness in Elliptic EHL Contacts With Entrainment Along the Major Contact Axis. Trans ASME. 2002;124:420–7.

58. Wang J, Yang P, Kaneta M, Nishikawa H. On the Surface Dimple Phenomena in Elliptical TEHL Contacts with Arbitrary Entrainment. Trans ASME. 2003;125:102–9.

59. Zhu D. Elastohydrodynamic Lubrication in Extended Parameter Ranges, Part Ill: Ellipticity Effect. Tribol Trans. 2003;46:585–91.

60. Holmes MJA, Evans HP, Snidle RW. Discussion. Tribol Trans. 2003;46:282–8.

61. Morales-Espejel GE, Dumont ML, Lugt PM. A Limiting Solution for the Dependence of Film Thickness on Velocity in EHL Contacts with Very Thin Films. Tribol Trans. 2005;48:317–27.

62. Damiens B. Modélisation de la lubrification sous-alimentée dans les contacts elastohydrodynamiques elliptiques [Internet] [PhD Thesis]. INSA de Lyon, FR; 2003. Available from: http://theses.insa-lyon.fr/publication/2003ISAL0037/these.pdf

63. Venner CH, Lubrecht AA. Revisiting film thickness in slender EHL contacts. Proc Inst Mech Eng Part C J Mech Eng Sci. 2010;224:2549–58.

64. Canzi A, Venner CH, Lubrecht AA. Film thickness prediction in elastohydrodynamically lubricated elliptical contacts. Proc Inst Mech Eng Part J J Eng Tribol. 2010;224:917–23.

65. Stahl K, Michaelis K, Mayer J, Weigl A, Lohner T, Omasta M, et al. Theoretical and Experimental Investigations on EHL Point Contacts with Different Entrainment Velocity Directions. Tribol Trans. 2013;56:5:728–38.

66. Pu W, Wang J, Zhang Y, Zhu D. A theoretical analysis of the mixed elastohydrodynamic

lubrication in elliptical contacts with an arbitrary entrainment angle. J Tribol. 2014;136:41505.

67. Chaomleffel J-P, Dalmaz G, Vergne P. Experimental results and analytical film thickness predictions in EHD rolling point contacts. Tribol Int. 2007;40:1543–52.

68. Westlake FJ, Cameron A. A Study of Ultra-Thin Lubricant Films Using and Optical Technique. Proc IMechE, Conf Proc. 1967;182 (7):75–8.

69. Hartl M, Krupka I, Poliscuk R, Liska M, Molimard J, Querry M, et al. Thin Film Colorimetric Interferometry. Tribol Trans. 2001;44 (2):270–6.

70. Johnson KL. Contact mechanics. 1st ed. Cambridge: Cambridge University Press; 1985.

71. Moes H. Lubrication and Beyond, Chapter 10: Survey of the Hertz Solution, Lectures Notes, code 115532. Enschede, The Netherlands: University of Twente; 2000.

72. Badulescu C, Bornert M, Dupré J-C, Equis S, Grédiac M, Molimard J, et al. Demodulation of Spatial Carrier Images : Performances Analysis of Several Algorithms Using a Single Image. Exp Mech. 2013;53:1357–70.

73. Born M, Wolf E. Principles of optics: electromagnetic theory of propagation, interference and diffraction of light. 1999.

74. Raisin J, Fillot N, Vergne P, Dureisseix D, Lacour V. Transient Thermal Elastohydrodynamic Modeling of Cam – Follower Systems: Understanding Performance. Tribol Trans. 2016;59:4:720–32.

75. Najji B, Bou-Saïd B, Berthe D. New formulation for lubrication with Non-Newtonian fluids. J Tribol. 1989;111(1):29–34.

76. Wu SR. A penalty formulation and numerical approximation of the Reynolds-Hertz problem of elastohydrodynamic lubrication. Int J Eng Sci. 1986;24–6:1001–13.

77. Raisin J, Fillot N, Dureisseix D, Vergne P, Lacour V. Characteristic times in transient thermal elastohydrodynamic line contact. Tribol Int. 2015;82–B:472–83.

78. Habchi W, Eyheramendy D, Bair S, Vergne P, Morales-Espejel GE. Thermal elastohydrodynamic lubrication of point contacts using a Newtonian/generalized Newtonian lubricant. Tribol Lett. 2008;30:41–52.

79. Cheng HS. A refined solution to the thermal-elastohydrodynamic lubrication of rolling and sliding cylinders. ASLE Trans. 1965;8, issue 4:397–410.

80. Moes H. Optimum similarity analysis with applications to elastohydrodynamic lubrication. Wear. 1992;159:57–66.

81. van Leeuwen HJ. The determination of the pressure viscosity coefficient of a lubricant through an accurate film thickness formula and accurate film thickness measurements. Proc Inst Mech Eng, Part J J Eng Tribol. 2009;223(8):1143–63.

82. Habchi W, Bair S, Vergne P. On friction regimes in quantitative elastohydrodynamics. Tribol Int. 2013;58:107–17.

83. Sany R. Modélisation d'un contact complexe dans les roulements à rouleaux coniques [mastersthesis]. INSA de Lyon; 2014.

84. Hertz H. Über die Berührung fester elastischer Körper. J für reine und Angew Math.

1881;92:156–71.

85. Ståhl J, Jacobson BO. A non-Newtonian model based on limiting shear stress and slip planes—parametric studies. Tribol Int. 2003;36:801–6.

86. Habchi W, Vergne P, Bair S, Andersson O, Eyheramendy D, Morales-Espejel GE. Influence of pressure and temperature dependence of thermal properties of a lubricant on the behaviour of circular TEHD contacts. Tribol Int. 2010;43:1842–50.

# Annexes

# V. Annexes

## 5.1. Annexe A: The calibration method

During this thesis, the differential colorimetric interferometric method developed by Molimard et al. (3,69) was improved in order to enable measurements on non-circular contacts. The previous method required a circular Hertzian contact because this method is based on the rotational invariant properties of the circle. In elliptical or torus on plane contact, this property is lost. Moreover, in circular contacts, an analytical expression of the gap in the Hertzian contact vicinity exists (see Equation 2.1-4), but no gap function is available for non-circular contacts.

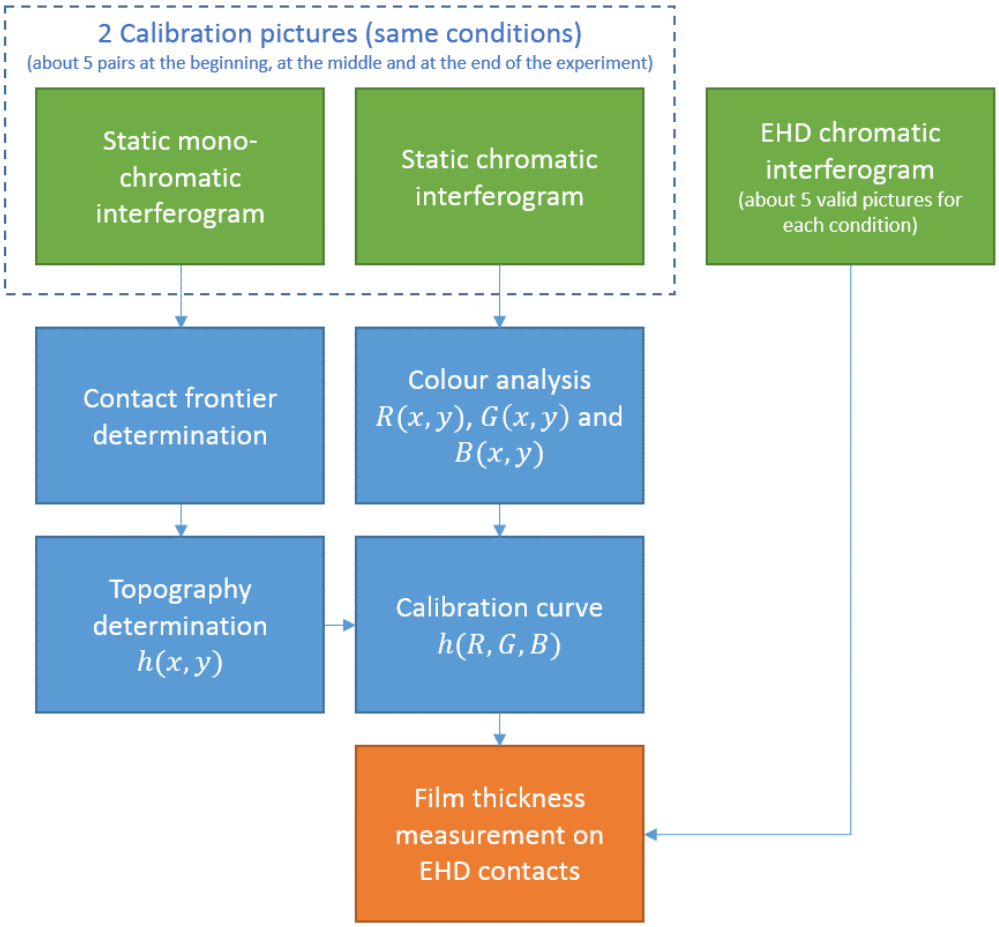


*Figure 5.1-1 – Algorithm of the new differential colorimetric method*

Therefore, a new method was developed, and its algorithm is presented in Figure 5.1-1. It is based on 2 calibration pictures made under the same conditions: a chromatic and a mono-chromatic interferogram of the Hertzian contact. Through the mono-chromatic interferogram,

the frontier of the contact is determined at first. Based on the position of this frontier and the dark fringes, the distribution of the gap is obtained in the contact vicinity: $h(x, y)$ is now determined. Through the chromatic interferogram, the distribution of the colour (defined by its decomposition in the RGB frames captured by a digital 3-CCD camera) is obtained. Then, a combination of the colour distribution and the gap distribution is made to get the calibration curve $h(R, G, B)$.

Thanks to this calibration curve, interferograms of static and EHD contact can be analysed. Indeed, any colour defined in the calibration curve corresponds to a single film thickness in the range $0 - 800\,nm$. In sections 2.1.3 and 3.3.2, the new differential colorimetric interferometry method is validated by the good accordance between the measurements and the numerical predictions under EHD conditions.

In Figure 5.1-2, the comparison is made between the film thickness measurement in a Hertzian static contact vicinity and a numerical result. The numerical model used here is the one described in Annexe B. The mating specimens are described in Table 2.1-1 and Table 2.1-2, where the steel convex specimen is the "Slender elliptical". The contact load is $w = 11.3\,N$. There is a very good accordance between the experimental and numerical results, in the two ellipse directions. The two graphs of Figure 5.1-2 confirm the validity of the new method developed in this thesis.

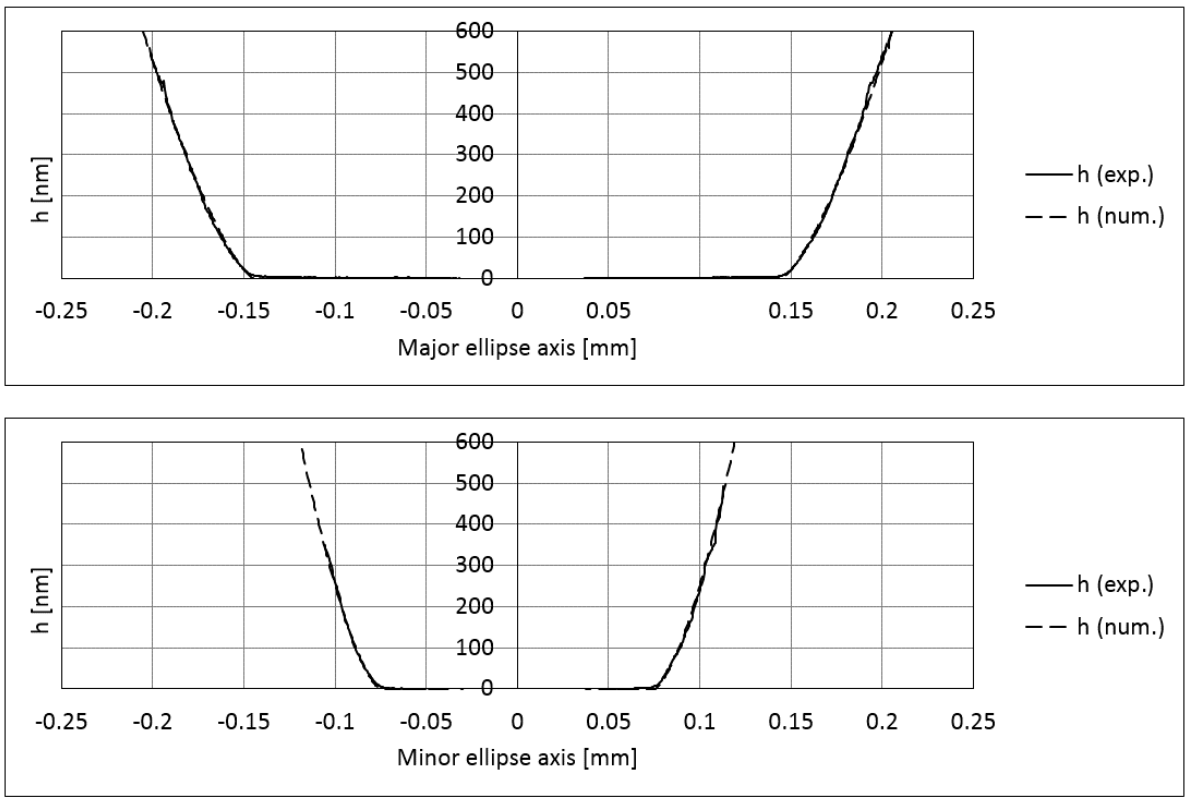


*Figure 5.1-2 – Comparison between the numerical results and the new method results in the vicinity of an elliptical Hertzian contact*

## 5.2. Annexe B: torus on plane static contact investigations

The biggest novelty of the thesis is the shape of the contact: it is neither elliptical nor linear. It is another shape, more complex than the elliptical contact, but still similar to it.

### a) Experimental tool

One of the challenges of the thesis is to apprehend this new contact and develop the geometrical tools to define it under static conditions. For this purpose, a dual approach is adopted. The Tribogyr test-rig described in section 3.1 provides opportunities to make contacts between a torus and a plane with a good positioning precision for the mating bodies (see Figure 5.2-1). Moreover, the plane is a glass disc and it enables to measure the position of the contact frontier by an in-situ observation. With this tool, it is possible to establish an experimental approach of the static contact behaviour.

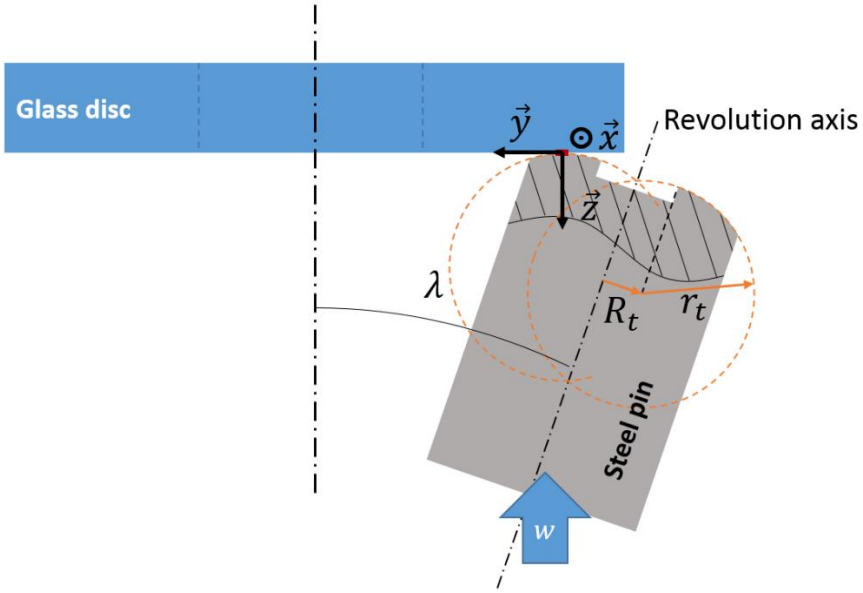


*Figure 5.2-1 - Steel torus and glass disc definition and geometrical relative positions in the Tribogyr test-rig*

Table 5.2-1 presents the conditions of the experiments with the test-rig. The data presented are the same than in chapter 4 but for the reader's convenience they are detailed in this annexe.

| Parameter [ Unit ] | Value | Description |
|---|---|---|
| $R_t\ [mm]$ | 0.011 | Torus major radius |
| $r_t\ [mm]$ | 0.040 | Torus minor radius |
| $E_b\ [Pa]$ | $210 \times 10^9$ | Bottom solid Young modulus |
| $E_t\ [Pa]$ | $62.8 \times 10^9$ | Top solid Young modulus |
| $\nu_b\ [-]$ | 0.3 | Bottom solid Poisson ratio |
| $\nu_t\ [-]$ | 0.2 | Top solid Poisson ratio |
| $\lambda\ [°]$ | $[-0.5\ \text{to}-6]$ | Spin angle |
| $w\ [N]$ | varying | Contact load |
| $e_n\ [N.m^{-3}]$ | $10^{18}$ | Penalty contact law parameter |
| $t_n\ [N.m^{-2}]$ | $10^8$ | Penalty contact law parameter |
| $depth\ [m]$ | varying | Penetration depth of the torus in the fictional plane |
| $\vec{F}\ [MPa]$ | varying | Contact pressure |

*Table 5.2-1 - Operating conditions for the static contact considered*

Under the conditions defined in Table 5.2-1, the contact is observed by a microscope through the glass disc. Figure 5.2-2 presents one of these contacts. The minor semi axis is defined similarly to the one of a classical ellipse, but the major semi axis has another definition: it is the distance between the two furthest extremities of the torus, along the arc of radius $R_r = R_t + r_t \sin(\lambda)$. This new definition was proposed by Sany (83) and has no great influence on the value of $2a$ when $a \ll R_r$. But when $\lambda$ becomes close to zero, $a$ increases significantly and $R_r$ decreases. As a consequence the contact shape sticks to the curvature of the arc defined by the radius $R_r$.

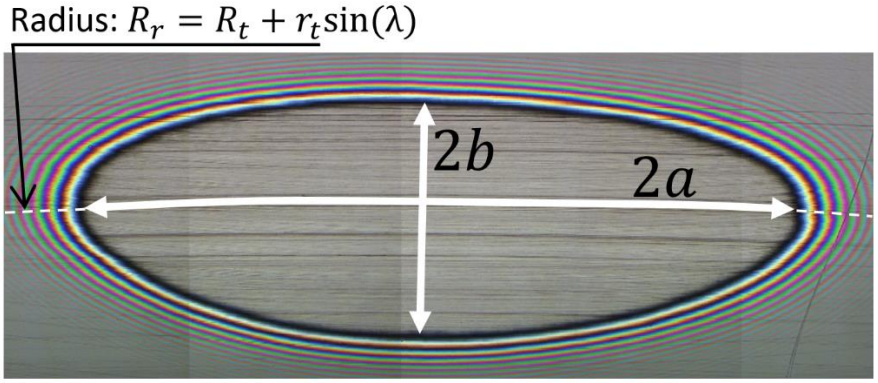


*Figure 5.2-2 - TOP contact,* w=240 N *and* $\lambda = -3°$

### b) Numerical tool

A numerical tool was also developed to study the TOP static conjunction. It is a finite element (FE) model. The model was developed jointly with Nicolas Fillot during the master thesis of Romain Sany (83). Figure 5.2-3 presents the contact law: it is based on a single body representation (the torus) on which a load is applied so that it mating a fictional half space. This half space is not represented in the actual model, but the reaction force is computed on the basis of the penetration depth of the torus in this half space. If $depth$ defined in Figure 5.2-3 is strictly negative it means that a penetration occurs and a very large stiffness response is applied. If $depth \geq 0$ there is no penetration and no contact pressure should occur. However, for consistency requirements, a 2nd order continuity of the $\vec{F}(depth)$ function is required and a negligible pressure is still applied. The torus body is supposed to have a linear elastic behaviour, defined by an equivalent Young modulus:

$$E_e = \frac{E_t \times E_b}{E_t + E_b} \qquad \textit{Equation 5.2-1}$$

and Poisson ratio:

$$\nu_e = \frac{\nu_t \times E_b + \nu_b \times E_t}{E_t + E_b} \qquad \textit{Equation 5.2-2}$$

This method is quite simple to implement, and gives reliable results under static conditions. The challenge is to define the adequate parameters $e_n$ and $t_n$. The larger they are, the stiffer the contact reaction is and the more precise is the contact behaviour determination. However, above $e_n = 10^{19}$ and $t_n = 10^9$, the convergence is very long. As a result, the parameters are defined as:

$$e_n = 10^{18} \text{ and } t_n = 10^8 \qquad \textit{Equation 5.2-3}$$

This choice is confirmed by a good accordance in more simple contacts (linear, circular and elliptical contacts) with Hertz theory. Though the results are not presented here, the developed model showed a good ability to predict the circular and elliptical contact pressure and

dimensions: the relative difference was below 1% between numerical and analytical predictions.

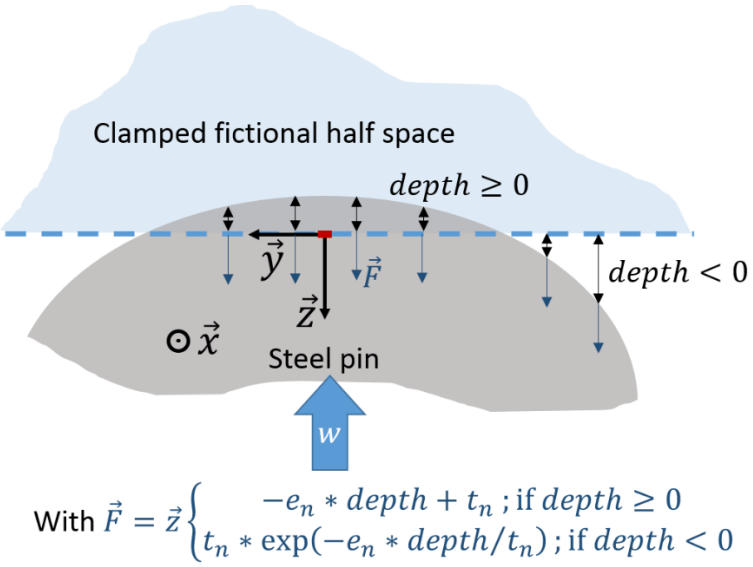


*Figure 5.2-3 - Penalty based contact model*

The evaluation of the model in the context of the TOP contact is done thanks to experimental measurements, as no precise analytical solution are available.

Indeed, the Hertz theory only proposes to model the bodies shape by their principal equivalent curvature radii (see section 1.3.4) at the contact centre. In the present case, the curvature radii of the mating surface vary in a large extent all over the contact area (see Figure 4.1-5). Hence the question: is it possible to approximate the TOP contact by an elliptical equivalent model? If not, is it possible to have a simplified model which allows for predicting the contact behaviour?

### c) Experimental validation

Tribogyr test-rig was used under precise conditions to generate TOP contacts. Though the model is already successfully validated by elliptical and linear contact comparison with analytical solutions, the contribution of an adequate experiment in the TOP case is useful.

Three load cases are reported here, $w = [240; 306; 610]\, N$ and the spin angle $\lambda = -3°$ was applied. The results for the model and the experiment are presented in Table 5.2-2. There is a good precision for the value of the major axis $a$ of the contact: it is a good news as it is in this direction that the curvature radii of the torus varies the most. However, the difference is larger for the value of the minor axis $b$. This may be explained by the difficulty to control the machining curvature radius in this direction: it should be $r_t = 40\, mm$ but a precise measurement of this radius is not possible.

| w [N] | Experimental | | Numerical | | Differences on: | |
|---|---|---|---|---|---|---|
| | 2a [mm] | 2b [mm] | 2a [mm] | 2b [mm] | a [%] | b [%] |
| 610 | 3.38 | 1.08 | 3.36 | 1.02 | −0.6 | −5.7 |
| 306 | 2.71 | 0.86 | 2.64 | 0.80 | −2.5 | −7.0 |
| 240 | 2.55 | 0.82 | 2.46 | 0.75 | −3.6 | −9.1 |

*Table 5.2-2 - Experimental validation of the model*

As a consequence of the comparison between numerical and experimental results, the model is validated and can be used to study the TOP contact.

### d) The influence of the spin angle $\lambda$

Thanks to the numerical model which was validated previously, a numerical study is proposed. The influence of the spin angle is investigated and a pressure distribution analytical model is proposed.

Spin angle has a significant influence on the static contact properties. From the same torus body and the same contact load, several spin angle values can generate very different contact shapes and pressure. Consequently, the spin angle is varied as follows:

$$\lambda = [-0.25°; -0.5°; -1.5°; -2.5°; -3.5°; -6°] \qquad \textit{Equation 5.2-4}$$

It corresponds to the range of configurations of the TOP FREC in real industrial applications. In this range, the numerical model is used, and the results are summarised in Figure 5.2-4. The numerical results are defined as presented in Figure 5.2-2 of Annexe B, but the analytical results are simply the ones defined by the Hertz theory.

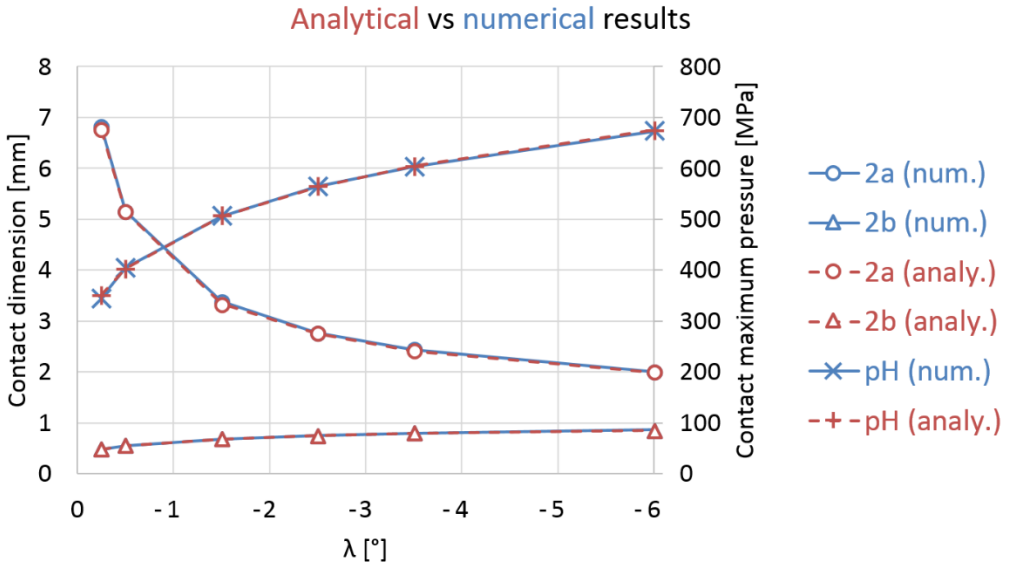


*Figure 5.2-4 - Comparison between analytical and numerical models*

The good accordance of Figure 5.2-4 confirms that the contact major axis should be considered as the distance along the radius $R_r$ between the extremities of the contact area. Figure 5.2-5 presents the contact with the smallest spin angle: it appears clearly that the pressurised area is not an ellipse but that it is a curved ellipse. Moreover, the curvature follows the $R_r$ arc.

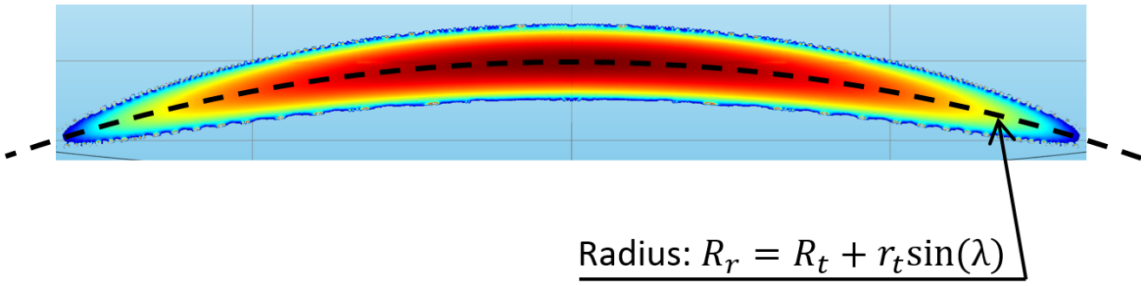


*Figure 5.2-5 – Pressure field of a TOP contact: $\lambda = 0.25°$; $a = 6.4\ mm$; $b = 0.5\ mm$; $max(p) = 346\ MPa$*

As a consequence, one proposes to use the Hertz theory for the prediction of the TOP contact pressure distribution. The subtlety of the proposed analytical prediction is that the TOP contact is not an ellipse, but it is an ellipse that follows the $R_r$ arc. Moreover, it is proposed that the pressure field is the one of the equivalent Hertz elliptical contact, but again it follows the arc. By substituting cylindrical and Cartesian system variables, the proposed pressure field reads (in the contact frame):

$$p = \begin{cases} \sqrt{1 - L_1^2 - L_2^2}, & \text{if } L_1^2 + L_2^2 \leq 1; \\ 0, & \text{otherwise,} \end{cases} \qquad \textit{Equation 5.2-5}$$

with $L_1 = \left(\frac{\sqrt{x^2+(y+R_r)^2}-R_r}{b}\right)$ and $L_2 = \left(\frac{R_r * \arctan\left(\frac{x}{y+R_r}\right)}{a}\right)$

This proposed pressure fields corresponds well to the numerical pressure field. Figure 5.2-6 presents the comparison. Given that the characteristic values $a$, $b$ and $p_h$ were already compared in Figure 5.2-4, the comparison of Figure 5.2-6 only pertains to the global field. Thanks to these two figures, an analytical approach of the static TOP contact pressure distribution appears very precise despite the differences with a classical elliptical contact. Indeed, the Hertz contact is originally dedicated to elliptical contacts.

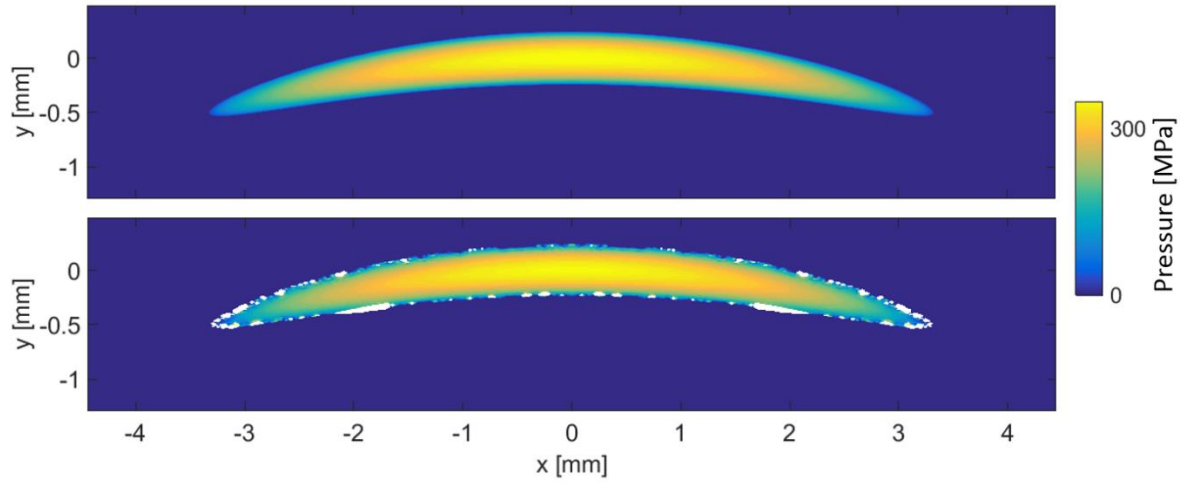


*Figure 5.2-6 – Pressure field comparison between analytical (based on Equation 5.2-5) and numerical solution*

In his analysis, Hertz (84) was maybe more visionary than he thought, and his work enables precise predictions in non-conventional configurations.

## 5.3. Annexe C: non-Newtonian lubricant hypothesis

In order to build a reliable and precise EHD model, advanced rheology models were established. They were based on an independent test campaign with three different rheometers. Figure 5.3-1 presents the characterisation results in terms of shear stress for Lubricant 3. It did not present any non-Newtonian behaviour in the tested range. Within the extended operating conditions of the Couette rheometer, it was not possible to increase the shear stress high enough to see a discrepancy to the Newtonian behaviour. Lubricant 2 presented similar results.

To investigate the transition between the Newtonian and the non-Newtonian regime, an oil from the literature and similar to Lubricant 3 and Lubricant 2 was selected; this oil had been characterised in a wider shear stress range and the non-Newtonian thinning was observed. A Carreau-Yasuda fit was applied to the experimental data of this supplementary oil. The Carreau-Yasuda fit was used to extrapolate how the Lubricant 3 would be thinned if it had behaved like the supplementary oil. In Figure 5.3-1, the Carreau extrapolation shows that a non-Newtonian trend may occur at a shear stress a little larger than the one explored. If the high pressure Couette rheometer was able to increase the shearing condition, a shear thinning may have been observed.

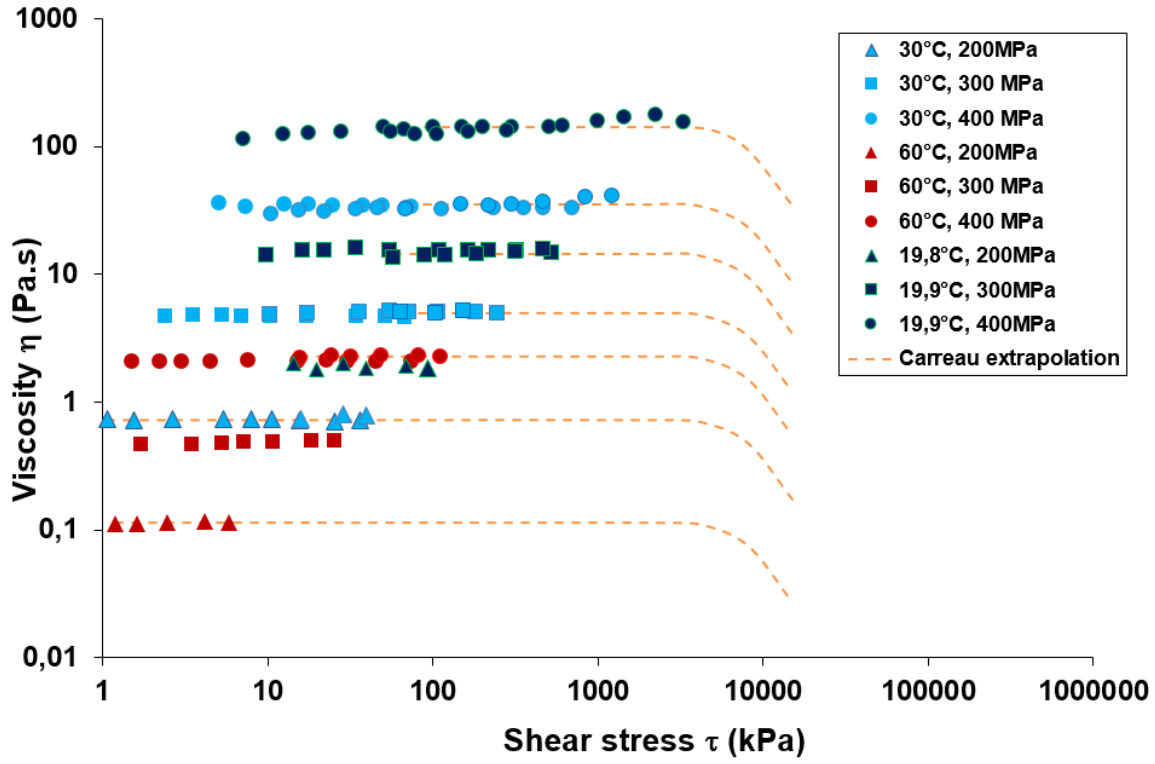


*Figure 5.3-1 – Lubricant 3 characterisation data and Carreau extrapolation*

Thanks to this consistent explanation to the absence of the shear thinning, it is possible to run simulations with a non-Newtonian model of the lubricant.

The generalized Carreau-Yasuda formulation (8) was selected and it reads:

$$\eta = \frac{\mu}{\left[1 + \left(\frac{\tau}{G_{CY}}\right)^{a_{CY}}\right]^{\frac{\frac{1}{n_{CY}}-1}{a_{CY}}}} \qquad \textit{Equation 5.3-1}$$

with $\mu$ the Newtonian viscosity, $\tau = \sqrt{\tau_{zx}^2 + \tau_{zy}^2}$ the shear stress norm, $\tau_{zx}$ and $\tau_{zx}$ the shear stresses in the contact plane along the x and y directions and $a_{CY}, n_{CY}$ and $G_{CY}$ are constants that were defined according to the experimental characterisation of the lubricant similar to Lubricant 2 and 3. The values of the constants are reported in Table 5.3-1.

| **Carreau-Yasuda parameters** | |
|---|---|
| **Parameter [Unit]** | **Value** |
| $a_{CY}\ [-]$ | 5 |
| $G_{CY}\ [Pa]$ | $7 \times 10^6$ |
| $n_{CY}\ [-]$ | 0.35 |

*Table 5.3-1 – Parameters of the Carreau-Yasuda model*

With the non-Newtonian description of the lubricant, the generalised viscosities become:

$$\frac{1}{\eta_e} = \int_0^h \frac{1}{\eta} dz \text{ and } \frac{1}{\eta_e'} = \int_0^h \frac{z}{\eta} dz \qquad \textit{Equation 5.3-2}$$

This means that the Equation 2.1-18 becomes:

$$\rho_e = \int_0^h \rho\, dz,\ \rho_e' = \int_0^h \left(\rho \int_0^z \frac{1}{\eta} dz'\right) dz,\ \rho_e'' = \int_0^h \left(\rho \int_0^z \frac{z'}{\eta} dz'\right) dz,$$
$$\bar{\varepsilon} = \frac{\eta_e}{\eta_e'}\rho_e' - \rho_e'',\ \rho_i^* = \rho_e' \eta_e \left(u_{t,i} - u_{b,i}\right) - \rho_e u_{b,i} \qquad \textit{Equation 5.3-3}$$

And at last, the generalised Reynolds equation (Equation 2.1-20) becomes:

$$\vec{\nabla}.\left((\bar{\varepsilon})\vec{\nabla}p\right) - \vec{\nabla}.\overrightarrow{\rho^*} = 0 \qquad \textit{Equation 5.3-4}$$

With this new formulation of the numerical model, Thermal non-Newtonian EHD simulations are possible. As the friction calculation are likely to be affected by the changes, the friction validation case presented in section 3.3.1 is computed anew and presented in Figure 5.3-2.

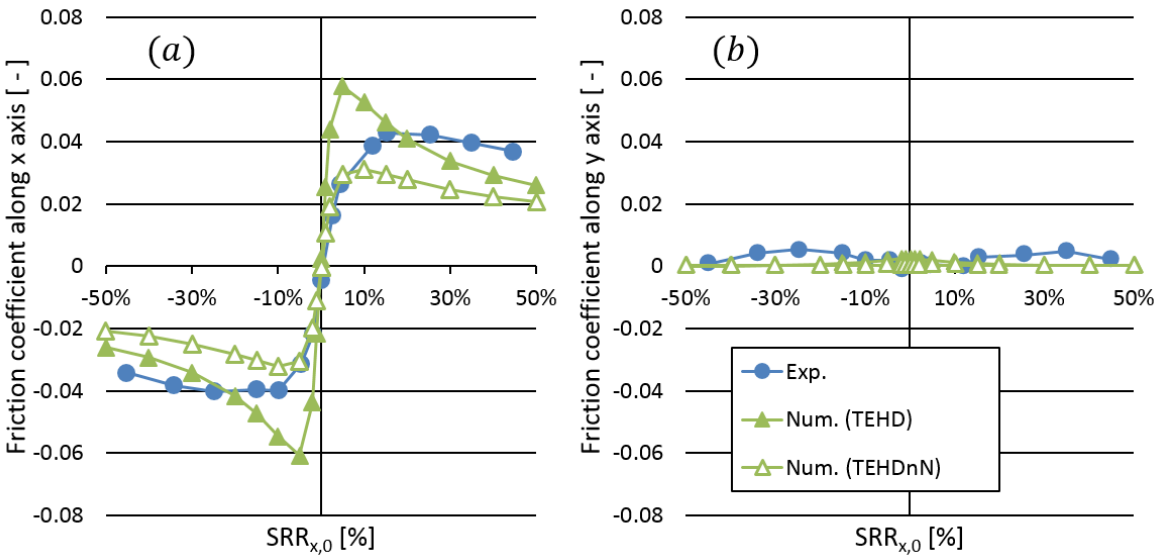


*Figure 5.3-2 - Friction coefficient along x direction (a, left) and y direction (b, right): comparison between experimental measurements (Exp.), thermal EHD numerical model (Num. (TEHD)) and thermal non-Newtonian EHD numerical model (Num. (TEHDnN)) results – reference case presented in Table 3.3-1*

The new numerical friction results (Thermal non-Newtonian EHD model) are different from the previous numerical results (Thermal EHD model): the new friction coefficient along x axis (see Figure 5.3-2a) is smaller with the non-Newtonian model, and the two numerical curves are different everywhere, but they follow similar trends. Indeed, after a nearly linear slope in the Newtonian region ($-5 < SRR_{x,0} < 5\%$), the two curves experience a limitation in the non-Newtonian region ($5\% < |SRR_{x,0}| < 20\%$). Then, the friction coefficient decreases in the thermal region ($20\% < |SRR_{x,0}|$).

The experimental curve is different from both numerical approaches. However, in the Newtonian region, the non-Newtonian friction curve is closer to the experimental results than the Newtonian one. To be more specific, the curve slope in the Newtonian region of the curve is very similar on the experimental and the non-Newtonian curve. On the contrary, the Newtonian curve is stiffer in this region. In the other regions, the experimental friction curve is clearly not similar to the numerical curves, whether the non-Newtonian effects are neglected or not.

Along the y axis, there is no significant change on the friction coefficient between the Newtonian and the non-Newtonian approaches: both of them appear similar, and they differ from the experimental friction coefficient.

It is noticeable that taking into account the non-Newtonian behaviour of the lubricant confers an improvement of the modelling precision, especially in the Newtonian region. However, this improvement does not allow for a quantitative prediction of the friction coefficient by the numerical model under more severe sliding conditions. There are still significant differences between the model and the experimental results. To diminish the discrepancies, it would be

mandatory to base the Carreau-Yasuda characterisation on the same oil than the one used during the friction experiments.

Another way to model the specifics of the lubricant in the torus-on-plane case was also explored. It consists in computing a Thermal EHD simulation (the same modelling than in the Chapters 2 and 3 of this document), but doing a post-treatment of the results with a limiting shear stress (LSS) assumption. The LSS model proposed initially by Ståhl and Jacobson (85) was used, with the revisions proposed by Habchi et al. (86) and Raisin et al. (74).

In this revised definition, the shear stress becomes independent of the apparent strain rate (defined by the velocity difference of the mating surfaces) when the shear stress reaches the limiting value:

$$\tau_L = \Lambda p \qquad \textit{Equation 5.3-5}$$

with $\Lambda$ the limiting shear stress coefficient and $p$ the pressure in the contact. Ståhl and Jacobson (85) affirm that $\Lambda$ typically varies between 0.03 and 0.15. In the absence of lubricant characterisation, and similarly to Raisin et al. (74), the LSS coefficient was arbitrary defined as $\Lambda = 0.05$.

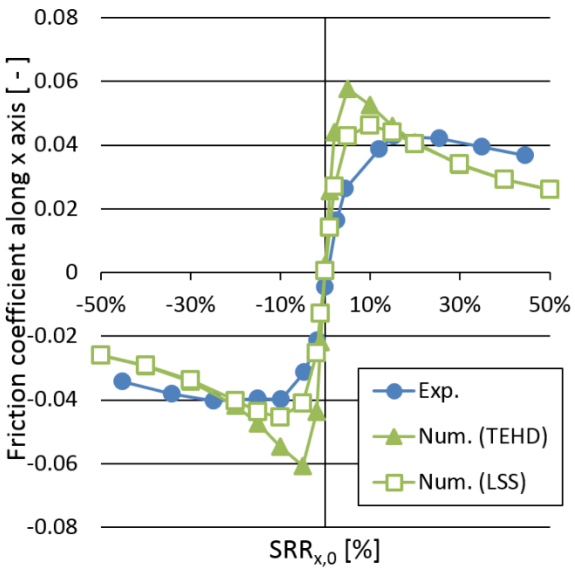


*Figure 5.3-3 – Friction coefficient along x direction: comparison between experimental measurements (Exp.), thermal EHD numerical model (Num. (TEHD)) and thermal EHD numerical model with limiting shear stress (Num. (LSS)) results – reference case presented in Table 3.3-1*

The results are presented in Figure 5.3-3 and a comparison is made between the thermal EHD model friction coefficient with and without LSS. As expected, there is a difference between the two numerical approaches, especially at the largest values of friction. In the non-Newtonian region of the curves ($5\% < |SRR_{x,0}| < 20\%$), the model which includes the LSS has a lower

friction coefficient than the one without LSS. In the other regions, the two numerical curves are similar.

Though the extrema of the numerical curve with LSS is closer to the extrema of the experimental curve, none of the numerical curves follows the trend of the experimental results.

In the context of EHD friction prediction, the thermal EHD approach shows the need for a more complex rheology modelling of the lubricant. For instance, a non-Newtonian modelling is mandatory. In the heavily loaded contacts, it is also necessary to take into account the LSS. However, this advanced approach should be based on an independent characterisation of the lubricant used in the experiment: it is probably what is missing here.

## 5.4. Annexe D: Tabulated values, elliptic cases

| | U [-] | W [-] | G [-] | M [-] | L [-] | k [-] | $h_c$ [nm] | $h_m$ [nm] | $h_{m,c}$ [nm] | $h_{m,l}$ [nm] |
|---|---|---|---|---|---|---|---|---|---|---|
| Case 1 | 2.38E-12 | 6.22E-07 | 4671 | 193 | 6.90 | 5.03 | 263 | 219 | 219 | 243 |
| | 2.09E-12 | 4.78E-07 | 4671 | 163 | 6.68 | 3.96 | 274 | 227 | 227 | 236 |
| | 1.75E-12 | 3.36E-07 | 4671 | 131 | 6.39 | 2.92 | 287 | 230 | 238 | 230 |
| | 1.38E-12 | 2.09E-07 | 4671 | 97.6 | 6.02 | 1.98 | 302 | 220 | 251 | 220 |
| | 1.13E-12 | 1.40E-07 | 4671 | 76.0 | 5.73 | 1.46 | 311 | 206 | 257 | 206 |
| | 8.61E-13 | 8.13E-08 | 4671 | 54.0 | 5.35 | 1.00 | 316 | 181 | 260 | 181 |
| | 6.38E-13 | 4.46E-08 | 4671 | 37.1 | 4.96 | 0.683 | 307 | 151 | 252 | 151 |
| | 4.92E-13 | 2.65E-08 | 4671 | 26.8 | 4.65 | 0.504 | 290 | 129 | 236 | 129 |
| | 3.45E-13 | 1.30E-08 | 4671 | 17.2 | 4.26 | 0.342 | 255 | 96 | 203 | 96 |
| | 2.55E-13 | 7.13E-09 | 4671 | 11.8 | 3.95 | 0.252 | 219 | 74 | 174 | 74 |
| | 2.00E-13 | 4.37E-09 | 4671 | 8.70 | 3.71 | 0.199 | 186 | 58 | 151 | 58 |
| Case 2 | 5.96E-13 | 4.14E-06 | 4671 | 3635 | 4.88 | 5.03 | 83 | 71 | 71 | 304 |
| | 5.22E-13 | 3.18E-06 | 4671 | 3082 | 4.72 | 3.96 | 88 | 76 | 76 | 199 |
| | 4.38E-13 | 2.24E-06 | 4671 | 2476 | 4.52 | 2.92 | 93 | 79 | 79 | 109 |
| | 3.46E-13 | 1.40E-06 | 4671 | 1841 | 4.26 | 1.98 | 99 | 62 | 84 | 62 |
| | 2.83E-13 | 9.35E-07 | 4671 | 1433 | 4.05 | 1.46 | 104 | 48 | 88 | 48 |
| | 2.15E-13 | 5.42E-07 | 4671 | 1019 | 3.78 | 1.00 | 107 | 34 | 92 | 34 |
| | 1.59E-13 | 2.97E-07 | 4671 | 700 | 3.51 | 0.683 | 113 | 25 | 95 | 25 |
| | 1.23E-13 | 1.77E-07 | 4671 | 506 | 3.29 | 0.504 | 113 | 18 | 96 | 18 |
| | 8.61E-14 | 8.67E-08 | 4671 | 324 | 3.01 | 0.342 | 111 | 10 | 93 | 10 |
| | 6.38E-14 | 4.76E-08 | 4671 | 223 | 2.79 | 0.252 | 101 | 7.6 | 86 | 7.6 |
| | 4.99E-14 | 2.91E-08 | 4671 | 164 | 2.63 | 0.199 | 96 | 6.5 | 81 | 6.5 |
| Case 3 | 2.38E-12 | 4.14E-06 | 4671 | 1285 | 6.90 | 5.03 | 217 | 186 | 186 | 394 |
| | 2.09E-12 | 3.18E-06 | 4671 | 1090 | 6.68 | 3.96 | 226 | 194 | 194 | 303 |
| | 1.75E-12 | 2.24E-06 | 4671 | 875 | 6.39 | 2.92 | 238 | 203 | 203 | 222 |
| | 1.38E-12 | 1.40E-06 | 4671 | 651 | 6.02 | 1.98 | 254 | 169 | 217 | 169 |
| | 1.13E-12 | 9.35E-07 | 4671 | 507 | 5.73 | 1.46 | 263 | 141 | 225 | 141 |
| | 8.61E-13 | 5.42E-07 | 4671 | 360 | 5.35 | 1.00 | 275 | 111 | 237 | 111 |
| | 6.38E-13 | 2.97E-07 | 4671 | 248 | 4.96 | 0.683 | 279 | 83 | 239 | 83 |
| | 4.92E-13 | 1.77E-07 | 4671 | 179 | 4.65 | 0.504 | 274 | 63 | 235 | 63 |
| | 3.45E-13 | 8.67E-08 | 4671 | 115 | 4.26 | 0.342 | 259 | 41 | 224 | 41 |
| | 2.55E-13 | 4.76E-08 | 4671 | 78.8 | 3.95 | 0.252 | 226 | 34 | 206 | 34 |
| | 2.00E-13 | 2.91E-08 | 4671 | 58.0 | 3.71 | 0.199 | 214 | 24 | 184 | 24 |
| Case 4 | 1.19E-11 | 4.14E-06 | 4671 | 384 | 10.3 | 5.03 | 674 | 578 | 578 | 696 |
| | 1.04E-11 | 3.18E-06 | 4671 | 326 | 10.0 | 3.96 | 701 | 601 | 601 | 648 |
| | 8.76E-12 | 2.24E-06 | 4671 | 262 | 9.56 | 2.92 | 736 | 606 | 629 | 606 |
| | 6.91E-12 | 1.40E-06 | 4671 | 195 | 9.01 | 1.98 | 778 | 558 | 664 | 558 |
| | 5.66E-12 | 9.35E-07 | 4671 | 152 | 8.57 | 1.46 | 802 | 505 | 685 | 505 |
| | 4.31E-12 | 5.42E-07 | 4671 | 108 | 8.00 | 1.00 | 821 | 428 | 701 | 428 |
| | 3.19E-12 | 2.97E-07 | 4671 | 74.0 | 7.42 | 0.683 | 812 | 345 | 692 | 345 |
| | 2.46E-12 | 1.77E-07 | 4671 | 53.5 | 6.96 | 0.504 | 778 | 280 | 659 | 280 |
| | 1.72E-12 | 8.67E-08 | 4671 | 34.3 | 6.36 | 0.342 | 695 | 203 | 583 | 203 |
| | 1.28E-12 | 4.76E-08 | 4671 | 23.6 | 5.90 | 0.252 | 597 | 149 | 508 | 149 |
| | 9.99E-13 | 2.91E-08 | 4671 | 17.3 | 5.55 | 0.199 | 515 | 112 | 443 | 112 |
| Case 5 | 2.38E-12 | 1.30E-05 | 4671 | 4016 | 6.90 | 5.03 | 195 | 170 | 170 | 665 |
| | 2.09E-12 | 9.95E-06 | 4671 | 3406 | 6.68 | 3.96 | 204 | 179 | 179 | 438 |
| | 1.75E-12 | 7.01E-06 | 4671 | 2736 | 6.39 | 2.92 | 217 | 187 | 187 | 246 |
| | 1.38E-12 | 4.36E-06 | 4671 | 2034 | 6.02 | 1.98 | 229 | 144 | 200 | 144 |
| | 1.13E-12 | 2.92E-06 | 4671 | 1583 | 5.73 | 1.46 | 240 | 109 | 210 | 109 |
| | 8.61E-13 | 1.69E-06 | 4671 | 1126 | 5.35 | 1.00 | 252 | 79 | 221 | 79 |
| | 6.38E-13 | 9.29E-07 | 4671 | 774 | 4.96 | 0.683 | 260 | 55 | 229 | 55 |
| | 4.92E-13 | 5.53E-07 | 4671 | 559 | 4.65 | 0.504 | 262 | 41 | 226 | 41 |
| | 3.45E-13 | 2.71E-07 | 4671 | 358 | 4.26 | 0.342 | 262 | 22 | 223 | 22 |
| | 2.55E-13 | 1.49E-07 | 4671 | 246 | 3.95 | 0.252 | 239 | 18 | 209 | 18 |
| | 2.00E-13 | 9.10E-08 | 4671 | 181 | 3.71 | 0.199 | 223 | 13 | 189 | 13 |

FOLIO ADMINISTRATIF

THESE DE L'UNIVERSITE DE LYON OPEREE AU SEIN DE L'INSA LYON

NOM : WHEELER DATE de SOUTENANCE : 05/12/2016

Prénoms : Jean-David, Lionel

TITRE : Non-Elliptical Point Contacts : the Torus-on-Plane Conjunction

NATURE : Doctorat Numéro d'ordre : 2016LYSEI131

Ecole doctorale : MEGA

Spécialité : Mécanique

RESUME :
Cette thèse est dédiée à l'étude des contacts lubrifiés tore plan sous diverses conditions. Ces contacts se situent à l'interface entre l'extrémité torique des rouleaux et le collet de la bague dans les roulements à rouleaux. La première complexité de cette étude provient de la géométrie particulière des solides concernés. La deuxième est générée par la cinématique complexe qui règne dans ces contacts. Afin de comprendre les mécanismes physiques à l'œuvre, une approche duale (expérimentale et numérique) est adoptée.
Le banc d'essai Jérotrib permet une première étude basée sur l'hypothèse que le contact élastohydrodynamique tore plan est similaire à un contact elliptique équivalent. Grâce à une méthode d'interférométrie optique en lumière blanche qui a été adaptée aux spécificités du contact en question, des mesures précises de l'épaisseur de film ont été effectuées dans un nombre significatif de conditions. Sur cette base, un modèle numérique thermo-élastohydrodynamique a été validé avec précision. Ce dernier a permis d'étudier les écoulements de fluide à l'entrée du contact afin de mettre en évidence leur influence sur le champ d'épaisseur de film.
Le modèle numérique a ensuite été amélioré afin de prendre en compte la vraie forme des solides. Il a été validé en épaisseur de film par le banc d'essai Tribogyr, dans des conditions similaires à celles rencontrées dans les vrais roulements. Il a été montré que le cisaillement du fluide est responsable de l'échauffement des solides, qui diminue par suite l'épaisseur de film : ceci souligne la nécessité de modéliser cet échauffement global pour prédire la séparation des surfaces. Par ailleurs, lors de l'étude, le champ de pression et d'épaisseur de film ont perdu leurs symétries à cause de la cinématique et de la forme des solides. Toutefois, le comportement du contact est resté similaire à celui d'un contact elliptique, en dehors de certains cas limites.

MOTS-CLÉS : Lubrification, élasto-hydrodynamique, contact ponctuel, contact tore-plan, elliptique, modélisation, expérimentation, frottement, épaisseur de film, pertes de puissance, écoulements, contact de grande dimension

Laboratoire de recherche : LaMCoS

Directeurs de thèse: P Vergne, D Philippon

Présidente de jury : A Fabre

Composition du jury : HP Evans, CH Venner, N Fillot, P Vergne, D Philippon, G E Morales-Espejel, J Molimard